



HAL
open science

Light propagation in integrated chains of metallic nanowires: towards a nano-sensing device

Ricardo Tellez Limon

► **To cite this version:**

Ricardo Tellez Limon. Light propagation in integrated chains of metallic nanowires: towards a nano-sensing device. Optics / Photonic. Université de Technologie de Troyes, 2014. English. NNT: 2014TROY0039 . tel-03358814

HAL Id: tel-03358814

<https://theses.hal.science/tel-03358814>

Submitted on 29 Sep 2021

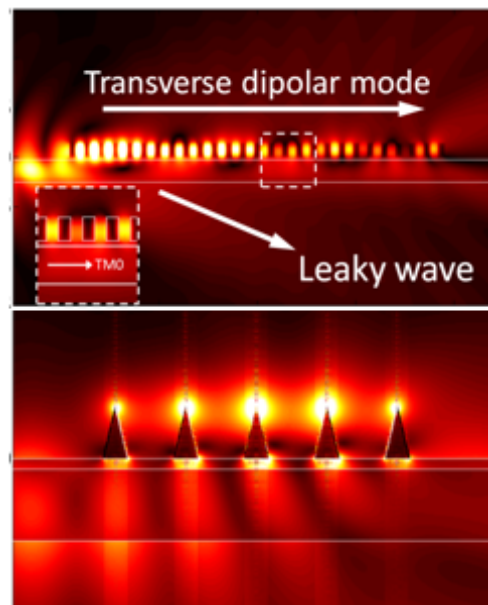
HAL is a multi-disciplinary open access archive for the deposit and dissemination of scientific research documents, whether they are published or not. The documents may come from teaching and research institutions in France or abroad, or from public or private research centers.

L'archive ouverte pluridisciplinaire **HAL**, est destinée au dépôt et à la diffusion de documents scientifiques de niveau recherche, publiés ou non, émanant des établissements d'enseignement et de recherche français ou étrangers, des laboratoires publics ou privés.

Thèse
de doctorat
de l'UTT

Ricardo TELLEZ LIMON

Light Propagation in Integrated Chains of Metallic Nanowires: Towards a Nano-sensing Device



Spécialité :
Optique et Nanotechnologies

2014TROY0039

Année 2014

THESE

pour l'obtention du grade de

**DOCTEUR de l'UNIVERSITE
DE TECHNOLOGIE DE TROYES
Spécialité : OPTIQUE ET NANOTECHNOLOGIES**

présentée et soutenue par

Ricardo TELLEZ LIMON

le 11 décembre 2014

**Light Propagation in Integrated Chains of Metallic Nanowires :
Towards a Nano-sensing Device**

JURY

P.-M. ADAM	PROFESSEUR DES UNIVERSITES	Président
M. S. BLAIZE	MAITRE DE CONFERENCES	Directeur de thèse
M. E. CENTENO	PROFESSEUR DES UNIVERSITES	Rapporteur
M. E. R. MENDEZ MENDEZ	INVESTIGADOR TITULAR	Examineur
M. A. MORAND	MAITRE DE CONFERENCES - HDR	Rapporteur
M. R. SALAS-MONTIEL	INGENIEUR DE RECHERCHE UTT	Directeur de thèse

Dedication

*To my mother, Virginia Limón Rebollar,
my father Ignacio O. Téllez López,
and my brother, Ignacio Téllez Limón.
Thank you for everything.*



Acknowledgments

I would like to thank to the "Conseil Régional Champagne-Ardenne" under the contract PLASMOBIO, by the financial support given for the pursuit of this PhD project.

To Dr. Sylvain BLAIZE and Dr. Rafael SALAS-MONTIEL by their invaluable guidance, encouragement, support and advice during these three years. Undoubtedly, you have been a great example of life and inspiration within and outside the research life. My thanks to you are endless.

To the members of the jury, Dr. Pierre-Michel Adam, Dr. Emmanuel Centeno, Dr. Eugenio Rafael Méndez Méndez, and Dr. Alain Morand for their critical reviews and comments that contributed to enrich the content of this thesis.

To all researchers, professors, technical and administrative staff, as well as all the students of the Laboratoire de Nanotechnologie et d'Instrumentation Optique (LNIO) of the University of Technology of Troyes (UTT). Thanks for your welcome and support during this time.

To the permanent and non-permanent members of the Mexican community of the LNIO, for bringing a little piece of Mexico into Troyes: Dr. Demetrio Macías Guzmán, Gabriela Fumagalli, Lydie Marillat, Verónica Pérez Chávez, Dr. Sergio de la Cruz Arreola, Jonathan Guerrero Muñoz, and the younger members, Gala, Gabriel and Juliette. Especially to Rocío Margoth Córdova Castro, for helping me during the first months after my arrival and inviting me to share her passion for science. Thank you to all of you guys, it would not have been the same without you.

To my friends and colleagues Josslyn Beltrán Madrigal, Kim Ngoc Nguyen, Aniello Apuzzo and Mickaël Février, for sharing with me your knowledge and many experiences inside and outside the laboratory.

To my always friend and confidant for many years, Raquel Rivera Vega. Despite everything, thank you for all your support and affection.

To my mother, Virginia Limón Rebollar, my father, Ignacio O. Téllez López, my brother, Ignacio Téllez Limón, my sister in law, Zandra E. Mondragón Ramírez, and my nephew, Zaig Téllez Mondragón. To my cousins Ma. Concepción Limón Arciga, J. Luis Padilla Tecpanécatl, and my nephew and godson, Luis Daniel Padilla Limón. This achievement has been only possible because of you. This work is dedicated to you as proof of my unconditional love to you.

And finally, but not the last, to my family and friends in Mexico. Too many people and so few lines. So many years and so many kilometers, but you have always been there. Your encouragement and support during not only these three years but all my life, have allowed me to achieve this big and joyful step. To each and every one of you my eternal gratitude and dedication of all this work.



Introduction

Since the invention of the microscope, optics has been closely related to the development of systems for the detection and analysis of chemical and biological substances. Chemical and biological sensing devices play an essential role in areas of humankind development as the environmental conservation and monitoring, disaster and disease prevention, industrial analysis and medical sciences.

Optical integrated systems have been largely used in the detection and characterization of biochemical substances. Moreover, the development of new technologies allows us the fabrication of integrated structures at nanoscale level. This feature opens a new window for the development of a new generation of biochemical sensors.

Based on the localized surface plasmons, in recent years, some authors have proposed different configurations of optical systems -including integrated structures- that allow the exaltation of the electromagnetic field in a small region of the space, being favored its interaction with biochemical substances.

These proposed integrated configurations include the interaction between a dielectric waveguide and localized surface plasmon waveguides. However, the absence of a generalized interpretation on the modes coupling mechanism between both waveguides, limits their study to the propagation of dipolar interactions between the nanoparticles.

For this reason in this work we present an exhaustive analysis of the modes propagated in a periodic array of metallic nanowires integrated on top of a dielectric waveguide.

This analysis is based on the so called Fourier modal method (FMM), also known as rigorous coupled wave analysis (RCWA). The implementation of perfectly matched layers, makes possible to suit this method to simulate the beam propagation along the integrated structure, and hence to characterize the optical properties of the structure.

We study two geometries of periodic arrays of metallic nanowires: rectangular-shaped and triangular-shaped nanowires. We demonstrate that, compared to the former case, the latter case presents a higher enhancement of the field when they are excited at their localized surface plasmon (LSP) resonance, via a dielectric waveguide placed in close proximity to them.

In order to validate the numerical results provided by the proposed method, we fabricate and experimentally characterize an integrated device consisting of a periodic array of gold nanowires placed on top of an ion-exchanged glass waveguide. We perform the characterization of the sample in the far-field by measuring the transmission spectrum at the output of the glass waveguide, and in the near-field by making use of near-field scanning optical microscopy (NSOM).

The numerical and experimental results suggest that our proposed integrated plasmonic device can be applied for the detection of chemical or biological substances.

Organization of the thesis

To have a comprehensive understanding of the design, fabrication and operation of the proposed system, the present thesis is divided into 5 chapters.

In Chapter 1 we give a brief introduction and description of previous concepts needed for a proper understanding of the thesis, as well as the main objective of this work.

In Chapter 2 we present the theoretical framework for the modal analysis of the integrated structures. This study is based on numerical calculations implemented with the so-called Fourier modal method (FMM), which is a well known rigorous method that enables to solve the Maxwell equations in the frequencies domain. This method permits to perform a modal analysis of the modes supported by the structures and generate dispersion curves. By implementing some adaptations to the method, we can also simulate the beam propagation to theoretically characterize the integrated structure by measuring the reflection, transmission and absorption spectra. The fundamentals and generalities on the numerical implementation of the FMM are described in Chapter 2.

In Chapter 3 we show the numerical results obtained for two kind of metallic structures: periodic arrays of gold rectangular nanowires and triangle-shaped nanowires (named for brevity nanocones). For the first one, nanowires of short and taller height are largely studied. A detailed description of the involved physical phenomena is given, demonstrating that the chain of nanowires supports three propagating Bloch modes, a dipolar longitudinal mode for short height nanowires, and a quadrupolar and a dipolar transverse mode for nanowires of taller height.

For the case of the nanocones, we present a parametric study of the LSP resonances present in an isolated nanocone and then in a periodic chain of nanocones on top of a glass substrate. We study the influence on the LSP resonance as a function of the incidence angle of the light and the period of the structure. As a result of this study, we demonstrate that the dipolar transverse mode is only excited at grazing angles for periodic structures. Finally, we study an integrated system that allows the excitation of the dipolar transverse mode that enhances the field at the top vertexes of the tips.

Chapter 4 concerns to the experimental results. First we present a general explanation of ion-exchanged waveguides, since they are advantageous for the elaboration of optical integrated systems. Then, based on the FMM, we design an optimal integrated device capable to excite the dipolar longitudinal mode via the fundamental TM₀ mode propagating in a glass waveguide. Subsequently, we present the fabrication process for the metallic nanowires (MNW) chain by making use of electron-beam lithography. The fabricated samples are characterized in the far-field regime in terms of their transmission spectra, and the obtained results are interpreted with the help of numerical simulations obtained with the FMM. In addition to the previous far-field characterization, by making use of an apertureless near-field scanning optical microscope (NSOM), we observe and map the near-field amplitude of the light propagating through the integrated structure.

Finally, in Chapter 5 we give a summary of the thesis as well as the general conclusions, potential applications of the designed integrated structure, and perspective work.

We include appendices to clarify the T- and S-matrix algorithms, the scattering matrix of a periodic grating, and the perfectly matched layers, concepts involved in the implementation of the Fourier modal method.

The references and bibliography are given at the end of the document, as well as a summary in french language.

Contents

List of Figures	13
List of Tables	23
1 Previous concepts	25
1.1 Surface plasmon polaritons	26
1.1.1 SPP excitation	27
1.2 SPP based waveguides	30
1.3 Localized surface plasmons	33
1.3.1 LSP based waveguides on metallic nanoparticles chains	34
1.4 Applications on plasmonics	36
1.4.1 Integrated plasmonic biosensors	37
1.5 Objective of the thesis	39
2 Numerical method	41
2.1 Modes propagation in multilayered media	42
2.1.1 Helmholtz equation	43
2.1.2 Dispersion relation	45
2.1.3 Boundary conditions	45
2.2 Modes propagation in an infinite periodic grating	46
2.2.1 Analytic treatment	49
2.2.2 Fourier modal method	53
2.2.3 Algorithm for the solution of the FMM	59
2.3 Beam propagation: aperiodic-FMM	61
2.3.1 Determination of the modes amplitudes	67
2.3.2 Electromagnetic field reconstruction	67
2.3.3 Absorbed power by the nanoparticles	69
2.4 Conclusions	70
3 Numerical analysis of integrated plasmonic structures	73
3.1 Dispersion curves	74
3.2 Modes propagation in an infinite array of MNW	76
3.2.1 Modes propagation in an isolated MNW chain	77
3.2.2 Modes propagation in a infinite array of MNW on top of a substrate	82
3.2.3 Modes propagation in an integrated system	85
3.3 Beam propagation in the integrated system	92
3.3.1 MNW of short height	93
3.3.2 MNW of large height	96
3.4 Triangular-shaped nanowires	99

3.4.1	Single MNC on top of a dielectric substrate	100
3.4.2	Short-period array of MNC on top of a dielectric substrate	104
3.4.3	Periodic array of MNC in an integrated system	110
3.5	Conclusions	113
4	Experimental results	117
4.1	Ion exchanged waveguides	118
4.2	Design of the integrated plasmonic structure	120
4.3	Fabrication of the plasmonic integrated structure	122
4.3.1	Fabrication problems	127
4.3.2	Nano-fabrication results	128
4.4	Experimental results	130
4.4.1	Far-field characterization of the sample	130
4.4.2	Near-field observations	137
4.5	Conclusions	147
5	Summary and Conclusions	151
5.1	Numerical results	152
5.1.1	Metallic nanowires	152
5.1.2	Triangular-shaped nanowires	153
5.2	Experimental results	155
5.3	Integrated plasmonic structures as nanosensing devices	156
5.4	Perspective work	158
	Appendices	161
A	T and S matrix algorithms	163
A.1	Boundary conditions	163
A.2	T-matrix method	164
A.2.1	Example: asymmetric waveguide	165
A.3	S matrix algorithm	167
B	S matrix of a periodic grating	171
C	Perfectly matched layers	175
	Bibliography	179
6	Résumé de la thèse	187
6.1	Presentation	187
6.2	Concepts préliminaires	188
6.2.1	Plasmons polaritons de surface	189
6.2.2	Plasmons localisés de surface	190
6.2.3	Biocapteurs plasmoniques intégrées	190
6.2.4	Objectif de la thèse	191
6.3	La méthode numérique	192
6.4	Analyse numérique des structures plasmoniques intégrées	194
6.4.1	Modes de propagation dans un réseau périodique de nanofils métalliques	195
6.4.2	Modes de propagation dans un réseau périodique de nanocônes métalliques	200

6.5	Résultats expérimentaux	204
6.5.1	Caractérisation de l'échantillon dans le champ lointain	206
6.5.2	Observations en champ proche	209
6.6	Résumé et conclusions	211
6.6.1	Perspectives de travail	212

List of Figures

1.1	Surface plasmon polariton. A transverse magnetic (TM) polarized wave impinging the interface between a dielectric and a metallic medium, gives rise to an evanescent wave propagating parallel to the interface surface, with a propagation constant k_{SPP} determined by the material properties. .	26
1.2	Dispersion curves for SPPs on an interface between half-spaces of a metal (Ag) and insulators with refractive index 1.0 (air) and 1.5 (glass). Image taken from Chapter 6 of reference (Kim et al., 2012).	28
1.3	Prism coupling to SPPs using total internal reflection with (a) Kretschmann and (b) Otto configurations. (c) The dispersion relation shows the phase matching of k_{SPP} with the air light-line. Images reproduced from reference (Maier, 2007).	29
1.4	Phase-matching of light to SPP using a grating.	30
1.5	SPP based waveguide. The SPPs propagating at the 1/2 and 2/3 interfaces are coupled between each other. When they have the same phase, a symmetric mode is created, and for a phase difference of π rad, an anti-symmetric mode takes place.	31
1.6	Dispersion relations for (a) a MIM: 25 nm free space surrounded by silver and gold, and (b) IMI: 25 nm silver layer surrounded by free space and other dielectric with refractive index $n = 1.1$. The Insulator-Metal SPP curve is also traced as reference. Plots taken from Chapter 6 of reference (Kim et al., 2012).	32
1.7	Localized surface plasmon: the restoring force experienced by a subwavelength conductive nanoparticle in presence of an oscillating electromagnetic field (at a time t_0), gives rise to a resonance mode, enhancing the field inside and in the near-field zone of the nanoparticle (at a time t_1) (Catchpole, 2006).	33
1.8	Normalized intensity near-field map of the coupling between Ag nanowires when perpendicularly illuminated with a TM polarized gaussian beam. (a) A single nanowire of thickness 50 nm and width 250 nm exhibits a dipolar behavior at its LSP resonance ($\lambda = 365$ nm). (b) When the nanowire is divided into two equal sections of width 100 nm and gap 50 nm, the LSP resonance is shifted at $\lambda = 375$ nm, exhibiting a coupling between these dipoles.	34
1.9	Normalized intensity maps of (a) a single cylinder of 50 nm diameter exhibiting a quadrupolar resonance at $\lambda = 340$ nm. (b) Placing a periodic array of cylinders, the quadrupoles are coupled between each other shifting the LSP resonance to $\lambda = 500$ nm.	35

1.10	Biosensor operation principle. A biosensor is a device that consists of a biologically or biophysically-derived sensing element (bioreceptor) integrated with a physical transducer that transforms a measurand into an output signal.	37
1.11	Scheme of the integrated plasmonic structure for sensing applications. On top of a glass substrate containing an ion-exchanged waveguide of low contrast refractive index, it is placed a periodic array of gold nanowires.	40
2.1	(a) Scheme of metallic nanowires chain on top of a dielectric waveguide. (b) The integrated system can be seemed as a multilayered media, where the metallic grating region is transformed into an equivalent homogeneous layer of effective index $n_{eff,q}$ determined by the q -th propagating mode.	42
2.2	Scheme of a multilayered media invariant in the y (out-of plane) direction. The substrate ($m = 1$) and superstrate ($m = N + 1$) are considered as semi-infinite media.	43
2.3	Diffraction of a plane wave on an infinite periodic array of metallic nanowires along the x -axis, of thickness t and period $\Lambda = w + g$, between two semi-infinite homogeneous media.	47
2.4	Scheme of a one-dimensional grating periodic along the x axis, and infinite along the z axis. The period of the structure is $\Lambda = w + g$	48
2.5	The Fourier transform of a periodic function $f(x)$ is a discrete function. Reciprocally, the inverse Fourier transform of a discrete function of constant step sampling ΔT is a periodic function.	54
2.6	Schematic representation of the FMM. (a) A single unitary cell of length Λ is taken from the MNW chain. (b) In the grating region, the effective indices of the supported modes propagating in the z direction of the complete structure, are computed by representing the refractive index profile in Fourier series along the x propagation axis. Finally (c), the diffracted modes are matched to the multilayered homogeneous structure by using the S-matrix algorithm, obtaining a complete characteristic matrix whose eigenvectors are solution of an infinite periodic structure in the reciprocal space.	55
2.7	Flowchart of the algorithm to find the proper modes of the integrated periodic structure.	60
2.8	Schematic representation of the aperiodic-FMM. (a) The complete finite structure is taken as a single unitary cell rotated perpendicularly to the x axis. (b) The cell is delimited with PML, forming a multilayered supercell of length Δ . By representing the index profile in Fourier series along the x axis, the effective index in each layer is determined. (c) Then, the characteristic matrix is described with periodic elements perpendicular to the z propagation axis.	62
3.1	Dispersion relations for a gold nanoparticle chain over a glass substrate above the total internal reflection regime for a spectral range from 570 – 714 nm. Green: 55 nm tall nanoparticles at an air/glass interface; blue: 30 nm tall nanoparticles at an air/glass interface; purple: 55 nm tall nanoparticles in a uniform glass environment. Results from reference (Crozier et al., 2007) computed with the FDTD method.	75

3.2	Scheme for the study of modes propagation in an infinite periodic array along the x axis of MNW immersed in a dielectric homogeneous medium of refractive index $n_d = 1.5$. The width is $w = 80$ nm, the period $\Lambda = 130$ nm and the height was set first to $e = 20$ nm, and then to 150 nm.	77
3.3	(a)Dispersion relations of an infinite chain of MNW along the x axis, of height $e = 20$ nm immersed in a dielectric homogeneous medium of refractive index $n_d = 1.5$ (glass). The structure supports a dipolar longitudinal propagation mode. This Bloch mode crosses the Bragg condition at $\lambda = 645$ nm. (b) The maximum propagation distance of the Bloch mode is of 1.14 μm	78
3.4	Energy density maps and electric field lines distribution of the dipolar longitudinal Bloch mode. (a) At the Bragg condition around $\lambda = 645$ nm, we identify the dipolar longitudinal coupling of the MNW chain. Out of the Bragg condition, around $\lambda = 667$ nm, we still observe the dipolar coupling.	79
3.5	(a)Dispersion relations for the quadrupolar (red dotted line) and dipolar transverse (blue dotted line) Bloch modes for an infinite chain along the x axis of MNW of height $e = 150$ nm immersed in a dielectric homogeneous medium of refractive index $n_d = 1.5$. (b) The propagation distance of the quadrupolar branch (upper red circles curve) is shorter than that of the dipolar transverse mode (blue circles curve).	80
3.6	Energy density maps and electric field lines distribution at the Bragg condition for (a) the quadrupolar Bloch mode at $\lambda = 540$ nm, and (b) the dipolar transverse Bloch mode at $\lambda = 916$ nm. The corresponding squares show the phase distributions and orientation of the charges.	81
3.7	Scheme of an infinite periodic array of MNW immersed in glass, on top of a semi-infinite dielectric substrate of refractive index $n_{sub} = 2.0$	82
3.8	Dispersion relation for the dipolar longitudinal Bloch mode (blue dotted line) for an infinite periodic array of MNW of height $e = 20$ nm immersed in glass ($n_d = 1.5$) and placed on top of a dielectric medium of refractive index $n_{sub} = 2.0$	83
3.9	Energy density maps and electric field lines distribution at the Bragg condition for the dipolar longitudinal Bloch mode at $\lambda = 696$ nm. The corresponding squares show the phase distributions and orientation of the charges.	83
3.10	Dispersion relations for the quadrupolar (red dotted line), dipolar transverse (blue dotted line) and SPP-like (green asterisks) Bloch modes for an infinite chain of MNW of height $e = 150$ nm immersed in glass ($n_d = 1.5$) and placed on top of a dielectric medium of refractive index $n_{sub} = 2.0$	84
3.11	Energy density maps and electric field lines distribution at the Bragg condition for (a) the quadrupolar Bloch mode at $\lambda = 562$ nm, (b) the SPP-like mode (dipolar longitudinal) at $\lambda = 655$ nm, and (c) the dipolar transverse Bloch mode at $\lambda = 997$ nm. The corresponding squares show the phase distributions and orientation of the charges.	85
3.12	Scheme of an infinite periodic array of MNW immersed in glass, approached to a dielectric waveguide of refractive index $n_{wg} = 2.0$. The thickness of the waveguide is $h_1 = 200$ nm and it is separated a distance $h_2 = 30$ nm from the MNW chain.	86

3.13	(a)Dispersion relations of the integrated structure. The TM fundamental mode of the waveguide (blue triangles) crosses the dipolar longitudinal mode of the isolated MNW chain immersed in glass (green asterisks), at $\lambda = 664$ nm. This generates anti-symmetric (red points) and symmetric (red circles) modes, that match the Bragg condition at $\lambda = 473$ nm and $\lambda = 660$ nm, respectively. (b) Inset in the crossing point region.	87
3.14	Energy density maps and electric field lines distribution at the Bragg condition for (a) the anti-symmetric (quadrupolar) Bloch mode at $\lambda = 473$ nm, and (b) the symmetric (dipolar longitudinal) Bloch mode at $\lambda = 660$ nm. The corresponding squares show the phase distributions and orientation of the charges.	88
3.15	(a)Dispersion relations of the integrated structure for MNW of height $e = 150$ nm. The TM fundamental mode of the waveguide (blue triangles) crosses the quadrupolar mode of the isolated MNW chain immersed in glass (green asterisks), around $\lambda = 546$ nm. This generates anti-symmetric (red points) and symmetric (red circles) modes, that match the Bragg condition around $\lambda = 468$ nm and $\lambda = 549$ nm, respectively. The dipolar transverse mode (blue dots) reaches the Bragg condition around $\lambda = 933$ nm, but it does not cross the TM fundamental mode of the waveguide, and no anti-symmetric modes is generated. (b) Inset in the crossing point region.	89
3.16	Energy density maps and electric field lines distribution at the Bragg condition for (a) the anti-symmetric (at $\lambda = 468$ nm), and (b) the symmetric (at $\lambda = 549$ nm) quadrupolar Bloch modes. The corresponding squares show the phase distributions and orientation of the charges.	90
3.17	Energy density map and electric field lines distribution at the Bragg condition ($\lambda = 933$ nm) for the dipolar transverse Bloch mode. The corresponding squares show the phase distributions and orientation of the charges. . .	91
3.18	Scheme of the beam propagation in a finite periodic array of MNW on a dielectric waveguide with core index $n_w = 2.0$. The fundamental TM mode of the dielectric waveguide is launched into the structure at $x = 0$. The mode propagates through the waveguide and couples to the modes of the metallic chain of gold nanowires.	92
3.19	Transmission (red curve), reflection (blue dashed curve) and absorption (black dotted curve) spectra of the finite integrated system with MNW of height $e = 20$ nm. The reflection curve has a maximum around $\lambda = 474$ nm, while the transmission exhibits two minimum values around $\lambda = 520$ nm and $\lambda = 678$ nm. The first is associated to a Bragg reflection, and the second one to the excitation of the dipolar longitudinal Bloch mode.	93
3.20	Near field map of the absolute value of the H_y component of the electromagnetic field. The periodic lobes observed inside the waveguide core are associated to a Bragg reflection.	94
3.21	$ H_y $ near-field map of the integrated system at the first minimum value in the transmission spectra at $\lambda = 520$ nm, which corresponds to a Bragg reflection.	95
3.22	$ H_y $ near-field map of the integrated system at the second minimum value in the transmission spectra at $\lambda = 678$ nm, corresponding to the excitation of the dipolar longitudinal Bloch mode.	95

3.23	Transmission (red curve), reflection (blue dashed curve) and absorption (black dotted curve) spectra of the finite integrated system with MNW of height $e = 150$ nm. The quadrupolar mode is excited at $\lambda = 559$ nm, and the constructive interference of the dipolar transverse mode is positioned around $\lambda = 990$ nm. The minimum around $\lambda = 1055$ nm, is a cavity effect. The Bragg reflections are located around $\lambda = 534$ nm and $\lambda = 960$ nm.	96
3.24	$ H_y $ near-field map of the integrated system at the second minimum value in the transmission spectra at $\lambda = 559$ nm, corresponding to the excitation of the quadrupolar Bloch mode.	98
3.25	$ H_y $ near-field map of the integrated system at the second minimum value in the transmission spectra at $\lambda = 990$ nm, corresponding to the excitation of the dipolar transverse Bloch mode.	98
3.26	Gold nanocone of width $w = 72$ nm and height $h = 144$ nm immersed in air ($n_{sup} = 1.0$), placed on top of a dielectric substrate of refractive index $n_{sub} = 1.5$. A TM polarized plane wave impinges the glass-air interface forming an angle θ_{inc} respect to the normal.	101
3.27	Transmission, reflection and absorption spectra as a function of the incidence angle. The absorption is maximum at $\lambda = 540$ nm and $\theta_{inc} = 43^\circ$	102
3.28	In plane (blue curves) and out-of plane (red dotted curves) far-field scattering patterns, of a dipole nearly placed on top of the glass substrate oriented at (a) 0° , (b) 45° , and (c) 90° respect to the interface air-glass (parallel to the x axis). The light scattered by the dipole towards the glass substrate, is preferentially radiated in the direction of the critical angle $\theta_c = 41.8^\circ$ (black dotted lines) respect to the $-z$ axis (from the substrate).	103
3.29	Energy density map and electric field lines distribution for a single nanocone over a glass substrate at $\lambda = 540$ nm and $\theta_{inc} = \theta_c = 41.8^\circ$. The electric field lines reveal a combination of dipolar transverse and dipolar longitudinal resonances, enhancing the optical field in the vertexes of the MNC.	104
3.30	Infinite periodic array of gold nanocones of width $w = 72$ nm and height $h = 144$ nm immersed in air ($n_{sup} = 1.0$), placed on top of a glass substrate ($n_{sub} = 1.5$). The incident TM polarized plane wave forms an angle θ_{inc} respect to the normal.	105
3.31	Transmission, reflection and absorption efficiency spectra as a function of the angle θ_{inc} for a MNC chain of period $\Lambda = 200$ nm. Two resonances are observed, the first one around the critical angle (like the isolated nanocone), and a second one that is only observable at grazing angles (near to the marker $R2$).	105
3.32	Transmission, reflection and absorption efficiency spectra for a plane wave with incident angles of (a) $\theta_{inc} = 43^\circ$ (around the critical angle) and (b) $\theta_{inc} = 82^\circ$ (the angle of markers $R1$ and $R2$).	106
3.33	Transmission, reflection and absorption efficiency spectra as a function of the period Λ of the MNC chain. Maximum absorption values are located at $(\lambda = 560$ nm, $\Lambda = 187$ nm), $(\lambda = 830$ nm, $\Lambda = 277$ nm) and $(\lambda = 660$ nm, $\Lambda = 442$ nm).	106
3.34	Normalized energy density maps and electric field lines distribution for the chain of MNC at the $R1$ resonance ($\lambda = 600$ nm and $\Lambda = 200$ nm).	108
3.35	Normalized energy density maps and electric field lines distribution for the chain of MNC at the $R2$ resonance ($\lambda = 800$ nm and $\Lambda = 200$ nm).	109

3.36	Normalized energy density map and electric field lines distribution for the chain of MNC at the $R3$ resonance, around $\lambda = 660$ nm and $\Lambda = 400$ nm. .	109
3.37	Periodic array of 5 gold nanocones of width $w = 72$ nm, height $h = 144$ nm and period $\Lambda = 200$ nm, placed on top of a glass substrate ($n_{sub} = 1.5$). At a distance $t_2 = 30$ nm from the glass-air interface is placed a dielectric waveguide of thickness $t_1 = 200$ nm and core refractive index $n_w = 2.0$. The supestrate is considered air ($n_{sup} = 1.0$).	110
3.38	Dispersion curves of the integrated system. The dipolar transverse Bloch mode of the MNC chain (green asterisks) crosses the TM0 mode (blue triangles) around $\lambda = 747$ nm, generating symmetric (red circles) and anti-symmetric (red dots) modes.	111
3.39	Normalized energy density maps and electric field lines distribution of the dipolar transverse Bloch mode, for an integrated chain of MNC over a dielectrcic waveguide. Both resonances correspond to the Bragg condition at (a) $\lambda = 653$ nm for the anti-symmetric mode, and (b) at $\lambda = 772$ nm for the symmetric mode.	112
3.40	Transmission (red curve), reflection (blue dashed curve) and absorption+scattering (black dotted curve) spectra of the finite integrated system with MNC of height $e = 144$ nm and width $w = 72$ nm. At 650 nm it is observed a Bragg reflection, while the dipolar transverse mode is efficiently excited at 810 nm.	113
3.41	Near field maps of (a) $ H $ and (b) $ E $ at $\lambda = 650$ nm, corresponding to the Bragg reflection of the anti-symmetric branch (minimum transmission) of the MNC structure integrated over a dielectric waveguide.	114
3.42	Near field maps of (a) $ H $ and (b) $ E $ at $\lambda = 810$ nm. The dipolar transverse mode is efficiently excited with the TM0 fundamental mode of the dielectric waveguide, resulting in a field enhancement at the top vertexes of the MNC.	115
4.1	Scheme of the fabricated sample, consisting in a periodic array of gold nanowires placed on top of a glass substrate containing an ion exchanged waveguide.	117
4.2	Ion exchange waveguide. The core is a local gradient of the refractive index.	118
4.3	Dispersion curves of periodic arrays of MNW of width $w = 70$ nm and height $e = 30$ nm and periods $\Lambda = \{80, 100, 120, 140, 160\}$ nm, placed on top of a dielectric substrate with refractive index $n_{sub} = 1.505$. Between the substrate and the MNW chain, is placed an ITO layer of thickness $h_2 = 10$ nm. The fundamental TM0 mode of an ion-exchanged waveguide of thickness $h = 1800$ nm is represented by the blue triangles.	120
4.4	Sample fabrication by e-beam lithography. (a) Sample cleaning. (b) Deposition of the ITO layer. (c) Deposition of PMMA and ESPACER [®] layers. (d) E-beam lithography to change the solubility of the PMMA. (e) Development of the sample. (f) Reactive ion-etching process to remove the PMMA traces. In (g) and (h), deposition of Cr and Au thin layers. (i) Lift-off process to remove the PMMA and leave only the MNW on the substrate. .	124
4.5	Lithography problems. (a) Bad annealing of the PMMA, (b) sample fabrication without RIE process, (c) excess of time in the ultrasound bath after lift-off, and (d) inaccurate lift-off.	127
4.6	Electronic microscope images of the MNW fabricated corresponding to the structure (a) $T1$, (b) $T2$ and (c) $T3$	128

4.7	Progressive zoom images captured with the electronic microscope for the structure $T3$. The MNW chain is perpendicularly placed to the ion-exchanged glass waveguides.	129
4.8	Scheme of the experimental setup for far-field transmission measurements.	130
4.9	(a) Micro-lensed fiber at the input of the glass waveguides. (b) Multimode fiber at the output of the waveguide.	131
4.10	Top view of the MNW when they are excited with (a) the TM_0 fundamental mode and (b) with the TE_0 mode. The LSP resonance of the MNW chain is not excited under TE polarization.	132
4.11	Normalized spectrum of the reference waveguide. The cut-off wavelength of the TM_0 mode is at $\lambda = 780$ nm, while for the TE_0 mode is at $\lambda = 820$ nm.	132
4.12	Normalized transmission spectrum of the $T1$ type structure. The minimal transmission is observed around a wavelength value $\lambda = 702$ nm.	133
4.13	Normalized transmission spectrum of the $T2$ type structure. The minimal transmission is observed around a wavelength value $\lambda = 675$ nm.	133
4.14	Normalized transmission spectrum of the $T2$ type structure. The excitation of the LSP propagating mode occurs around $\lambda = 668$ nm.	133
4.15	Transmission (red) and reflection (blue) spectra obtained with the FMM for the $T1$ type structure. The minimal transmission is observed around a wavelength value $\lambda = 625$ nm.	135
4.16	Transmission (red) and reflection (blue) spectra obtained with the FMM for the $T2$ type structure. The minimal transmission is observed around a wavelength value $\lambda = 605$ nm.	135
4.17	Transmission (red) and reflection (blue) spectra obtained with the FMM for the $T3$ type structure. The minimal transmission is observed around a wavelength value $\lambda = 598$ nm.	135
4.18	Operation principle of the NSOM technique. (a) Out of the core of the waveguide, an evanescent field is also propagated. (b) Approaching a nanotip to the surface of the sample, the evanescent wave is scattered, resulting in a perturbation of the transmitted or scattered optical field, as a function of the frequency of the nanotip.	137
4.19	Schematic representation of the apertureless NSOM. The optical field scattered by the nanotip, is collected with an optical fiber and then converted into an electrical signal with an APD. This signal is demodulated with a lock-in amplifier using as reference the frequency of the nanotip.	138
4.20	Schematic representation of the H-NSOM. The beam of light coming out from the laser is divided in four diffracted orders with two crossed AO. The fundamental order is chosen as probe signal, while the fourth order is used as reference signal. The probe signal is perturbed by the nanotip, and the scattered field is combined with the reference beam; this interference is converted into an electrical signal with an APD. The oscillation frequency of the nanotip is subtracted from the AO modulation signal, serving as demodulation frequency for the signal coming from the APD. The interference between the reference and the probe signal provides the information from the phase of the optical field in the scanned region.	139
4.21	(a) Intensity and (b) phase near-field maps measured with the H-NSOM technique, for an ion-exchanged glass waveguide.	140

4.22	(a) A profile along a line in the phase map is plotted. (b) By taking the Fourier transform of this profile, we can deduce the effective index of the mode propagating through the waveguide. For this case, the obtained value was $n_{eff} = 1.527 \pm 0.17$	140
4.23	(a) Topography and (b) intensity near-field maps of the integrated plasmonic structure obtained with the NSOM technique. The grating region starts at a distance around $8 \mu\text{m}$. (c) FFT images of the zones M1, M2, and M3 marked in (b). The frequency corresponding to the fundamental mode remains almost unchanged in the three zones.	142
4.24	(a) Topography and (b) intensity NSOM near-field maps of the <i>M2</i> region. (c) The corresponding FFT of this region reveals the presence of three spatial frequencies marked as <i>P1</i> , <i>P2</i> and <i>P3</i> . They correspond, respectively, to the light-line of the substrate, a substrate radiated mode and the TM0 mode.	143
4.25	(a) Transmission, (b) reflection and (c) absorption spectra for an infinite periodic array as a function of the period when illuminating from the substrate with a TM polarized plane wave at a grazing angle of 82° respect to the normal of the surface. For periods larger than 120 nm , the absorption band remains almost unchanged, meaning that no dipolar coupling between the MNW is expected, only their LSP excitation is achieved. The blue and red lines correspond to the Bragg condition for the substrate and ITO layer, respectively.	145
4.26	Near-field maps of the $ H_y $ component for a wavelength $\lambda = 685 \text{ nm}$, computed with the aFMM for a finite chain of 200 gold nanowires with period (a) $\Lambda = 100 \text{ nm}$ (T0), and (b) $\Lambda = 186 \text{ nm}$ (T2). The height of the MNW is $e = 30 \text{ nm}$. An efficient interaction of the TM0 mode of the ion exchanged waveguide with the MNW periodic array, is only observable for the shorter period.	146
4.27	(a) Near-field map of the $ H_y $ component at $\lambda = 670 \text{ nm}$, and (b) transmission and reflection spectra, of a periodic array of 200 gold nanowires of width $w = 80 \text{ nm}$, height $e = 30 \text{ nm}$ and period $\Lambda = 100 \text{ nm}$, placed on top of an ion exchanged glass waveguide with core effective index $n_{wg} = 1.505$. The transmission spectrum exhibits a minimum value at a wavelength $\lambda = 670 \text{ nm}$, where the near-field map exhibits a strong coupling between the TM0 mode of the photonic waveguide, and the dipolar longitudinal mode of the plasmonic structure.	149
5.1	Transmission and reflection spectra corresponding to the case of the MNW chain of short height studied in section 3.3.1, when the superstrate refractive index is $n_{sup} = 1.45$ (blue), $n_{sup} = 1.50$ (red), and $n_{sup} = 1.55$ (green). The Bragg reflection remains at the same wavelength value, while the longitudinal dipolar resonance is red-shifted when increasing the refractive index.	157
5.2	Integrated plasmonic structure for sensing applications in biological sciences. Antibodies are easily attached to the chain of MNW. The presence of an antigen will change the refractive index of the superstrate, leading to a shift in the wavelength resonance of the mode supported by the MNW chain.	158

A.1	Scheme of an asymmetric 2D waveguide of width $d_2 = w$ and dielectric function ε_2 . The substrate ε_1 and superstrate ε_3 are semi-infinite in regions $z < 0$ and $z > d_2$, respectively, and the interfaces are localized at $d_1 = 0$ and at $d_2 = w$	166
C.1	Scheme of the computational window of size e , between two PML layers of width $q/2$. The total length of the unitary cell is Δ	175
6.1	Plasmon polariton de surface : l'incidence d'une onde électromagnétique avec polarisation TM donne lieu à une onde évanescente qui se propage parallèlement à la surface d'interface.	189
6.2	Schéma d'une structure plasmonique intégrée pour des applications de capteur.	192
6.3	Chaîne périodique de nanofils d'or intégrée sur une guide d'onde diélectrique.	195
6.4	Courbes de dispersion pour une structure périodique de nanofils d'or de $e = 20$ nm d'hauteur intégrée sur une guide d'onde diélectrique. Le mode dipolaire longitudinal est couplé avec le mode fondamentale TM0 du guide d'onde diélectrique à une longueur d'onde $\lambda = 664$ nm.	196
6.5	Densité d'énergie et distribution des lignes de champ électrique pour le mode dipolaire longitudinal à la condition de Bragg à une longueur d'onde $\lambda = 645$ nm.	196
6.6	(a) Spectres de transmission, réflexion et absorption pour une chaîne de 27 nanofils d'or d'hauteur 20 nm, intégrée sur une guide d'onde diélectrique. La première valeur minimale dans la courbe de transmission ($\lambda = 520$ nm) est due à une réflexion de Bragg, et la deuxième ($\lambda = 678$ nm) à l'excitation du mode dipolaire longitudinal. (b) Quand le mode dipolaire longitudinal est excité, il y a un échange d'énergie entre les nanofils d'or et le guide d'onde.	197
6.7	Courbes de dispersion pour une structure périodique de nanofils d'or d'hauteur $e = 150$ nm intégrée sur une guide d'onde diélectrique. Le mode quadripolaire est couplé avec le mode fondamental TM0 du guide d'onde diélectrique à une longueur d'onde $\lambda = 546$ nm.	197
6.8	Densité d'énergie et distribution des lignes du champ électrique des nanofils d'or avec une hauteur de 150 nm, calculés à la condition de Bragg pour (a) le mode quadripolaire ($\lambda = 540$ nm) et (b) le mode dipolaire transversal ($\lambda = 916$ nm).	198
6.9	Spectres de transmission, réflexion et absorption pour la structure plasmonique intégrée de nanofils d'or avec une hauteur de 150 nm. L'excitation des modes quadripolaire et dipolaire transversal sont trouvés aux longueurs d'onde $\lambda = 559$ nm et $\lambda = 990$ nm, respectivement.	199
6.10	Cartes de champ proche (a) du mode quadripolaire et (b) du mode dipolaire transversal. Dans les deux cas est observé un échange d'énergie entre la guide d'onde diélectrique et le réseau de nanofils d'or.	199
6.11	Structure plasmonique intégrée conformée par un réseau périodique de 5 nanocônes d'hauteur $h = 144$ nm, largeur $w = 72$ nm et périodicité $\Lambda = 200$ nm, placé sur la surface d'un substrat du verre ($n_{sub} = 1.5$) contenant une guide d'onde diélectrique d'indice de réfraction $n_w = 2.0$, d'épaisseur $t_1 = 200$ nm, enterré à une profondeur $t_2 = 30$ nm. Le superstrat est de l'air ($n_{sup} = 1.0$).	200

6.12	Spectres de transmission, de réflexion et d'absorption d'une chaîne de nanocônes d'or en fonction de l'angle d'incidence d'une onde plane avec polarisation TM. La période de la structure est fixée à 200 nm. Le mode dipolaire transversal $R2$ est excité seulement aux angles rasants.	201
6.13	Spectres de transmission, réflexion et absorption d'une chaîne de nanocônes d'or en fonction de leur périodicité. Des valeurs maximales d'absorption sont localisées aux longueurs d'onde $\lambda = 560$ nm (proche du point R1), $\lambda = 830$ nm (proche du point R2), et $\lambda = 660$ nm (proche du point R3).	202
6.14	Distribution de la densité d'énergie (normalisées aux valeurs maximales) et lignes du champ électrique pour les résonances (a) R1 ($\lambda = 600$ nm, $\Lambda = 200$ nm), (b) R2 ($\lambda = 800$ nm, $\Lambda = 200$ nm), et (c) R3 ($\lambda = 660$ nm, $\Lambda = 400$ nm).	202
6.15	(a) Courbes de dispersion du réseau périodique de nanocônes d'or intégré avec une guide d'onde, et (b) spectres de transmission, de réflexion et d'absorption pour une chaîne de 5 nanocônes.	203
6.16	Distribution de champ électrique à une longueur d'onde $\lambda = 810$ nm. Le mode dipolaire transversal est efficacement excité avec le mode fondamental TM0 du guide d'onde, on obtient en conséquence une forte exaltation du champ optique au sommet des nanocônes.	204
6.17	Cartographie du champ proche du composant $ H_y $ pour une chaîne de 200 nanofils d'or de hauteur 30 nm et période $\Lambda = 100$ nm, intégrée sur la surface d'une guide à échange d'ions. Quand la longueur d'onde du mode fondamental TM0 est $\lambda = 685$ nm, le mode dipolaire longitudinal est excité.	205
6.18	Images par microscopie électronique des réseaux type (a) T1, (b) T2 et (c) T3, fabriqués sur un substrat de verre.	206
6.19	Images en champ-lointain de la diffusion des nanofils d'or quand ils sont excités avec le mode (a) TM0 et (b) TE0 du guide d'onde à échange d'ions. Sous polarisation TM, la résonance du plasmon localisé est bien excité le long la chaîne de nanofils, tandis que pour le mode TE il y a une faible interaction.	207
6.20	Spectres de transmission expérimentaux (à gauche) et théoriques (à droite) pour chacune des structures: (a) et (b) pour la structure T1; (c) et (d) pour la structure T2; (e) et (f) pour la structure T3.	208
6.21	Cartes de l'intensité (a) et de la phase (b) du champ électromagnétique du mode propagé à une longueur d'onde $\lambda = 632.8$ nm, mesurées avec l'H-NSOM. En utilisant la transformée de Fourier, on a trouvé que l'indice effective du mode propagé à une valeur $n_{eff} = 1.52 \pm 0.17$	209
6.22	Cartes de (a) la topographie et (b) l'amplitude de la structure intégrée. L'exaltation du champ optique n'est pas dû à un mode propagatif, mais à l'exaltation collective des plasmones localisés.	210

List of Tables

4.1	Values of width, gap, period and length of the three different arrays of MNW fabricated on top of the glass substrate.	129
4.2	Comparison of the experimental and numerical wavelengths values for the MNW resonances. The difference between the numerical and experimental values of the LSP resonance wavelength is around 70 nm.	136
6.1	Longueur totale et période des réseaux de nanofils fabriqués par lithographie électronique dans la surface d'un substrat du verre.	205

Chapter 1

Previous concepts

The interaction of electromagnetic fields with nano-structured metals shows complex and interesting optical properties. This subject has been largely studied since the beginnings of 20th century. However, recent advances regarding the structure, manipulation and observation at nanoscale level, have attracted the attention of the scientific community, giving rise to a new research area: plasmonics, the science of plasmons.

Plasmons are basically the quantification of the oscillation of a free electron gas, moving in a background of positive ions, due to the presence of an electromagnetic field. There are two types of plasmons: the volume plasmons and the surface plasmons polaritons. The first ones are only excited by the collision of a particle with the gas, whereas the seconds can be excited by photon interaction with the plasma.

The present chapter is concerned to the general description of the fundamental concepts needed to a better understanding of the physical phenomena related to the integrated plasmonic system that is presented in this thesis. First, we explain the surface plasmons resonances, their excitation mechanisms and their use as light guiding systems and as sensing devices. Then, we describe the localized surface plasmons resonances, as well as their applications in light guiding systems. General applications of nanostructured metals in integrated systems are also presented, as well as the general objective of the thesis.

1.1 Surface plasmon polaritons

Surface plasmons polaritons (SPP) are electromagnetic excitations propagating at the interface between a dielectric and a conductor material, evanescently confined in the perpendicular direction (Figure 1.1). At the dielectric-metal interface, the conduction electrons of the metal can be treated like a plasma: a free electron gas moving towards a background of positive cores. As the electrons oscillate in response to an applied electromagnetic field, electromagnetic waves arise via the coupling of the electromagnetic field to the oscillations of the electron plasma of the conductor.

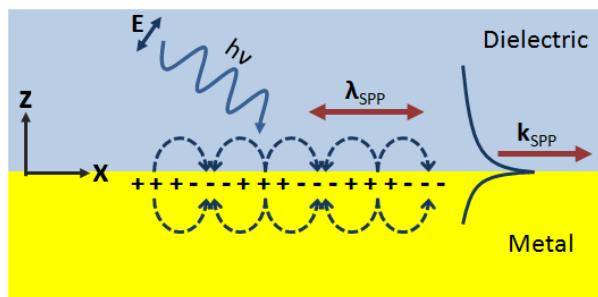


Figure 1.1: Surface plasmon polariton. A transverse magnetic (TM) polarized wave impinging the interface between a dielectric and a metallic medium, gives rise to an evanescent wave propagating parallel to the interface surface, with a propagation constant k_{SPP} determined by the material properties.

We can explain the optical properties of a material by its dielectric function $\varepsilon(\omega)$, which in general is a complex quantity that depends on the frequency ω , being its imaginary part associated to the quantity of the absorption inside the medium. Because the conductive electrons at the metal-dielectric interface can be treated as a plasma, the dielectric function of the metal can be expressed in terms of the Drude model by the expression

$$\varepsilon(\omega) = 1 - \frac{\omega_p^2}{\omega(\omega + i\gamma)}, \quad (1.1)$$

where ω_p is the bulk plasma frequency and γ is a damping factor that arises from the frequency in the electrons collisions. Assuming that $\gamma = 0$ (perfect conductor), from the comparison between ω and ω_p we can deduce the behavior of the electromagnetic waves arriving to the metal. If $\omega < \omega_p$, the dielectric constant is negative, therefore its square root is purely imaginary, which involves the reflection of the incident wave. On

the contrary, if $\omega_p < \omega$, the square root of the dielectric constant is real and the incident wave can propagate in the medium with a small attenuation (Kim et al., 2012).

By making use of the Maxwell equations, it is possible to describe the interaction of an electromagnetic field at the dielectric-metal interface depicted in Figure 1.1. If we consider that the system is invariant in the out-of-plane direction, when solving the wave equation for harmonic waves propagating along the x direction (parallel to the interface), two sets of equations can be obtained for transverse electric (TE) or transverse magnetic (TM) polarized waves. By application of the boundary conditions on the conservation of the tangential component of the field, it can be shown that SPP waves are only excited if the incident electromagnetic field is TM polarized (Maier, 2007). Moreover, the propagation constant of the SPP waves, k_{SPP} , must satisfy the dispersion relation

$$k_{SPP} = k_0 \sqrt{\frac{\varepsilon_m \varepsilon_d}{\varepsilon_m + \varepsilon_d}}, \quad (1.2)$$

where $k_0 = \omega/c$ is the propagation constant in the free space, ε_d and ε_m are the dielectric functions of the dielectric and metal, respectively. To achieve a propagating wave, k_{SPP} must be real, condition achieved if it is simultaneously accomplished that $\varepsilon_m \varepsilon_d < 0$ and $\varepsilon_m + \varepsilon_d < 0$. The first condition implies that one of the permittivities must be positive and the other negative. The second condition states that the absolute value of the negative permittivity must be higher than the positive one. These conditions can be achieved for metals, as can be verified by the Drude model (eq. (1.1)), where a perfectly conductor metal have negative permittivities for $\omega < \omega_p$ (or $\lambda > \lambda_p$).

From the dispersion relation (eq. 1.2), it is clear that the resonance of the plasmon frequency depends not only on the optical properties of the metal, but also on the dielectric constant of the dielectric medium. This important fact has been largely studied for the potential application of SPPs in sensing devices, as will be later explained.

1.1.1 SPP excitation

The SPPs cannot be directly excited by light beams as $k_{SPP} > k_d$, where k_d is the wavevector in the dielectric medium of refractive index n_d , i.e. $k_d = \omega/cn_d$. Therefore,

the projection along the interface of the momentum $k_x = k_d \sin \theta$ of photons impinging at an angle θ from the surface normal is always smaller than the SPP propagation constant k_{SPP} , even at grazing incidence. As shown in Figure 1.2, the SPP dispersion curve lies below the light-line of the dielectric material ($\omega = ck_d$), and excitation by three-dimensional light beams cannot be possible unless special techniques for phase-matching are employed (Maier, 2007).

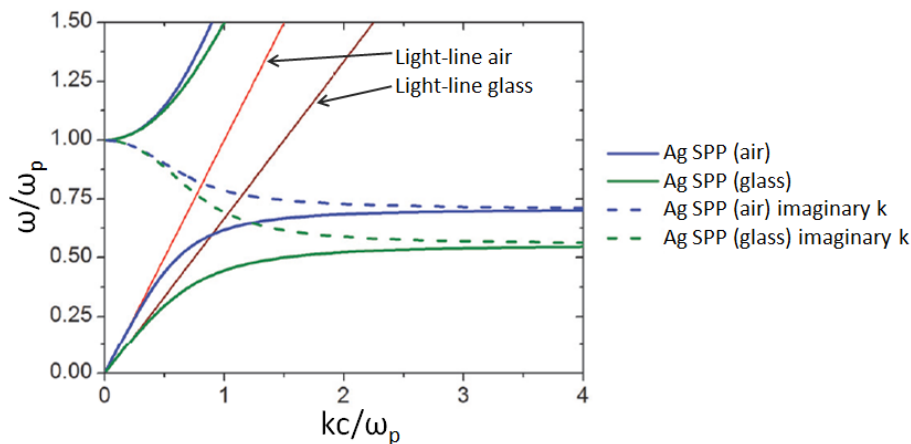


Figure 1.2: Dispersion curves for SPPs on an interface between half-spaces of a metal (Ag) and insulators with refractive index 1.0 (air) and 1.5 (glass). Image taken from Chapter 6 of reference (Kim et al., 2012).

Prism coupling

Phase-matching to SPPs can be achieved in a three-layer system consisting of a thin metal film between two insulators of different dielectric constants, for example, by placing the thin metallic layer on top of a dielectric prism, and considering air as the second dielectric medium, as schemed in Figure 1.3.

A beam reflected at the interface between the prism with dielectric constant ε^1 , and the metal will have a momentum $k_x = k\sqrt{\varepsilon} \sin \theta$, which is sufficient to excite the SPPs at the metal-air interface, as can be observed in the dispersion curves of Figure 1.3c.

There are two possible configurations for prism coupling. The first one is known as Kretschmann configuration (Fig. 1.3a), in which a thin metallic layer is deposited on top of the glass prism. A beam impinging from the glass side at an angle greater than the

¹The dielectric constant ε is related to the refractive index n of the medium by relationship $n = \sqrt{\varepsilon\mu}$, with μ the magnetic permeability of the medium. At optical frequencies we can consider $\mu = 1$.

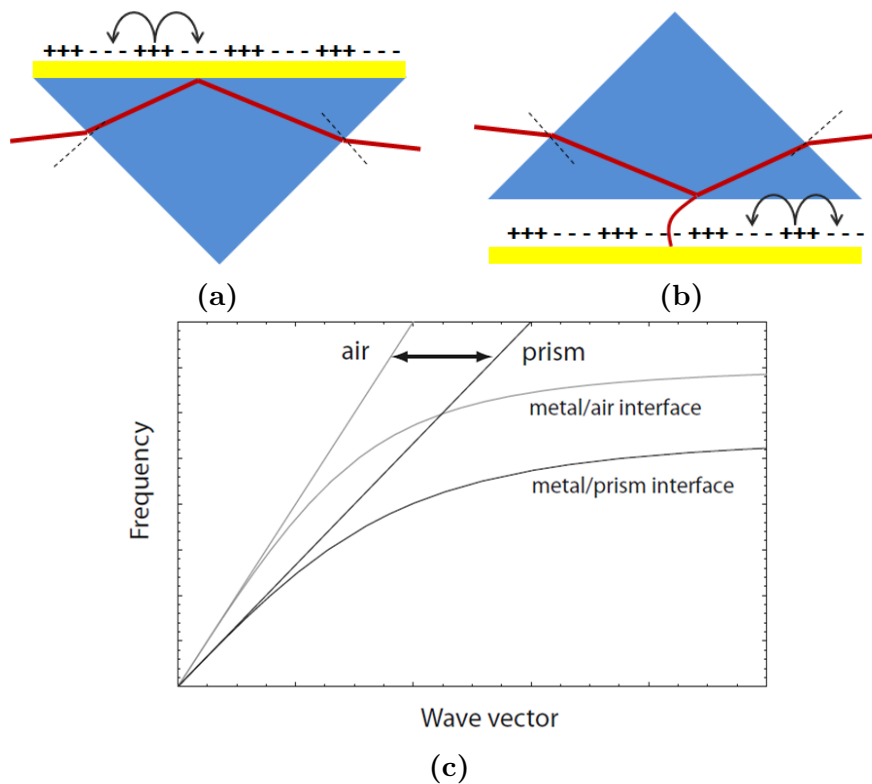


Figure 1.3: Prism coupling to SPPs using total internal reflection with (a) Kretschmann and (b) Otto configurations. (c) The dispersion relation shows the phase matching of k_{SPP} with the air light-line. Images reproduced from reference (Maier, 2007).

critical angle for total internal reflection, creates an evanescent wave at the prism-metal interface. These photons tunnel through the metal layer and excite the SPPs at the metal-air interface.

The second geometry is the so-called Otto configuration (Fig. 1.3b), in which the prism is separated from the metallic film by a thin air gap. Total internal reflection takes place at the prism-air interface, exciting the SPPs via tunneling to the metal-air interface.

We must remark that the excitation of SPPs using phase-matching via $k_{SPP} = k\sqrt{\epsilon} \sin \theta$ are inherently leaky waves, i.e. they lose energy not only due to the absorption inside the metal, but also due to leakage of radiation into the prism: the excited propagation constants lie within the prism light-cone. The SPP excitation manifests itself as a minimum in the reflected beam intensity, which is due to the destructive interference between the leaky radiation and the reflected part of the excitation beam.

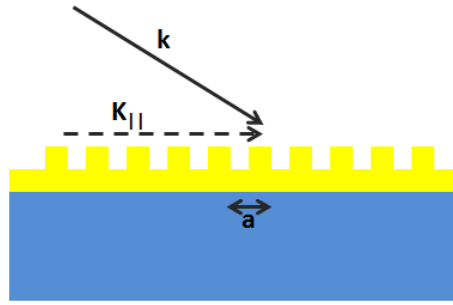


Figure 1.4: Phase-matching of light to SPP using a grating.

Grating coupling

The phase match between k_d and k_{SPP} can be also achieved by patterning the surface of the metal with a grating of grooves or holes with periodicity a , as depicted in Figure 1.4. Phase matching takes place whenever is satisfied the condition

$$k_{SPP} = k \sin \theta \pm ng, \quad (1.3)$$

where $g = 2\pi/a$ is the reciprocal vector of the grating and $n = 1, 2, 3, \dots$. The SPPs excitation is also detected as a minimum in the reflected light. The reverse process can also take place: SPPs propagating along the surface modulated with a grating can couple to light and become radiated. The gratings can also consist of a dielectric material. In general, SPPs can be excited on films in areas with random surface-roughness.

Practical applications of SPP in integrated photonic circuits requires high efficiency coupling schemes. Plasmonic components allow efficient matching with conventional dielectric optical waveguides and fibers, which can be used to channel energy over large distances to plasmon waveguides and cavities. This efficient matching will then enable high confinement guiding and localized field enhancement.

1.2 SPP based waveguides

The geometry of a thin layer (medium 2) between two media (1 and 3) is presented in Figure 1.5. As previously discussed for a dielectric-metal geometry, only TM-polarized waves can excite the SPPs. This condition is also valid for other geometries invariant in

the out-of-plane direction.

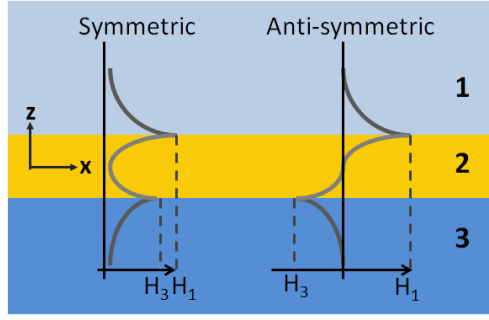


Figure 1.5: SPP based waveguide. The SPPs propagating at the 1/2 and 2/3 interfaces are coupled between each other. When they have the same phase, a symmetric mode is created, and for a phase difference of π rad, an anti-symmetric mode takes place.

The geometry depicted in Figure 1.5 can be used as a SPP waveguide as long as it is fulfilled the dispersion relation (see Appendix A)

$$\frac{\left(\frac{\alpha_2}{\varepsilon_2} - \frac{\alpha_3}{\varepsilon_3}\right) \left(\frac{\alpha_2}{\varepsilon_2} - \frac{\alpha_1}{\varepsilon_1}\right)}{\left(\frac{\alpha_2}{\varepsilon_2} + \frac{\alpha_3}{\varepsilon_3}\right) \left(\frac{\alpha_2}{\varepsilon_2} + \frac{\alpha_1}{\varepsilon_1}\right)} = e^{i2\alpha_2 d}, \quad (1.4)$$

where d is the thickness of medium 2, and

$$\alpha_i = \sqrt{\left(\frac{\omega}{c}\right)^2 \varepsilon_i - \beta^2}, \quad (1.5)$$

for $i = 1, 2, 3$. The solution to this dispersion relation means that the SPP propagating at the interface 1 – 2 is coupled to the SPP at the interface 2 – 3. Moreover, two families of solutions are expected from this equation: even (symmetric) and odd (anti-symmetric) modes. The symmetric mode arises when the SPPs propagating at each interface have the same phase, whereas a phase difference of π rad between them give rise to the anti-symmetric mode.

Two configurations of the mediums 1, 2 and 3 are possible: the Insulator-Metal-Insulator (IMI) or the Metal-Insulator-Metal (MIM) configuration. To describe the behavior of the SPPs in this kind of structures, let us consider the dispersion curves plotted in Figure 1.6 taken from reference (Kim et al., 2012).

In the dispersion relation of the MIM configuration (Fig. 1.6a), the mode under the Insulator-Metal (IM) dispersion tends to infinity in the lower plasma frequency ω_p (silver),

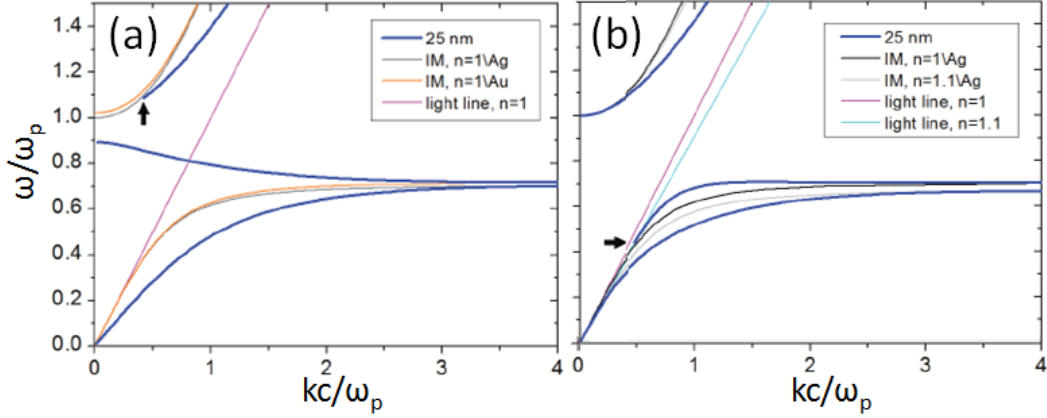


Figure 1.6: Dispersion relations for (a) a MIM: 25 nm free space surrounded by silver and gold, and (b) IMI: 25 nm silver layer surrounded by free space and other dielectric with refractive index $n = 1.1$. The Insulator-Metal SPP curve is also traced as reference. Plots taken from Chapter 6 of reference (Kim *et al.*, 2012).

while the mode above the IM dispersion tends to infinity in the higher ω_p (gold). Silver has lower plasma frequency than gold. Therefore, the IM dispersion of silver and vacuum remains under the IM dispersion of gold and vacuum. Between the ω_p of the two half-spaces, there is a gap. In addition, the anti-symmetric mode (upper branch) presents a cut-off frequency above the plasma frequencies of both metals when it reaches the IM dispersion of silver and vacuum (arrow in Fig. 1.6a).

The dispersion curve IMI, is presented in Figure (Fig. 1.6b). The even mode appears under the IM dispersion with the high refractive-index dielectric. For very low frequencies, this mode converges to the light line of the same dielectric. The odd mode appears above the IM dispersion with the low refractive-index dielectric. Close to the respective ω_p , the wavevector of this mode tends to infinity. For lower frequencies, there is a cut-off. This odd mode vanishes when it reaches the light line of the high refractive-index dielectric (arrow in Fig. 1.6b).

The regions pointed with arrows, correspond to frequencies where the modes are confined between the two external media, i.e. these structures behave as plasmonic waveguides. The number of supported modes by the structures depend on the thickness of the middle layer as well as the optical properties of the media. However, we must point that this waveguiding behavior is only satisfied for TM polarized waves.

1.3 Localized surface plasmons

We have seen in the preceding section that SPPs are propagating, dispersive electromagnetic waves coupled to the electron plasma of a conductor at a dielectric interface. However, there is another kind of plasmon excitation: localized surface plasmons (LSP). Unlike SPPs, localized plasmons are non-propagating excitations of the conduction electrons of metallic nanostructures coupled to the electromagnetic field.

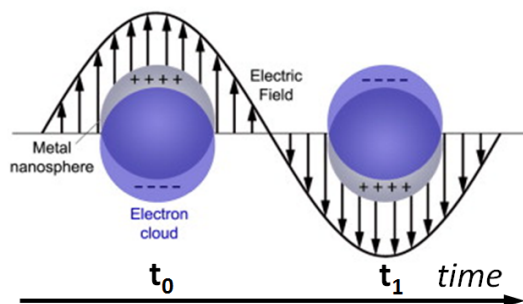


Figure 1.7: Localized surface plasmon: the restoring force experienced by a subwavelength conductive nanoparticle in presence of an oscillating electromagnetic field (at a time t_0), gives rise to a resonance mode, enhancing the field inside and in the near-field zone of the nanoparticle (at a time t_1) (Catchpole, 2006).

Localized surface plasmons are surface electromagnetic modes associated to the collective oscillations of the conducting electrons at the boundaries of metallic nano-particles (MNPs) (Bohren and Huffman, 1998). These modes arise from the scattering problem of a sub-wavelength conductive particle in an oscillating electromagnetic field (Figure 1.7). The curved finite shape of the particle exerts a restoring force on the driven electrons, such that a resonance arise, leading to a field amplification inside the particle and in the near-field zone outside of it.

From this fact, it becomes clear that the resonance wavelength of the LSP is highly dependent on the geometry of the particle, as well as the refractive index of the surrounding medium. Furthermore, LSP modes provide a highly confined electromagnetic field that can be used to probe a very small volume of matter (Kelly et al., 2003), and also can be applied in optical sensing devices (Hutter and Fendler, 2004).

A detailed description of the LSP resonances makes necessary the study of light scattering by small particles, subject emerging from the scope of the present thesis. However,

the reader may refer, for example, to the textbooks of S. A. Maier (Maier, 2007) or C. F. Bohren (Bohren and Huffman, 1998) for a larger and comprehensive explanation of this subject.

1.3.1 LSP based waveguides on metallic nanoparticles chains

Light propagation through periodic arrays of MNPs has already been demonstrated in several previous works (Weber and Ford, 2004; Koenderink and Polman, 2006; Koenderink et al., 2007; Popov et al., 2007; Yang and Crozier, 2008; Hochman and Leviatan, 2009; Simsek, 2010). This propagation mechanism is explained by LSP near-field coupling between consecutive particles excited at their proper resonances. Due to this coupling effect, the MNP chains can behave as metallic waveguides.

To observe this coupling effect, we performed numerical examples by making use of the integral equation method (Valencia et al., 2003; Tellez-Limon, 2011). A single Ag nanowire of thickness 50 nm, width 250 nm and invariant in the out-of-plane direction, is immersed in air and perpendicularly illuminated with a Gaussian beam at its LSP resonance ($\lambda = 365$ nm). We note that it behaves like a single dipole, with a field enhancement at its corners (Figure 1.8a). When this nanowire is divided into two equal sections of width 100 nm each one and separated a distance of 50 nm from each other, the nanowires act once again like individual dipoles that are coupled between them, forming a dimer, with a LSP resonance shifted to $\lambda = 375$ nm (Figure 1.8b).

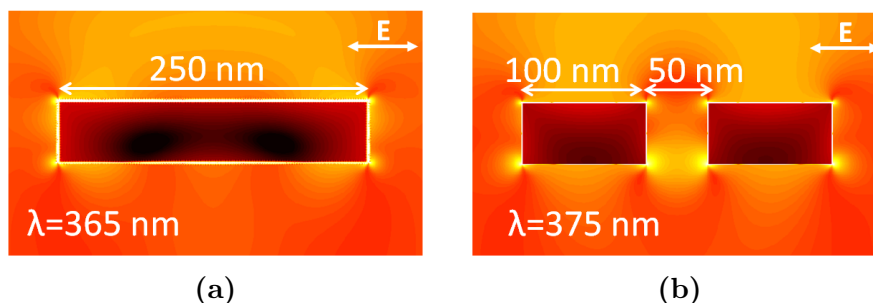


Figure 1.8: Normalized intensity near-field map of the coupling between Ag nanowires when perpendicularly illuminated with a TM polarized gaussian beam. (a) A single nanowire of thickness 50 nm and width 250 nm exhibits a dipolar behavior at its LSP resonance ($\lambda = 365$ nm). (b) When the nanowire is divided into two equal sections of width 100 nm and gap 50 nm, the LSP resonance is shifted at $\lambda = 375$ nm, exhibiting a coupling between these dipoles.

We can also observe the coupling effect for quadrupolar resonances. For example, if we illuminate with a Gaussian beam an Ag cylinder of 50 nm diameter immersed in air, at its LSP resonance ($\lambda = 340$ nm) it exhibits a quadrupolar resonance (Figure 1.9a). Then if consecutive cylinders are placed parallel to the lightening direction (horizontal direction in Figure 1.9b), the cylinders are once again coupled between each other, resulting in a shift of the LSP resonance to $\lambda = 500$ nm and exhibiting a field enhancement perpendicularly to the propagation direction of the field.

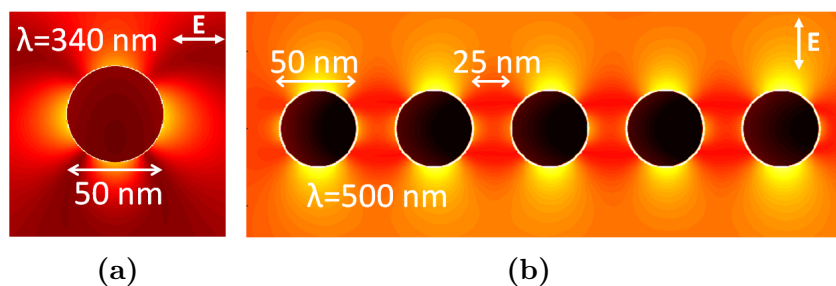


Figure 1.9: Normalized intensity maps of (a) a single cylinder of 50 nm diameter exhibiting a quadrupolar resonance at $\lambda = 340$ nm. (b) Placing a periodic array of cylinders, the quadrupoles are coupled between each other shifting the LSP resonance to $\lambda = 500$ nm.

These simple examples demonstrate that a near-field coupling between consecutive MNP is achievable due to the near-field interaction when the particles are illuminated at their LSP resonance.

We can well understand this coupling effect with an eigenmode scrutiny of the plasmonic modes in the MNP chain. However, the large majority of the analysis made by other authors (Koenderink and Polman, 2006; Koenderink et al., 2007; Christ et al., 2003; Crozier et al., 2007) has been done above the light-line in the dispersion relations (as will be explained in detail in Chapter 3), where the modes of the chain can be excited only with radiative modes, that is, from the free space or from the substrate. The longitudinal (L), transverse out-of-plane (T2) (Crozier et al., 2007), and higher multipolar chain modes (Wei et al., 2010) are among the eigenmodes that are reported above the light-line region.

To study the MNP mode excitation below the light-line limit, some authors have proposed the integration of MNP chains on top of a dielectric waveguide (Quidant et al., 2004; Février et al., 2012b; Arango et al., 2012), but the choice of the incident transverse electric (TE) mode of the waveguide limits the excitation of one kind of chain mode,

namely the dipolar transverse (T1) mode (Fevrier et al., 2012a; Apuzzo et al., 2013).

1.4 Applications on plasmonics

We have mentioned in previous sections that optical excited plasmons can enhance the optical field in the near-field close vicinity of the excited region. Furthermore, their resonance wavelength is highly dependent on the material properties not only of the metal, but also of the surrounding dielectric medium. For the particular case of localized surface plasmons, their resonance is also highly dependent on the shape of the metallic nanoparticle.

For this reason, plasmons can be applied in different research areas, such as telecommunications, quantum information, biology, chemistry, electronics, and medicine, among many others. Examples of already demonstrated applications of plasmon excitation are

- Plasmonic lasers and metal-cavity nanolasers (Hill et al., 2007),
- Plasmonic modulators to encode electric signals onto SPPs and the transform the information back into an optical signal (Nikolajsen et al., 2007),
- Plasmonic photodetectors and amplifiers (Ishi et al., 2005),
- Plasmonic waveguides to perform nano-scale optical circuits (Dionne et al., 2006),
- Enhancement of emissive processes and nonlinearities (Maier, 2007),
- Spectroscopy and sensing (Passaro et al., 2007),
- Metamaterials and imaging (perfect lens) (Pendry, 2000),
- Efficiency improvement on the radiation absorption of solar cells (Lal et al., 2011).

The enlisted elements does not reflect all the research done about this subject. Everyday emerge new ideas on the application of plasmons excitation, being these ideas related to the nano-fabrication techniques and available technologies. However, one of the most promising applications of plasmonics is the development of optical integrated nano-devices.

For example, plasmonics devices can act as a bridge between current diffraction-limited microphotronics and bandwidth-limited nanoelectronics, i.e. to overcome the huge size mismatch between large-scale integrated photonics and small-scale integrated electronics.

Integrated plasmonics can also serve in the improvement of spectroscopic measurements techniques, like fluorescence, Raman scattering, and second harmonic generation.

1.4.1 Integrated plasmonic biosensors

Of particular interest in the context of the present thesis, is the utilization of integrated optical structures as sensing nanodevices. A brief description of the operating principles of these sensors is given below.

To detect chemical or biological substance (analytes) it is exploited the interaction of the electromagnetic radiation with the samples. This is done by evaluating the change of a particular optical parameter and relating it to the concentration of the analyte.

Sensors that have a receptor part based on a biochemical principle are named biosensors. A bioreceptor is a biological molecular system that adopts a biochemical mechanism for analyte recognition. A transducer is then used to transform the measurand into a useful signal (Passaro et al., 2007). The operation principle of a biosensor is schemed in Figure 1.10.

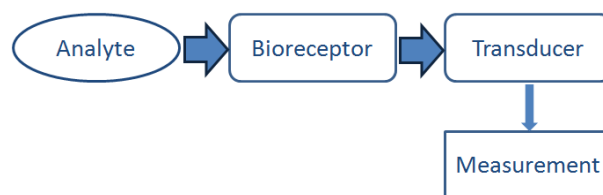


Figure 1.10: Biosensor operation principle. A biosensor is a device that consists of a biologically or biophysically-derived sensing element (bioreceptor) integrated with a physical transducer that transforms a measurand into an output signal.

The most used bioreceptors are based on antibody-antigen interactions. The antibodies are complex bio-molecules formed by a hundred of amino acids arranged in a large Y-shaped ordered sequence. The antibody recognizes a specific target, which is called antigen. The interaction between antibodies and antigens is highly specific because their molecular structures are complementary. Antigen-antibody reaction specificity enables to

use antibodies as specific detectors capable to sense the analyte of interest even if their amount is very small or if a great number of other chemical substances are present in the sample.

Among the transduction mechanism used in optical sensors can be found (Passaro et al., 2007; Lobnik et al., 2012)

- Fluorescence: energetic transition from an excited state to a lower energy level producing photon emission,
- Raman scattering: energy exchange between incident photon and scattering molecules,
- Absorption change: relation between a solution absorbance to an analyte dispersed in this solution concentration,
- Photon migration spectroscopy: combination of experimental measurements and model-based data analysis to measure the bulk absorption properties of highly scattering media,
- Effective index change in guiding structures: shift of propagating optical mode effective index induced in a guiding structure,
- Surface plasmon resonance: charge-density oscillation that may exist at the interface between two media with dielectric constants of opposite signs.

Surface plasmon resonance (SPR) transduction is of particular interest in the reference frame of the concepts studied in previous sections. SPR is a surface optical technique that measures minute changes in refractive index at a metal-coated surface. As SPPs are evanescently bounded and they are sensitive to dielectric perturbations at the surface, metallic structures can be used to sense the binding of molecules to the surface. SPR allows for both quantitative and qualitative analysis of binding interactions in real-time, making it ideally suited for probing weak interactions that are difficult to study with other methods (Linman and Cheng, 2010).

Moreover, metallic nanoparticles can be coupled between each other when they are excited at their LSP resonance, and since this resonance is highly dependent on the shape

of the particles, their implementation in sensing devices can improve the sensitivity of the measured signal.

Integrated optical sensors are the most commonly exploited structures for biochemical sensing applications. These structures adopt a waveguide to confine optical power and are based on evanescent field sensing. They exhibit interesting advantages such as compactness, very high sensitivity and possibility of mass production.

This feature is the object of study in the present thesis: the analysis of an integrated plasmonic structure whose characteristics could be applied in the detection of chemical or biological substances.

1.5 Objective of the thesis

Even if the research field of LSPR sensors have been largely studied and successful experimental demonstrations of LSPR sensing have been done, there is a research area that can be explored to improve their performance and to reduce the sensing area of such devices, and hence achieve single cell or molecule sensing. The use of integrated photonic devices for sensing applications based on periodic arrays of MNPs is a platform that could allow such improvements.

Although these integrated arrays have also been proposed, there is a lack of a generalized explanation of the modes coupling mechanism in periodic arrays of MNPs. This situation suggests the implementation of a numerical method capable to explain the physical phenomena involved in the design and characterization of the integrated structures.

The main objective of the thesis is thus to perform a modal analysis of the near-field coupling mechanism in an hybrid structure consisting of a photonic waveguide integrated with a chain of periodic metallic nanowires. This structure can be applied in the development of chemical or biological sensing devices.

This modal analysis is performed by making use of the so-called Fourier modal method (FMM), a rigorous numerical tool that can be suited to analyze the dispersion curves of the supported modes of the integrated structure, as well as simulate the beam propagation along the structure.

We analyze two kind of integrated structures, the first corresponding to a periodic array of metallic nanowires of rectangular cross-section (MNW), and the second to a periodic array of metallic nanowires of triangular cross-section (nanocones).

To provide experimental evidence of the numerical results obtained with the proposed method, we fabricated and characterized in far and near-field regimes an optical integrated device consisting of a periodic array of gold nanowires placed on top of a glass substrate containing an ion-exchanged waveguide, as depicted in Figure 1.11.

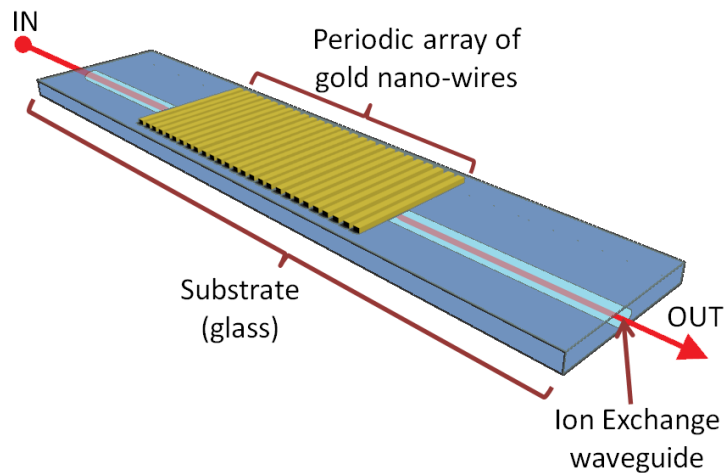


Figure 1.11: Scheme of the integrated plasmonic structure for sensing applications. On top of a glass substrate containing an ion-exchanged waveguide of low contrast refractive index, it is placed a periodic array of gold nanowires.

As will be evidenced in the following chapters, the obtained results indicate that the performed structures can be used as sensing devices for biological or chemical applications. This is because the LSP resonance is highly dependent on the refractive index of the surrounding medium, allowing the integrated structure to measure real-time changes of the environment effective index.

Chapter 2

Numerical method

As we introduced in the Chapter 1, a periodic array of metallic nanoparticles (MNP) can behave as a plasmonic waveguide by near-field coupling between consecutive NP for an excitation close to their LSP resonance. This behavior implies that a system of coupled waveguides can be achieved by integrating a periodic array of MNP on top of a dielectric waveguide. In order to predict the modal and propagation properties of light when passing through the integrated system, it is necessary to implement a numerical tool that can be adapted to the study of periodic arrays of metallic nanoparticles, as well their characterization in terms of the beam propagation.

In this chapter we present a numerical method for the analysis of such integrated plasmonic structures and the generalities of its numerical implementation. To have a better understanding of the physical phenomena related in this modal analysis, we first present the solution of modes propagating in a multilayered media, and then an analytic approach that describes the coupling of the diffracted modes from an infinite periodic metallic grating to the multilayered structure. The analytic expression found is the dispersion relation whose solutions are the Bloch modes supported by the periodic grating. Even if this approach have been used to perform modal analysis of integrated gratings in multilayered structures (Tishchenko, 2005), we will not use this approximation. We only present it to have a conceptual understanding of the coupling mechanism of the diffracted modes to the multilayered structure.

Another possible and efficient way to find the electromagnetic modes of a periodic

grating is the expansion of the medium parameters and the electromagnetic field into Fourier series. Such method of solution is the so-called Fourier modal method (FMM). For this method we present the general algorithm used for solving the eigenvalue problem by making use of the S matrix method, as well as the reconstruction of near-field maps of the excited modes.

Even when the FMM properly describes the modes propagation in infinite periodic arrays of metallic nanoparticles, the coupled integrated system under study is of finite dimension. To overcome this situation, the FMM is then suited to non periodic finite structures, letting us to simulate the beam propagation along the integrated structure. This feature allow us to characterize the integrated plasmonic structure in terms of their transmission, reflection and absorption spectra, as well as the computation of near-field maps in the region of interest.

2.1 Modes propagation in multilayered media

In Chapter 1 we introduced an optical integrated system consisting of a periodic chain of metallic nanoparticles (MNP) on top of a dielectric waveguide, as exhibits Figure 2.1(a).

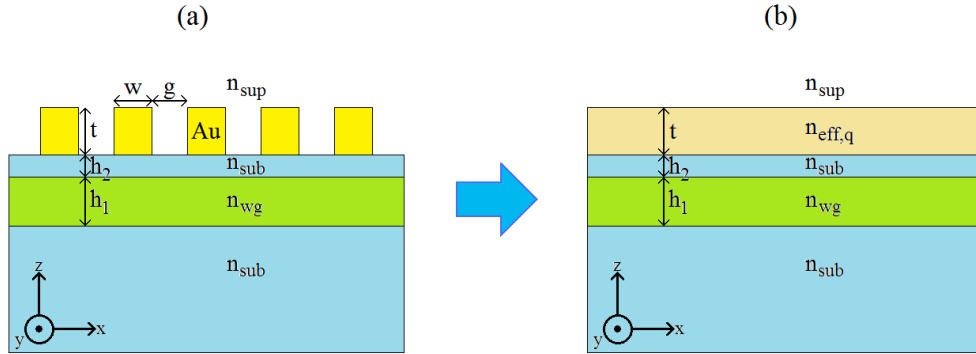


Figure 2.1: (a) Scheme of metallic nanowires chain on top of a dielectric waveguide. (b) The integrated system can be seamed as a multilayered media, where the metallic grating region is transformed into an equivalent homogeneous layer of effective index $n_{eff,q}$ determined by the q -th propagating mode.

In general, the modal method exploits the fact that the light diffracted by the grating region can be coupled to the adjacent layers to the grating. Since each mode propagates with a certain propagation constant, the grating region can be regarded as a uniform

homogeneous layer of effective index $n_{\text{eff},q}$ determined by the q -th propagating mode. Then, the complete structure can be treated as a multilayered system (Fig. 2.1).

Firstly, we present the way to compute the modes propagating in a multilayered homogeneous media. The problem of the diffracted modes arising from the grating region will be treated in a later section.

To determine the propagation constants in a multilayered media, let us consider the structure represented in Figure 2.2. This multilayered structure is invariant in the out-of-plane y axis direction, and the waves are considered to travel in the positive direction of the x axis. The following analysis can be applied for both transverse electrical (TE) or transverse magnetic (TM) polarized fields.

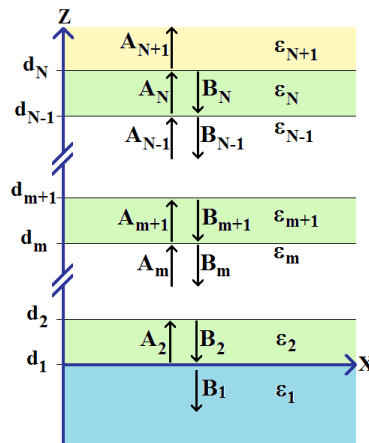


Figure 2.2: Scheme of a multilayered media invariant in the y (out-of plane) direction. The substrate ($m = 1$) and superstrate ($m = N + 1$) are considered as semi-infinite media.

2.1.1 Helmholtz equation

Let us consider that the system schemed in Fig. 2.2 is free of external currents or sources. For this case, the Maxwell equations in the free space are given as (Jackson, 1998)

$$\nabla \cdot \mathbf{D}(\mathbf{r}, \omega) = 0, \quad (2.1)$$

$$\nabla \cdot \mathbf{H}(\mathbf{r}, \omega) = 0, \quad (2.2)$$

$$\nabla \times \mathbf{E}(\mathbf{r}, \omega) = i \frac{\omega}{c} \mathbf{H}(\mathbf{r}, \omega), \quad (2.3)$$

$$\nabla \times \mathbf{H}(\mathbf{r}, \omega) = -i \frac{\omega}{c} \mathbf{D}(\mathbf{r}, \omega), \quad (2.4)$$

which satisfy the constitutive relation

$$\mathbf{D}(\mathbf{r}, \omega) = \varepsilon(\omega) \mathbf{E}(\mathbf{r}, \omega). \quad (2.5)$$

Taking into account the invariance of the system in the y direction, from eq. (2.3) we obtain the relations

$$\frac{\partial E_y}{\partial z} = -i \frac{\omega}{c} H_x, \quad (2.6)$$

$$\frac{\partial E_x}{\partial z} - \frac{\partial E_z}{\partial x} = i \frac{\omega}{c} H_y, \quad (2.7)$$

$$\frac{\partial E_y}{\partial x} = i \frac{\omega}{c} H_z, \quad (2.8)$$

and by making use of the constitutive relation (2.5), from eq. (2.3) we get

$$\frac{\partial H_y}{\partial z} = i \frac{\omega}{c} \varepsilon(\omega) E_x, \quad (2.9)$$

$$\frac{\partial H_x}{\partial z} - \frac{\partial H_z}{\partial x} = -i \frac{\omega}{c} \varepsilon(\omega) E_y, \quad (2.10)$$

$$\frac{\partial H_y}{\partial x} = -i \frac{\omega}{c} \varepsilon(\omega) E_z. \quad (2.11)$$

As a TE polarized field only have a component of the electric field in the perpendicular direction y , i. e. $\psi_{TE} = (H_x, E_y, H_z)$, the set of equations (2.6), (2.10) and (2.8) lead us to the relationship

$$\left[\frac{\partial^2}{\partial x^2} + \frac{\partial^2}{\partial z^2} + \left(\frac{\omega}{c} \right)^2 \varepsilon(\omega) \right] \psi_{TE}(x, z|\omega) = 0. \quad (2.12)$$

In a similar way, eqs. (2.9), (2.7) and (2.11) define a TM polarized field $\psi_{TM} =$

(E_x, H_y, E_z) , being obtained

$$\left[\frac{\partial^2}{\partial x^2} + \frac{\partial^2}{\partial z^2} + \left(\frac{\omega}{c} \right)^2 \varepsilon(\omega) \right] \psi_{TM}(x, z|\omega) = 0. \quad (2.13)$$

The equations (2.12) and (2.13) have both the same mathematical structure and correspond to the Helmholtz equation for TE or TM polarized fields, respectively.

2.1.2 Dispersion relation

By solving the Helmholtz differential equation, we can describe the modes propagation along the multilayered structure for both TE or TM polarization. To this purpose, we represent the field in the m -th layer of Fig.2.2 as a sum of propagative and counter-propagative waves in the z direction, and propagative in the positive direction of the x axis, which can be expressed as

$$\psi_m(x, z|\omega) = A_m e^{-i\alpha_m z} e^{-i(\omega t + \beta_m x)} + B_m e^{i\alpha_m z} e^{-i(\omega t + \beta_m x)}. \quad (2.14)$$

A direct substitution of relation (2.14) into the Helmholtz equation lead us to the dispersion relation

$$\beta_m = \sqrt{\left(\frac{\omega}{c} \right)^2 \varepsilon_m(\omega) - \alpha_m^2}. \quad (2.15)$$

This means that all the TE or TM electromagnetic fields with the form of equation (2.14) will be propagated along the structure if their propagation constants are matched by the condition given by equation (2.15). These solutions are known as *modes*, which are fields that maintain their polarization and spatial distribution at any position along the stratified media.

2.1.3 Boundary conditions

We can determine the propagation constant $\beta(\alpha_m)$ that satisfies the dispersion relation (2.15), as an eigenvalue problem by linking the diffracted modes at the interface between two subsequent layers, taking into account that they must have the same propagation

constant in the positive direction of x : $\beta_{m+1} = \beta_m$.

To this purpose boundary conditions are needed. These conditions are the continuity and the conservation of the tangential components of the electromagnetic field when passing from one medium to another (Jackson, 1998). These conditions allow us to express the eigenvalue problem in a matrix form, however, we also need to implement boundary conditions for the diffracted modes at the superstrate and the substrate layers.

As depicted in Figure 2.2, the bottom and top layers are considered as semi-infinite media and no external sources are considered. Then, we only should consider the modes that are diffracted out from the multilayered stack, in other words, no reflected waves are expected. This situation lead us to impose the boundary conditions $A_1 = B_{N+1} = 0$.

By applying these conditions, the obtained eigenvalue problem is reduced to the computation of a single matrix that describes all the diffracted components in the multilayered media. This formulation is known as the S matrix algorithm (or equivalently the T matrix method), and it is explained in detail in the Appendix A.

The elements of the \mathbf{S} matrix that describes the complete structure, are related to the propagation constant of the modes supported by the multilayered media. These propagation constants can then be computed by equating the determinant of this matrix to zero, ($\det \{\mathbf{S}\} = 0$). With this result, we can also determine the amplitudes and then to reconstruct the electromagnetic field.

Now we need to compute the diffracted modes in the grating region. This problem is discussed in the following section.

2.2 Modes propagation in an infinite periodic grating

As mentioned in the previous section, we need to compute the diffracted modes in the grating region of the integrated structure. This section is concerned to the study of propagating modes in an infinite periodic metallic grating of thickness t , width w , and period Λ , between two homogeneous media of permittivities $\varepsilon_{(1)}$ and $\varepsilon_{(2)}$, as presented in Figure 2.3.

Let us consider that the incident field is a plane wave impinging the structure from

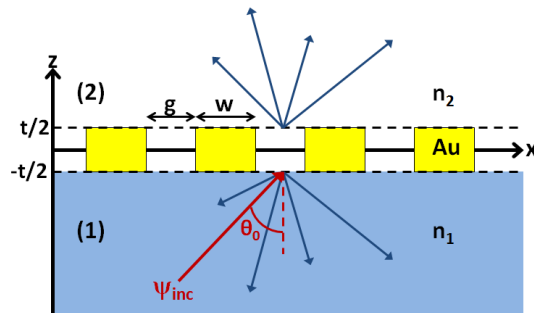


Figure 2.3: Diffraction of a plane wave on an infinite periodic array of metallic nanowires along the x -axis, of thickness t and period $\Lambda = w + g$, between two semi-infinite homogeneous media.

the substrate (medium 1), whose wavevector \mathbf{k} forms an incident angle θ_0 respect to the z axis. We can describe this plane wave as

$$\psi_{inc}(x, z|\omega) = \psi_0^1 e^{ik_x x} e^{ik_0^1(z+t/2)} e^{-i\omega t}, \quad (2.16)$$

where

$$k_x = \frac{\omega}{c} n_1 \sin \theta_0, \quad (2.17)$$

$$k_0^1 = \frac{\omega}{c} n_1 \cos \theta_0, \quad (2.18)$$

n_1 is the refractive index of the substrate, and ψ_0^1 is the amplitude of the incident plane wave.

At the first interface (from medium 1 to the grating region), the plane wave is partially transmitted and reflected. The transmitted part is converted into the diffraction modes of the grating, and the reflected fraction is converted into diffracted orders to the medium 1. The excited modes of the grating reach the second interface (grating-medium 2), where they are partially transmitted and converted into the diffracted orders of medium 2, and partially reflected to the modes of the grating.

We can describe the diffracted orders in the adjacent media to the grating as the sum of propagative and counter-propagative diffraction orders along the z axis. These diffracted orders can be expressed in terms of Rayleigh-Fourier expansions with a constant spatial period around a central spatial frequency given by the zeroth order of the incident plane

wave (Tishchenko, 2005). This can be written as

$$\psi^j(x, z|\omega) = \sum_{m=-\infty}^{\infty} e^{ik_{xm}x} \left[A_m^j e^{-ik_m^j(z+h/2)} + B_m^j e^{ik_m^j(z+h/2)} \right] e^{-i\omega t}, \quad (2.19)$$

where

$$k_{xm} = k_x + \frac{2\pi m}{\Lambda}, \quad (2.20)$$

$$k_m^j = \sqrt{\left(\frac{\omega}{c}\right)^2 n_j^2 - k_{xm}^2}, \quad (2.21)$$

A_m^j and B_m^j are up and down amplitudes, respectively, of each diffracted order, Λ is the period of the structure, and the script $j = 1, 2$ denotes the medium.

For simplicity and without loss of generality, we only study the case of a three layered media, but the expansion given in equation (2.19) is a general expression that can be extended to a multilayered system.

The idea now is to find the diffracted modes in the grating region as a function of the incident plane wave, and match them to the diffraction orders of the adjacent homogeneous media. At this point, the thickness t of the MNW is not a matter of interest, because this value will be taken into account when determining the propagation constant of the modes supported by the three-layered system of Fig. 2.3. Then, we can regard the grating region like a periodic array of infinite gratings along the z axis, as depicted in Figure 2.4. The widths of regions I and II are w and g , respectively, so the period of the structure along the x axis is $\Lambda = w + g$.

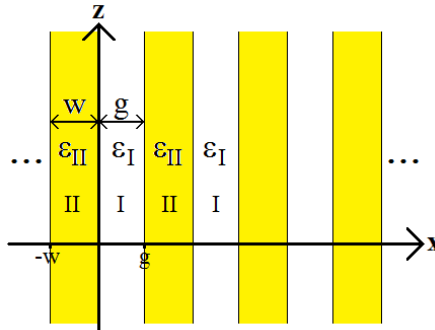


Figure 2.4: Scheme of a one-dimensional grating periodic along the x axis, and infinite along the z axis. The period of the structure is $\Lambda = w + g$.

The TE or TM diffracted modes propagating through the structure of Fig. 2.4, must

satisfy the Helmholtz equation that for an arbitrary field $\psi_y(x, z|\omega)$, is given by

$$\left[\frac{\partial^2}{\partial x^2} + \frac{\partial^2}{\partial z^2} + \left(\frac{\omega}{c} \right)^2 \varepsilon_j(\omega) \right] \psi_y^j(x, z|\omega) = 0, \quad (2.22)$$

with $j = I, II$.

In the following sections, we explain two possible ways to find these modes. The first solution is an analytic process that can be used to determine the propagation constant of each one of the diffracted modes (Tishchenko, 2005). With the second method, we solve the same eigenvalues problem in the frequencies domain by describing the dielectric function of the periodic structure in Fourier series. This is the so-called Fourier modal method.

We must clarify that all the numerical results that will be presented in Chapters 3 and 4, were obtained by making use of the Fourier modal method. The analytic treatment is only used to explain the physical meaning of the modal method.

2.2.1 Analytic treatment

We can write the total electromagnetic field that is solution to the Helmholtz equation (2.22) in the grating region, as the infinite sum

$$\psi_y(x, z) = \sum_{q=0}^{\infty} \psi_{y,q}(x, z) = \sum_{q=0}^{\infty} \psi_q(x) \left[A_q e^{-i\beta_q z} + B_q e^{i\beta_q z} \right], \quad (2.23)$$

where β_q is the propagation constant of the mode of order q , and $\psi_q(x)$ is the lateral field distribution of the q -th order mode. We can find the up and down amplitudes A_q and B_q , by using boundary conditions at the interfaces $z = \pm t/2$.

To determine the distribution of the electromagnetic field for a single mode q , let us assume that this grating mode propagates with constant β_q up or down in the z direction. Without loss of generality, we only consider the propagation in the upward direction. In both media I and II of the grating region, at the n -th vertical interface the waves are partially reflected and transmitted in the x direction. Then, we can express the

distribution of the electromagnetic field for a given mode in each medium as

$$\psi_{y,q}^j(x, z|\omega) = e^{ik_x n \Lambda} e^{-i\beta_q z} e^{-i\omega t} \left[C_q^j e^{i\alpha_j x} + D_q^j e^{-i\alpha_j x} \right], \quad (2.24)$$

with $j = I, II$ and $k_x = \left(\frac{\omega}{c}\right) n_1 \sin \theta_0$, being θ_0 the incidence angle of the plane wave, and n an arbitrary integer. Knowing that the propagation constant satisfies the relationship $\beta_q = 2\pi n_{\text{eff},q}/\lambda$, we then obtain

$$\alpha_j = \left(\frac{\omega}{c}\right) \sqrt{n_j^2 - n_{\text{eff},q}^2}. \quad (2.25)$$

The field $\psi_{y,q}(x, z|\omega)$ traveling along the x direction, as well as its tangential components, must be continuous at the edge of the interface $n\Lambda$, with n an integer number (Jackson, 1998). Also, since we are dealing with a periodic structure, we can apply the Bloch theorem, that states that the field at the edge of the period $\tau = (n+1)\Lambda$ must be the same at the edge of the period $\tau = n\Lambda$ multiplied by a phase factor $e^{ik_x \Lambda}$, which is related to the incidence angle of the field respect to the z axis, θ_0 (Sheng et al., 1982). These boundary and periodicity conditions are mathematically expressed as

$$\psi_{y,q}^I(x, z|\omega) \Big|_{x=n\Lambda} = \psi_{y,q}^{II}(x, z|\omega) \Big|_{x=n\Lambda}, \quad (2.26)$$

$$\left(\frac{1}{\varepsilon_I}\right)^p \frac{\partial \psi_{y,q}^I(x, z|\omega)}{\partial x} \Big|_{x=n\Lambda} = \left(\frac{1}{\varepsilon_{II}}\right)^p \frac{\partial \psi_{y,q}^{II}(x, z|\omega)}{\partial x} \Big|_{x=n\Lambda}, \quad (2.27)$$

$$\psi_{y,q}^I(x, z|\omega) \Big|_{x=n\Lambda+g} = e^{ik_x \Lambda} \psi_{y,q}^{II}(x, z|\omega) \Big|_{x=n\Lambda-w}, \quad (2.28)$$

$$\left(\frac{1}{\varepsilon_I}\right)^p \frac{\partial \psi_{y,q}^I(x, z|\omega)}{\partial x} \Big|_{x=n\Lambda+g} = e^{ik_x \Lambda} \left(\frac{1}{\varepsilon_{II}}\right)^p \frac{\partial \psi_{y,q}^{II}(x, z|\omega)}{\partial x} \Big|_{x=n\Lambda-w}, \quad (2.29)$$

where $p = 0$ for TE polarization, and $p = 1$ for TM polarization (Jackson, 1998).

By the substitution of equation (2.24) into the boundary conditions (2.26)-(2.29) we obtain a set of four equations whose determinant can be equated to zero to ensure that the system of equations have no trivial solution. With this substitution, we get the dispersion

relation

$$\cos(\alpha_I g) \cos(\alpha_{II} w) - \frac{1}{2} \left[\frac{\alpha_I \nu_{II}}{\nu_I \alpha_{II}} + \frac{\alpha_{II} \nu_I}{\nu_{II} \alpha_I} \right] \sin(\alpha_I g) \sin(\alpha_{II} w) = \cos(k_x \Lambda), \quad (2.30)$$

where $\nu_I = \nu_{II} = 1$ for TE polarization, and $\nu_I = \varepsilon_I$ and $\nu_{II} = \varepsilon_{II}$ for TM polarization.

In general, the relationship (2.30) exhibits a transcendental function with no analytic solution, and to solve it we need to implement numerical approximations (Botten et al., 1981a,b; Sheng et al., 1982). To verify the consistence of this relationship, if we take the limit case when $g \rightarrow 0$ for normal incidence respect to the propagation axis ($k_x = 0$), we expect that the effective index of the structure be the same of the medium II . Applying this limit to equation (2.30) it is straightforward to show that

$$n_{\text{eff},q} = \sqrt{n_{II}^2 - \frac{2\pi q}{w(\omega/c)}}, \quad (2.31)$$

for $q = 0, \pm 1, \pm 2, \dots$, since $\cos(\alpha_{II} w) = 1 \Leftrightarrow \alpha_{II} w = 2q\pi$. Then, for the fundamental mode $q = 0$ we get $n_{\text{eff},0} = n_{II}$, which was our original assumption.

For TE polarization it must be satisfied that $\nu_I = \nu_{II} = 1$. Then, the equation (2.30) only has solutions (propagating modes) in the domain $n_{\text{eff},q}^2 \geq 0$. All other modes are exponentially decaying along z and do not propagate energy through the grating array. The shorter is the grating period Λ , the less number of modes can be propagated (Tishchenko, 2005).

For TM polarization $\nu_I = \varepsilon_I$ and $\nu_{II} = \varepsilon_{II}$. Then, the equation (2.30) always has at least one solution in the domain $n_{\text{eff},q}^2 \geq \max[n_I^2, n_{II}^2]$. This solution has a plasmon nature. On the contrary, for TE polarization there is a possibility to not have solutions in the domain $\min[n_I^2, n_{II}^2] < n_{\text{eff},q}^2 < \max[n_I^2, n_{II}^2]$, which is the case for small dielectric thickness. A complete and detailed analysis of all the possible solutions of equation (2.30) can be found in reference (Foresti et al., 2006).

At this point, the modes diffracted by the grating are not necessarily the supported modes of the three-layered structure. To ensure that they are guided modes, we must impose boundary conditions.

Such conditions are that the diffracted orders to the substrate and superstrate layers are only outgoing fields, and that they are not back-reflected into the structure. In other words, that the amplitudes of all the diffracted modes given in equation (2.19) vanish at the infinite: $A_m^1 = B_m^2 = 0$.

Once we get the propagating modes, the amplitudes in each one of the homogeneous layers can be obtained by making use of relationship (2.23) and the S-matrix algorithm (Appendix A). The deduction of the S-matrix for the grating region is described in the Appendix B.

Physical interpretation of propagating modes

We know from waveguide theory (Marcuse, 1981) that the energy redistribution on the junction between two waveguides is determined by the modal field overlap integrals and the modes propagation constants. Only those modes with a good overlap can exchange energy, allowing a high energy transmission.

If the period of the metal-dielectric grating is short, no diffraction is expected because the waves are evanescent and do not propagate energy to the dielectric surrounding mediums. It only propagates TM polarized waves. If the dielectric part of the grating is not very thin, the fundamental TM mode of the grating is a plasmonic-like wave, with a propagation constant

$$\beta_{0,TM} \cong \frac{\omega}{c} \sqrt{\frac{\varepsilon_I \varepsilon_{II}}{\varepsilon_I + \varepsilon_{II}}}, \quad (2.32)$$

which is the propagation constant of a metal-dielectric surface plasmon (Tishchenko, 2005).

The detailed analysis of the dispersion equation (2.30) as given in reference (Foresti et al., 2006), predicts that the diffraction properties of a lamellar grating can be applied to an integrated system working like a directional coupler.

In a directional coupler, the energy distribution between both waveguides depends on the relative phase difference between the traveling modes. The coupling length is a

function of the difference between the modal propagation constants:

$$L = \frac{\pi}{\beta_0 - \beta_1}, \quad (2.33)$$

with a beating period equal to $2L$.

2.2.2 Fourier modal method

We have explained that the modal analysis of an infinite periodic array of MNW involves the expansion in Rayleigh series of the diffracted plane-wave above and below the grating region (eq. (2.23)). The modes inside the grating are computed as Bloch modes (eq.(2.24)), and by imposing boundary conditions at the grating interfaces, we can compute the field amplitudes everywhere.

Another possible way to solve this eigenvalue problem is by making use of the Fourier modal method (FMM), a well known rigorous method that solves the Maxwell equations in the frequencies domain. It is a modal method that is based on the expansion in Fourier series of all the electromagnetic quantities involved in the Maxwell equations: \mathbf{E} , \mathbf{H} , ε and μ .

The reason for using these expansions arises from the fact that the Fourier transform of a periodic function of length L in the real space results in a discrete function in the Fourier domain. Reciprocally, the inverse Fourier transform of a discrete function with constant sampling steps of size ΔT in the Fourier domain, results in a periodic function, as illustrated in Figure 2.5. This means that, instead of solving the problem for an infinite periodic array of nanoparticles, we only need to take one single period of the structure in the Fourier domain.

The general solution of the FMM consist in two main steps:

- i) The calculation of the eigenvalues and eigenvectors of a matrix with constant elements that characterizes the diffracted wave propagation and coupling (the eigenvectors representing the characteristic modes of the periodic array) in a profile of the propagation axis, as well as the effective indices corresponding to these modes,

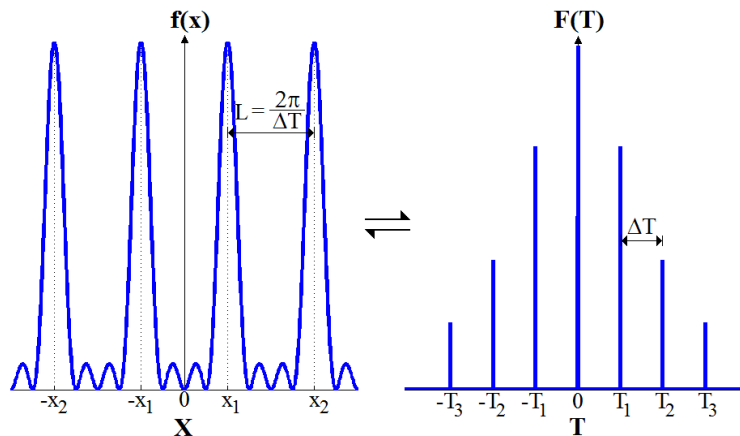


Figure 2.5: The Fourier transform of a periodic function $f(x)$ is a discrete function. Reciprocally, the inverse Fourier transform of a discrete function of constant step sampling ΔT is a periodic function.

and

- ii) The reconstruction of the total electromagnetic field by solving a linear system deduced by the boundary conditions for normal and tangential components of the electric and magnetic fields, taking into account that for each mode exists a forward and a back-forward component.

The complete characteristic matrix of the multilayered structure is the product of the characteristic sub-matrices in each layer, and the S-matrix method can be also applied (see Appendix A).

In this work we only present the generalities of the method, but a detailed description can be found in the PhD thesis of Eric Silberstein (Silberstein, 2002), Grégory Leblond (Leblond, 2009) and Laurent Arnaud (Arnaud, 2008), as well as in references (Hugonin and Lalanne, 2005; Li and Haggans, 1993; Lalanne and Silberstein, 2000; Chateau and Hugonin, 1994; Elson, 2001; Botten et al., 1981a; Moharam and Gaylord, 1981; Burckhardt, 1966; Moharam et al., 1995; Li, 1996; Chateau and Hugonin, 2003)¹.

To have a better comprehension of the physical representation of the problem, let's take a look into the scheme of Figure 2.6, where is shown an infinite MNW chain of period Λ , on top of a multilayered dielectric system. The algorithm of the FMM for this structure

¹The objective of this work does not relies in the implementation of the numerical method, but in the analysis of the modes propagation in an integrated chain of metallic nanoparticles. The numerical method was previously developed by our working group and only few modifications in the parameters of the structure were implemented.

is as follows.

We take a single unitary cell of the entire structure of length Λ as in the Figure 2.6(a). Now, we compute the effective indices of the modes in the grating region of the unitary cell by solving the Maxwell equations in the frequency domain, which can be achieved by describing the refractive index profile $n = \sqrt{\varepsilon\mu}$, as well as the electromagnetic field components in Fourier expansions (Fig. 2.6(b)). We must remark that for a number of harmonics N in the Fourier series, there are $2N + 1$ effective indices (one for each one of the modes propagating in the z direction of the multilayered structure).

Once that we have computed the effective indices of the modes, we have a multilayered homogeneous structure whose amplitudes and coupled modes can be found by making use of the S-matrix algorithm, obtaining a unique characteristic matrix (Fig. 2.6(c))

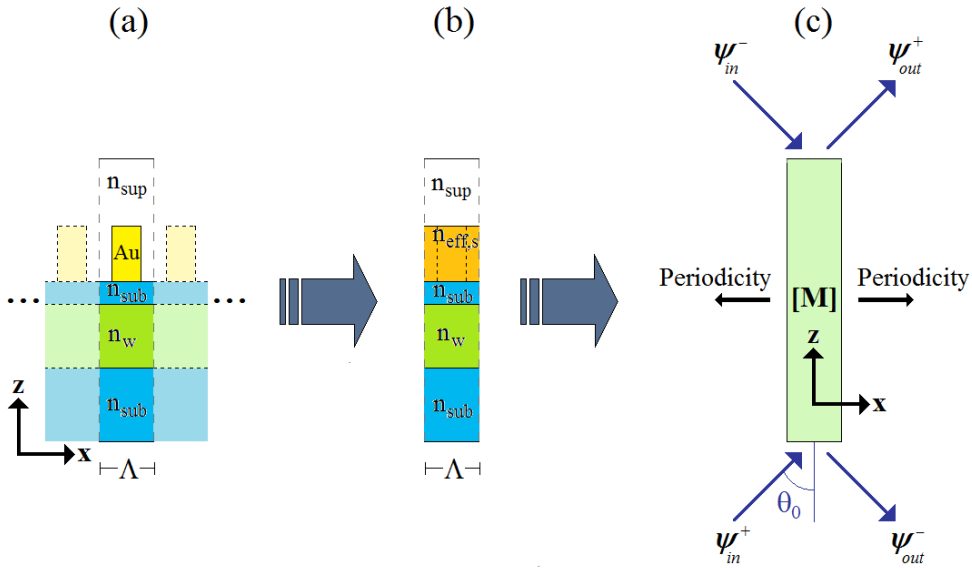


Figure 2.6: Schematic representation of the FMM. (a) A single unitary cell of length Λ is taken from the MNW chain. (b) In the grating region, the effective indices of the supported modes propagating in the z direction of the complete structure, are computed by representing the refractive index profile in Fourier series along the x propagation axis. Finally (c), the diffracted modes are matched to the multilayered homogeneous structure by using the S-matrix algorithm, obtaining a complete characteristic matrix whose eigenvectors are solution of an infinite periodic structure in the reciprocal space.

The complete characteristic matrix of the unitary cell is associated to the effective index, the angle of incidence of the field and the period of the structure. Then, we determine the modes by finding the complex solutions of the relationship $\det[\mathbf{M}^{-1}(\alpha_x)]$, where α_x is the normalized propagation constant.

We must note that as we are working in the frequency domain for a single section of the structure, the Bloch modes are solution of an infinite number of nanowires in the reciprocal space, bounded in the transverse direction.

Finally, we can determine the amplitudes of the electromagnetic field in each region by imposing boundary conditions.

To determine the modes propagation in the grating region of the unitary cell as an eigenvalue problem, the starting point is the Helmholtz equation given by

$$\frac{\partial^2 \psi}{\partial x^2} + \frac{\partial^2 \psi}{\partial z^2} = -k_0 \varepsilon(\omega) \psi, \quad (2.34)$$

where $k_0 = \omega/c$, and where we have supposed that $\mu = 1$ (assumption valid for almost all materials in the optical spectrum). By making the coordinate transformation $z' = k_0 z$, the Helmholtz equation becomes

$$\frac{\partial^2 \psi}{\partial x^2} + k_0^2 \frac{\partial^2 \psi}{\partial z'^2} = -k_0 \varepsilon(\omega) \psi. \quad (2.35)$$

This coordinate transformation provide us a better handling of the variables, and allow us to implement directly in the equations the effective index of the modes, instead of its propagation constant ($n_{\text{eff},s} z' = \beta_s z$). Since the periodicity of the structure is taken along the x direction, we expand the permittivity and the transverse component of the fields Fourier series around a central frequency determined by the incident plane wave as

$$\varepsilon(x) = \sum_{l=-\infty}^{\infty} C_l e^{il\gamma x}, \quad (2.36)$$

$$\psi_{TE}(x, z') = \sum_{n=-\infty}^{\infty} S_n e^{i\gamma x} e^{in_{\text{eff},s} z'}, \quad (2.37)$$

$$\psi_{TM}(x, z') = \sum_{n=-\infty}^{\infty} U_n e^{i\gamma x} e^{in_{\text{eff},s} z'}, \quad (2.38)$$

where $\gamma = 2\pi n/\Lambda + \gamma_0$ is the reciprocal lattice vector (analogous to a crystallographic array), $\gamma_0 = k \sin \theta_0$ (with θ_0 the incidence angle), and $n_{\text{eff},s}$ is the effective index of the s -th mode.

For simple grating structures with alternating regions of refractive indices n_I (dielectric) and n_{II} (metal), as depicted in Figure 2.4, the Fourier harmonics for the permittivity are given by

$$\begin{aligned} C_0 &= n_{II}^2 w + n_I^2 (1 - w) \\ C_l &= (n_{II}^2 w + n_I^2) \frac{\sin(\pi l w)}{\pi l}, \end{aligned} \quad (2.39)$$

where w is the width of the MNW, and C_0 is the average value of the relative permittivity and not the permittivity of the free space (Moharam et al., 1995). In general, C_l is complex for lossy gratings.

TE polarization

If we substitute equations (2.36) and (2.37) in the transformed Helmholtz equation, we get

$$\sum_{n=-\infty}^{\infty} [-k_0^2 n_{\text{eff},s}^2 - q^2 \gamma^2] S_n e^{in\gamma x} = -k_0^2 \sum_{m=-\infty}^{\infty} \sum_{l=-\infty}^{\infty} C_l S_m e^{i(l+m)\gamma x}, \quad (2.40)$$

and by making $q = l + m$ in order to project over the basis of the vector $e^{iq\gamma x}$, we have

$$-n_{\text{eff},s}^2 S_q = \frac{q^2 \gamma^2}{k_0^2} S_q - \sum_n C_{q-n} S_n. \quad (2.41)$$

Denoting by $[C]$ the Toeplitz matrix² related to $\varepsilon(\omega)$, and defining the diagonal matrix $[K]$ where the element at the position (n, n) is given by $n \frac{\gamma}{k_0}$, we can write the equation (2.41) in a matrix form as

$$-n_{\text{eff},s}^2 [S] = [A] [S], \quad (2.42)$$

with

$$[A] = [K] \cdot [K] - [C]. \quad (2.43)$$

This means that the eigenvalues of the matrix $[A]$ give us the different effective indices of all the supported modes. Their eigenvectors give us directly the coefficients of the Fourier series of $[S]$ for the s -th mode.

The precision of the calculation is directly related to the number of Fourier coeffi-

²The Toeplitz matrix is a square matrix of constant diagonal elements defined from a vector \mathbf{a} such that the element (i, j) of the matrix is given as $A_{i,j} = a_{i-j}$.

cients (harmonics), which are also related to the number of modes. If we describe ε with $[-2N, 2N]$ harmonics, we obtain $2N + 1$ different modes, but only $[-N, N]$ harmonics for the fields.

TM polarization

As the mathematical form of the fields for TE and TM polarization is the same, we obtain a similar matrix expression (2.43) if equations (2.36) and (2.38) are directly substituted into the Helmholtz equation (2.35). Nevertheless, since the conservation of the tangential components for TM polarization impose an inverse factor of the dielectric function $\varepsilon(\omega)$, the numerical results will converge more slowly for certain components of the field (Li and Haggans, 1993). One way to overcome this situation is by rewriting the Helmholtz equation for TM polarization as

$$\frac{\partial}{\partial x} \left[\frac{1}{\varepsilon(\omega)} \frac{\partial \psi}{\partial x} \right] + \frac{k_0^2}{\varepsilon(\omega)} \frac{\partial^2 \psi}{\partial z'^2} = -k_0^2 \psi, \quad (2.44)$$

where $z' = k_0 z$. Substituting equations (2.36) and (2.38) into (2.44) and projecting over the basis of the vector $e^{iq\gamma x}$, it can be demonstrated that

$$-n_{\text{eff},s}^2 U_q = \sum_n C_{n-q} \left[\frac{q\gamma}{k_0} \sum_n \frac{q\gamma}{k_0} C_{n-q}^{-1} U_n - U_q \right], \quad (2.45)$$

that we can write in a matrix form as

$$-n_{\text{eff},s}^2 [U] = [A] [U], \quad (2.46)$$

with

$$[A] = [C] \cdot ([K] \cdot [C]^{-1} \cdot [K] - [I]), \quad (2.47)$$

where

$[U]$ is the Fourier coefficients vector,

$[K]$ is a square diagonal matrix whose element (n, n) is given by $n \frac{\gamma}{k_0}$,

$[C]$ is the Toeplitz matrix with the Fourier coefficients of $\varepsilon(\omega)$, and

$[I]$ is the identity matrix.

Another numerical amelioration developed by Lifeng Li (Li, 1996) consist in expressing the relationship (2.47) as (Lalanne and Silberstein, 2000)

$$[A] = [D]^{-1} \cdot ([K] \cdot [C]^{-1} \cdot [K] - [I]), \quad (2.48)$$

where $[D]$ is the Toeplitz matrix containing the Fourier coefficients of $1/\varepsilon(\omega)$. Even when these mathematical expressions are equivalent, this simple reformulation guarantees the numerical convergence of the solutions. For the case of TE polarization, the A matrix remains without changes.

At this moment, we know how to determine the eigenvectors (modes) in the grating region. As we explained in the analytic solution, the total electromagnetic field in each one of the homogeneous layers can be expressed as the superposition of the diffracted orders (Arnaud, 2008). We can also represent this superposition in a matrix way similar to equations (2.37) and (2.38), with $S_n = 1$ (or $U_n = 1$), $\gamma = (2n\pi/\Lambda) + k_0 n_m \sin \theta_0$, and $n_{\text{eff}} = (1/k_0) \sqrt{k_0^2 n_m^2 - \gamma^2}$, with $k_0 = \omega/c$ and n_m the refractive index of the m th homogeneous layer.

With these elements, we can then build up the S matrix of the entire multilayered structure. Once again, to ensure that the diffracted modes are propagating in the multilayered media, these modes must propagate out of the substrate and superstrate layers, and not backreflected to the structure. These boundary conditions are given as $A_1 = B_{N+1} = 0$, having into account that there are $2N + 1$ A and B different amplitudes (the same number of harmonics or diffracted waves).

2.2.3 Algorithm for the solution of the FMM

The calculation of the effective index of the propagating modes is not so simple, since we must face the numerical solution of a complex transcendental function.

One possible solution to overcome this problem is by searching a family of solutions

as a function of the wavelength, instead as a function of the effective index. This makes necessary to consider the wavelength as a complex quantity. This is just a numerical trick that is justified by the fact that the propagation constant that relates the wavelength and the effective index is a complex number, i. e. $\lambda = 2\pi n_{\text{eff}} / (\beta' + \beta'')$, where β' and β'' the real and imaginary parts of the propagation constant, respectively. So, $\lambda = \text{Re}[\lambda] + \text{Im}[\lambda]$.

To implement numerically this solution, we only need to fix β_{eff} in the first Brillouin zone from $-\mathbf{K}/2$ to $\mathbf{K}/2$ (the diagonal matrix of elements $n\gamma/k_0$) at least as long as we are concerned with real values. This method is equivalent to propose a real effective index within a real domain, and to find the complex solutions of λ that satisfy the dispersion relation. This approach is classically used in solid-state physics to calculate the band diagram of semiconductors (Wang et al., 2003).

We scheme the algorithm for the numerical solution of the propagating modes in the integrated structure in Figure 2.7.

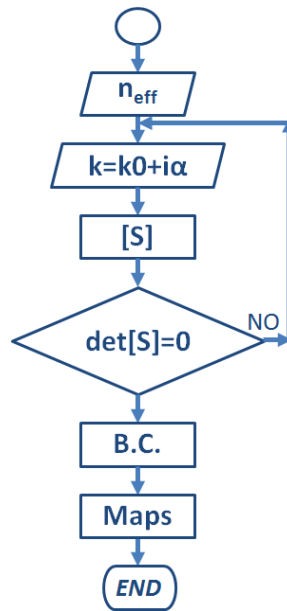


Figure 2.7: Flowchart of the algorithm to find the proper modes of the integrated periodic structure.

The first step is to fix the effective index n_{eff} as a real value. Then for a given wavelength value we compute the wavevector k that is solution to the eigenvalue problem in the grating region. For this value is computed the S matrix of the complete multilayered media. Then, we determine and evaluate the determinant of the S matrix. If the determinant is equal to zero, the boundary conditions (B.C.) are implemented and the

near-field maps are reconstructed. Else, another value of the wavevector is proposed and evaluated. This cycle is performed for different values of the effective index until the dispersion curves can be easily read.

Near-field maps reconstruction

To reconstruct the near-field maps, we need to describe the incident plane wave in the form of Rayleigh-Fourier series, as described in equation (2.19), with the zeroth order ($m = 0$) equal to the field of equation (2.16), and the higher orders equal to zero.

To this purpose, we fix the boundary conditions such that in the superstrate layer the incoming amplitudes be equated to zero ($B_{N+1} = 0$) for all the harmonics, and in the substrate layer all the incoming amplitudes are also equated to zero ($A_1 = 0$), except for the fundamental harmonic. The fundamental harmonic (zeroth order) correspond to the incident plane wave.

The wavevector of the plane wave is given as $k_1 = k_0 n_{\text{eff}}$, which corresponds to an evanescent wave because $n_{\text{eff}} = n_{\text{sub}} \sin \theta_0 > n_{\text{sub}}$, then the excitation is always below the light-line limit of the substrate. This numerical formulation is equivalent to the prism coupling that we described in Figure 1.3 to excite the surface plasmons.

We must remark that the near-field map that we obtain is an approximation of the proper mode. This is because we select a plane wave with an effective index that better excites the Bloch mode of the structure. Also, the near-field map is the result of the superposition of the incident wave and the computed mode. Then, the field exponentially increases when moving away in the substrate. For this reason, the size of the substrate in the near-field map must be reduced to avoid numerical instabilities.

2.3 Beam propagation: aperiodic-FMM

The FMM was originally conceived to solve infinite periodic structures because only one single period of the infinite structure was taken into account. Nevertheless, in the early 2000, P. Lalanne (Lalanne and Silberstein, 2000) showed that by making few modifications, the method can be applied to finite aperiodic structures. This extension is achieved

if we consider the complete finite structure as a single unitary cell of length Δ (super-cell technique), and if we take the periodicity of the Fourier expansions perpendicularly to the propagation axis, or equivalently by rotating the structure 90° , as depicted in Figure 2.8.

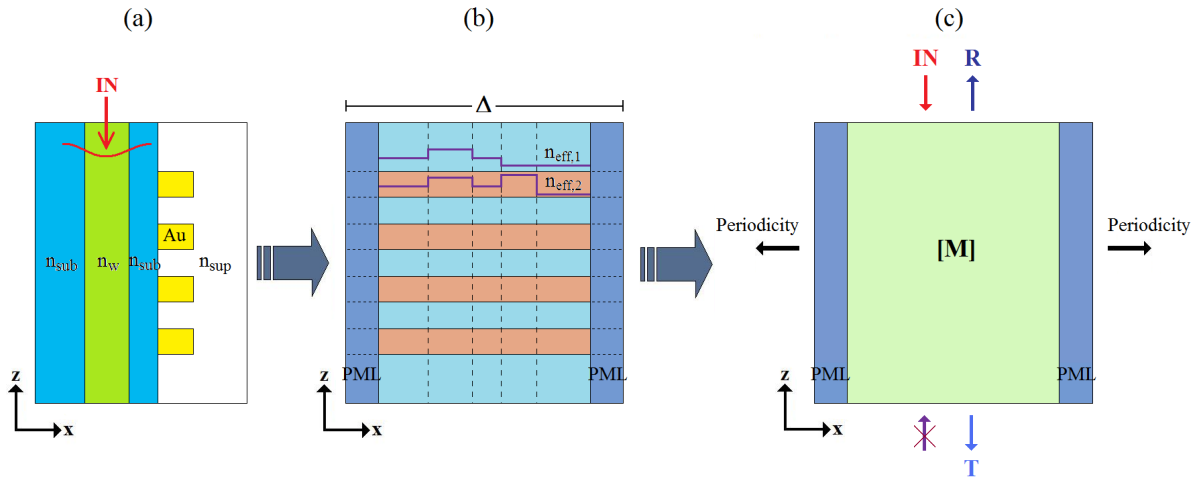


Figure 2.8: Schematic representation of the aperiodic-FMM. (a) The complete finite structure is taken as a single unitary cell rotated perpendicularly to the x axis. (b) The cell is delimited with PML, forming a multilayered super-cell of length Δ . By representing the index profile in Fourier series along the x axis, the effective index in each layer is determined. (c) Then, the characteristic matrix is described with periodic elements perpendicular to the z propagation axis.

Since the unitary cell is artificially periodized, an aliasing effect takes place between adjacent cells. This numerical effect is physically interpreted as the interference of forward and back-forward waves at the edges of the unitary cell.

There are two possible solutions to avoid this contamination: to increase the distance between adjacent cells (which implies to increase the sampling rate or equivalently the number of harmonics) or to include at the end of the computational window, perfectly matched layers (PML) that perfectly absorb the scattered field and avoid any reflections (Lalanne and Jurek, 1998).

The algorithm for solving this finite structure is almost the same than that used in the case of the infinite chain of MNW. We divide the complete finite structure (Fig. 2.8(a)) perpendicularly to the propagation axis into different subsections. For each one of these sections we compute the effective index in order to obtain an homogeneous multilayered system (Fig. 2.8(b)). At the end (left and right) of the multilayered array we place

the PML. With this inclusion, we obtain a characteristic matrix with periodic elements perpendicular to the z propagation axis (Fig. 2.8(c)).

The perfectly matched layers are defined as absorbent media in which the electromagnetic waves can be transmitted but not reflected (Berenger, 1994). They can be described as anisotropic media whose permittivity, $[\varepsilon]_{PML}$, and permeability, $[\mu]_{PML}$, are described as tensors such that

$$\frac{[\varepsilon]_{PML}}{\varepsilon} = \frac{[\mu]_{PML}}{\mu} = \begin{bmatrix} \alpha & 0 & 0 \\ 0 & 1/\alpha & 0 \\ 0 & 0 & \alpha \end{bmatrix}, \quad (2.49)$$

where ε and μ are the permittivity and permeability of the adjacent media to the PML, respectively, and α a complex number (Appendix C).

The inclusion of the PMLs at the edges of the unitary cell makes necessary the description of the Maxwell equations, bearing in mind the contribution of the magnetic permeability of the fields ($\mu \neq 1$).

TE polarization

If we consider the permittivity and permeability of the fields, the Helmholtz equation for TE polarization is then given by

$$\frac{\partial}{\partial x} \left[\frac{1}{\mu_{zz}} \frac{\partial \psi_{TE}}{\partial x} \right] + \frac{1}{\mu_{xx}} \frac{\partial^2 \psi_{TE}}{\partial z^2} = -k_0^2 \varepsilon_{yy} \psi_{TE}. \quad (2.50)$$

Then, expanding ψ_{TE} , ε_{yy} and μ_{zz} in Fourier series as

$$\psi_{TE}(x, z) = \sum_{n=-\infty}^{\infty} S_n^y e^{in\gamma x}, \quad (2.51)$$

$$\varepsilon_{yy} = \sum_{l=-\infty}^{\infty} C_l^y e^{il\gamma x}, \quad (2.52)$$

$$\mu_{zz} = \sum_{l=-\infty}^{\infty} M_l^z e^{il\gamma x}, \quad (2.53)$$

and using the inverse Laurent rule (Popov and Neviere, 2001) for μ_{xx}

$$\frac{1}{\mu_{xx}} = \sum_{l=-\infty}^{\infty} M_l^x e^{il\gamma x}, \quad (2.54)$$

we can represent the Helmholtz equation (2.50) in a matrix form as $-n_{\text{eff},s}^2 [S_y] = [A] [S_y]$ with

$$[A] = [M_x]^{-1} \cdot ([K] \cdot [M_z]^{-1} \cdot [K] - [C_y]), \quad (2.55)$$

where

$[M_x]$ the Toeplitz matrix with Fourier coefficients of $1/\mu_{xx}$,

$[M_z]$ the Toeplitz matrix with Fourier coefficients of μ_{zz} ,

$[K]$ the square diagonal matrix whose element (n, n) is given by $n \frac{\gamma}{k_0}$, and

$[C_y]$ the Toeplitz matrix with the Fourier coefficients of ε_{yy} .

TM polarization

For the case of TM polarization, we can write the Helmholtz equation that takes into account the permittivity and permeability of the fields as

$$\frac{\partial}{\partial x} \left[\frac{1}{\varepsilon_{zz}} \frac{\partial \psi_{TM}}{\partial x} \right] + \frac{1}{\varepsilon_{xx}} \frac{\partial^2 \psi_{TM}}{\partial z^2} = -k_0^2 \mu_{yy} \psi_{TM}, \quad (2.56)$$

and the expansions of ψ_{TM} , μ_{yy} and ε_{zz} in Fourier series as

$$\psi_{TM}(x, z) = \sum_{n=-\infty}^{\infty} U_n^y e^{in\gamma x}, \quad (2.57)$$

$$\mu_{yy} = \sum_{l=-\infty}^{\infty} M_l^y e^{il\gamma x}, \quad (2.58)$$

$$\varepsilon_{zz} = \sum_{l=-\infty}^{\infty} C_l^z e^{il\gamma x}, \quad (2.59)$$

$$\frac{1}{\varepsilon_{xx}} = \sum_{l=-\infty}^{\infty} C_l^x e^{il\gamma x}. \quad (2.60)$$

With this formulation, we can represent the Helmholtz equation (2.56) in a matrix form as $-n_{\text{eff},s}^2 [U_y] = [A] [U_y]$ with

$$[A] = [C_x]^{-1} \cdot \left([K] \cdot [C_z]^{-1} \cdot [K] - [M_y] \right), \quad (2.61)$$

where

$[C_x]$ the Toeplitz matrix with Fourier coefficients of $1/\varepsilon_{xx}$,

$[C_z]$ the Toeplitz matrix with Fourier coefficients of ε_{zz} ,

$[K]$ the square diagonal matrix whose element (n, n) is given by $n \frac{\gamma}{k_0}$, and

$[M_y]$ the Toeplitz matrix with the Fourier coefficients of μ_{yy} .

As we can note, the equations for TE and TM polarization are similar, it is only necessary to exchange the permittivity for the permeability.

Since the permittivity is described as a function of the position along the x axis ($\varepsilon = \varepsilon(x)$), we can numerically find their Fourier coefficients with standard computational implementations, such as the fast Fourier transform (FFT), being its precision proportional to the sampling points used to describe the profile.

Coordinates transformation

Another option to solve the electromagnetic contamination at the edges of the unitary cell, is by enlarging the size of the computational window. We can artificially perform this enlargement by making a coordinates transformation avoiding to increment the number of harmonics in the Fourier series.

This coordinate transformation is done in the variable $x : x = f(X)$ such that

$$\frac{\partial}{\partial x} = \frac{1}{f'(X)} \frac{\partial}{\partial X}. \quad (2.62)$$

Then for example, in the case of TM polarization the Helmholtz equation (2.56) becomes

$$\frac{\partial}{\partial x} \left[\frac{1}{f'(X) \varepsilon_{zz}} \frac{\partial \psi_{TM}}{\partial X} \right] + \frac{f'(X)}{\varepsilon_{xx}} \frac{\partial^2 \psi_{TM}}{\partial z^2} = -k_0^2 f'(X) \mu_{yy} \psi_{TM}. \quad (2.63)$$

By choosing $f(X) = \alpha X$, we get

$$\frac{\partial}{\partial x} \left[\frac{1}{\alpha \varepsilon_{zz}} \frac{\partial \psi_{TM}}{\partial X} \right] + \frac{\alpha}{\varepsilon_{xx}} \frac{\partial^2 \psi_{TM}}{\partial z^2} = -k_0^2 \alpha \mu_{yy} \psi_{TM}, \quad (2.64)$$

which is the Helmholtz equation associated to the PML (Appendix C). This means that we can interpret the PML as a linear coordinates transformation.

Describing the inverse derivative of the coordinates transformation in Fourier series as

$$\frac{1}{f'(X)} = \sum_{n=-\infty}^{\infty} f_n e^{in\gamma X}, \quad (2.65)$$

we can write the A matrix as

$$[A] = [C_x]^{-1} \cdot ([F] \cdot [K] \cdot [C_z]^{-1} \cdot [F] \cdot [K] - [M_y]), \quad (2.66)$$

for TM polarization, and

$$[A] = [M_x]^{-1} \cdot ([F] \cdot [K] \cdot [M_z]^{-1} \cdot [F] \cdot [K] - [C_y]), \quad (2.67)$$

for TE polarization, being $[F]$ the Toeplitz matrix containing the Fourier coefficients of $1/f'(X)$.

If we select the parameter α as a complex number, we can introduce an absorbing media. To do this, we need to make an isometric transformation such that $\text{Im}[\alpha] = 0$ in the region of the unitary cell, and α diverging when approaching to the PML.

The coordinates that we use in this work are the ones proposed by Lalanne (Hugonin and Lalanne, 2005):

$$F(X) = \begin{cases} X, & \text{for } |X| < \zeta/2 \\ \text{sign}(X) \left\{ \frac{\zeta}{2} + \frac{q}{\pi(1-\xi)} \left[\tan(\arg) - \frac{\xi}{\sqrt{1-\xi}} \tan \left[\sqrt{1-\xi} \tan(\arg) \right] \right] \right\}, & \text{for } \zeta/2 < |X| < d/2 \end{cases} \quad (2.68)$$

where $\arg = \pi \frac{|X| - \frac{\zeta}{2}}{q}$, ζ is the zone of the isometric linear transformation, and $q = \Delta - e$ is the region where the complex transformation takes place. ξ is a complex parameter

associated to the absorption coefficient of the medium.

2.3.1 Determination of the modes amplitudes

To determine the amplitudes of each one of the modes (eigenvectors), we represent the waves traveling inside each one of the sections in the unitary cell as the sum of upward and downward waves. They can be expanded as

$$\psi_y^{(p)} = \sum_{q=-\infty}^{\infty} \left[b_q^{(p)} e^{-in_{\text{eff},q}^{(p)}(z-z_{p-1})} + d_q^{(p)} e^{in_{\text{eff},q}^{(p)}(z-z_{p-1})} \right] M_q^{(p)}, \quad (2.69)$$

$$M_q^{(p)} = \sum_{m=-\infty}^{\infty} W_{m,q}^{(p)} e^{im\gamma x}, \quad (2.70)$$

where $W_{m,q}^{(p)}$ is one component of the q -th eigenvector (q -th mode), m denotes the term S_m of the Fourier series, and p is the section of interest in the unitary cell.

$b_q^{(p)}$ and $d_q^{(p)}$ are the amplitudes of the upward and downward modes, respectively. It must be remarked that one amplitude is the same for all the Fourier coefficients of a given mode (Cao et al., 2002).

Just as in the case of the modal analysis, we can solve the passing relationships between two adjacent sections by making use of the S-matrix algorithm, having into account the conservation of the tangential components of the fields \mathbf{E} and \mathbf{H} , as described in detail in references (Cao et al., 2002; Leblond, 2009).

2.3.2 Electromagnetic field reconstruction

Once obtained the A matrix, we can numerically compute their eigenvalues $n_{\text{eff},s}$ as well as their eigenvectors $[W_s]$ (modes). Since the eigenvector of a certain mode give us the Fourier coefficients of the field, we just need to reinject these coefficients to obtain the field values, and then we can reconstruct the field map.

This means that we can write the field evaluated in a certain point (x, z) in Fourier series as

$$\psi_y(x, z) = \sum_{s=-\infty}^{\infty} c_s M_s(x, z), \quad (2.71)$$

$$M_s(x, z) = \sum_{n=-\infty}^{\infty} W_{n,s} e^{in\gamma x} e^{ik_0 n_{\text{eff},s} z}, \quad (2.72)$$

where $n_{\text{eff},s}$ is the effective index of the s -th mode propagating in the z negative direction (the incidence direction), and c_s represents the excitation weight of the mode. The vector $[c]$ that regroups all the excitation weights of the modes, represents the coordinates of ψ_y in the basis of the modes.

From the transverse component of the electromagnetic field ψ_y it is possible to know the other field components by making use of the Maxwell equations. For TE polarization, the transverse component is E_y , so H_x and H_z are obtained from relationships (2.6) and (2.8), respectively. In a similar way, for TM polarization, the transverse component of the field is H_y , so the relationships (2.9) and (2.11) give us the E_x and E_z components, respectively.

For TE polarization we obtain

$$H_z(x, z) = \sum_{n=-\infty}^{\infty} U_n^z e^{in\gamma x}; \quad U_r^z = \frac{\gamma}{\omega\mu_0} \sum_{j=-\infty}^{\infty} j M_{r-j}^x S_j, \quad (2.73)$$

and

$$H_x(x, z) = \sum_{n=-\infty}^{\infty} U_n^x e^{in\gamma x}; \quad (2.74)$$

$$U_r^x = \frac{k_0}{\omega\mu_0} \sum_{q=-\infty}^{\infty} V_{r,q} (-c_q) e^{ik_0 n_{\text{eff},q} z}; \quad V_{r,q} = n_{\text{eff},q} \sum_{j=-\infty}^{\infty} M_{r-j}^x W_{j,q}. \quad (2.75)$$

Similarly, for TM polarization we get

$$E_z(x, z) = \sum_{n=-\infty}^{\infty} S_n^z e^{in\gamma x}; \quad S_r^z = \frac{\gamma}{\omega\varepsilon_0} \sum_{j=-\infty}^{\infty} j C_{r-j}^z U_j, \quad (2.76)$$

and

$$E_x(x, z) = \sum_{n=-\infty}^{\infty} S_n^x e^{in\gamma x}; \quad (2.77)$$

$$S_r^x = -\frac{ik_0}{\omega\varepsilon_0} \sum_{q=-\infty}^{\infty} V_{r,q} (-c_q) e^{ik_0 n_{\text{eff},q} z}; \quad V_{r,q} = n_{\text{eff},q} \sum_{j=-\infty}^{\infty} C_{r-j}^x W_{j,q}. \quad (2.78)$$

2.3.3 Absorbed power by the nanoparticles

The FMM allows us to measure the optical power transmitted to the end of the dielectric waveguide, as well as the reflected power at the input of the system.

Because our system includes metallic materials, a quantity of particular interest is the field absorbed by the structure. This quantity can be determined with the relationship (Yariv and Yeh, 2003)

$$\langle P_{abs} \rangle = -\frac{1}{2} k_0 \varepsilon_0 c \int \varepsilon_r'' \mathbf{E} \cdot \mathbf{E}^* dS, \quad (2.79)$$

where $k_0 = \omega/c$ is the wavenumber, ε_0 and c the permittivity and speed of light in the free space, respectively, and ε_r'' is the imaginary part of the dielectric function in the differential area element dS . The asterisk denotes the complex conjugate of the electric field.

It must be noted that for the case of TM polarization, we can determine the components of the electric field from the magnetic component via the relationships

$$E_x = \frac{i}{ck_0 \varepsilon_0 \varepsilon_r} \frac{\partial H_y}{\partial z}, \quad (2.80)$$

$$E_z = \frac{-i}{ck_0 \varepsilon_0 \varepsilon_r} \frac{\partial H_y}{\partial x}, \quad (2.81)$$

where ε_r is the complex permittivity in the differential area element dS .

To normalize the absorption of equation (2.79), we divide it by the incident power given as

$$P_0 = \frac{1}{2} \varepsilon_0 c n_{\text{eff}} \int |\mathbf{E}|^2 dS, \quad (2.82)$$

for TE polarization, and

$$P_0 = \frac{1}{2} \frac{n_{\text{eff}}}{\varepsilon_0 c} \int \frac{|\mathbf{E}|^2}{\varepsilon_r} dS, \quad (2.83)$$

for TM polarization.

2.4 Conclusions

The analysis of a periodic chain of metallic nanowires integrated on top of a dielectric waveguide can be performed in terms of the propagating modes along the structure.

We can face this analysis by considering the complete integrated structure as a multilayered medium, and matching the diffracted modes in each interface between two adjacent layers, giving place to an eigenvalue problem. To this purpose the grating region must be modeled as an homogeneous medium with a certain effective index for each one of the diffracted modes, such that the total electromagnetic field in this region satisfies the Helmholtz equation (eq. (2.22)).

Two possible ways to find the proper modes in the grating region are possible. The first method is to consider the grating region as a multilayered infinite periodic medium (Fig. 2.4) and to impose periodic conditions (Bloch theorem), being found a dispersion relation for each one of the diffracted modes. These modes are then coupled to the diffracted modes of the adjacent substrate and superstrate layers and the solution is found.

One possible way to find the proper modes in the grating region, is considering that the electromagnetic field in the grating region can be treated like in a multilayered media, as the sum of propagating and counter-propagating modes. Considering periodic boundary conditions (Bloch theorem), an analytic expression for the dispersion relations of the diffracted modes is found. These modes are matched to the diffracted modes of the adjacent layers, and the eigenvalue problem is then solved.

However, a second solution to find the proper modes in the grating region was proposed: the Fourier modal method. This method solves the Helmholtz equation (eq. (2.34)) by expressing the permittivity as well as the electromagnetic field components in Fourier series, i.e., by solving the Helmholtz equation in the frequencies domain. This formulation allowed us to express the effective index of all the diffracted modes in a matrix form. This matrix was then incorporated to the \mathbf{S} matrix that describes the complete multilayered structure, in such a way that the total number or supported modes by the integrated structure can be computed by imposing boundary conditions that relate the incoming

and outgoing diffracted modes.

As we demonstrated, the advantage of using the FMM formulation is that perfectly matched layers (PML) can be implemented as a coordinates transformation without significant changes in the numerical formalism. The inclusion of these PMLs allowed us to extend the modes computation to non periodic structures, and, hence, to simulate the beam propagation along the integrated system.

The beam propagation simulations complete the modal analysis, allowing us to characterize an integrated structure in terms of the transmission and reflection of the propagated optical field at the output and input of the system, respectively. Also the absorbed power by the metallic nanoparticles can be measured.

Even when it is necessary to increase the number of harmonics to have a good convergence in the numerical results (leading to an increase of the computation time), the FMM is a convenient rigorous method to study the near-field interaction between metallic nanoparticles periodically arranged, and their interaction with a dielectric waveguide, as will be presented in the next chapter.

The numerical results that will be presented in the following chapters are based on the numerical implementation of the Fourier modal method: for the computation of the modes supported by the integrated structure, we will use the FMM (section 2.2.2), and for the beam propagation along the integrated structure, we will use the aperiodic FMM (section 2.3).

Chapter 3

Numerical analysis of integrated plasmonic structures

As we mentioned in Chapter 1, a periodic array of metallic nanoparticles (MNP) can behave as a plasmonic waveguide, allowing the light transmission through them. This effect is due to the near-field coupling between consecutive particles when they are excited at their localized surface plasmon (LSP) resonance.

Nevertheless, the large majority of the analysis performed by other authors has been done above the light-line in the dispersion relations, where the modes of the chain can be excited by illuminating the structures from the free-space or from the substrate.

Recently, MNP chain integrated on top of a dielectric waveguide was investigated in order to study the light propagation along the MNP chain below the light-line. Depending on the inter-particles distance, the MNP arrays can be designed for very compact Bragg gratings (Quidant et al., 2004; Fevrier et al., 2012b) or compact directional couplers between the MNP chain and the dielectric waveguide (Fevrier et al., 2012a; Apuzzo et al., 2013). Similarly, the integration of a Yagi-Uda antenna based on MNP chain deposited on top of a dielectric waveguide was also demonstrated in reference (Arango et al., 2012). However, so far, the choice of the incident transverse electric (TE) mode of the waveguide limits the excitation of one kind of chain mode, namely the transverse dipolar chain mode (Crozier et al., 2007). The longitudinal mode, as well as the transverse out-of-plane and higher multipolar chain modes have never been studied below the light line.

Based on the Fourier modal method, in this chapter we numerically analyze a LSP-based integrated structure. We particularly study the modes supported by a periodic array of metallic nanowires (MNW) below the light-line in the dispersion relation and their excitation with the fundamental transverse magnetic (TM) mode of a dielectric waveguide placed in the close proximity of the MNW array. To do so, we first analyze the isolated MNW chain embedded in a homogeneous dielectric medium, then on top of a dielectric substrate, and finally we approach to them a dielectric waveguide. To this purpose, first we will describe how to interpret the dispersion curves of a waveguiding system.

The following results are an expanded explanation of references (Tellez-Limon et al., 2013) and (Tellez-Limon et al., 2014).

3.1 Dispersion curves

Like in the case of waveguide theory, we can perform the analysis of the modes propagating through a periodic array of metallic nanoparticles in terms of the dispersion curves. These curves directly relate the propagation constant with the wavelength of a given mode. A detailed description of them reveals the physical behavior of any waveguided system.

In order to understand the physical meaning of the dispersion curves, we will use the example given in Fig. 3.1, where are depicted the dispersion curves of a periodic array of gold nanoparticles placed on top of a glass substrate. These curves (taken from reference (Crozier et al., 2007)) were numerically computed using the finite-difference time-domain (FDTD) method. We will not pay attention to the details of these data, but to the physical interpretation of the curves.

For light propagating in a non-dispersive media, its dispersion relation is given by $k_x = 2\pi n/\lambda$, where k_x is the wavevector in the propagation direction (propagation constant) and n the refractive index of the homogeneous medium. This relationship defines the so-called light-line of the homogeneous media. In Fig. 3.1, the light-lines corresponding to the air ($n_{air} = 1.0$) and glass ($n_{glass} = 1.5$) are represented by the red and blue continuous curves, respectively.

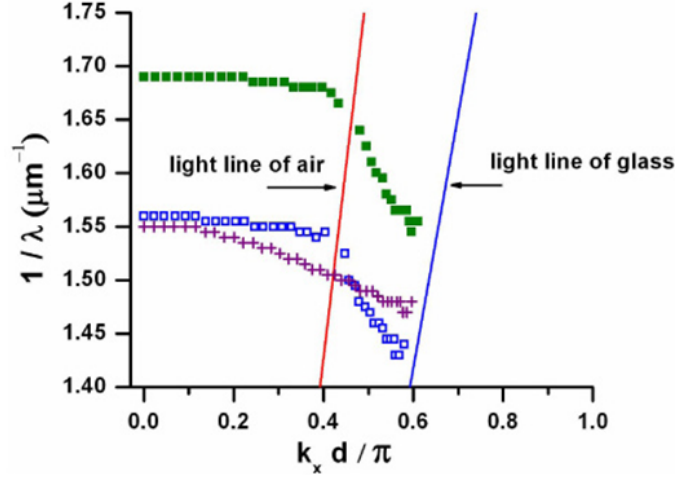


Figure 3.1: Dispersion relations for a gold nanoparticle chain over a glass substrate above the total internal reflection regime for a spectral range from 570 – 714 nm. Green: 55 nm tall nanoparticles at an air/glass interface; blue: 30 nm tall nanoparticles at an air/glass interface; purple: 55 nm tall nanoparticles in a uniform glass environment. Results from reference (Crozier *et al.*, 2007) computed with the FDTD method.

These light-lines define three regions. The first one, for $k_x < k_{x,air}$, corresponds to the region where the modes radiate into the air. These are the so-called radiation modes. In the second region, between the air and glass light-lines ($k_{x,air} < k_x < k_{x,glass}$), the energy of the modes is radiated into the glass, and they are named substrate radiation modes. Finally, the third region, where $k_x > k_{x,glass}$, encloses to the modes whose electromagnetic energy is not radiated to the air neither to the glass, i. e. its energy is confined to the waveguide structure. These are the confined or guided modes (Yariv and Yeh, 2003).

We must note that the dispersion curve is normalized to the Bragg condition¹ given by $k_{Bragg} = \pi/\Lambda$, where Λ is the period of the structure. With this normalization is possible to identify the modes in terms of the Brillouin zones. This representation is widely used in semiconductors to analyze the forbidden bands of the electrons as well as in photonic crystals.

In the example of Fig. 3.1, we observe that all the modes propagated through the nanoparticles radiate into the air or into the substrate, and no confined modes are present. This is the case of large majority of works dealing with modes propagation in MNP chains,

¹The Bragg condition is analogous to the Bragg plane used in crystallography (Kittel, 2004). The edges of the Brillouin zones define the Bragg planes. Since the lattice vector is one-dimensional for the MNW array, the Bragg plane is a scalar quantity.

and it is due to the lighting mechanism of the structures: if the chain of particles is illuminated from the superstrate, the energy of the modes leaks to the air, and illuminating them from the substrate leads to a leak to the glass. That is to say, even when the nanoparticles are coupled between each other, the light will not be efficiently propagated through them, and we cannot expect a waveguiding behavior.

One possible way to excite the modes confined in a MNP structure, is to use a strongly localized source placed into their near-field, for example with a dipolar source or with a dielectric waveguide. The later is the main object of this work: an integrated system able to excite the confined modes of a MNW chain and, at the same time, to detect the variations of these propagating modes when changing the parameters of the structure.

3.2 Modes propagation in an infinite array of MNW

As we described in Chapter 2, the FMM allows us to determine the propagation constant of the modes supported by an infinite periodic structure and then to compute its dispersion curves. We can also evaluate the electromagnetic field in the vicinity of the structure and reconstruct the near-field maps. Based on this method, we studied the modes propagation in an infinite chain of gold nanowires.

We studied three cases. First the modes supported by an infinite array of MNW immersed in a dielectric homogeneous medium (glass). Secondly, the same MNW chain placed on top of a dielectric substrate of refractive index $n_{sub} = 2.0$. And finally, the case of a dielectric waveguide of refractive index $n_{sub} = 2.0$ placed in close proximity to the MNW chain immersed in glass. In order to observe the behavior of the LSP resonance of the MNW for different aspect ratios, for the three cases we set the height of the MNW to 20 nm and 150 nm. The values of the dielectric function of the gold nanowires were taken from reference (Palik, 1985).

Once analyzed the supported modes of the structure, we numerically characterized the beam propagation in an integrated structure of a finite array of MNW placed on top of a dielectric waveguide, in terms of the transmission, reflection and absorption of the electromagnetic field.

3.2.1 Modes propagation in an isolated MNW chain

The system as depicted in Figure 3.2, consists of an infinite periodic array along the x axis, of gold nanowires invariant in the y direction immersed in a homogeneous dielectric medium of refractive index $n_d = 1.5$ (glass). The width of the nanowires as well as the period of the structure were fixed to $w = 80$ nm and $\Lambda = 130$ nm, respectively (the separation between them is $g = 50$ nm). We studied two cases. The first corresponding to a height of the nanowires of $e = 20$ nm, and the second for a height of $e = 150$ nm.

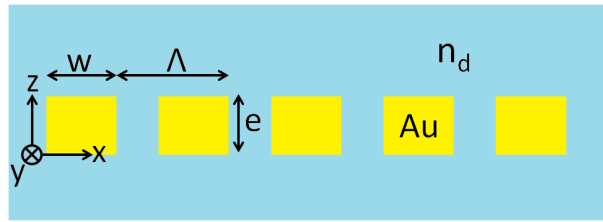


Figure 3.2: Scheme for the study of modes propagation in an infinite periodic array along the x axis of MNW immersed in a dielectric homogeneous medium of refractive index $n_d = 1.5$. The width is $w = 80$ nm, the period $\Lambda = 130$ nm and the height was set first to $e = 20$ nm, and then to 150 nm.

Isolated MNW of short height

The calculated dispersion curve for the array of MNW with a height of $e = 20$ nm is depicted in Figure 3.3a. The black vertical line delimits the first Brillouin zone. The dark green curve corresponds to the light-line of the dielectric homogeneous medium surrounding the MNW chain, normalized to the Bragg condition.

Below the light-line we observe a branch associated to a propagating mode (red dotted curve). Since this mode is solution of the Bloch waves propagating in the periodic array of MNW, we call it a Bloch mode.

The propagation distance of the Bloch mode can be obtained by making use of the relationship (Maier, 2007)

$$L_p = \frac{1}{2k''}, \quad (3.1)$$

where k'' is the imaginary part of the wave-vector. As we can see in Fig.3.3b, the propagation distance of the dipolar longitudinal mode below the light-line varies from 220 nm

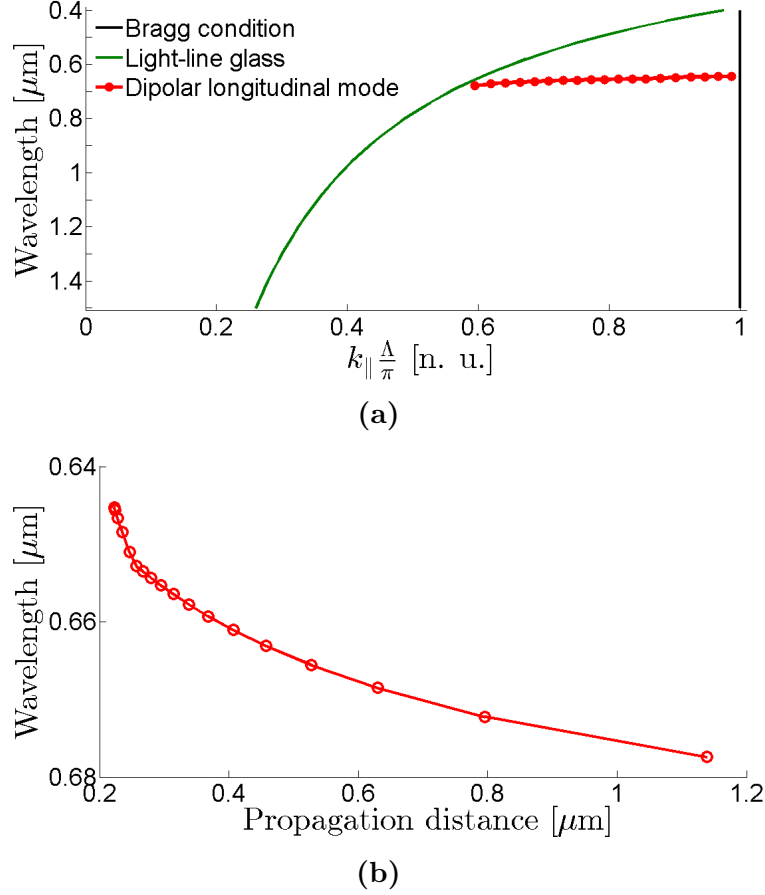


Figure 3.3: (a) Dispersion relations of an infinite chain of MNW along the x axis, of height $e = 20$ nm immersed in a dielectric homogeneous medium of refractive index $n_d = 1.5$ (glass). The structure supports a dipolar longitudinal propagation mode. This Bloch mode crosses the Bragg condition at $\lambda = 645$ nm. (b) The maximum propagation distance of the Bloch mode is of $1.14 \mu\text{m}$.

to $1.14 \mu\text{m}$.

At the edge of the first Brillouin zone, the branch of the Bloch mode crosses the Bragg condition ($k_{\parallel} = \pi/\Lambda$) around $\lambda = 645$ nm. At this wavelength the Bloch wave is stationary and the MNW chain exhibits unambiguously, longitudinal LSP resonances. This effect is emphasized by the electric field lines plotted in Figure 3.4a where a phase shift of π rad is observed between each 2 subsequent nanowires. This phase shift means that each one of the MNW behaves as an electric dipole orientated along the x propagation axis.

Out of the Bragg condition, for example around $\lambda = 667$ nm ($k_{\parallel} = 0.641\pi/\Lambda$), the Bloch mode becomes propagative and the electric field lines remain mainly longitudinally orientated inside the nanowires (Fig. 3.4b). For this reason, this branch in the dispersion relation is called the dipolar-like longitudinal Bloch mode.

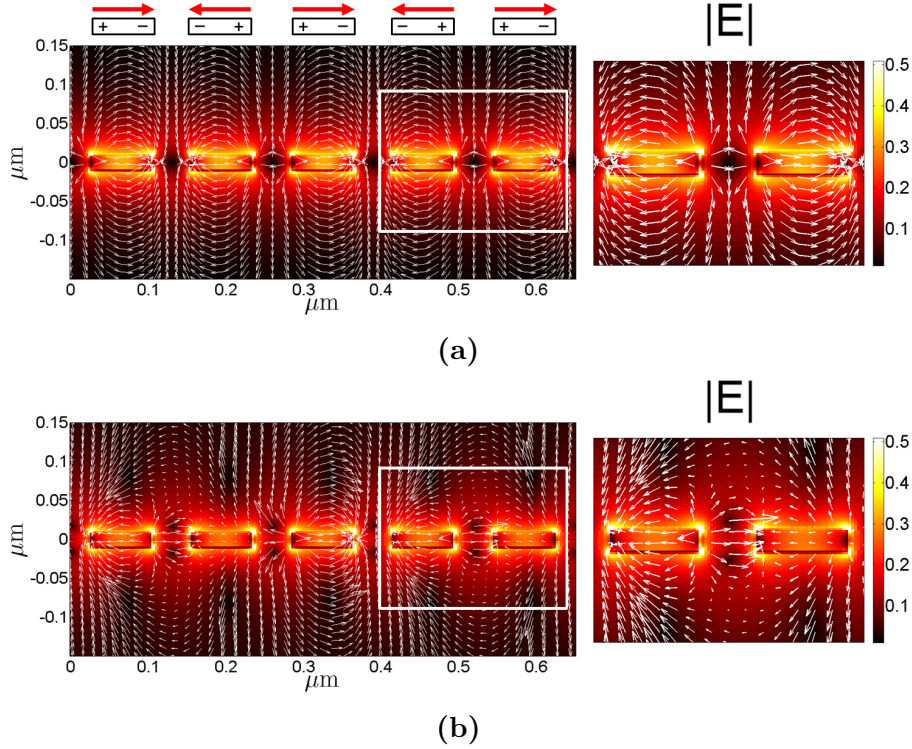


Figure 3.4: Energy density maps and electric field lines distribution of the dipolar longitudinal Bloch mode. (a) At the Bragg condition around $\lambda = 645$ nm, we identify the dipolar longitudinal coupling of the MNW chain. Out of the Bragg condition, around $\lambda = 667$ nm, we still observe the dipolar coupling.

Isolated MNW chain of large height

For MNW with height $e = 150$ nm, the dispersion curves exhibit two Bloch modes, as we can observe in Figure 3.5a. Like in the case of the MNW of smaller height, we use energy density maps and their corresponding electric field lines distributions to identify the nature of each one of the eigenmodes branches.

For the upper branch (red dotted curve) that relies in the wavelengths range around $\lambda \in (540 - 660)$ nm, a periodic quadrupolar-like LSP excitation is recognized with a phase shift of π rad between adjacent nanowires at the edge of the first Brillouin zone (Fig. 3.6a). This quadrupolar mode is analogous to the asymmetric mode observed in propagating surface plasmons for thin metallic layers (Kim et al., 2012).

The two Bloch modes branches that we observe in the dispersion curves, can be explained in analogy to the surface plasmon polariton (SPP) propagating in a thin metallic layer surrounded by a dielectric media (Kim et al., 2012).

When a TM polarized field passes from a dielectric to a metallic medium, a charge

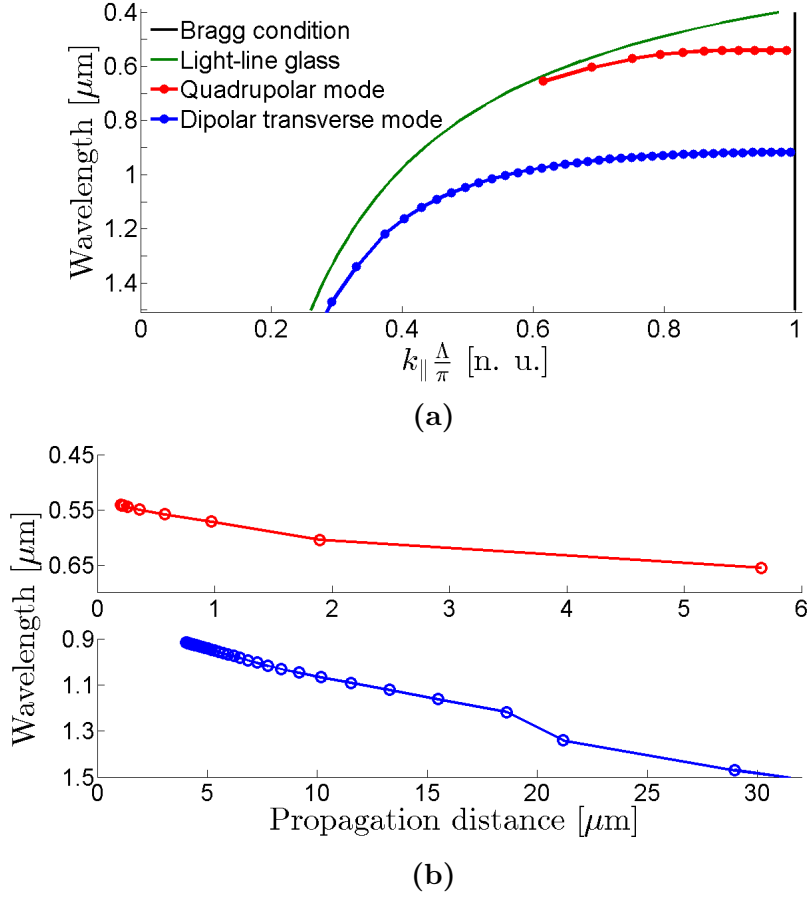


Figure 3.5: (a) Dispersion relations for the quadrupolar (red dotted line) and dipolar transverse (blue dotted line) Bloch modes for an infinite chain along the x axis of MNW of height $e = 150$ nm immersed in a dielectric homogeneous medium of refractive index $n_d = 1.5$. (b) The propagation distance of the quadrupolar branch (upper red circles curve) is shorter than that of the dipolar transverse mode (blue circles curve).

density is created at the interface between both media since the electric field has a component parallel to it. These charges are the result of the dipolar moment experienced by the electrons in the conductive level of the atoms of the metal when interacting with the electromagnetic field.

To predict the behavior (distribution) of these charges, we can recall the dispersion curves of an insulator-metal-insulator structure (Fig. 1.6b), which can be obtained by applying boundary conditions and assuming the superposition of propagative and counter-propagative waves (see Appendix A). The dispersion relation of equation (A.14) reveals two solutions for the \mathbf{H} field amplitudes of the waves propagating at the dielectric-metal interfaces, one with the amplitudes in phase and the other with their amplitudes in opposite phase, as schemed in Figure 1.5. These solutions are known as the symmetric and

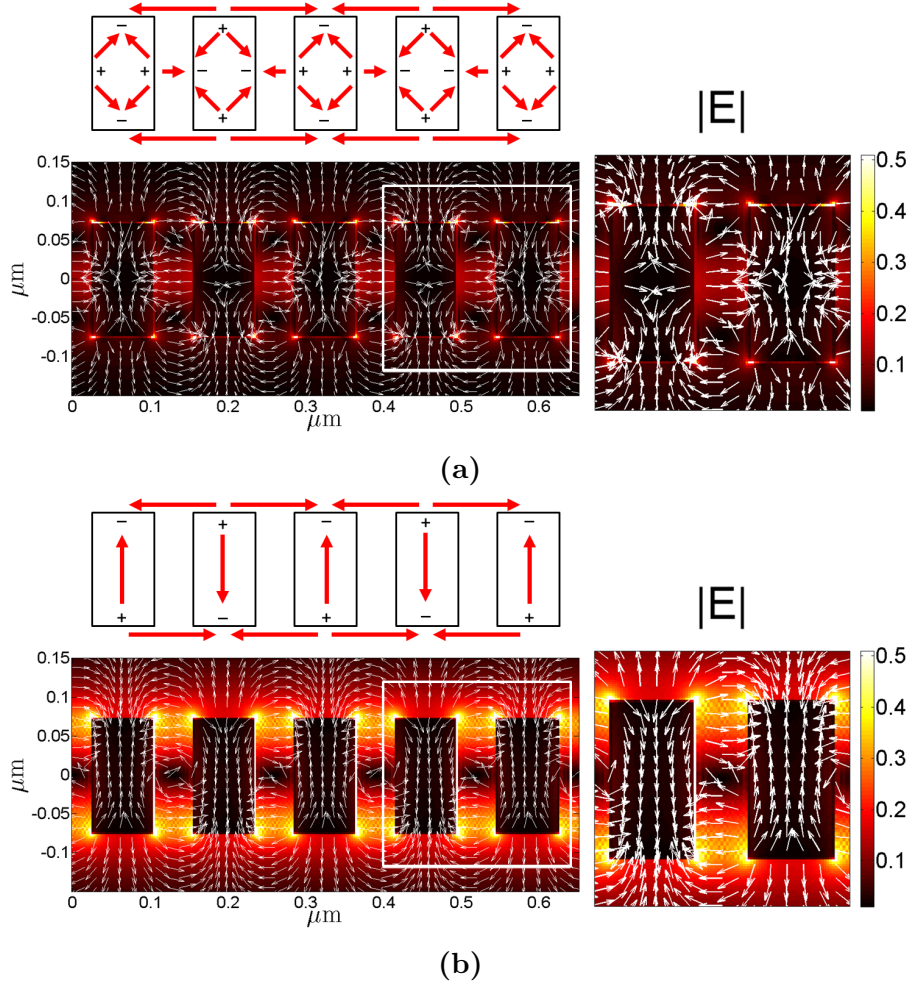


Figure 3.6: Energy density maps and electric field lines distribution at the Bragg condition for (a) the quadrupolar Bloch mode at $\lambda = 540$ nm, and (b) the dipolar transverse Bloch mode at $\lambda = 916$ nm. The corresponding squares show the phase distributions and orientation of the charges.

anti-symmetric modes.

The second branch relying in the wavelengths range around $\lambda \in (900 - 1500)$ nm (blue dotted curve), exhibits a dipolar like LSP resonance perpendicular to the x propagation axis, as can be corroborated in the energy density maps of Figure 3.6b. This mode is the so called dipolar transverse Bloch mode.

As can be observed in Figure 3.5b, the propagation distance of the quadrupolar mode is shorter than the one of the dipolar transverse mode. The first one varies from $0.19 \mu\text{m}$ to $5.6 \mu\text{m}$, while the second one varies from $4 \mu\text{m}$ to $31 \mu\text{m}$.

With these results we demonstrate that the MNW chain behaves as a plasmonic waveguide, whose Bloch propagating modes depend on their aspect ratio (height of the nanowires): the dipolar modes are orientated along the principal axis of the nanowires,

while the quadrupolar mode can be seemed as the interference of the out-of-phase dipoles along the principal axis of the MNW.

3.2.2 Modes propagation in a infinite array of MNW on top of a substrate

We have demonstrated that the chain of metallic nanowires supports the propagation of Bloch modes whose coupling effect is ruled by their aspect ratio, resulting in a dipolar longitudinal mode for the MNW of short height, and quadrupolar and dipolar transverse modes for those of taller height.

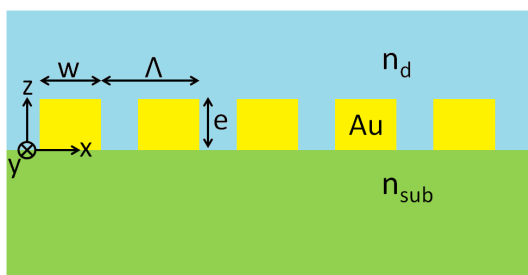


Figure 3.7: Scheme of an infinite periodic array of MNW immersed in glass, on top of a semi-infinite dielectric substrate of refractive index $n_{sub} = 2.0$.

Now, we analyze the effect induced to these modes for the MNW chain placed on top of a dielectric semi-infinite substrate of refractive index $n_{sub} = 2.0$, and surrounded with the same homogeneous dielectric medium ($n_d = 1.5$), as depicted in Figure 3.7.

MNW of short height

The dispersion curves for a periodic array of MNW of height $e = 20$ nm, are plotted in Figure 3.8. The light lines of the substrate and the superstrate are represented by the pink and dark-green curves, respectively.

In the dispersion curves of Fig.3.8, we can observe one branch relying below the substrate light line in a spectral range from 696 nm to 730 nm (blue dots). This mode crosses the Bragg condition (at the edge of the first Brillouin zone) around a wavelength value $\lambda = 696$ nm.

To identify the nature of this mode, we trace energy density maps and electric field

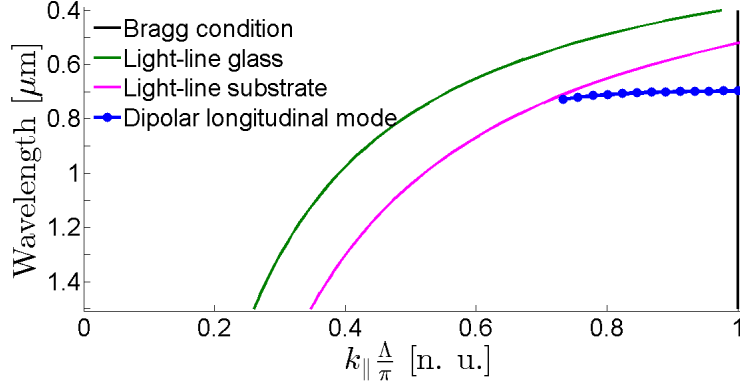


Figure 3.8: Dispersion relation for the dipolar longitudinal Bloch mode (blue dotted line) for an infinite periodic array of MNW of height $e = 20$ nm immersed in glass ($n_d = 1.5$) and placed on top of a dielectric medium of refractive index $n_{sub} = 2.0$.

lines distribution at the crossing point between the Bloch mode and the Bragg condition (Figure 3.9).

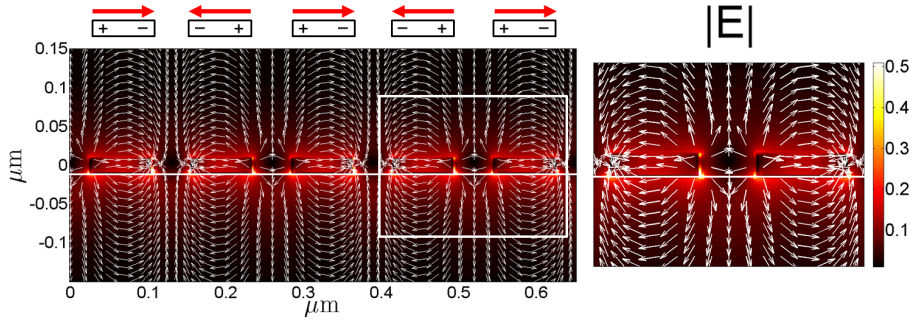


Figure 3.9: Energy density maps and electric field lines distribution at the Bragg condition for the dipolar longitudinal Bloch mode at $\lambda = 696$ nm. The corresponding squares show the phase distributions and orientation of the charges.

The field lines distribution in Fig.3.9, reveals a near-field coupling between the MNW due to a dipolar interaction between them, with the dipoles parallel oriented to the substrate-superstrate interface. This is the same dipolar longitudinal Bloch mode observed in the chain of MNW immersed in an homogeneous medium (Fig. 3.4a), but in this case, the mode is shifted to longer wavelengths (red shift). This shift is because the LSP resonance of the MNW is modified by the presence of the substrate with higher refractive index than the superstrate.

MNW of large height

For MNW of height $e = 150$ nm, we obtained three branches in the dispersion relations (Fig. 3.10). The upper and bottom branches are once again related to the quadrupolar (Fig. 3.11a) and dipolar transverse (Fig. 3.11c) Bloch modes, respectively. Since the presence of the substrate induces changes in the \mathbf{k} wavevector, these modes are shifted in spatial frequency relative to those of the isolated MNW array.

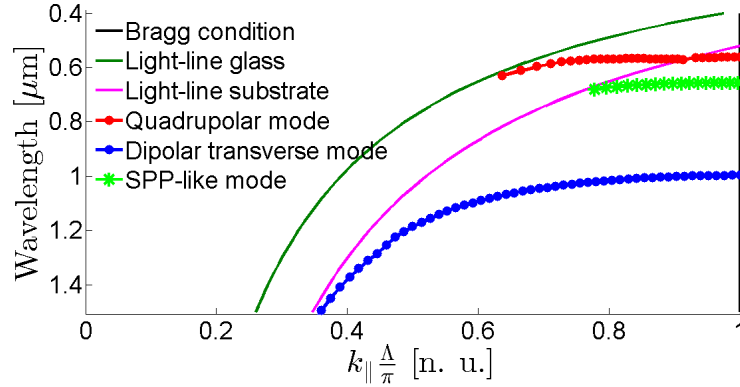


Figure 3.10: Dispersion relations for the quadrupolar (red dotted line), dipolar transverse (blue dotted line) and SPP-like (green asterisks) Bloch modes for an infinite chain of MNW of height $e = 150$ nm immersed in glass ($n_d = 1.5$) and placed on top of a dielectric medium of refractive index $n_{sub} = 2.0$.

We can interpret these modes as the symmetric and anti-symmetric surface plasmon polariton (SPP) matched at the dielectric-metal interfaces (Fig. 1.5). Since the height of the MNW is larger than the skin-depth, the charges distribution is favored along the z axis direction between the MNW. This result, leads us to conclude that the charges distribution takes place along the principal (larger) axis of the MNW.

The middle branch belongs to the excitation of a SPP-like mode. This is because the applied field induces longitudinal dipoles at the metal-substrate interface, and since the separation of the MNW is shorter than their width ($w < g$), a near-field interaction arises between them, like in a metallic layer (Fig. 3.11b). We must note that this mode only exists when the light propagating in the metallic nanoparticles and in the dielectric medium, have the same \mathbf{k} wavevectors values. In this case, this condition is only achievable when the resonance is below the light line of the substrate, and for this reason the branch exhibits a cut-off around this limit.

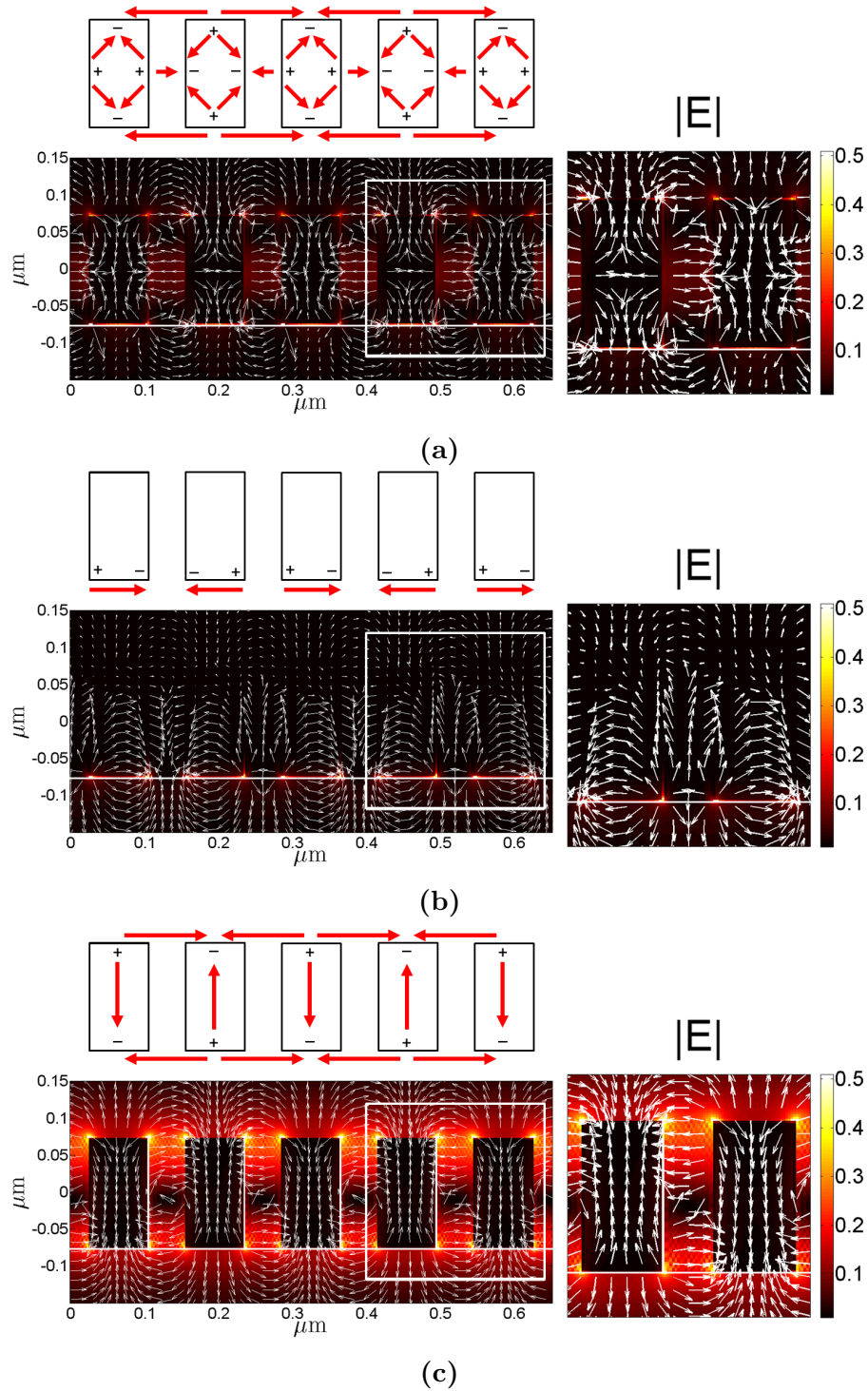


Figure 3.11: Energy density maps and electric field lines distribution at the Bragg condition for (a) the quadrupolar Bloch mode at $\lambda = 562$ nm, (b) the SPP-like mode (dipolar longitudinal) at $\lambda = 655$ nm, and (c) the dipolar transverse Bloch mode at $\lambda = 997$ nm. The corresponding squares show the phase distributions and orientation of the charges.

3.2.3 Modes propagation in an integrated system

Up to now, we have demonstrated that the MNW chain act as a plasmonic waveguide supporting the propagation of Bloch modes as a function of their aspect ratio.

This behavior implies that if we approach a dielectric waveguide to the structure, it is possible to have a directional coupling between the modes of the MNW chain and the modes of the dielectric waveguide, resulting in an optical integrated waveguide system.

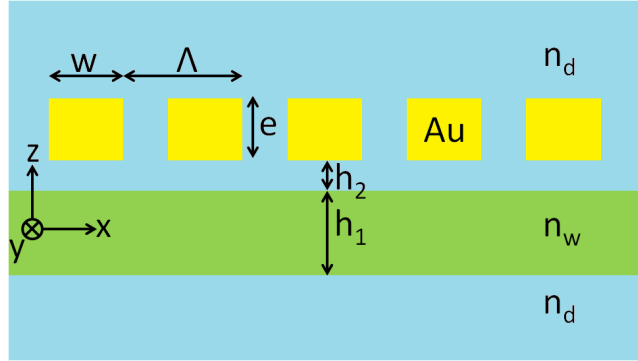


Figure 3.12: Scheme of an infinite periodic array of MNW immersed in glass, approached to a dielectric waveguide of refractive index $n_{wg} = 2.0$. The thickness of the waveguide is $h_1 = 200$ nm and it is separated a distance $h_2 = 30$ nm from the MNW chain.

In this section, we analyze the coupling and propagation of modes in an integrated structure as schemed in Figure 3.12. The system consists of a MNW chain immersed on the same homogeneous dielectric medium than before with refractive index $n = 1.5$ (glass). Then, a silicon nitride dielectric waveguide of height $h_1 = 200$ nm and core refractive index $n_{wg} = 2.0$ is approached to the MNW a distance $h_2 = 30$ nm. The thickness h_1 of the waveguide was previously determined to support only the fundamental transverse magnetic (TM₀) mode in a wavelengths spectral range from 400 nm to 1.5 μm . We chose the silicon nitride core to have a strong confinement of the light inside the waveguide.

MNW of short height

The curves in Figure 3.13a show the dispersion relation of the integrated structure and of the isolated chain of MNW. The green and pink solid lines represent the light-lines of the superstrate (glass) and waveguide core, respectively. The blue triangles curve describes the dispersion relation of the fundamental TM mode of the isolated waveguide. We can verify that only one mode is supported by the dielectric waveguide in the spectral range from 400 nm to 1.5 μm . The green asterisks line belongs to the dipolar longitudinal Bloch mode supported by the isolated chain of MNW immersed in glass.

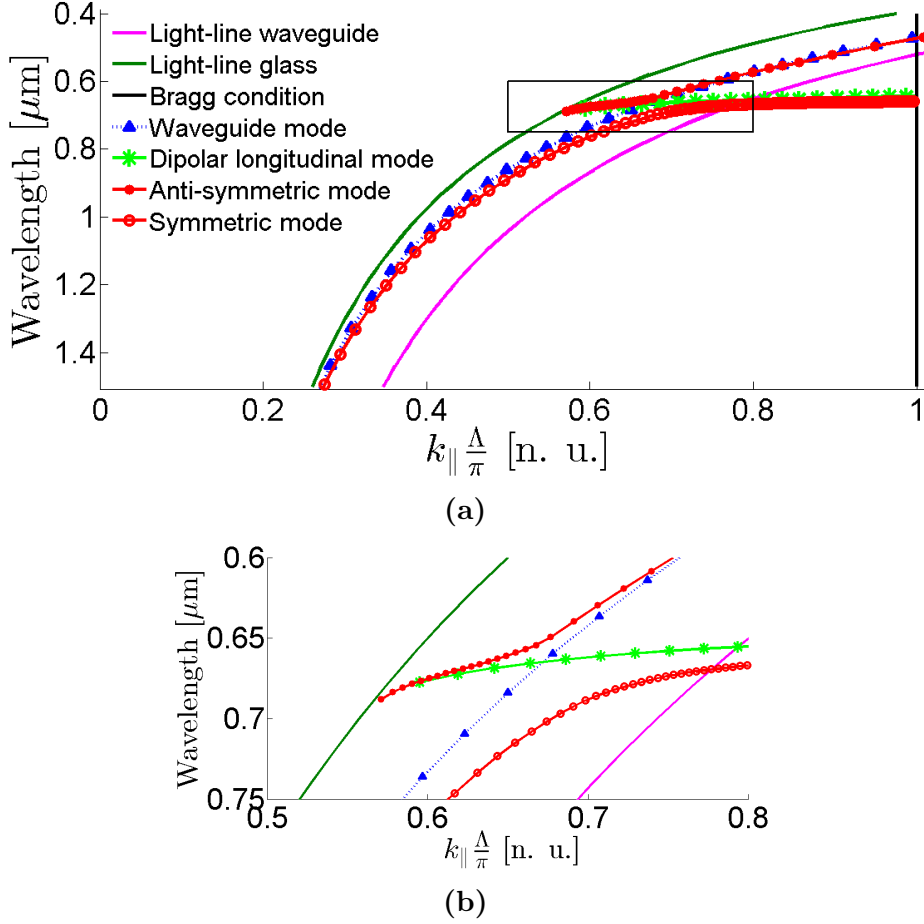


Figure 3.13: (a) Dispersion relations of the integrated structure. The TM fundamental mode of the waveguide (blue triangles) crosses the dipolar longitudinal mode of the isolated MNW chain immersed in glass (green asterisks), at $\lambda = 664$ nm. This generates anti-symmetric (red points) and symmetric (red circles) modes, that match the Bragg condition at $\lambda = 473$ nm and $\lambda = 660$ nm, respectively. (b) Inset in the crossing point region.

As we can observe in Figure 3.13b, there is an intersection point between the fundamental TM mode of the dielectric waveguide and the dipolar longitudinal Bloch mode around $\lambda = 664$ nm ($k_{||} = 0.672(\pi/\Lambda)$). Then, as in a two coupled waveguide system, symmetric (red circles) and anti-symmetric (red dots) modes are generated around the crossing point value. This anticrossing point implies that the chain of MNW acts as a plasmonic waveguide, whose dipolar longitudinal Bloch mode is coupled to the TM₀ mode of the dielectric waveguide.

To verify the anti-symmetric and symmetric nature of the two anti-crossing branches in the dispersion curves, we plotted energy density maps and electric field lines at the edge of the first Brillouin zone. Around $\lambda = 473$ nm, the upper branch exhibits a quadrupolar

(anti-symmetric) coupling between the MNW (Fig. 3.14a), while the lower branch, around $\lambda = 660$ nm, reveals a dipolar longitudinal (symmetric) coupling effect (Fig. 3.14b).

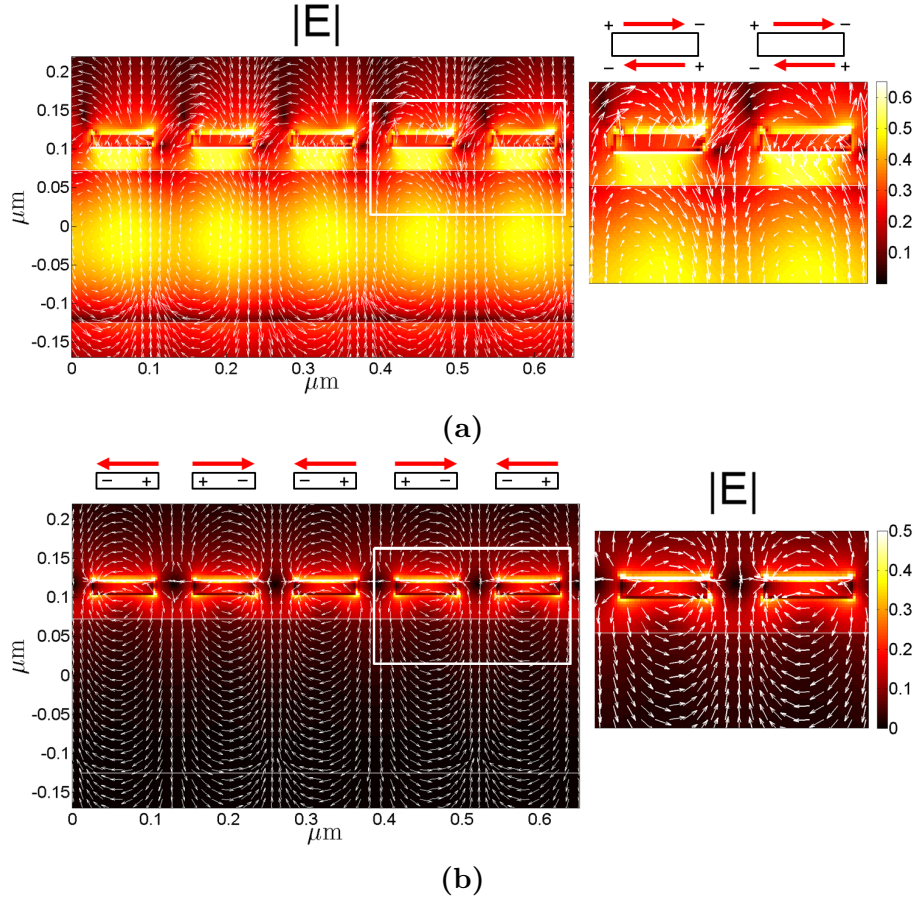


Figure 3.14: Energy density maps and electric field lines distribution at the Bragg condition for (a) the anti-symmetric (quadrupolar) Bloch mode at $\lambda = 473$ nm, and (b) the symmetric (dipolar longitudinal) Bloch mode at $\lambda = 660$ nm. The corresponding squares show the phase distributions and orientation of the charges.

At the Bragg condition limit, the anti-symmetric mode tends to the TM₀ mode of the dielectric waveguide, i.e. the mode is confined to the waveguide core. For this reason, as we can observe in Figure 3.14a, the energy density is higher inside the waveguide. Reciprocally, the symmetric mode tends to the dipolar longitudinal mode of the isolated MNW chain, being observed in Fig. 3.14b a higher energy in the plasmonic waveguide than in the dielectric waveguide core.

With these results, we can expect a vertical energy coupling of the light propagating through the waveguide with the array of MNW.

MNW of large height

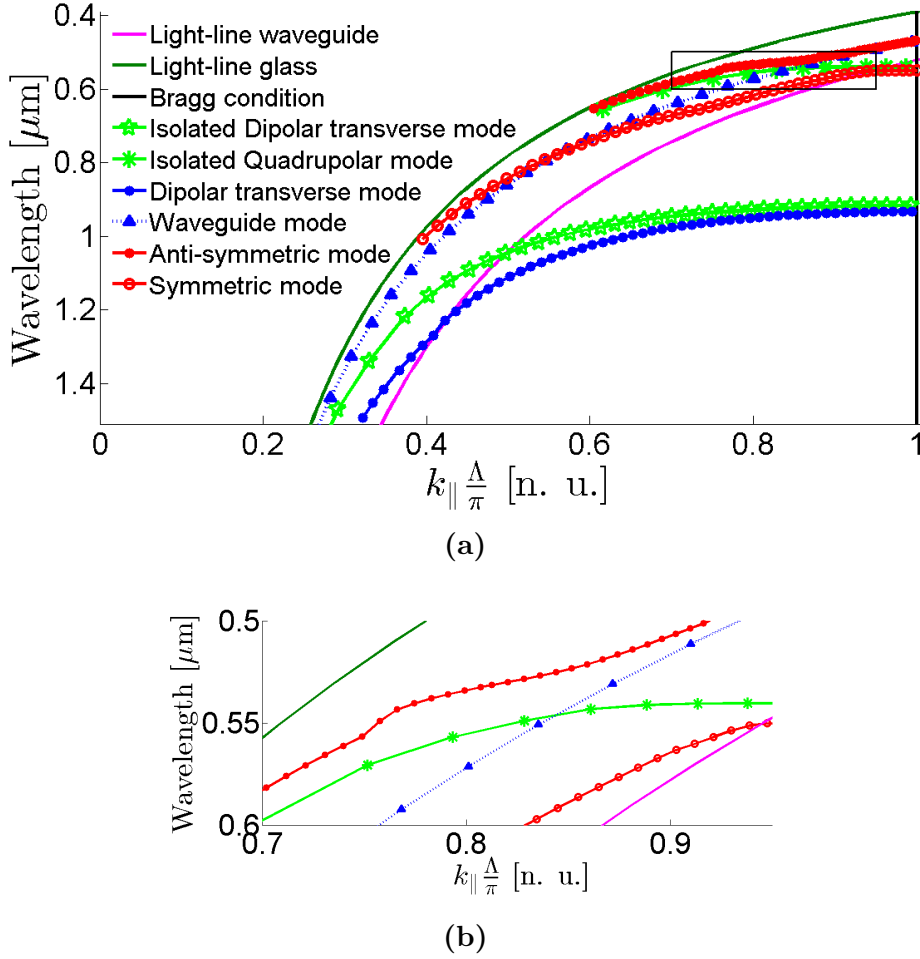


Figure 3.15: (a) Dispersion relations of the integrated structure for MNW of height $e = 150$ nm. The TM fundamental mode of the waveguide (blue triangles) crosses the quadrupolar mode of the isolated MNW chain immersed in glass (green asterisks), around $\lambda = 546$ nm. This generates anti-symmetric (red points) and symmetric (red circles) modes, that match the Bragg condition around $\lambda = 468$ nm and $\lambda = 549$ nm, respectively. The dipolar transverse mode (blue dots) reaches the Bragg condition around $\lambda = 933$ nm, but it does not cross the TM fundamental mode of the waveguide, and no anti-symmetric modes is generated. (b) Inset in the crossing point region.

The dispersion curves of the integrated system with a MNW chain of height $e = 150$ nm are presented in Figure 3.15a. Once again we represent the superstrate and waveguide core light-lines with green and pink solid lines, respectively, and the blue triangles line indicates the dispersion curve of the fundamental TM mode supported by the dielectric waveguide. The green asterisk curve and the green stars curve show the quadrupolar and dipolar transverse Bloch modes of the isolated MNW immersed in the glass homogeneous

medium.

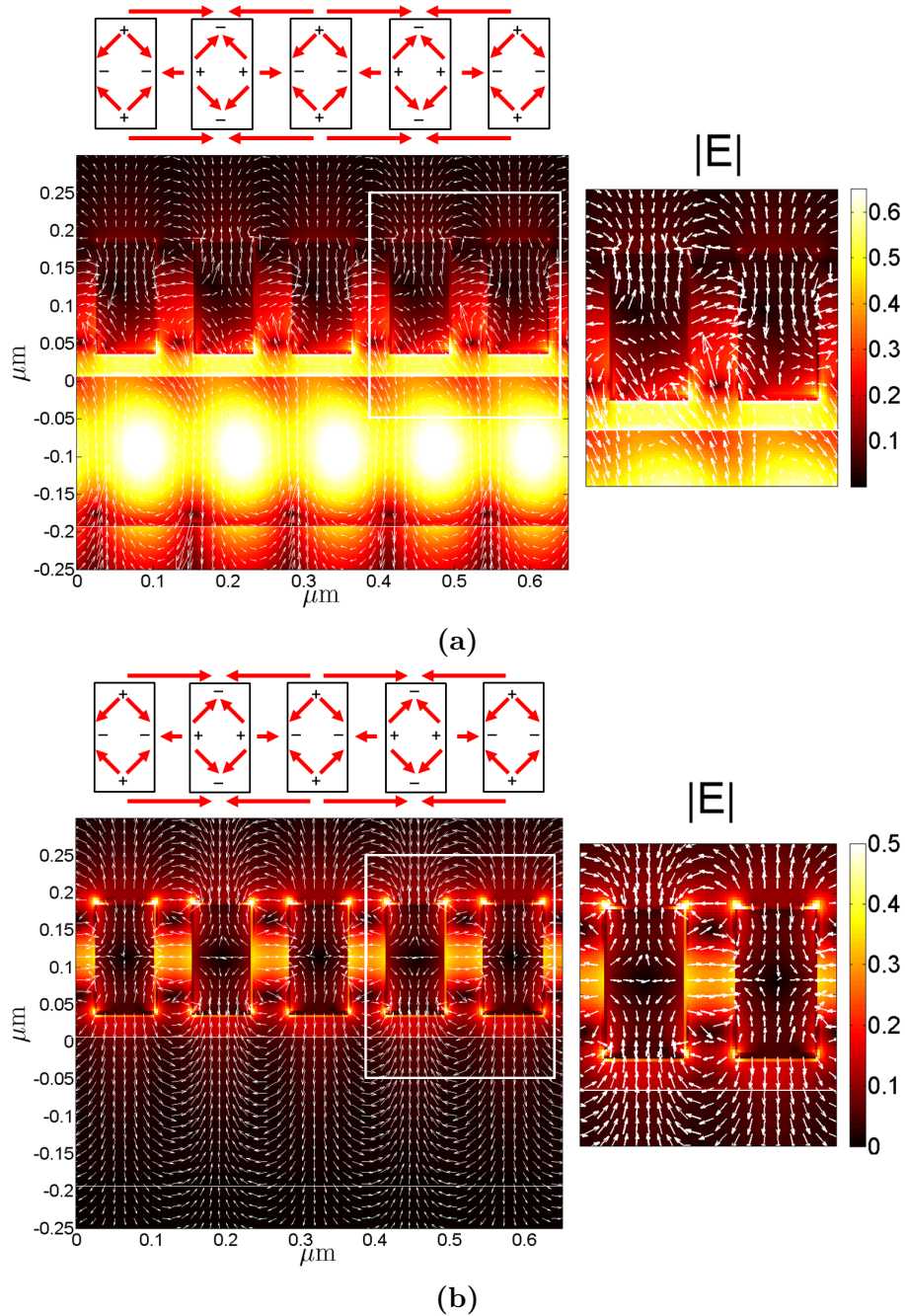


Figure 3.16: Energy density maps and electric field lines distribution at the Bragg condition for (a) the anti-symmetric (at $\lambda = 468$ nm), and (b) the symmetric (at $\lambda = 549$ nm) quadrupolar Bloch modes. The corresponding squares show the phase distributions and orientation of the charges.

The quadrupolar Bloch mode branch crosses the TM₀ mode of the dielectric waveguide around $\lambda = 546$ nm ($k_{\parallel} = 0.843 (\pi/\Lambda)$), generating, once again, anti-symmetric (red dots) and symmetric (red circles) branches. Their energy density maps and electric field lines are plotted in Figures 3.16a and 3.16b, respectively. From these figures we can observe

that even when the field lines are distorted for the anti-symmetric branch, the charges distribution is the same for both cases. Nevertheless, for the anti-symmetric branch the energy is highly confined inside the waveguide, since it tends to the dielectric waveguide mode at the Bragg condition limit (around $\lambda = 468$ nm). Reciprocally, the energy of the symmetric branch is confined into the MNW chain at the Bragg condition (around $\lambda = 549$ nm).

In opposition to the quadrupolar mode, the dipolar transverse Bloch mode does not cross the TM0 waveguide mode at any point. Then we not observe the anti-crossing phenomena, but the mode is confined below the waveguide light-line in a larger spectral range than the isolated MNW dipolar transverse mode.

Because of the presence of the dielectric waveguide, the \mathbf{k} wavevector of the dipolar transverse mode is altered, in such a way that this mode is confined below the waveguide light-line in a larger spectral range (blue dots) than the isolated MNW dipolar transverse Bloch mode (green stars). The energy density map and electric field lines distribution computed at the Bragg condition (around $\lambda = 933$ nm), are schemed in Figure 3.17.

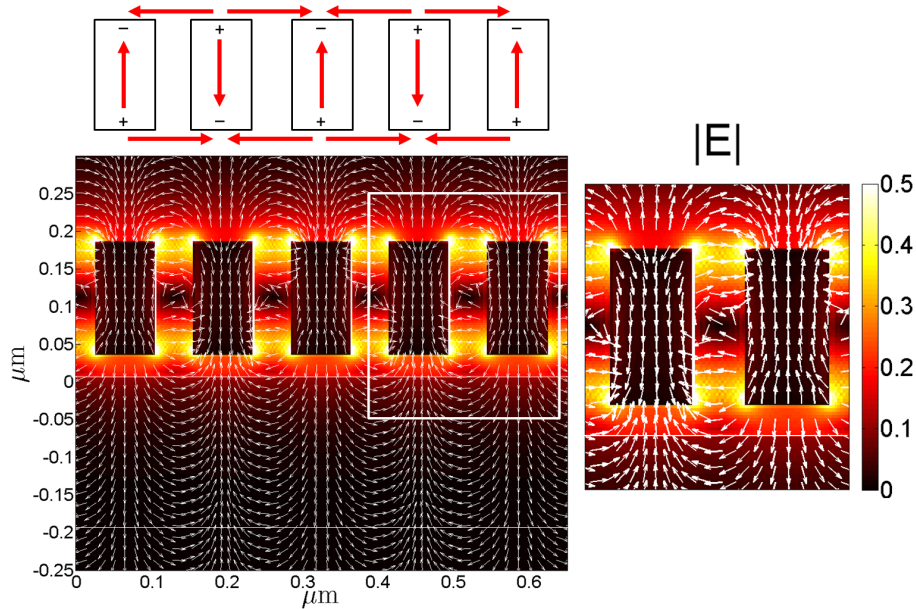


Figure 3.17: Energy density map and electric field lines distribution at the Bragg condition ($\lambda = 933$ nm) for the dipolar transverse Bloch mode. The corresponding squares show the phase distributions and orientation of the charges.

3.3 Beam propagation in the integrated system

As we have demonstrated, the Bloch modes propagating through the periodic array of MNW can be coupled to the fundamental TM₀ mode of a dielectric waveguide nearly placed to them, being expected an energy exchange between the dielectric and the plasmonic waveguides.

The FMM method allows us to determine the beam propagation through this kind of systems. Then in the following we present a deeper study of the integrated structure in terms of the interaction of TM polarized light traveling along the dielectric waveguide with a finite array of MNW, as schemed in Figure 3.18.

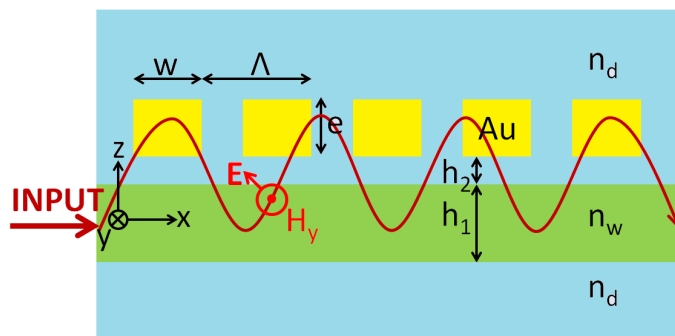


Figure 3.18: Scheme of the beam propagation in a finite periodic array of MNW on a dielectric waveguide with core index $n_w = 2.0$. The fundamental TM mode of the dielectric waveguide is launched into the structure at $x = 0$. The mode propagates through the waveguide and couples to the modes of the metallic chain of gold nanowires.

The system consist of a finite periodic array of 27 gold nanowires of width $w = 80$ nm and period $\Lambda = 130$ nm, placed at a distance $h_2 = 30$ nm from a dielectric waveguide of thickness $h_1 = 200$ nm and core refractive index $n_w = 2.0$. At the input of the system, at $x = 0$, we launch the TM₀ mode supported by the dielectric waveguide.

We computed the normalized transmission and reflection spectra at the output and input of the dielectric waveguide, as well as the absorption of the structure in a spectral range from 400 nm to 1.5 μm . To observe the light interaction between the structures, we calculated near field maps of the amplitude of the H_y component of the TM polarized light.

As before, MNW of short ($e = 20$ nm) and large ($e = 150$ nm) height are studied.

3.3.1 MNW of short height

In Figure 3.19 we plot the normalized transmission (red curve), reflection (blue dashed curve) and absorption (black dotted curve) spectra.

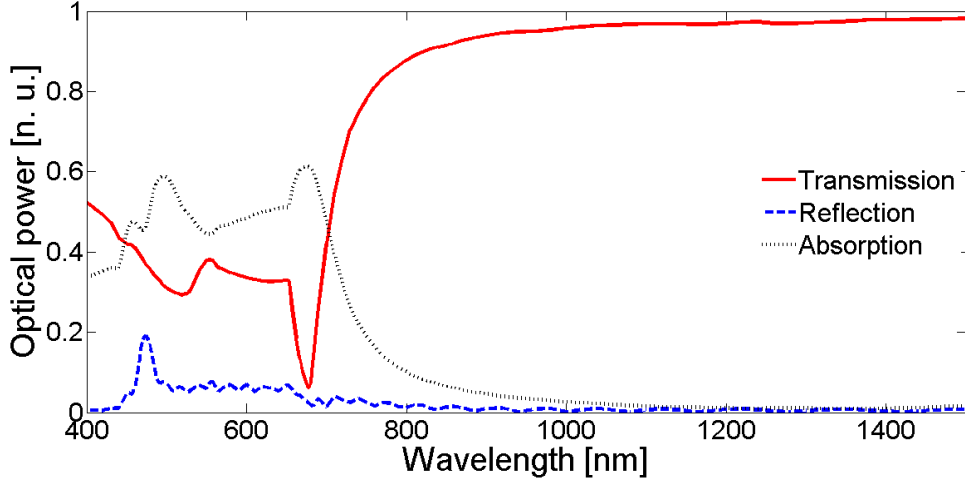


Figure 3.19: Transmission (red curve), reflection (blue dashed curve) and absorption (black dotted curve) spectra of the finite integrated system with MNW of height $e = 20$ nm. The reflection curve has a maximum around $\lambda = 474$ nm, while the transmission exhibits two minimum values around $\lambda = 520$ nm and $\lambda = 678$ nm. The first is associated to a Bragg reflection, and the second one to the excitation of the dipolar longitudinal Bloch mode.

As we can observe, the reflection curve exhibits a maximum value around $\lambda = 474$ nm. This wavelength corresponds to the anti-symmetric Bloch mode at the Bragg condition on the dispersion curve of Fig. 3.13a. This means that, since we are dealing with a periodic array, we obtain a Bragg reflection to the input of the structure. This effect can be observed in the near-field map of Figure 3.20.

The transmission curve presents two minimum values. The first one, located around $\lambda = 520$ nm, is associated to the Bragg reflection of the incident field due to the periodicity of the structure. This condition can be verified with the expression

$$\lambda_{Bragg} = \frac{2n_{\text{eff}}\Lambda}{m}, \quad (3.2)$$

where n_{eff} is the effective index of the guided mode, Λ the period of the MNW array, and m the Bragg order. From the dispersion relations, we can obtain the effective index of the dipolar longitudinal Bloch mode with the relationship $k_{\parallel} = (2\pi/\lambda)n_{\text{eff}}$. According

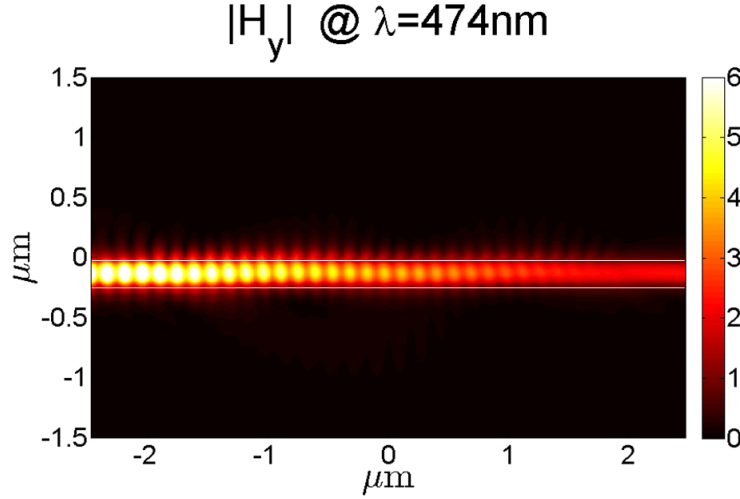


Figure 3.20: Near field map of the absolute value of the H_y component of the electromagnetic field. The periodic lobes observed inside the waveguide core are associated to a Bragg reflection.

to the dispersion curves of Fig. 3.13a, at $\lambda = 520$ nm, the effective index of the anti-symmetric mode is $n_{\text{eff}} = 1.801$, and since $\Lambda = 130$ nm, the Bragg reflection occurs around $\lambda_{\text{Bragg}} = 468$ nm, which is a value close to the maximum observed in the reflection spectra.

The difference in the wavelengths of the minimum transmission and maximum reflection cannot be easily explained since many physical phenomena can contribute to this difference. In first place, the grating acts like an spatial filter: we have many optical cavities formed by the individual nanowires, and a large optical cavity formed by the complete finite array of periodic nanowires; then, the diffracted orders can be back-reflected to the input of the waveguide but at a different wavelength. Also, the Bragg reflection favors the absorption of the electromagnetic field (the absorption spectra exhibits a maximum value around $\lambda = 496$ nm), and from the Mie scattering theory, it is known that the extinction spectra of a metallic nanoparticle is red-shifted with respect to the absorption spectra (Bohren and Huffman, 1998; Cordova-Castro, 2014). Then the minimum in the transmission curve can also be attributed to the optical field scattered out-off the integrated structure by the first and last nanowire. This shift in the resonance of the transmission and absorption spectra have been also observed in other works (Tan et al., 2012), however, there is no explanation for this phenomena. The complete understanding of this situation is open to discussion for perspective work out of the scope of this thesis.

The second minimum in the transmission spectrum at $\lambda = 678$ nm, is due to the

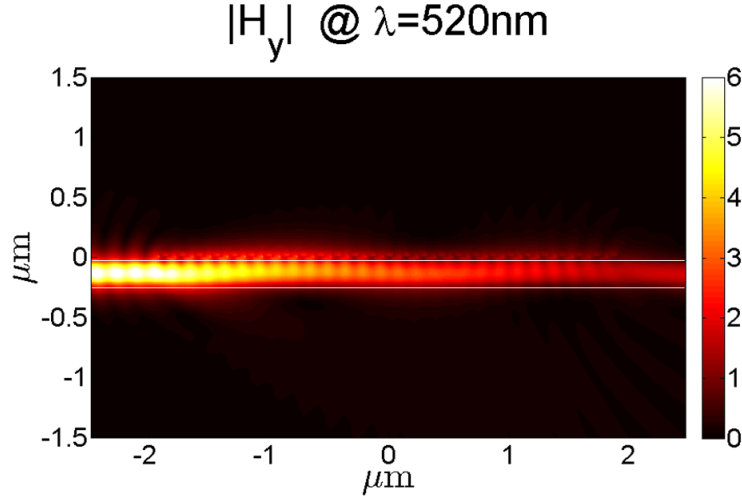


Figure 3.21: $|H_y|$ near-field map of the integrated system at the first minimum value in the transmission spectra at $\lambda = 520$ nm, which corresponds to a Bragg reflection.

excitation of the dipolar longitudinal Bloch mode. As was observed in the dispersion curves of Fig. 3.13a, this wavelength value corresponds to the anticrossing region of the symmetric and anti-symmetric modes, around $k_{\parallel} = 0.672(\pi/\Lambda)$. At this wavelength, the dipolar longitudinal Bloch mode is efficiently coupled to the dielectric TM₀ mode, obtaining a periodic energy beating from the dielectric waveguide to the MNW chain, as we observe in the near-field map of Figure 3.22.

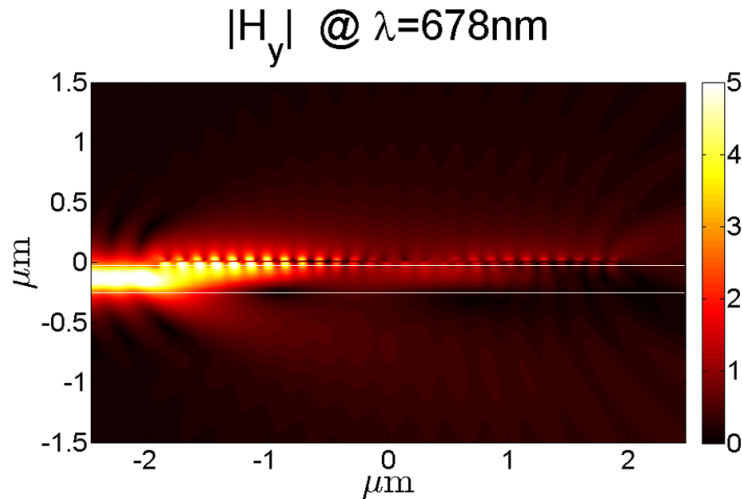


Figure 3.22: $|H_y|$ near-field map of the integrated system at the second minimum value in the transmission spectra at $\lambda = 678$ nm, corresponding to the excitation of the dipolar longitudinal Bloch mode.

This energy beating confirms our assumption that the MNW chain is acting as a plasmonic waveguide. The spatial half-period or the coupling length in the field map is

$L_c = 961$ nm. From coupled mode theory, the coupling length can be estimated with the relationship $L_c = \lambda / (2\Delta n_{\text{eff}})$ (equation (2.33)), where Δn_{eff} is the difference of the effective index between the symmetric and anti-symmetric modes at a given wavelength λ . From the dispersion curves (Fig. 3.13a) at $\lambda = 678$ nm, we have $n_{\text{eff},1} = 1.542$ and $n_{\text{eff},2} = 1.904$, and therefore $L_c = 936$ nm, which is consistent with the previous value of 961 nm.

These results demonstrate that the proposed integrated structure is acting as a two waveguide interferometric system formed by the dielectric and plasmonic waveguides.

3.3.2 MNW of large height

The dispersion curves of the integrated system for a MNW array of height $e = 150$ nm (Fig. 3.15a), reveal that an efficient directional coupling with a dielectric waveguide is expected for the quadrupolar Bloch mode. For the dipolar transverse mode, the field is confined between the nanowires, so an energy beating with the evanescent field of the dielectric waveguide is also expected.

In Figure 3.23 are plotted the normalized reflection (blue dashed curve), transmission (red curve) and absorption (black dotted curve) in a spectral range from 400 nm to 1.5 μm .

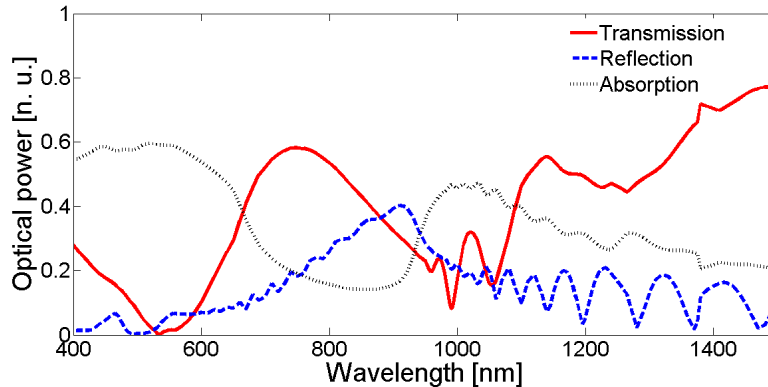


Figure 3.23: Transmission (red curve), reflection (blue dashed curve) and absorption (black dotted curve) spectra of the finite integrated system with MNW of height $e = 150$ nm. The quadrupolar mode is excited at $\lambda = 559$ nm, and the constructive interference of the dipolar transverse mode is positioned around $\lambda = 990$ nm. The minimum around $\lambda = 1055$ nm, is a cavity effect. The Bragg reflections are located around $\lambda = 534$ nm and $\lambda = 960$ nm.

The reflection curve exhibits three main maximum values placed around $\lambda_{R1} = 465$ nm, $\lambda_{R2} = 559$ nm, and $\lambda_{R3} = 910$ nm. They correspond, respectively, to the anti-symmetric quadrupolar, symmetric quadrupolar and dipolar transverse Bloch modes at the Bragg condition limit in the dispersion curves.

The transmission curve also exhibits several minimum values. Bragg reflections are observed around $\lambda = 534$ nm and $\lambda = 960$ nm. The first one correspond to the Bragg reflection of the symmetric quadrupolar Bloch mode, while the second is due to the Bragg reflection of the dipolar transverse mode. This observation can be verified with the expression (3.2). For example, from the dispersion curves, the Bragg reflection of order $m = 1$ for the dipolar transverse mode has an effective index $n_{\text{eff},\text{transv}} = 3.52$, giving $\lambda_{\text{Bragg}} = 915$ nm, which is close to the value of the maxima in the main reflection band (λ_{R3}). At the Bragg condition, the symmetric quadrupolar branch has an effective index value of $n_{\text{eff}} = 2.12$, so $\lambda_{\text{Bragg}} = 551$ nm, which is also close to the second maximum λ_{R2} in the reflection curve.

Efficient excitation of the quadrupolar and dipolar transverse Bloch modes are observed respectively, around $\lambda = 559$ nm and $\lambda = 990$ nm in both transmission and absorption spectra.

For the first one, a directional coupling takes place from the dielectric waveguide to the MNW chain because the quadrupolar and the TM0 modes crosses around this value, generating an anti-crossing phenomena between the symmetric and anti-symmetric branches, like in the case of the MNW chain of small height.

This effect is confirmed in the near-field map of Figure 3.24, where we note an energy beating from the waveguide to the nanowires chain. From the dispersion curves, at $\lambda = 559$ nm, the effective indices of the anti-symmetric and symmetric branches are $n_{\text{eff},\text{Asym}} = 1.6$ and $n_{\text{eff},\text{Sym}} = 1.968$, so the spatial half period of the coupling length (eq. (2.33)) is $L_c = 759$ nm.

Concerning to the excitation of the dipolar transverse Bloch mode, the directional coupling is not the main process since we do not observe the anti-crossing phenomena in the dispersion curves. Nevertheless, as depicted in Figure 3.25, close to $\lambda = 990$ nm, the TM0 launched mode is coupled to the array of nanowires. A vertical energy beating is

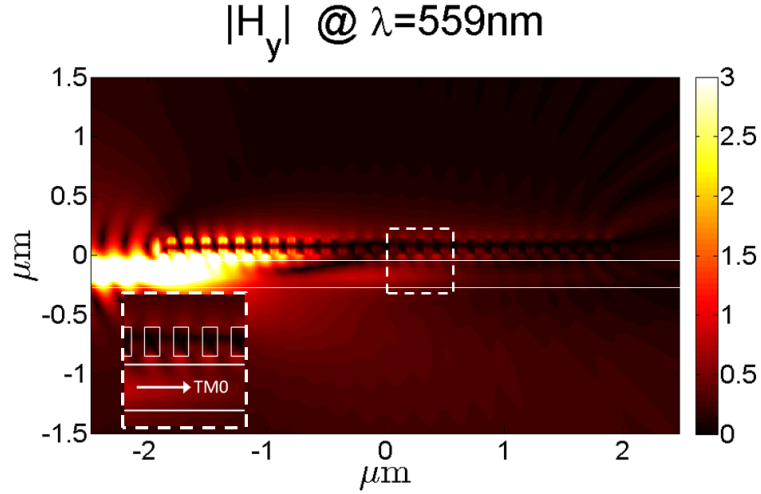


Figure 3.24: $|H_y|$ near-field map of the integrated system at the second minimum value in the transmission spectra at $\lambda = 559$ nm, corresponding to the excitation of the quadrupolar Bloch mode.

visible (weakly contrasted) in the near-field map, and it is attributed to an interference pattern between guided and leaky modes.

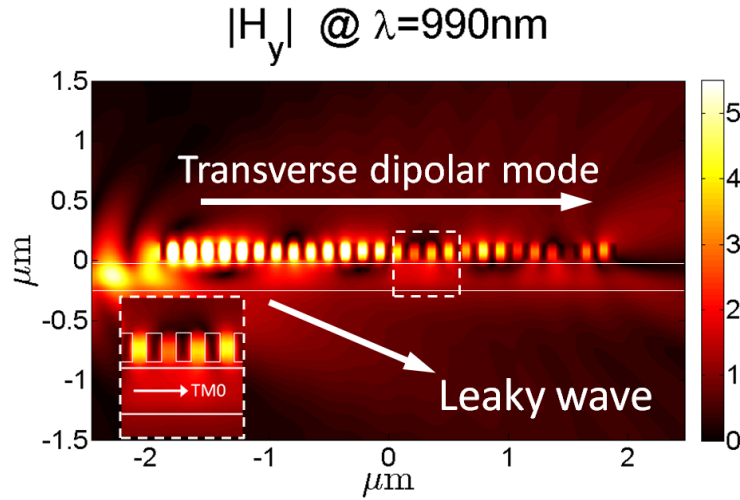


Figure 3.25: $|H_y|$ near-field map of the integrated system at the second minimum value in the transmission spectra at $\lambda = 990$ nm, corresponding to the excitation of the dipolar transverse Bloch mode.

From the dispersion curves, at $\lambda = 990$ nm, the effective index of the dipolar transverse branch is $n_{\text{eff}} = 2.213$, and from the near-field map the beating period is $2L_c = 1.17$ μm . Then, from equation (2.33), the leaky mode has an effective index close to 1.3, which is a value above the light-line of the surrounding medium ($n_d = 1.5$).

Since the finite array of MNW has a finite length ($D = 27\Lambda - g = 3.46$ μm), it can be seen as a cavity. Then, the transmission spectrum changes abruptly between $\lambda = 900$ nm

and $\lambda = 1100$ nm as a result of the interference between multiple reflections at the edges of the array. We can determine the wavelength separation between adjacent transmission minima like in a Fabry-Perot optical cavity via the relationship

$$\Delta\lambda = \frac{\lambda^2}{2Dn_{\text{eff}}}, \quad (3.3)$$

where D is the length of the cavity and n_{eff} is the effective index of the mode at the central wavelength λ .

From the dispersion curves, at $\lambda = 990$ nm, $n_{\text{eff}} = 2.213$, so $\Delta\lambda = 65$ nm, generating the minima that we observe in the transmission curve at $\lambda = 1055$ nm.

Finally, as was predicted in the plots of Figure 3.5b, the propagation distance of the quadrupolar Bloch mode, is shorter than the one of the dipolar transverse mode.

These results proves again that our integrated structure is acting as a vertical coupling system, showing the excitation of the quadrupolar and dipolar transverse Bloch modes.

The advantage of the MNW chain of taller height, is that two modes are excited with the same integrated structure. The first one in the visible range and the second in the near-infrared regime.

3.4 Triangular-shaped nanowires

We demonstrated that a chain of metallic nanowires behaves as a plasmonic waveguide, whose propagating modes depend on the aspect ratio of the MNW. When we integrated this chain on top of a dielectric waveguide, a vertical coupling took place and two modes interfered, creating an energy beating pattern.

On the other hand, it is well known that LSP resonances depend on the geometry of the metallic nanoparticles (Noguez, 2007). One of the most interesting shapes and barely exploited in integrated systems, are the nanocone shaped particles. This is because the nanocones present a field enhancement (hot spots) at their vertexes (Kelly et al., 2003; Kontio et al., 2009). This property can be applied, for example, in the detection of a small number of molecules.

For example, D'Agostino and co-authors (D'Agostino et al., 2013) have demonstrated that the LSP resonance of a metallic nanotip is strongly influenced by the curvature radius of its apex. Also, Fleischer and co-authors (Schafer et al., 2013) explained the role of the aspect ratio for a single nanocone on top of a substrate. These studies have been done by illuminating the nanoparticles from the substrate or the superstrate, where only radiated modes can be obtained.

However, so far the propagation of modes in periodic arrays of triangular-shaped nanowires (from now on referred as nanocones) have not yet been reported. Like in the case of metallic nanowires, we can place the chains of metallic nanocones (MNC) in close proximity to a dielectric waveguide, forming an integrated system.

Based on the Fourier modal method, in the following sections we perform a parametric study of the LSP resonances of a chain of MNC as a function of its periodicity and the incidence angle of the impinging light. To this purpose, first we study the spectral response of a single nanocone placed on top of an homogeneous dielectric substrate. Then we analyze the way that this response is affected by the collective effect of a periodic array of MNC. Finally, we study the way we can apply these results to an integrated system. We analyze the first two cases with the rigorous coupled wave analysis (RCWA), or FMM for an infinite periodic array of nanoparticles, and the last case with the FMM for finite non-periodic structures.

It must be remarked that since the nanocones are formed by a staircase approximation, it is necessary to increment the number of harmonics to have a good convergence in the spectral results (Popov et al., 2002). However, this situation can lead to the apparition of hot-spots at the corners of the stairs in the near-field maps. So, a previous convergence study must be performed in order to have the proper balance between the number of steps forming the nanocones and the number of harmonics.

3.4.1 Single MNC on top of a dielectric substrate

Let us consider the structure depicted in Figure 3.26, which consists of a gold nanocone of height $h = 144$ nm and width $w = 72$ nm, placed on top of an homogeneous dielectric

medium of refractive index $n_{sub} = 1.5$ (glass). We consider air as superstrate ($n_{sup} = 1.0$).

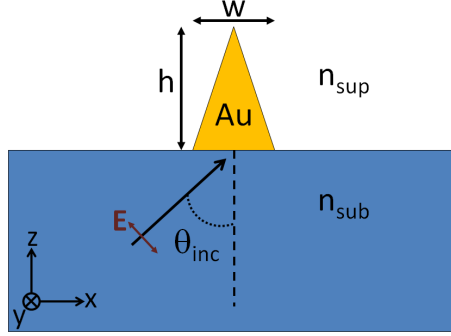


Figure 3.26: Gold nanocone of width $w = 72$ nm and height $h = 144$ nm immersed in air ($n_{sup} = 1.0$), placed on top of a dielectric substrate of refractive index $n_{sub} = 1.5$. A TM polarized plane wave impinges the glass-air interface forming an angle θ_{inc} respect to the normal.

It must be noted that the RCWA is implemented for infinite periodic arrays of nanoparticles. So, in order to study one single nanocone, it is necessary to avoid the near-field interaction between them. One way to avoid this interaction is by increasing the period of the structure, such that we can only observe the LSP resonance of a single nanocone and not the chain modes of the array. However, when increasing the period we must also augment the number of harmonics of the Fourier series, which increases the computation time and also can lead to numerical instabilities. For this reason, a careful study of the numerical convergence must be previously done.

Here we do not present this convergence study, but we observed that for a period above $5 \mu\text{m}$ there was no longer any interaction between the nanocones. Then the period of the array of triangle-shape nanowires was fixed to $6 \mu\text{m}$. Similarly, to have a good convergence in the spectral curves, we fixed a number of 601 harmonics for the Fourier expansions.

To analyze the spectral response in transmission, reflection and absorption of the structure depicted in Fig. 3.26, we illuminated the base of the MNC with a TM polarized plane wave, whose \mathbf{k} wavevector forms an angle θ_{inc} with respect to the normal at the glass-air interface.

The plots of Figure 3.27 show the transmission (to the superstrate), reflection (to the substrate) and absorption (of the nanocone) of the system as a function of the incidence

angle.

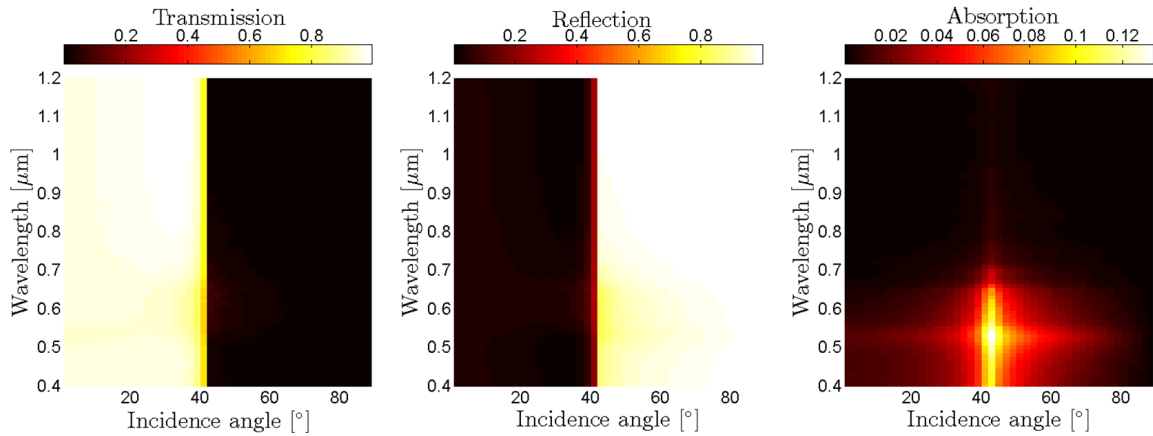


Figure 3.27: Transmission, reflection and absorption spectra as a function of the incidence angle. The absorption is maximum at $\lambda = 540$ nm and $\theta_{inc} = 43^\circ$.

The maximal absorption efficiency is observed for an incidence angle around 43° and a wavelength value $\lambda = 540$ nm. This angle value is near to the critical angle for total internal reflection (TIR) for a glass-air interface.

The critical angle is defined as $\theta_c = \arcsin(n_{sup}/n_{sub})$, where n_{sub} and n_{sup} are the refractive indices of the substrate and superstrate, respectively. This condition is only achievable if $n_{sub} > n_{sup}$, and if the wave propagates from the substrate to the superstrate. For the case of a glass-air system $\theta_c = 41.8^\circ$.

For angles smaller than 43° , the absorption spectral bands are narrower while for larger angles are wider. This means that the absorption of the electromagnetic field by the nanocone is more efficient if the plane wave is in the TIR regime.

The observation of the maximum absorption around the critical angle arises from the fact that at TIR regime, the electromagnetic field transmitted to the superstrate is an evanescent wave which propagates laterally to the surface, and that have a polarization state is in general elliptical (Azzam, 2011; Novotny and Hecht, 2006). Around the critical angle, the elliptical polarization state is almost linear with the major axis perpendicularly oriented to the glass-air interface, being generated a dipole-like source at the superstrate. Furthermore, the polarization ellipticity varies very rapidly (as $1/\sin(\theta_{inc})$) with θ_{inc} closed to $\pi/2$. The corresponding wave in the superstrate propagates parallelly to the surface (often referred as "lateral wave" in the literature). This means that a wave impinging the

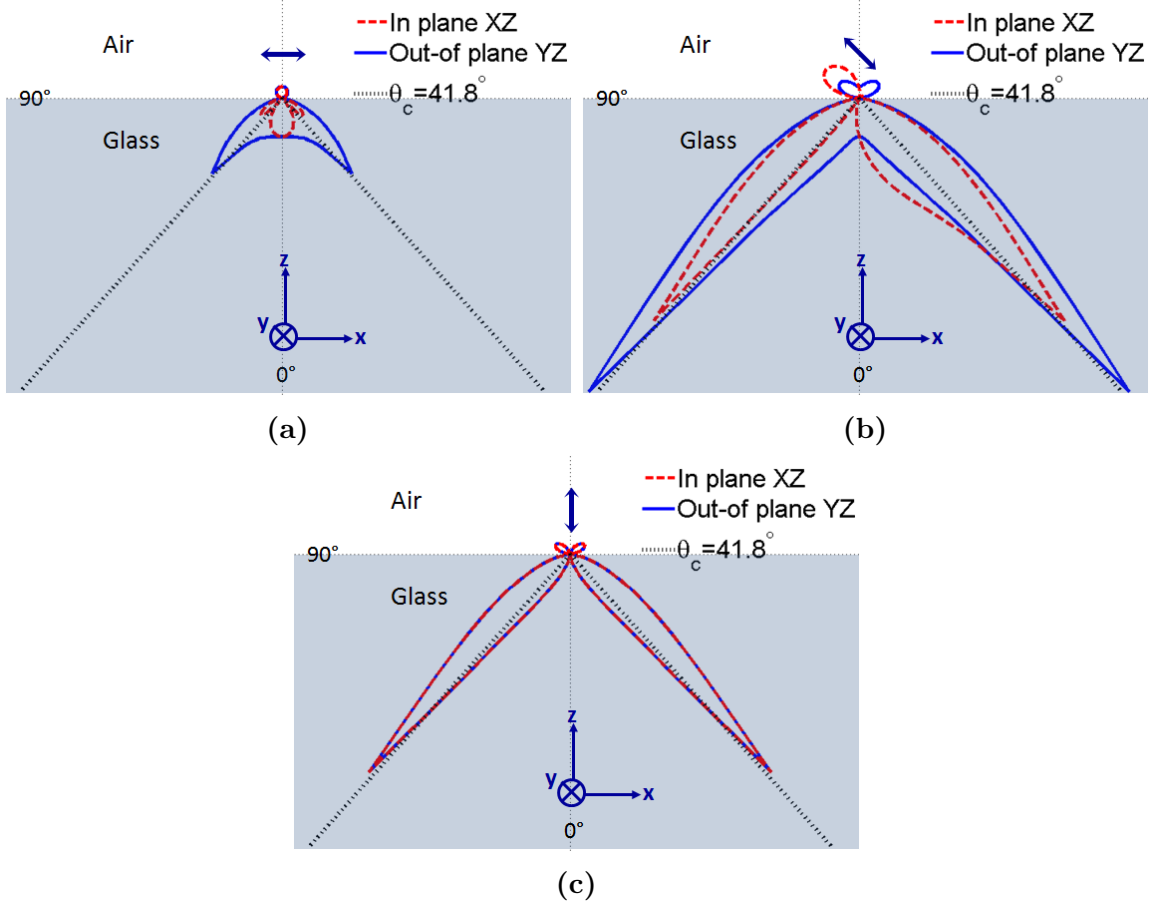


Figure 3.28: In plane (blue curves) and out-of plane (red dotted curves) far-field scattering patterns, of a dipole nearly placed on top of the glass substrate oriented at (a) 0° , (b) 45° , and (c) 90° respect to the interface air-glass (parallel to the x axis). The light scattered by the dipole towards the glass substrate, is preferentially radiated in the direction of the critical angle $\theta_c = 41.8^\circ$ (black dotted lines) respect to the $-z$ axis (from the substrate).

surface at an infinite distance from the scatterer will be coupled into a lateral wave. By reducing the spatial extent of the incident wave, the enhancement of absorption efficiency at the critical angle can be significantly reduced. On the other hand, for an air-glass interface, it can be demonstrated that for a dipole perpendicularly oriented and placed in the air superstrate and near to the interface, its radiation pattern towards the substrate is favored in a direction close to the critical angle (Novotny and Hecht, 2006), as we show in the far-field scattering patterns of Figure 3.28. This means that light coupled around this angle will efficiently excite the perpendicularly oriented dipole at the superstrate, and hence the interaction of the incident plane wave with the metallic nanoparticle will be enhanced.

At the critical angle for a wavelength $\lambda = 540$ nm, the near-field map of Figure 3.29

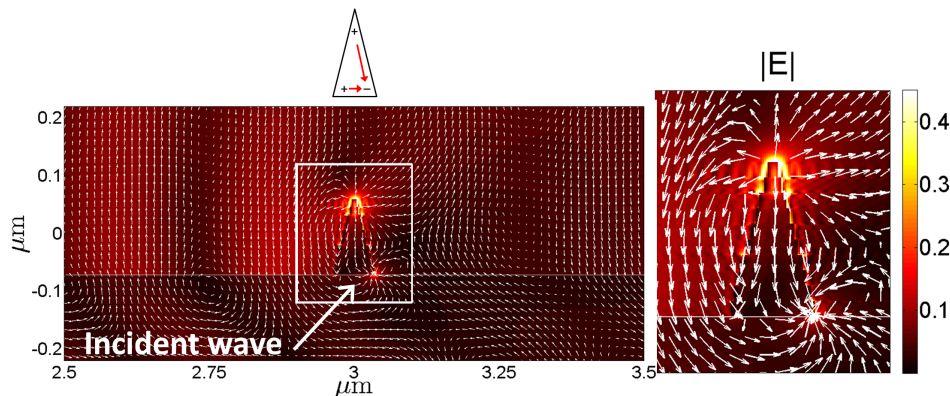


Figure 3.29: Energy density map and electric field lines distribution for a single nanocone over a glass substrate at $\lambda = 540$ nm and $\theta_{inc} = \theta_c = 41.8^\circ$. The electric field lines reveal a combination of dipolar transverse and dipolar longitudinal resonances, enhancing the optical field in the vertexes of the MNC.

shows that the nanocone exhibits an enhancement of the field at the opposite vertexes of the incident wave. The distribution of the electric field lines reveals a dipolar transverse excitation perpendicularly oriented to the glass-air interface. However, we can also observe that at the basis of the nanocone the field lines are slightly distorted due to the weak influence of a dipolar longitudinal momentum. For this reason, the optical field is enhanced at the vertexes of the MNC.

To determine if this resonance can be transformed into a propagative mode, we reduced the period of the MNC must to allow the near-field interaction between them. This treatment is described in the next section.

3.4.2 Short-period array of MNC on top of a dielectric substrate

The structure to analyze is schemed in Figure 3.30. It consists of an infinite periodic array of gold nanocones of height $h = 144$ nm, width $w = 72$ nm and period Λ . The superstrate and substrate have a refraction index $n_{sup} = 1.0$ and $n_{sub} = 1.5$, respectively. Once again, the TM plane wave impinges at an angle θ_{inc} respect to the normal at the interface.

In first place, we perform a spectral response analysis of the structure as a function of the incidence angle of the plane wave, fixing the period of the structure to $\Lambda = 200$ nm. The results are plotted in Figure 3.31.

The results presented in Figure 3.31 show two branches of resonances. The first one,

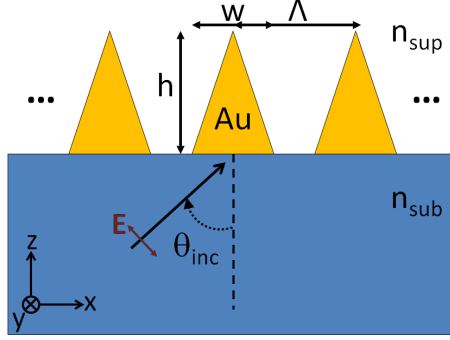


Figure 3.30: Infinite periodic array of gold nanocones of width $w = 72$ nm and height $h = 144$ nm immersed in air ($n_{sup} = 1.0$), placed on top of a glass substrate ($n_{sub} = 1.5$). The incident TM polarized plane wave forms an angle θ_{inc} respect to the normal.

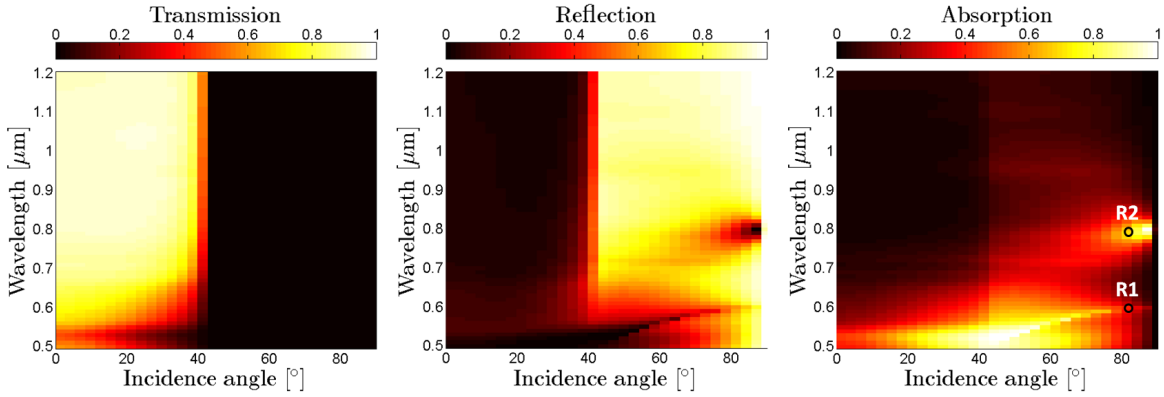


Figure 3.31: Transmission, reflection and absorption efficiency spectra as a function of the angle θ_{inc} for a MNC chain of period $\Lambda = 200$ nm. Two resonances are observed, the first one around the critical angle (like the isolated nanocone), and a second one that is only observable at grazing angles (near to the marker $R2$).

is efficiently excited around the critical angle ($\theta_{inc} = 43^\circ$) and $\lambda = 530$ nm, near to the maximum value for the isolated nanowire (Fig. 3.32a).

The second resonance is efficiently excited only at grazing angles, exhibiting a maximum excitation for a wavelength value around $\lambda = 800$ nm and a grazing angle around $\theta_{inc} = 88^\circ$, near to the marker $R2$ in the absorption spectra (Fig. 3.32b). This resonance was not observed for the isolated nanowire, then we assume that it is due to the near-field interaction between the triangular-shaped nanowires.

To corroborate if the second resonance is due to a near-field coupling effect between the MNC, we now present a spectral response analysis of the structure as a function of its periodicity. Since the field enhancement is favored for plane waves impinging in the TIR regime, we fix the incidence angle to a grazing value $\theta_{inc} = 82^\circ$, the same angle of

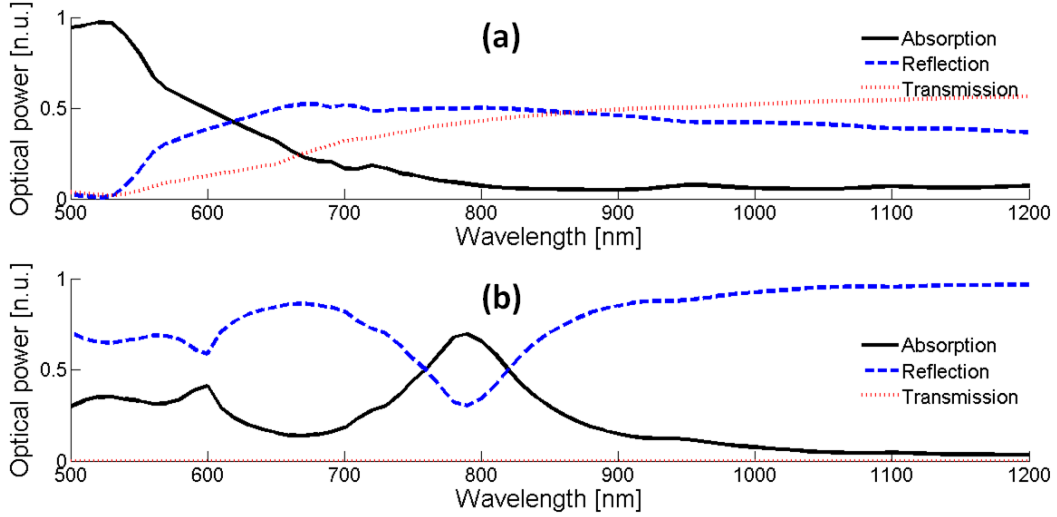


Figure 3.32: Transmission, reflection and absorption efficiency spectra for a plane wave with incident angles of (a) $\theta_{inc} = 43^\circ$ (around the critical angle) and (b) $\theta_{inc} = 82^\circ$ (the angle of markers R1 and R2).

the marker R2 in Fig. 3.31.

In the plots of Figure 3.33 we trace the efficiency of the transmission, reflection and absorption of the electromagnetic field as a function of the period of the MNC chain. The blue and red lines represent the zones of Brillouin of the glass substrate and air superstrate, respectively, for subsequent Bragg orders.

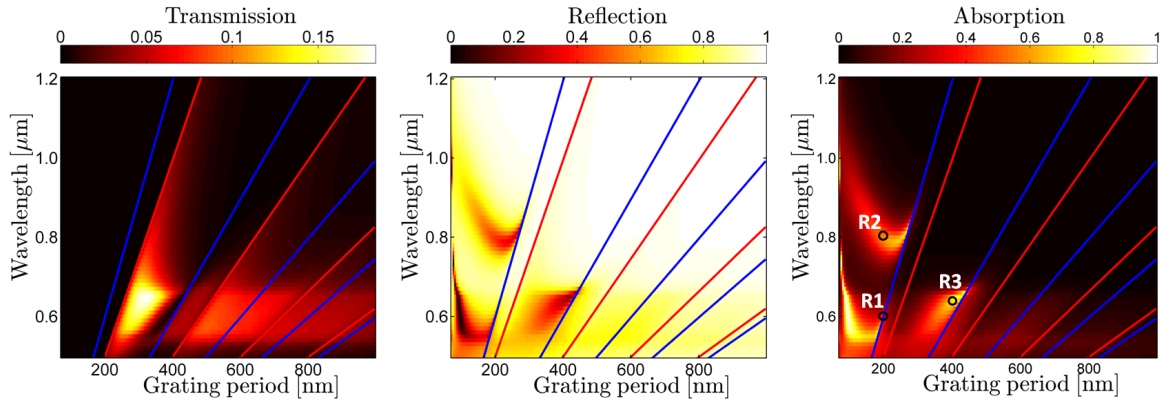


Figure 3.33: Transmission, reflection and absorption efficiency spectra as a function of the period Λ of the MNC chain. Maximum absorption values are located at $(\lambda = 560 \text{ nm}, \Lambda = 187 \text{ nm})$, $(\lambda = 830 \text{ nm}, \Lambda = 277 \text{ nm})$ and $(\lambda = 660 \text{ nm}, \Lambda = 442 \text{ nm})$.

To determine the Bragg orders as a function of the period of the chain Λ , and the incidence angle θ_{inc} , we considered that the diffraction of the incident plane wave by the

grating is described by the Bragg formula

$$\beta_{inc} - \beta_{\Lambda} = \frac{2m\pi}{\Lambda}, \quad (3.4)$$

where $\beta_{inc} = (2\pi n_{sub}/\lambda) \sin \theta_{inc}$. According to eq. (3.4), the condition to find the existence of the m th diffracted order in the substrate is $\beta_{\Lambda(m)} = -2\pi n_{sub}/\lambda$, leading to

$$\lambda = n_{sub} (1 + \sin \theta_{inc}) \frac{\Lambda}{m}, \quad (3.5)$$

and the condition for the diffracted orders in the superstrate is $\beta_{\Lambda(m)} = -2\pi n_{sup}/\lambda$, obtaining

$$\lambda = (n_{sup} + n_{sub} \sin \theta_{inc}) \frac{\Lambda}{m}. \quad (3.6)$$

As we are in the TIR regime, the transmission efficiency in the first zone of Brillouin is almost negligible. For subsequent zones of Brillouin, the diffraction orders generate a non-zero transmission, showing a maximum value above the second zone of Brillouin around $\lambda = 650$ nm. This maximum transmission band corresponds to the minimum band in the reflection curve at the second (and subsequent) zone of Brillouin. Since this mode is observable simultaneously above and below the substrate and superstrate limits, it is associated to a radiated mode.

In both reflection and absorption spectra we can distinguish two resonances in the first Brillouin zone (minimum in reflection and maximum in absorption). These resonances correspond to an excitation of the chain of nanowires. At the Bragg condition, the first resonance (shorter wavelengths values) exhibits a maximum value around a wavelength $\lambda = 560$ nm and period $\Lambda = 187$ nm, while the second one (larger wavelengths) has a maximum value at the Bragg condition around $\lambda = 830$ nm and $\Lambda = 277$ nm. In the second Brillouin zone it is also observable a third resonance, showing a maximum value in the second order Bragg condition around $\lambda = 660$ nm and period $\Lambda = 442$ nm.

To determine the nature of each one of these resonances, we plot near-field energy density maps for three different values, marked by the points $R1$, $R2$ and $R3$ in Figure 3.33 (the markers $R1$ and $R2$ are the same than in Fig. 3.31).

The resonance $R1$ is placed around $\lambda = 600$ nm and $\Lambda = 200$ nm, and as can be seen in the near-field map of Figure 3.34, a multipolar coupling takes place between the MNC, giving place to a field enhancement at the lower apexes. This is the near-field coupling of the resonance observed in the isolated nanowire (Fig. 3.29).

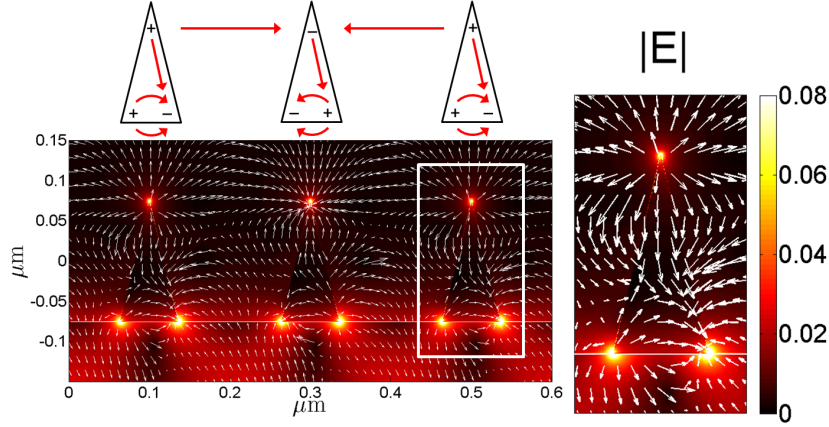


Figure 3.34: Normalized energy density maps and electric field lines distribution for the chain of MNC at the $R1$ resonance ($\lambda = 600$ nm and $\Lambda = 200$ nm).

For the resonance $R2$ placed around $\lambda = 800$ nm and $\Lambda = 200$ nm, the energy density map of Figure 3.35 shows an enhancement of the field at the top vertexes of the MNC. This mode is due to a dipolar transverse coupling between the MNC, as we can confirm by the electric field lines distribution. This field enhancement was not observable for the case of the isolated nano-cone, so it is a chain mode only achievable if the period of the structure is short enough to favor the interaction between the MNC and if we illuminate the sample with a plane wave at a grazing angle.

The third resonance $R3$, located around a wavelength $\lambda = 660$ nm and period $\Lambda = 400$ nm, is due once again to the near-field coupling of the dipolar transverse mode observed in Fig. 3.35. We can note that the electric field lines emerge-out from all the upper apexes of the MNC, in other words, all the transverse dipoles have the same orientation, with a phase difference between them of 2π rad. This is because the period to achieve this resonance is twice the period of resonance $R2$, where the transverse dipoles had a phase difference of π rad. In the base of the MNC we can observe a deformation of the electric field lines. This effect is because the near-field coupling between the MNC is weaker, and the dipolar longitudinal resonance obtained for the isolated nanocone starts to arise.

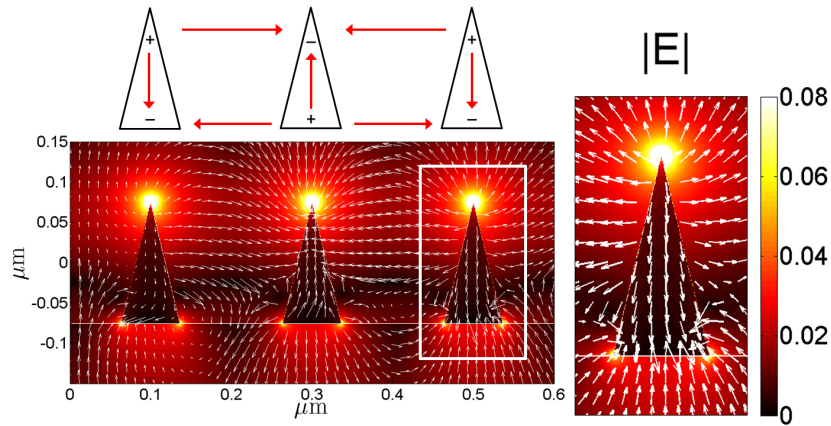


Figure 3.35: Normalized energy density maps and electric field lines distribution for the chain of MNC at the $R2$ resonance ($\lambda = 800$ nm and $\Lambda = 200$ nm).

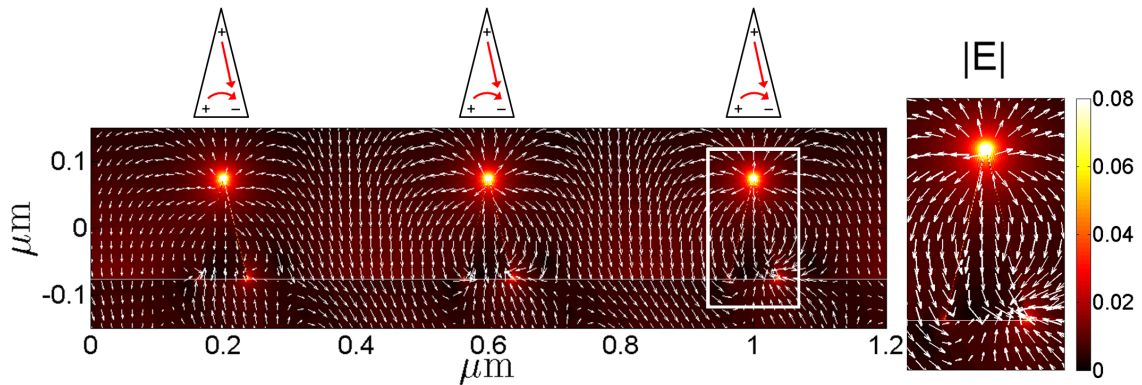


Figure 3.36: Normalized energy density map and electric field lines distribution for the chain of MNC at the $R3$ resonance, around $\lambda = 660$ nm and $\Lambda = 400$ nm.

These novel results demonstrate that the field enhancement of the MNC chain is only observable if the structure is excited from the substrate at grazing angles, and it is solely achievable if there is a near-field interaction between the MNC, i.e., if the period of the structure is shorter than the wavelength of the incident light.

This result implies that the Bloch mode of the MNC chain can be coupled to the propagative mode of a dielectric waveguide, giving place to an integrated optical device, since light will propagate through the waveguide at a grazing angle respect to the glass-air interface. Moreover, the excited Bloch mode will enhance the field at the upper apex of the MNC.

3.4.3 Periodic array of MNC in an integrated system

The integrated structure studied is schemed in Figure 3.37. It consists of a finite chain of 5 gold nanocones of height $h = 144$ nm, width $w = 72$ nm and period $\Lambda = 200$ nm, placed on top of a glass substrate of refractive index $n_{sub} = 1.5$. The superstrate is air ($n_{sup} = 1.0$). Immersed in the substrate at a distance $t_2 = 30$ nm from the interface glass-air, we place a dielectric waveguide of thickness $t_1 = 200$ nm and core refractive index $n_w = 2.0$. The thickness of the waveguide was previously determined to support the propagation of the TM₀ fundamental mode in a spectral range from 400 nm to 1.2 μ m.

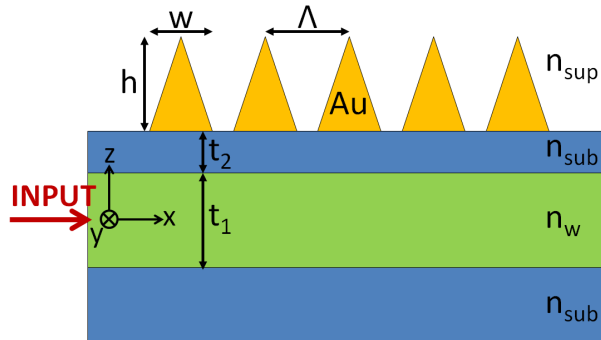


Figure 3.37: Periodic array of 5 gold nanocones of width $w = 72$ nm, height $h = 144$ nm and period $\Lambda = 200$ nm, placed on top of a glass substrate ($n_{sub} = 1.5$). At a distance $t_2 = 30$ nm from the glass-air interface is placed a dielectric waveguide of thickness $t_1 = 200$ nm and core refractive index $n_w = 2.0$. The superstrate is considered air ($n_{sup} = 1.0$).

The TM₀ mode of the dielectric waveguide is propagated in the x positive direction from the input of the waveguide at $x = 0$. We compute the transmission and reflection of the TM₀ mode respectively, at the output and input of the waveguide. We also determine the extinction (absorption plus scattering) of the system.

The plot of Figure 3.38 shows the dispersion curves of the integrated system. The blue, green and pink curves represent the light-lines of the air, glass and core of the waveguide, respectively, while the black vertical line represents the Bragg condition (edge of the first Brillouin zone). The blue triangles curve is the dispersion curve of the TM₀ fundamental mode supported by the waveguide.

The advantage of using the excitation with a dielectric waveguide, is that we can

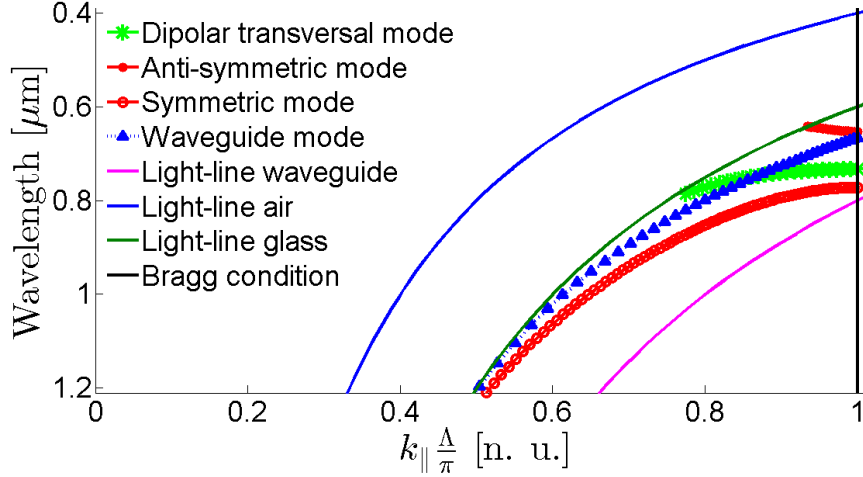


Figure 3.38: Dispersion curves of the integrated system. The dipolar transverse Bloch mode of the MNC chain (green asterisks) crosses the TM_0 mode (blue triangles) around $\lambda = 747$ nm, generating symmetric (red circles) and anti-symmetric (red dots) modes.

match the wavevectors of the propagating modes along the structure. Also, as the system is illuminated with a light beam propagating in parallel direction to the glass-air interface, we only excite the dipolar transverse Bloch mode. The green asterisks represent the dispersion curve of this mode for a chain of MNC placed on top of the glass substrate.

The dipolar transverse mode crosses the fundamental TM_0 mode of the dielectric waveguide around a wavelength value $\lambda = 747$ nm, giving place to an anti-crossing phenomenon of the symmetric (red circles) and anti-symmetric (red dots) modes. This phenomenon is a characteristic result of vertical coupling between two waveguides, in this case the dielectric waveguide and the plasmonic waveguide formed by the chain of MNC.

The field maps of Figure 3.39 show the energy density and electric field lines distribution of the anti-symmetric and symmetric modes at the Bragg condition, the first one around $\lambda = 653$ nm and the second around $\lambda = 772$ nm. As we can observe, both modes present a dipolar transverse field-lines distribution, being the field more enhanced in the anti-symmetric mode.

Now, by making use of the FMM for non-periodic structures, we compute the beam propagation for a finite array of 5 gold nanowires as depicted in Fig. 3.37. The input TM polarized mode is launched from the left side of the structure at $x = 0$, being measured the normalized reflection and transmission at the input and output of the dielectric waveguide,

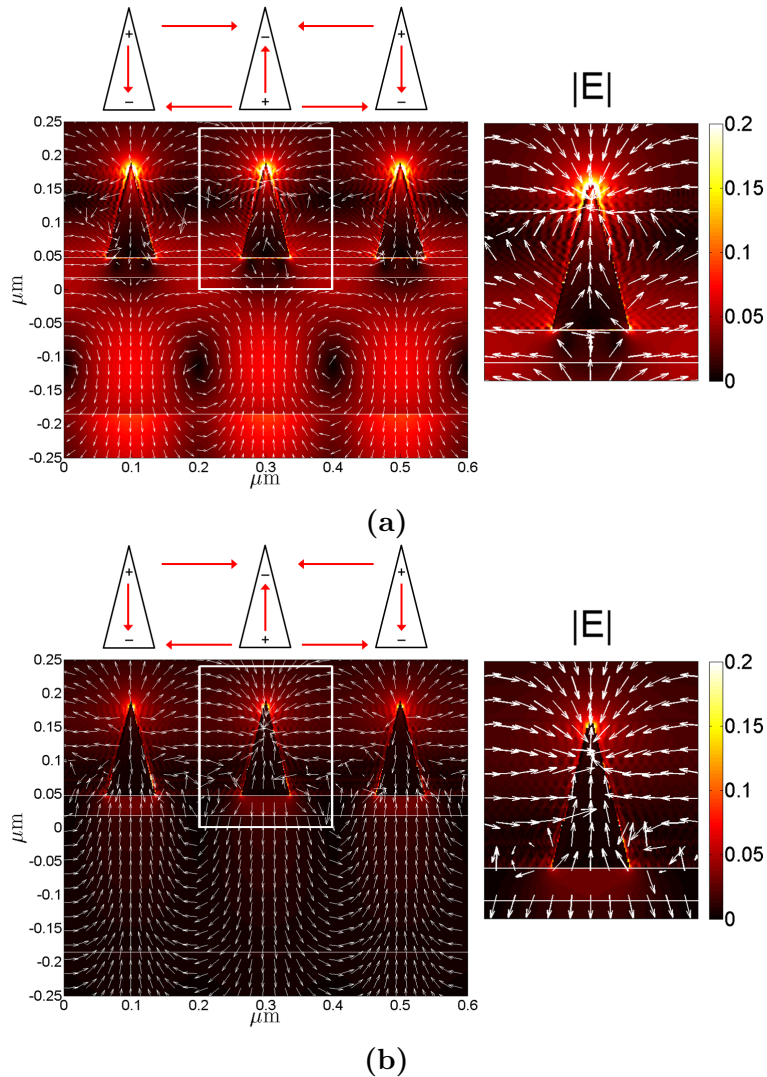


Figure 3.39: Normalized energy density maps and electric field lines distribution of the dipolar transverse Bloch mode, for an integrated chain of MNC over a dielectric waveguide. Both resonances correspond to the Bragg condition at (a) $\lambda = 653$ nm for the anti-symmetric mode, and (b) at $\lambda = 772$ nm for the symmetric mode.

respectively. Since both quantities are normalized, we also calculate the sum of the absorbed and scattered field (extinction).

The plot in Figure 3.40 shows the normalized transmission (red curve), reflection (blue dashed curve) and absorption plus scattering (black dotted curve) spectra of the electromagnetic field in the integrated structure.

The transmission curve exhibits two minimum values. The first one, around $\lambda = 650$ nm, corresponds to the Bragg reflection of the anti-symmetric Bloch mode, which is also observable as a maximum in the reflection curve around $\lambda = 660$ nm.

The second minimum in the transmission spectrum is located around $\lambda = 810$ nm, and

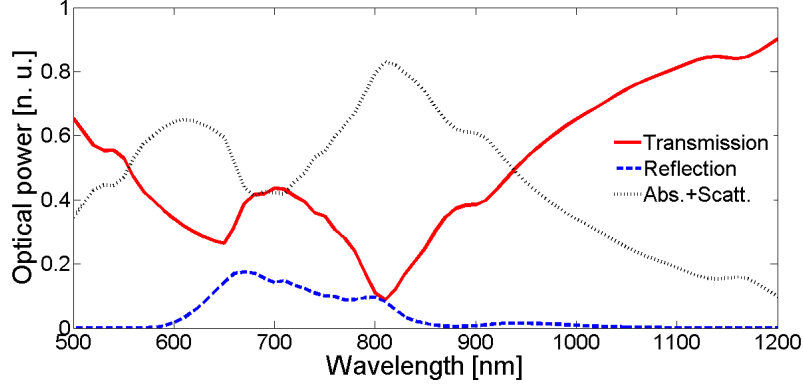


Figure 3.40: Transmission (red curve), reflection (blue dashed curve) and absorption+scattering (black dotted curve) spectra of the finite integrated system with MNC of height $e = 144$ nm and width $w = 72$ nm. At 650 nm it is observed a Bragg reflection, while the dipolar transverse mode is efficiently excited at 810 nm.

corresponds to the excitation of the dipolar transverse Bloch mode. At this same wavelength value, the absorption+scattering is maximum, having an efficiency of excitation around 82%.

In Figures 3.41 and 3.42 are plotted the $|H|$ and $|E|$ near-field maps for the minimum values of the transmission curve. A Bragg reflection behavior is observed around $\lambda = 650$ nm without an efficient excitation of the MNC; but around $\lambda = 810$ nm, we observe the near-field coupling between the MNC, with a field enhancement at the top vertexes of the structure.

These results demonstrate that a chain of MNC supports the propagation of a dipolar transverse Bloch mode that can be efficiently coupled to a dielectric waveguide placed in close proximity to the chain. Because of the perpendicular orientation of the dipoles, the field is enhanced at the apex of the tips, representing an advantage for sensing device systems.

3.5 Conclusions

By making use of the FMM, in this chapter we studied two kinds of integrated plasmonic systems, the first one consisting of a chain of gold rectangular-shaped nanowires, and the second of a chain of gold triangle-shaped nanowires.

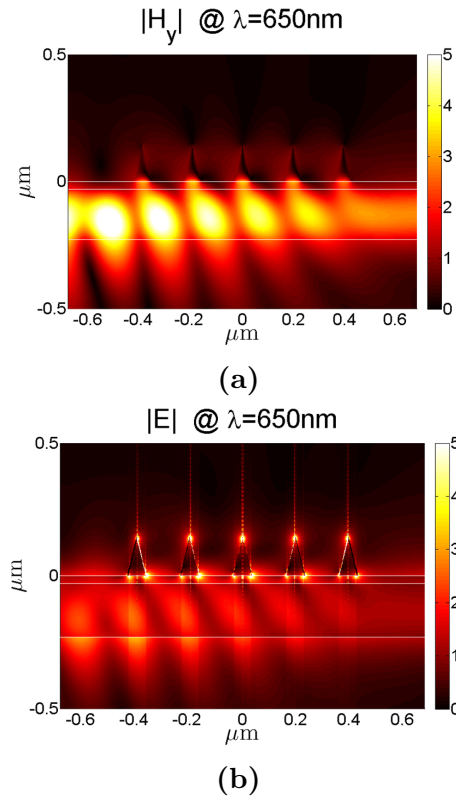


Figure 3.41: Near field maps of (a) $|H_y|$ and (b) $|E|$ at $\lambda = 650 \text{ nm}$, corresponding to the Bragg reflection of the anti-symmetric branch (minimum transmission) of the MNC structure integrated over a dielectric waveguide.

For the first case we demonstrated that a chain of MNW behaves as a plasmonic waveguide since it supports the propagation of Bloch modes. These modes were the result of a near-field interaction between the MNW. Moreover, they were confined modes that can be efficiently excited with the TM₀ mode of a dielectric waveguide placed in close proximity.

For MNW of height $e = 20 \text{ nm}$, the periodic array supported the propagation of one dipolar longitudinal Bloch mode, whereas for MNW of taller height (150 nm) the array supported quadrupolar and dipolar transverse Bloch modes.

Because the array of MNW behaves as a plasmonic waveguide, a vertical coupling between the Bloch modes and the fundamental TM₀ mode of a dielectric waveguide took place, leading to a coupling system.

Since LSP resonances are highly dependent on the shape of the nanoparticles, we presented a second structure, the case of a periodic array of gold triangle-shaped nanowires (nanocones).

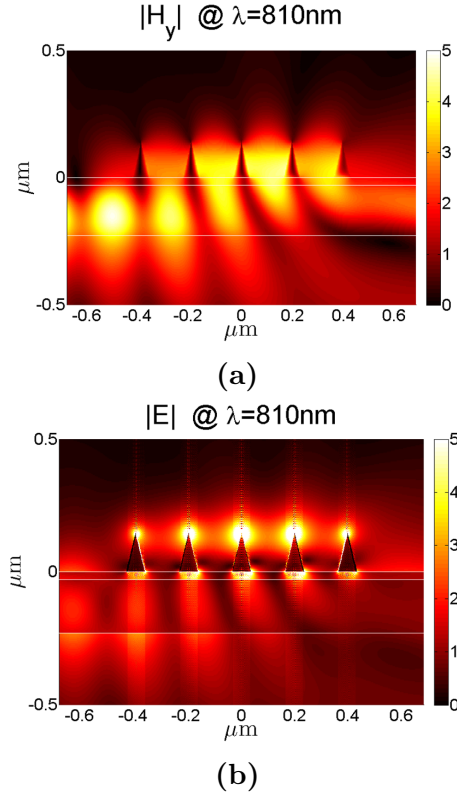


Figure 3.42: Near field maps of (a) $|H|$ and (b) $|E|$ at $\lambda = 810 \text{ nm}$. The dipolar transverse mode is efficiently excited with the TM_0 fundamental mode of the dielectric waveguide, resulting in a field enhancement at the top vertexes of the MNC.

It was observed that for a single nanocone illuminated from a glass substrate, the LSP resonance produced a field enhancement on the upper vertex of the tip. This resonance was achieved when the light impinged the nanowire in the total internal reflection regime.

Then, when a periodic array was studied, we observed that the nanocones chain supported multipolar and dipolar transverse modes. The later enhanced the field at the top vertex of the cones, like a tip effect. Also, this mode was only excited when the light coming from the substrate was at a grazing angle.

Thus, by placing a dielectric waveguide in the substrate, the dipolar transverse mode was efficiently excited with the TM_0 fundamental mode of the waveguide, generating once again a vertical coupling between them.

For both kind of structures, the transmission spectra measured at the end facet of the dielectric waveguide exhibited a minimum value at the LSP resonance wavelength. This property can be applied to create an integrated sensing device for biological or chemical substances.

To experimentally corroborate this coupling mechanism, in the following chapter we present the experimental demonstration of the excitation of the dipolar longitudinal LSP resonance, when a periodic array of gold nanowires is excited with the fundamental TM₀ mode of a dielectric waveguide immersed in a glass substrate. The fabrication parameters as well as the measurements techniques are also explained.

Chapter 4

Experimental results

In the previous chapter were presented some numerical results that suggest that a periodic array of metallic nanoparticles integrated on top of a dielectric waveguide can be applied in the detection of chemical or biological substances, or as a localized source to enhance the optical field in a small region of the space. To validate these predictions, in this chapter we present a series of experimental results that confirm the capability of the FMM method in the design and analysis of an integrated plasmonic structure.

To this purpose, we firstly design an integrated structure able to support the propagation of the dipolar longitudinal mode in a periodic array of gold nanowires placed on top of an ion exchanged waveguide (Figure 4.1). The characteristics of this kind of waveguides is briefly introduced in the first section of this chapter.

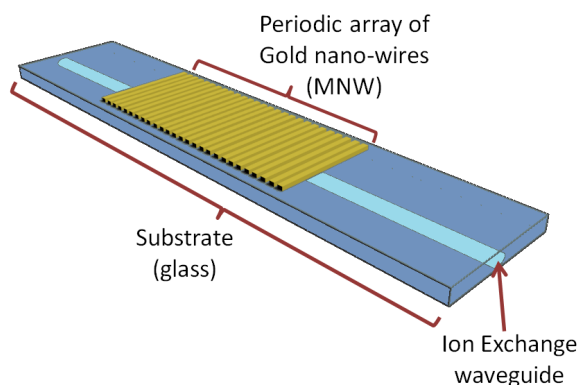


Figure 4.1: Scheme of the fabricated sample, consisting in a periodic array of gold nanowires placed on top of a glass substrate containing an ion exchanged waveguide.

Once analyzed the characteristics of the designed structure, we present a general expla-

nation of the ion exchange waveguides, as well as the detailed description of the electron-beam lithography process used for the nanofabrication of the samples.

The samples are then characterized in far-field by measuring their transmission spectra and we compare them with numerical results obtained with the FMM. Also, by making use of the near field scanning optical microscopy (NSOM) technique, we measured the near-field interaction of the optical field in the fabricated structure.

A deep analysis of the experimental results confirms that the FMM is a trustful numerical tool for the design and study of the modes propagation in integrated plasmonic structures.

4.1 Ion exchanged waveguides

A waveguide is a physical structure that allows the propagation of electromagnetic waves. Among the several types of waveguides can be found the so-called glass waveguides, which are formed by a well defined channel where the substrate (glass), present a gradient of the refractive index (Figure 4.2)

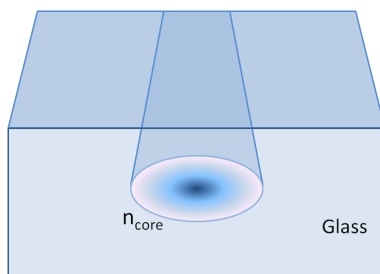


Figure 4.2: Ion exchange waveguide. The core is a local gradient of the refractive index.

Due to their low-cost fabrication, their compatibility with optical fibers, low propagation losses and high stability, the glass waveguides are frequently used for integrated optics applications, like multiplexers for optical communications, or sensing devices for chemical or biological applications.

This kind of waveguides are fabricated by using different techniques, like ion exchange or ion implantation. However, ion exchange is the most popular technique, being particularly attractive for particles manipulation on surfaces.

Glass ion exchange consists in the local substitution of relatively mobile ions (typically Na^+) originally in glass by other ions with different size and polarizability, giving place to a change of the refractive index in the selected regions, allowing patterning of waveguiding regions into planar substrates (Tervonen and S. Honkanen, 2013).

Normally, the ion exchange fabrication process is made in one or two general process steps, depending on the desired properties. The first step is to introduce the ions into the glass substrate. This process can be made by thermal ion exchange from a molten salt source (like silver nitrate $AgNO_3$) through a patterned mask, or also by field-assisted ion migration from a molten salt or a thin metallic film to an anode.

Once established the ions in the region of interest, the concentration of the ions can be modified in order to tailor the waveguide properties. This modification can be done by thermal annealing to redistribute the ions by diffusion inside the glass. This annealing produces buried waveguides, since the ions originally in glass are replaced back into the substrate at the surface, while the ions forming the waveguide are diffused deeper. This process can also be done by electric field-assisted burial.

The thermal diffusion processes do not require a sophisticated laboratory equipment, but they must be done with a precise temperature control to properly melt the salt source. For field-assisted processes with molten salts, the processing equipment is somehow more complicated, since electrical contacts must be done to the anode and cathode sides of the substrate, and these need to be maintained in electrical isolation.

As the waveguides can be wider than the ion source width due to lateral diffusion, narrow lithography linewidths are needed for single-mode waveguides. In particular, for deeply buried single-mode waveguides, the linewidth of the mask may need to be between 1 and 2 μm . Buried waveguides are immune to surface defects and environmental perturbations, and they can be efficiently coupled to optical fibers.

The most widely used ions in the fabrication process are Ag^+ and K^+ . Potassium ions are used to produce low-loss surface waveguides, but because of the stress suffered by these ions, they are not efficient to make buried waveguides. Silver ions are more efficient for waveguide fabrication. They allow to obtain relatively higher refractive indexes. However, high concentrations of silver can produce metallic clusters in glass, leading to waveguide

losses.

To characterize the optical properties of the glass waveguides, it is often used the prism coupling technique, since it is possible to excite selected modes in the waveguide in order to measure individual mode propagation losses; the intensity distribution for each excited mode can then be observed at the waveguide output.

4.2 Design of the integrated plasmonic structure

In chapter 3 we demonstrated that a periodic array of gold nanowires of short height supports the propagation of a dipolar longitudinal mode, and that this mode could be efficiently coupled to the TM₀ fundamental mode of a dielectric waveguide placed in close vicinity to them.

Using the FMM method, we now study the modes supported by an infinite periodic array of gold nanowires of height $e = 30$ nm, placed on top of a semi-infinite dielectric substrate of refractive index $n_{sub} = 1.505$, similar to the effective index of the core of an ion-exchanged waveguide. Also, an ITO layer of thickness $h = 10$ nm is placed between the MNW and the substrate (Figure 4.1). The reason for placing this layer is explained in the section corresponding to the nanofabrication process.

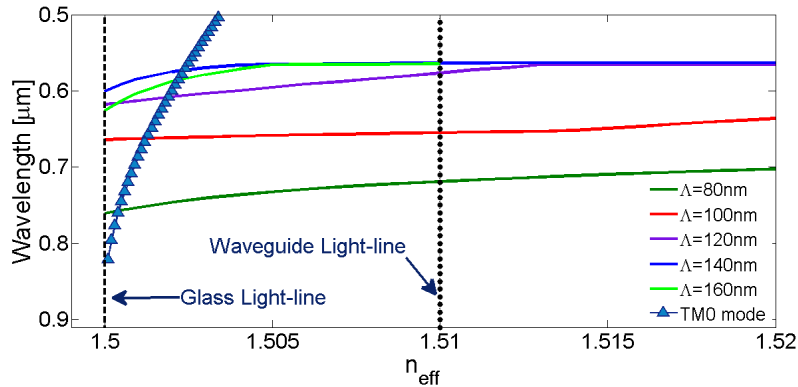


Figure 4.3: Dispersion curves of periodic arrays of MNW of width $w = 70$ nm and height $e = 30$ nm and periods $\Lambda = \{80, 100, 120, 140, 160\}$ nm, placed on top of a dielectric substrate with refractive index $n_{sub} = 1.505$. Between the substrate and the MNW chain, is placed an ITO layer of thickness $h_2 = 10$ nm. The fundamental TM₀ mode of an ion-exchanged waveguide of thickness $h = 1800$ nm is represented by the blue triangles.

In Figure 4.3 we present the dispersion curves of the effective index of the mode

supported by the infinite chain of MNW for different periods: $\Lambda = 80$ nm (dark green), $\Lambda = 100$ nm (red), $\Lambda = 120$ nm (purple), $\Lambda = 140$ nm (blue), and $\Lambda = 160$ nm (light green). The fundamental TM₀ mode of the ion-exchanged waveguide is represented with the blue triangles curve. Light-lines of glass and waveguide are also plotted.

From these curves, we note that the modes supported by the MNW of periods longer than $\Lambda = 80$ nm are coupled to the TM₀ mode of the ion-exchanged waveguide. When the period of the MNW is greater than $\Lambda = 140$ nm, the resonance converges to a constant wavelength value around $\lambda = 560$ nm.

The physical interpretation of these results becomes clear by recalling the characteristics of SPP and LSP waveguides (Chapter 1). It is obvious that if the gap between the MNW is reduced (shorter periods), the MNW chain tends to a thin metallic layer, so the dipolar longitudinal mode will tend to the SPP mode of an IMI waveguide (Figure 1.6). In opposition, when the gap between the MNW is increased, there will not be any longer a near-field interaction between them, and the dispersion curve will correspond to the mode of the LSP resonance of an individual nanowire (as the case of the single metallic nanocone (Chapter 3)). This is the effect observed in the dispersion relations of Fig. 4.3: when the period of the MNW is shorter (below $\Lambda = 80$ nm) the excited mode is a SPP resonance, whereas for periods greater than $\Lambda = 140$ nm, the dispersion curves converge to the LSP resonance of a single nanowire.

Between these two limits exists an optimal case when the MNW are still interacting between each other, and could be efficiently coupled with the TM₀ mode of the ion-exchanged waveguide. According to the dispersion curves, this optimal situation is achieved when the period of the chain of MNW is around $\Lambda = 100$ nm, and a wavelength value around $\lambda = 662$ nm.

In order to experimentally verify these results, we fabricated an integrated system by using a glass substrate containing ion exchange waveguides, and patterning a periodic structure of gold nanowires by electron-beam lithography. The fabrication process is detailed in the following section, as well as the obtained structure.

4.3 Fabrication of the plasmonic integrated structure

To fabricate the sample depicted in Figure 4.1, we used electron-beam lithography, which consists in the application of a focused electron beam to imprint a pattern or structure on a material sensitive to electric charges (resist). Thus, the electron beam changes the solubility of the resist, permitting the selective removal of the exposed or non-exposed regions of the resist by making use of a solvent (developer).

There are two kind of resists, positive and negative resists. The first ones are those in which the portion exposed to the electrons-beam becomes soluble to the developer solvent, and the non-exposed areas remains insoluble. The negative resists inversely behaves, i.e. the regions exposed to the electrons-beam remain insoluble. Among the resists used for lithography processes, the PMMA (Poly-methyl methacrylate) is the most popular, which is a transparent synthetic polymer that can be customized to behave as a positive or negative resist.

The electrons beam is generated by an electronic microscope that accelerate and focus the electrons in a small region by making use of magnetic condensers (often named magnetic lenses in analogy to the optical microscopes), reaching up to 20 nm of printing resolution.

The electron-beam lithography is performed in several steps: patterning, developing, metal deposition, and lift-off. However, it is a state of the art process, and the fabrication parameters can substantially change depending on the desired pattern.

An important aspect to take into account in the patterning process, is the diffusion of the electrons on the surface. If a dielectric material is going to be patterned, it is necessary to add a conductive layer to avoid charges effects. For this process, generally are used thin Aluminum layers that can be removed later with chemical substances. Nevertheless, there is a risk that these substances have a non-desired effect on the substrate, or also to leave metallic residual traces on the substrate surface. One way to avoid this problem, is by making use of a charge dissipation liquid polymer named ESPACER[®], which is an aqueous solution without organic solvents. The practicality of this liquid is that it can be

deposited over the sample by spin-coating and it can be removed with water.

The detailed process for the patterning of the metallic nanowires chain on top of the ion exchanged waveguides, is enlisted below and schemed in Figure 4.4.

1. Sample cleaning

The first step is to clean the surface of the glass substrate containing the ion exchanged waveguides. To do this, the substrate was immersed in a solution of water and detergent DECON90, and it was subjected to ultrasound for 3 minutes. After removing the detergent with water, the sample was cleaned with Isopropyl alcohol (IPA), and dried with air (Fig. 4.4a).

2. ITO deposition

To improve the diffusion of electrons in the lithography process, we placed on the surface of the substrate a thin layer of Indium Tin Oxide (ITO), which is a conductive material. The layer was deposited by electron-beam vapor deposition, fixing its thickness to 10 nm. Then, the sample was heated with a hot plate at 220° C by 15 minutes (Fig. 4.4b).

The heating process improves the electrical and optical characteristics of the ITO, it becomes less resistive and more transparent, and since the thickness of the layer is not so large, it will not significantly modify the properties of the ion exchanged waveguides. The heating process increases the roughness of the ITO layer which could generate non-desired scattering effects. For this reason, the temperature and heating time must be adjusted according to the size of the sample (Hu et al., 2004).

3. PMMA and ESPACER[®] deposition

Once placed the ITO layer, by using a spin-coating machine we deposited a 200 nm thickness layer of a solution of PMMA in MIBK (proportion 30 g/L), which was heated in the hot plate at 180° C during 10 minutes. This process allows to evaporate the acetone solvent and solidify the polymer. The resist used was a positive resist. Once annealed the sample, we also deposited by spin-coating an ESPACER[®] layer

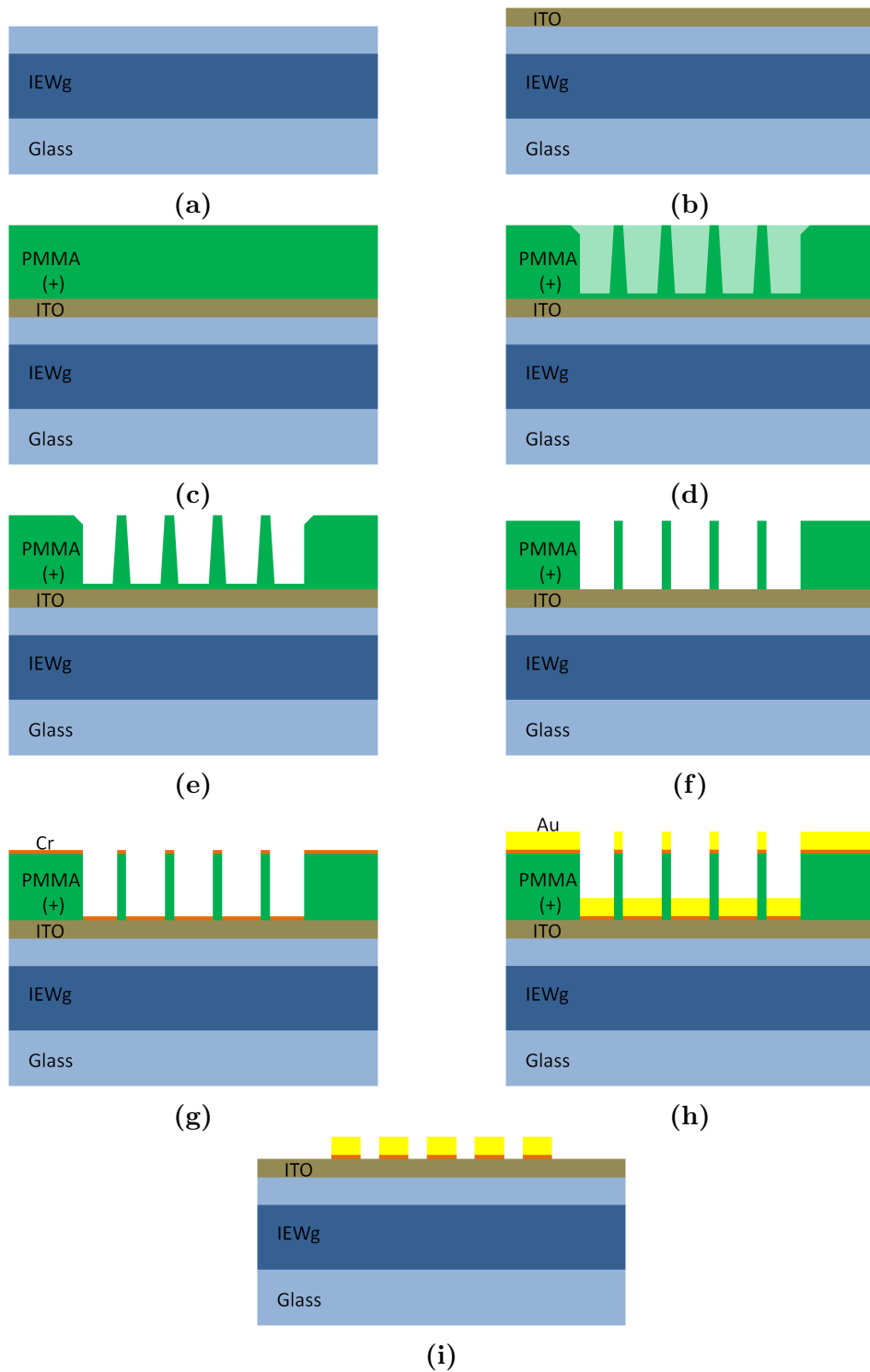


Figure 4.4: Sample fabrication by e-beam lithography. (a) Sample cleaning. (b) Deposition of the ITO layer. (c) Deposition of PMMA and ESPACER[®] layers. (d) E-beam lithography to change the solubility of the PMMA. (e) Development of the sample. (f) Reactive ion-etching process to remove the PMMA traces. In (g) and (h), deposition of Cr and Au thin layers. (i) Lift-off process to remove the PMMA and leave only the MNW on the substrate.

¹ to ensure the charges diffusion and lead to a better imprinting of the MNW (Fig. 4.4c).

4. Electron-beam lithography

The prepared sample was placed inside the electronic microscope (e-line Raith) to make the e-beam lithography process. Even when the control system and the computational software of the microscope is quite simple, the lithography process for the fabrication of the MNW is an state of the art process, since many parameters must be taken into account in function of the used materials, like the energy of the electrons beam, the writing speed and the correction of the aberrations of the beam. This calibration process must be done in close vicinity to the lithography area, being exposed these testing areas to the e-beam. This calibration can cause the apparition of additional motifs in the samples surface. The used parameters for the lithography process were a dose factor of 650 pC/cm, step-size of 0.0096 μm and beam energy of 10 keV (Fig. 4.4d).

5. Sample development

After the lithography, the sample was developed, i.e. we removed the polymer from the exposed areas to the e-beam. To do this, the sample was firstly dipped 2 minutes into water to remove the ESPACER[®] from the substrate. Then, the sample was immersed in a solution of Methyl Isobutyl Ketone (MIBK) with Isopropyl alcohol (IPA) during 1 minute gently whirling the container to remove the resist. Immediately after, the sample was dipped into IPA pending 20 seconds to stop the action of the developer liquid. This is a similar process to the one used in analog photography -which is now less used-. In order to improve the developing process, the developer liquid (MIBK:IPA) was used at a low temperature of 5° C (Fig. 4.4e).

6. Descum process

The developing process can leave resist residuals in the exposed areas, leading to problems in the nanowires fabrication. To remove all these traces, the sample was

¹The spin coating parameters for the ESPACER[®] layer deposition were the same than those of the PMMA. The thickness of the ESPACER[®] was smaller than the PMMA due to the viscosity of the liquid.

exposed to a plasma reactive ion etching process. This process also reduced the roughness of the PMMA walls, increasing the quality in the MNW structure. The etching plasma was created with Oxygen ions and the sample was exposed for 5 seconds (Fig. 4.4f).

7. Thin film deposition

As the size of the imprinted channels was very small, the gold is not be efficiently attached to substrate, and for this reason, it must be employed an intermediary layer that acts like a glue. A useful material to this purpose is Chromium (Fig. 4.4g).

Thus, by electron-beam thermal deposition we placed a 3 nm thickness layer of chrome (Cr) over the imprinted face, and then a gold (Au) layer of the desired thickness, having care that the thickness of the metallic layer was smaller than $1/3$ of the resist layer. That is, if the resist thickness is of 200 nm, the height of the nanowires could not be taller than 60 nm, otherwise the resist would not be properly removed in the lift-off process (Fig. 4.4h).

8. Lift-off

The last step consist in the removal of the remaining resist on the sample, such that it also be removed the metal out of the channels. This process is known as lift-off, and it was done by leaving the sample immersed in acetone during 24 hours. After this time, the PMMA was diluted and only the metallic motifs remained. To clean the sample, we took-out the sample of the acetone and we washed it with IPA, and finally air dried. This is a very crucial step in the fabrication process. If the PMMA is not uniformly deposited, the solvent does not adequately penetrate into the resist, and the metallic layer could not be properly removed (Fig. 4.4i).

A useful technique to help in the removal of the resist, was to place the sample in the acetone container and place it during one or two seconds in the ultrasound, and then we cleaned it with IPA. However this process must be carefully done, otherwise the MNW can be also removed.

4.3.1 Fabrication problems

The process previously described is not simple, it requires time to make several proofs and to study the different variables involved in each step.

We observed that there was a compromise between the width of the MNW and the separation between them: if the width of the nanowires was reduced, the gap increased, and vice versa. This was because in the lift-off process if the gap between the MNW was reduced, the solvent could not penetrate into the channels, and if their width was reduced, the contact area with the substrate was diminished, making them easily removed from the substrate. In our case, the minimum width achieved for the MNW was of 65 nm, and the minimum gap of 90 nm.

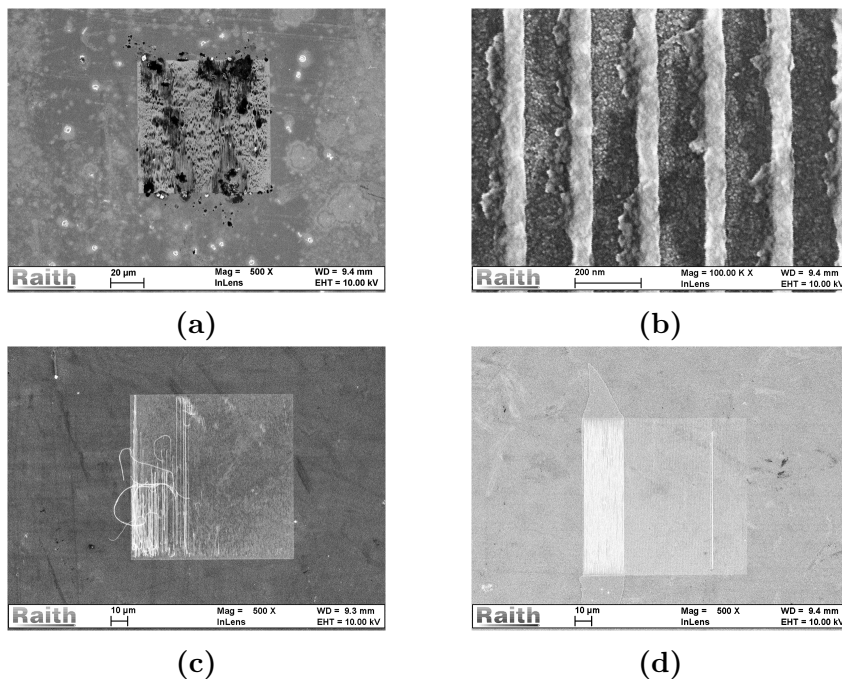


Figure 4.5: *Lithography problems. (a) Bad annealing of the PMMA, (b) sample fabrication without RIE process, (c) excess of time in the ultrasound bath after lift-off, and (d) inaccurate lift-off.*

As the period of the MNW chain was really small, their height could not be taller than 50 nm. If their height/width aspect ratio is larger, the MNW are easily removed in the lift-off process, or they lean to the sides.

Other problem linked to the fabrication process, is when depositing the PMMA by spin-coating the layer was not uniform in the extremities of the substrate: at the edges of

the sample the thickness was thicker than at the center due to the viscosity and surface tension of the resist. For this reason, the lithography must be done in the center of the substrate.

We show some illustrations related to the fabrication problems in the images of Figure 4.5. These images were taken by electronic microscopy.

4.3.2 Nano-fabrication results

To fabricate the integrated system of MNW on top of a dielectric waveguide, we used a glass substrate of 1 cm by 1 cm, containing several ion exchanged waveguides, each one of width $\sim 2 \mu\text{m}$ and a separation of $50 \mu\text{m}$ between them (measures obtained with an optical microscope). The glass waveguides are single mode having a cut-off wavelength around $\lambda = 780 \text{ nm}$ for the fundamental TM_0 mode, and $\lambda = 820 \text{ nm}$ for the fundamental TE_0 mode.

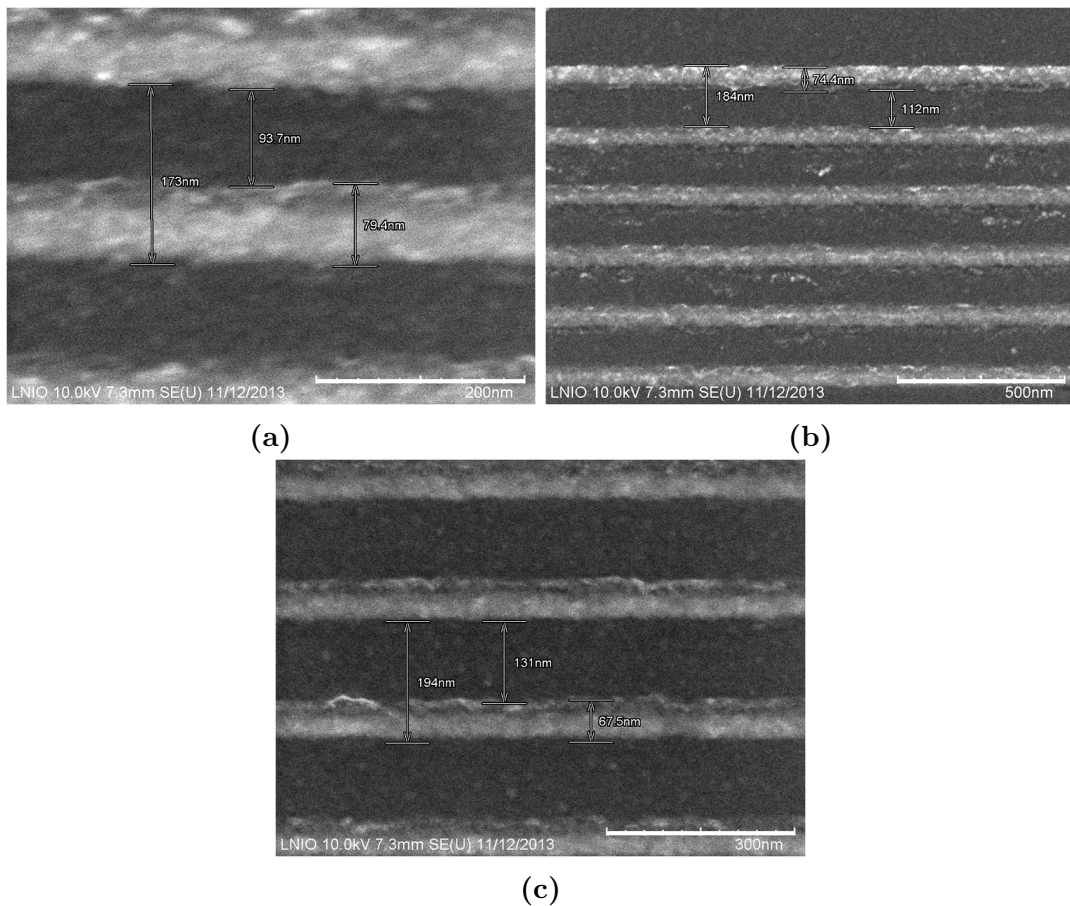


Figure 4.6: Electronic microscope images of the MNW fabricated corresponding to the structure (a) T1, (b) T2 and (c) T3.

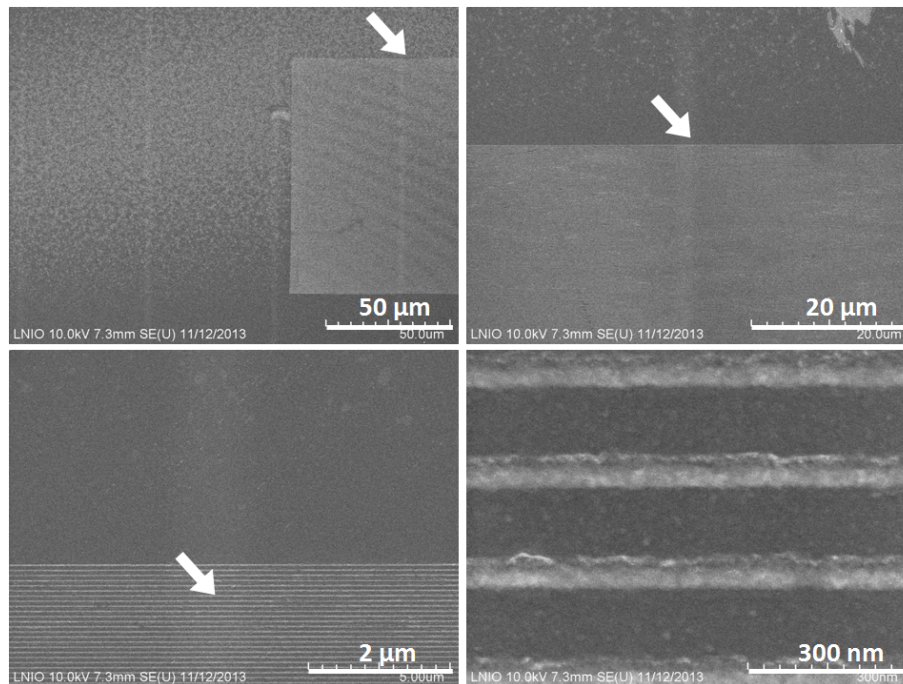


Figure 4.7: Progressive zoom images captured with the electronic microscope for the structure $T3$. The MNW chain is perpendicularly placed to the ion-exchanged glass waveguides.

The structures of gold nanowires that we fabricated are shown in Figures 4.6. The height of the MNW is of 30 nm, being elaborated three different periods for the structures, labeled as $T1$ (Fig. 4.6a), $T2$ (Fig. 4.6b) and $T3$ (Fig. 4.6c). The values of the width w , gap g , period Λ and length L of each MNW, are shown in Table 4.1. Each one of the periodic arrays contains 500 nanowires.

Structure	w	g	Λ	L
T1	79 nm	94 nm	173 nm	300 μm
T2	74 nm	112 nm	186 nm	600 μm
T3	67 nm	131 nm	198 nm	300 μm

Table 4.1: Values of width, gap, period and length of the three different arrays of MNW fabricated on top of the glass substrate.

4.4 Experimental results

4.4.1 Far-field characterization of the sample

As we demonstrated in Chapter 3, if at the input of the dielectric waveguide it is launched a TM polarized wave, at the output face will be observed a minimal transmission at a wavelength value corresponding to the excitation of the LSP resonance of the MNW chain. So, in order to characterize our integrated structures, we performed far-field transmission measurements with the experimental setup schemed in Figure 4.8.

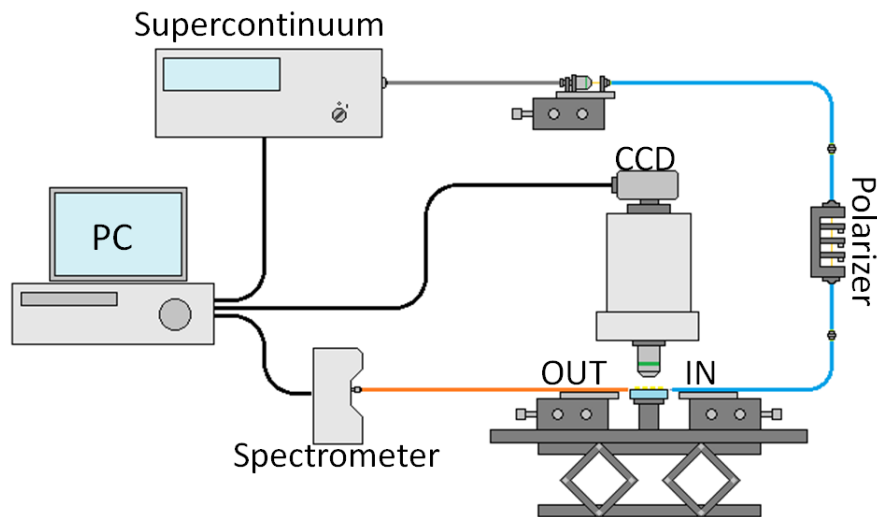


Figure 4.8: Scheme of the experimental setup for far-field transmission measurements.

The setup consist of broad-band spectrum beam generated with a super-continuum laser (Fianium SC 450 – 4) that emits light in the spectral range from 450 nm to 1800 nm. The light emanating from the source is coupled with a microscope objective (Olympus 20× 0.40NA) mounted in a multi-axial micro-displacement platen, to a single-mode polarization maintaining optical fiber (PM630-HP). This fiber is plugged to a three stages polarization rotator (OZ-Optics FPR-11-11-780-5/125-P-P-1&2&3-40-3A3A-3-1) to select the TM polarization of the beam. The output of the polarization rotator, is then plugged to a single-mode polarization maintaining lensed fiber (OZ-Optics TPMJ-3A-633-4/125-0.25-30-2-11-2). The micro-lens at the fiber output allows to have an efficient coupling of the light to the glass waveguides (Fig. 4.9a).

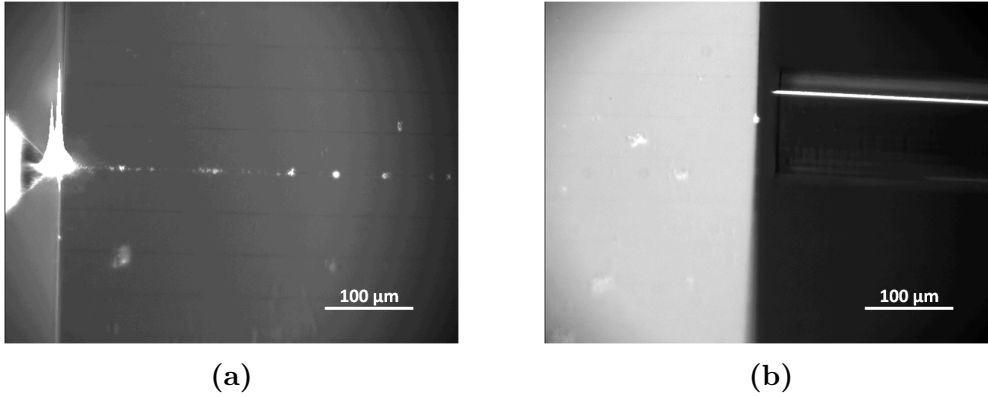


Figure 4.9: (a) Micro-lensed fiber at the input of the glass waveguides. (b) Multimode fiber at the output of the waveguide.

At the output of the glass waveguide is placed a multimode fiber (AFS50/125Y) to collect the light (Fig. 4.9b). The end facet of the multimode fiber is plugged to an spectrometer (Ocean Optics Maya 2000Pro) able to detect in the spectral range from 200 to 1105 nm, with a bandwidth resolution of 0.41 nm.

In order to align the to the input and output of the sample, this setup is mounted on an optical microscope stage (objective Olympus 20× 0.40NA) assembled to a CCD camera (Andor Luca S). To adjust the focal length of the objective, the sample and the platens used to displace the fibers are mounted onto a motorized lab-jack.

Results

To observe the spectral response of the structures, it is necessary to normalize the spectra of the glass waveguides containing the MNW chains, to a reference waveguide, i.e., to a waveguide without nanowires. This reference waveguide help us in the determination of the cut-off wavelengths for the TE and TM fundamental modes. The plot in Figure 4.11, shows the normalization spectra for TM polarized light. In the curve we observe two main maximal values, corresponding to the excitation of the TM and TE fundamental modes of the glass waveguide. The first one exhibits a cut-off wavelength at $\lambda = 780$ nm, whereas the second is cutting at $\lambda = 820$ nm. This result is natural, since the TE mode can be propagated to longer wavelengths than that for the TM mode. It must be remarked that the TE mode cannot be completely removed with the polarization rotator, but its intensity is much more less than the one of the TM₀ mode.

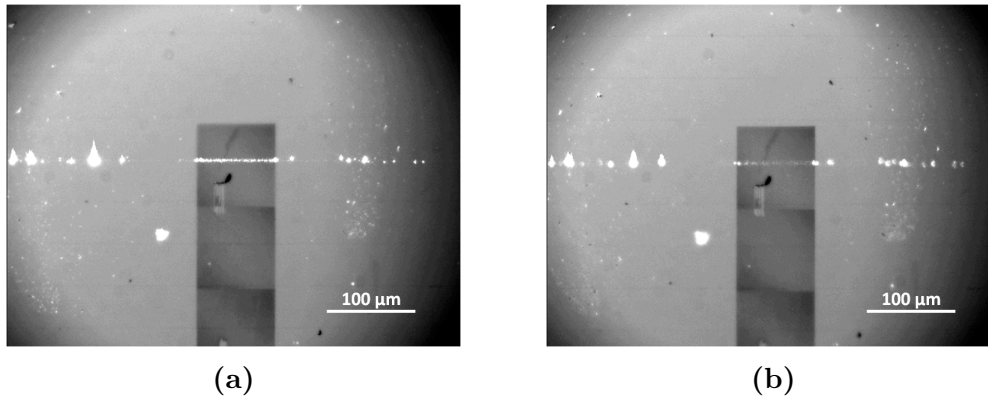


Figure 4.10: Top view of the MNW when they are excited with (a) the TM₀ fundamental mode and (b) with the TE₀ mode. The LSP resonance of the MNW chain is not excited under TE polarization.

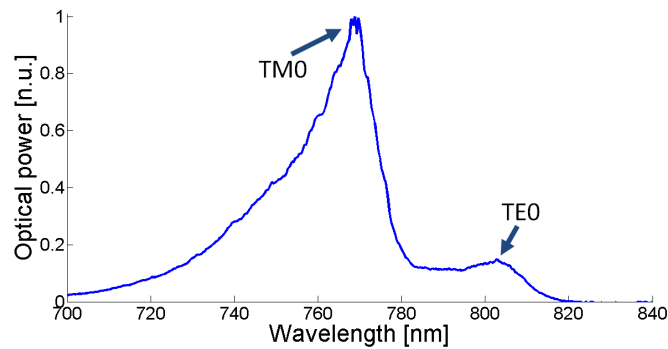


Figure 4.11: Normalized spectrum of the reference waveguide. The cut-off wavelength of the TM₀ mode is at $\lambda = 780$ nm, while for the TE₀ mode is at $\lambda = 820$ nm.

The plots in Figures 4.12 - 4.14 show the transmission spectra experimentally obtained for each one of the structures $T1$, $T2$ and $T3$, respectively. These spectra are already normalized to the reference waveguide. The blue dots curve are the experimental data, whereas the green curve is a polynomial fitting of these data.

For the three types of structures, the transmission curves exhibit a local minimal value placed at 785 nm. This result is because the portion of the TE polarized light propagating through the waveguide is being scattered because of the presence of the MNW chain, but it is not related to a propagating mode.

The excitation of the LSP modes corresponds to the first minimum value observed in the three spectral curves. For the $T1$ -type structure (Fig. 4.12), the minimum in transmission is observed around a wavelength value $\lambda = 702$ nm, for the $T2$ structure (Fig. 4.13) around $\lambda = 675$ nm, and for the $T3$ (Fig. 4.14) around $\lambda = 668$ nm.

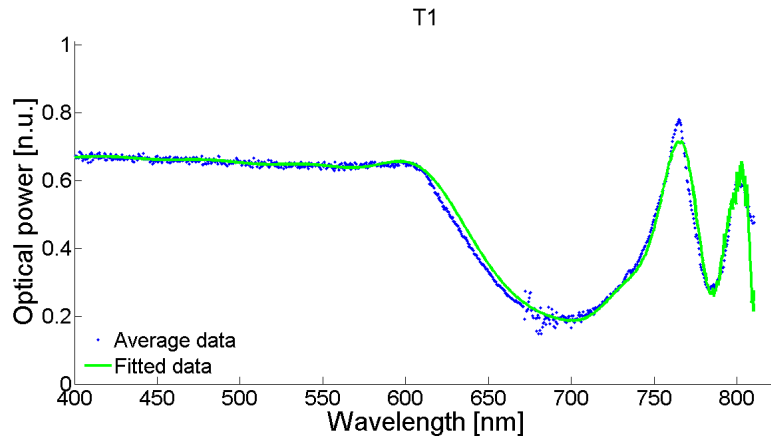


Figure 4.12: Normalized transmission spectrum of the T1 type structure. The minimal transmission is observed around a wavelength value $\lambda = 702$ nm.

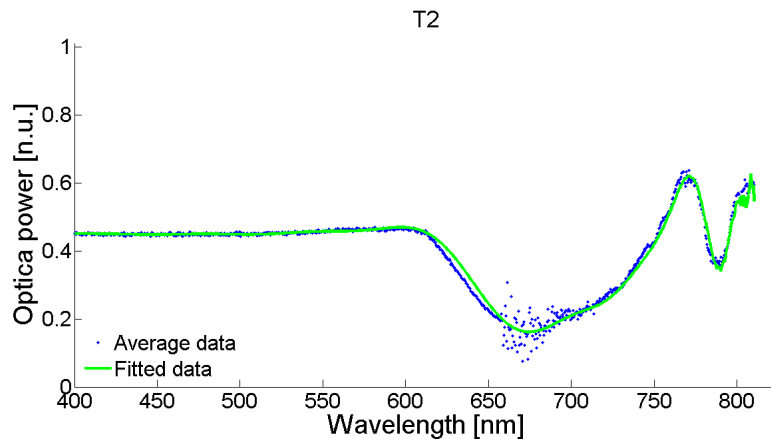


Figure 4.13: Normalized transmission spectrum of the T2 type structure. The minimal transmission is observed around a wavelength value $\lambda = 675$ nm.

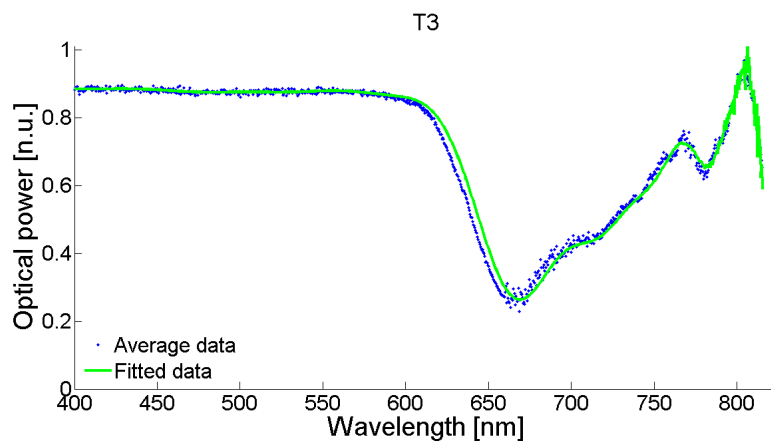


Figure 4.14: Normalized transmission spectrum of the T2 type structure. The excitation of the LSP propagating mode occurs around $\lambda = 668$ nm.

This means that the wavelength of the LSP resonance mode is inversely proportional to the period of the structure. That is, when the period of the structure is increased, the LSP resonance mode is blue-shifted. This is an expected result for dipolar LSP resonances in

coupled metallic nanoparticles (Kelly et al., 2003; Christ et al., 2003). Moreover, according to the numerical results presented in Chapter 3, the height of the MNW (30 nm) is not enough to support neither a quadrupolar nor a dipolar transversal propagating mode.

Comparison to numerical results

To theoretically corroborate the experimental spectra, we performed numerical computations by making use of the FMM.

We must remark that the ion-exchanged waveguides were not fabricated in our laboratory, they were developed by the Teem Photonics company. No specifications of the thickness, burial depth or effective refractive index of the glass waveguide were provided. The only known parameter of the waveguides was the transmission spectra measured in our facilities.

Then, in order to have an approximation of these parameters, numerical computations were performed by using the cut-off wavelength value of the TE and TM fundamental modes supported by the waveguide, and using standard refractive index values for the substrate and the core.

According to our computations, for a fixed index of refraction of the substrate of 1.5 (glass), effective index core of 1.505, and a burial depth of 100 nm, the thickness of the waveguides core must be of 1.8 μm . Obviously these parameters are not very precise, and play an important role in the near-field interaction of the evanescent wave with the MNW chain.

However, since the numerical method computes the effective index of the multilayered system, the transmission spectrum is not importantly affected by these parameters, but it changes abruptly when changing the parameters of the metallic nanowires (width, period and height) as well as the thickness of the ITO layer.

Then, using the glass waveguide parameters previously mentioned, and the geometric parameters of the MNW obtained by direct observation with electron-beam microscopy (Table 4.1), we performed the numerical computations. The obtained normalized transmission and reflection spectra are depicted in Figures 4.15, 4.16 and 4.17.

Due to computational limitations, the numerical spectra were performed for a finite

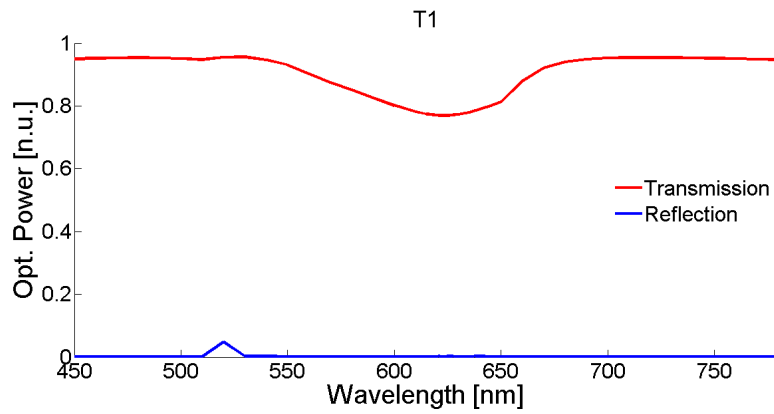


Figure 4.15: Transmission (red) and reflection (blue) spectra obtained with the FMM for the T1 type structure. The minimal transmission is observed around a wavelength value $\lambda = 625$ nm.

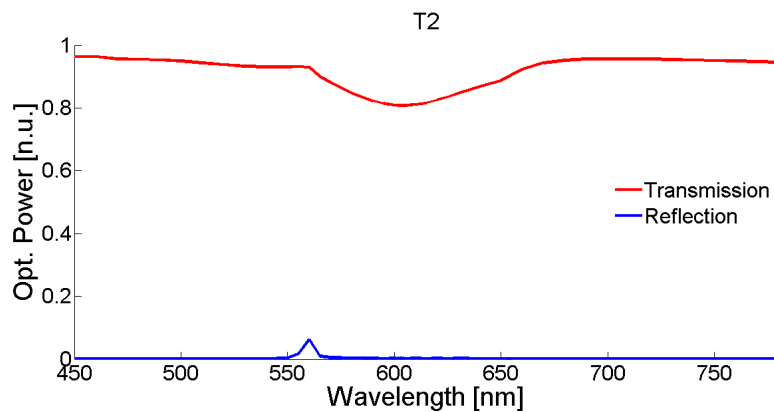


Figure 4.16: Transmission (red) and reflection (blue) spectra obtained with the FMM for the T2 type structure. The minimal transmission is observed around a wavelength value $\lambda = 605$ nm.

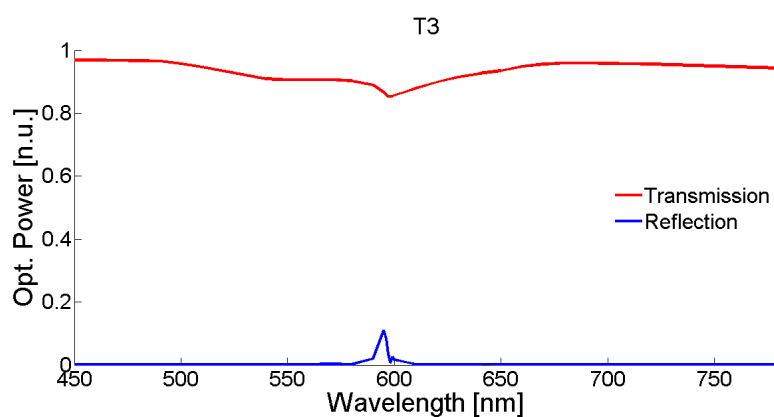


Figure 4.17: Transmission (red) and reflection (blue) spectra obtained with the FMM for the T3 type structure. The minimal transmission is observed around a wavelength value $\lambda = 598$ nm.

chain of 200 gold nanowires instead of the 450 of the fabricated samples, resulting in a higher transmission with respect to the experimental curves. The values of the dielectric

constant of the gold were taken from (Palik, 1985).

For the $T1$ structure, the LSP resonance corresponding to the excitation of the dipolar longitudinal mode is located around a wavelength value of $\lambda = 623$ nm (minimal transmission), while the Bragg reflection is observed around $\lambda = 520$ nm (Fig. 4.15). The $T2$ structure present a minimum value in transmission around $\lambda = 604$ nm, and the Bragg reflection is placed around $\lambda = 560$ nm (Fig. 4.16).

Finally, the $T3$ type structure presents a minimum transmission value around $\lambda = 598$ nm and the Bragg reflection is located around 595 nm (Fig. 4.17). Since the Bragg reflection and the dipolar longitudinal mode excitation wavelengths are nearly placed, the broadband of the curve is reduced in comparison to the $T1$ and $T2$ spectra. This behavior was also observed in the broadband of the experimental spectra.

As we also observed in the experimental results, when increasing the period of the structure, the LSP resonance of the MNW is blue-shifted, i.e. the wavelength resonance is reduced.

A notable remark when comparing the experimental and numerical spectra, is the difference in the resonance wavelength values, $\Delta\lambda$, as presented in Table 4.2. The difference between these values is almost constant for the three structures, and it is about 70 nm.

Structure	Experiment	FMM	$\Delta\lambda$
T1	702 nm	623 nm	79 nm
T2	675 nm	604 nm	71 nm
T3	668 nm	598 nm	70 nm

Table 4.2: Comparison of the experimental and numerical wavelengths values for the MNW resonances. The difference between the numerical and experimental values of the LSP resonance wavelength is around 70 nm.

The causes of this wavelength values are due to several facts. The first one is that the fabricated samples are not perfect, they present a roughness that affects the LSP resonance. Also, as we have mentioned before, the numerical parameters of the thickness, burial depth and effective refractive index of the core were estimated by assuming standard values. Other reason that is really important is that the dielectric constant values of the gold used in the numerical simulations were taken from reference (Palik, 1985), and they do not correspond precisely to the real values of the gold used in the fabrication.

Additionally, the maximal resolution of the electron-beam microscope used to measure the fabricated structures is of 20 nm, meaning that the width and period of the structure can also vary. The last important difference is that the calculations were performed for a two-dimensional structure invariant in the out-of-plane direction, while the experimental structure is a three-dimensional finite structure.

However, the shape of the transmission spectra for both experimental and theoretical results, is almost the same for the three cases. This result reveals that the physical behavior of the near-field interactions between the MNW and the dielectric waveguide is well described by the numerical method. That is, the Fourier modal method is a good numerical approach in the design and theoretical characterization of integrated plasmonic structures.

4.4.2 Near-field observations

To characterize the sample in the near-field regime, we used the NSOM technique. The Near-field Scanning Optical Microscopy (NSOM) is a useful tool of sub-wavelength resolution for the observation of electromagnetic fields in nanostructured systems. It breaks the far-field resolution limit by exploiting the properties of the evanescent waves. This resolution is achieved by placing a nanotip probe near to the analyzed sample. Then, the tip converts the evanescent field bounded to the surface of the sample in a scattered field, which is collected, and detected in the far field (Figure 4.18).

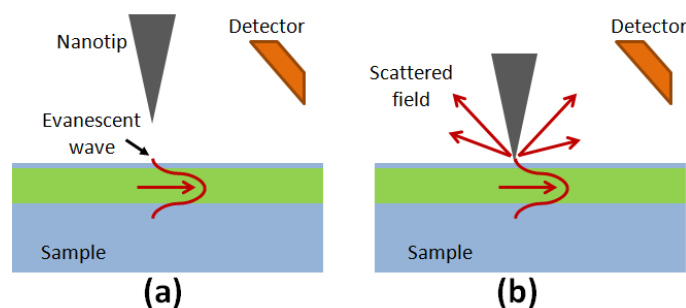


Figure 4.18: Operation principle of the NSOM technique. (a) Out of the core of the waveguide, an evanescent field is also propagated. (b) Approaching a nanotip to the surface of the sample, the evanescent wave is scattered, resulting in a perturbation of the transmitted or scattered optical field, as a function of the frequency of the nanotip.

The operating principle for the apertureless-NSOM is as follows. A sample is placed under an Atomic Force Microscope (AFM) in tapping mode, that measures the topography of the sample. The nanotip used in the AFM scatters the evanescent wave into the free space, and this light is collected with a microscope objective and coupled to a single-mode optical fiber. This collected signal is then measured with an Avalanche Photo-Diode (APD) that transforms the optical field into an electrical signal. Since the scattered field is modulated by the frequency of oscillation of the nanotip, using a lock-in amplifier both signals, the scattered field and the nanotip frequency, are demodulated to obtain the intensity of the optical field propagating in the sample. The configuration is schemed in Figure 4.19.

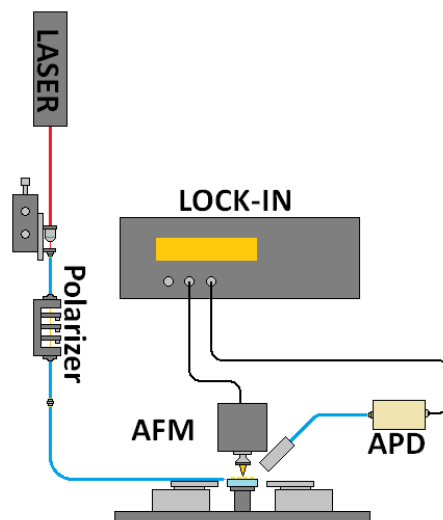


Figure 4.19: Schematic representation of the apertureless NSOM. The optical field scattered by the nanotip, is collected with an optical fiber and then converted into an electrical signal with an APD. This signal is demodulated with a lock-in amplifier using as reference the frequency of the nanotip.

A variation of the apertureless NSOM is the so-called Heterodyne detection (H-NSOM) (Balistreri et al., 2000; Abashin et al., 2006), a technique that permits the near-field measurement of both amplitude and phase of the optical field under investigation. The principle operation of the H-NSOM technique is depicted in Figure 4.20.

Unlike the apertureless-NSOM, the H-NSOM uses a reference signal to interfere with the modulated field scattered by the sample (Balistreri et al., 2000). The beam coming out from the laser source is splitted with two acousto-optic modulators (AO). The first AO split the beam in two diffracted orders, and both of them are then transmitted to a second

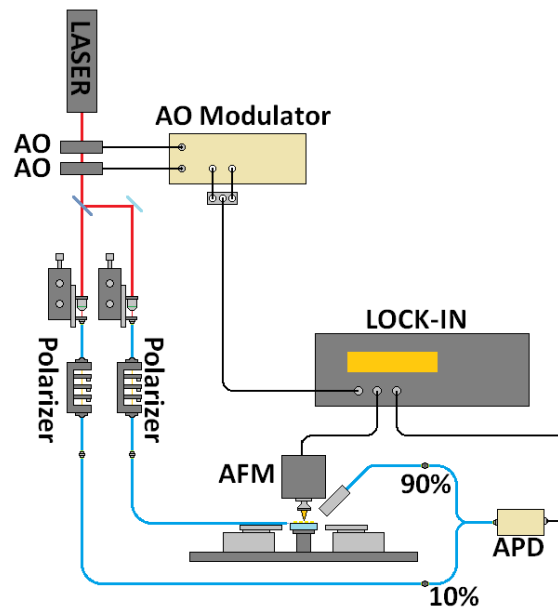


Figure 4.20: Schematic representation of the H-NSOM. The beam of light coming out from the laser is divided in four diffracted orders with two crossed AO. The fundamental order is chosen as probe signal, while the fourth order is used as reference signal. The probe signal is perturbed by the nanotip, and the scattered field is combined with the reference beam; this interference is converted into an electrical signal with an APD. The oscillation frequency of the nanotip is subtracted from the AO modulation signal, serving as demodulation frequency for the signal coming from the APD. The interference between the reference and the probe signal provides the information from the phase of the optical field in the scanned region.

AO perpendicularly oriented respect to first one. This second AO divide the first two diffracted orders into four diffracted orders. The specular component (the zero diffracted order) is used to be transmitted to the sample (probe signal), whereas the +1 order of the second AO obtained from the -1 order of the first AO, is used as the reference signal.

With the use of optical fibers, the beam is coupled to the ion-exchanged waveguide of the sample, and the scattered light is collected with a microscope objective and coupled to a single-mode optical fiber. Then, by making use of a fiber coupler, we make interfere the scattered field with the reference beam. This optical interference is converted to an electrical signal with an APD. Once again, the AFM nanotip perturbs the scattered field with the same frequency of the oscillation of the tip. The AFM signal is then subtracted from the AO modulation signal, and it is mixed in the lock-in amplifier to demodulate the measured scattered signal. This heterodyne configuration allows us to detect the optical signal at lower modulation frequencies, and since we have an interferometric system, it is

possible to recover the amplitude and the phase of the optical field propagating through the structure (Abashin et al., 2006).

Ion exchanged waveguide

By making use of the H-NSOM configuration, we obtained amplitude and phase near-fields maps for a sample containing an ion exchanged glass waveguide. The results are shown in Figure 4.21. Using the discrete Fourier transformation, it was possible to determine the effective index of the optical mode supported by the waveguide. For this particular sample we obtained an effective index of $n_{wg} = 1.527 \pm 0.17$, as depicted in Figure 4.22.

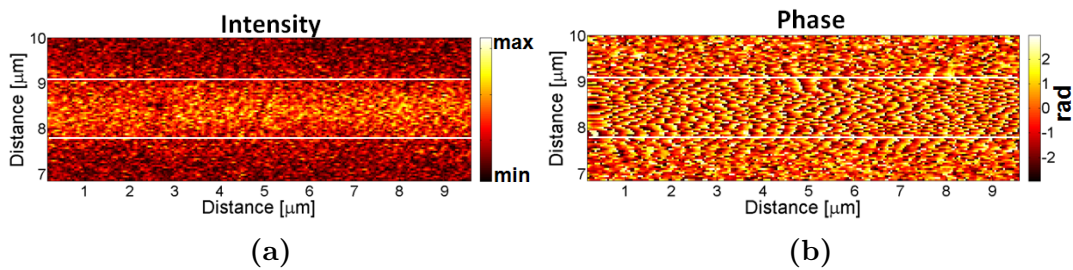


Figure 4.21: (a) Intensity and (b) phase near-field maps measured with the H-NSOM technique, for an ion-exchanged glass waveguide.

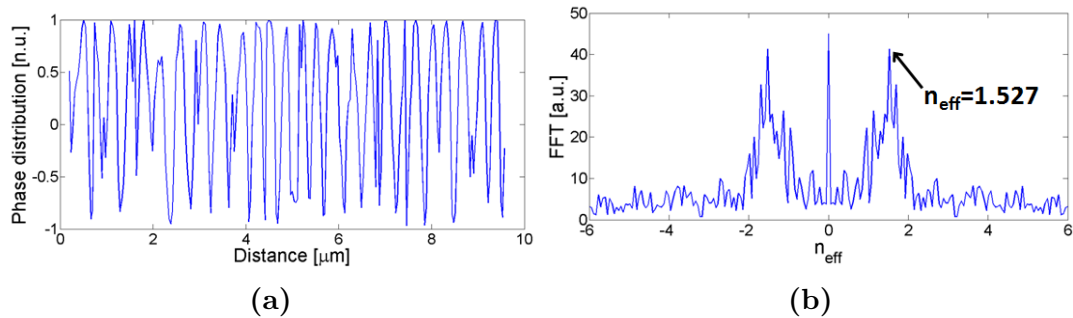


Figure 4.22: (a) A profile along a line in the phase map is plotted. (b) By taking the Fourier transform of this profile, we can deduce the effective index of the mode propagating through the waveguide. For this case, the obtained value was $n_{eff} = 1.527 \pm 0.17$.

These results were obtained by using a He-Ne laser ($\lambda = 632.8$ nm) with an optical power of 10 mW. However, the optical signal coupled to the waveguide was not enough to obtain a better resolution in the phase maps. Unfortunately, we did not account with a coherent source of higher optical power in order to observe a better modulation of the

field. As will be shown in the following section, this effect was crucial in the determination of the near-field measurements for the sample containing the gold nanowires chain.

Integrated plasmonic structure

The optical power of the He-Ne laser that we used for the heterodyne detection was not enough to observe the excitation of the plasmonic resonance in the MNW chain. This was because when passing the beam through all the optical components there are many losses, and also, since the gold nanowires absorb the electromagnetic field and reflect it to the input of the waveguide, it was not possible to observe the perturbation of the nanotip to the transmitted light in the APD. For this reason it was necessary to use a more intense source.

To excite the MNW and observe the scattered light from the nanotip, we used a laser diode operating at a wavelength $\lambda = 660$ nm, with an optical power of 75 mW. However, this source was not useful for the heterodyne detection, because its coherence length was not long enough to observe the interference between the reference and the probe beams. For this reason, instead of using the H-NSOM, we made use of the apertureless NSOM. With this setup we could only perform only intensity observations.

The results plotted in Figures 4.23a and 4.23b, show the near-field maps of the topology and intensity, respectively, directly obtained with the apertureless-NSOM. We obtained these images by measuring consecutive regions of the integrated plasmonic structure, each one of large $8 \mu\text{m}$. In the intensity map, we can clearly note the exaltation of the optical field in the grating region.

In the intensity map (Fig.4.23b), it is observed a pattern of oblique fringes in different regions of the map. This fringes pattern is the result of the interference of the probe beam propagating through the structure and the background field collected with the fiber. This background signal contains the information of the scattered field perturbed by the AFM tip, as well as the static background noise. However, as detailed in reference (Blaize et al., 2002), we can recover the information of the effective index of the propagating from these fringes pattern, by making use of the Fourier transform of the intensity map.

The images in Figure 4.23c show the bidimensional fast Fourier transform (FFT) in

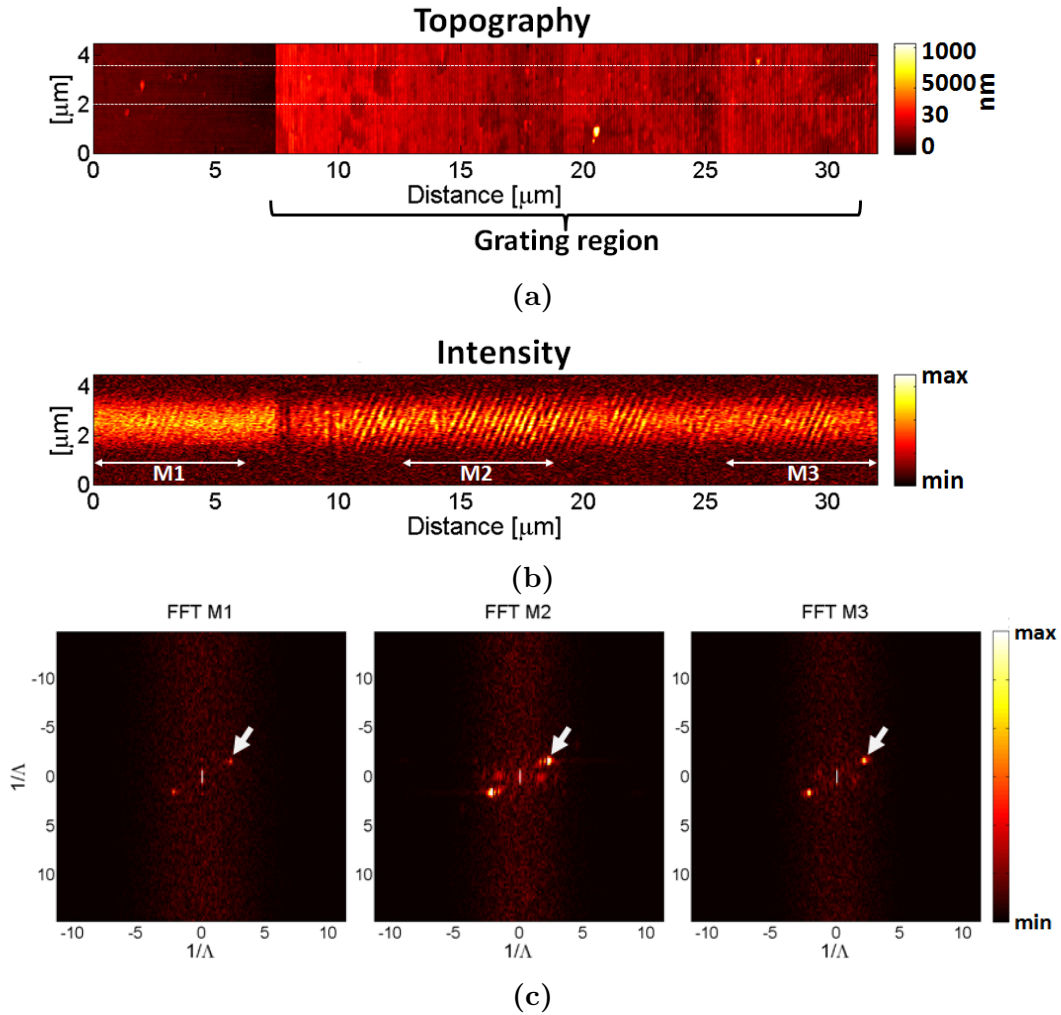


Figure 4.23: (a) Topography and (b) intensity near-field maps of the integrated plasmonic structure obtained with the NSOM technique. The grating region starts at a distance around 8 μm . (c) FFT images of the zones M1, M2, and M3 marked in (b). The frequency corresponding to the fundamental mode remains almost unchanged in the three zones.

the regions marked as $M1$, $M2$ and $M3$ in the intensity map. Each region consist of an area of 6 μm (horizontal) by 4.5 μm (vertical). The $M1$ region correspond to a zone without MNW. The region $M2$ is placed around 6 μm and 18 μm , respectively, from the beginning of the MNW grating.

In each one of the FFT images, we can observe a spatial frequency that remains almost in the same position along the vertical direction (pointed with arrows). This spatial frequency results from the fringes pattern and it corresponds to the detection of the TM_0 fundamental mode propagated in the ion exchanged waveguide. The corresponding effective index of this frequency can be obtained by multiplying the free-space wavelength

of the source $\lambda = 660$ nm by the measured spatial frequency, i.e. $n_{eff} = \lambda/\Lambda$. In each one of the regions $M1$, $M2$ and $M3$, the effective index of the TM0 mode has a value around $n_{eff, TM0} = 1.496 \pm 0.073$. The precision of this measurements is related to the resolution of the images (256 pixels each $10 \mu\text{m}$). This effective index value is in agreement to the one measured for the ion exchanged waveguide without MNW presented in the previous section ($n_{eff} = 1.527 \pm 0.17$).

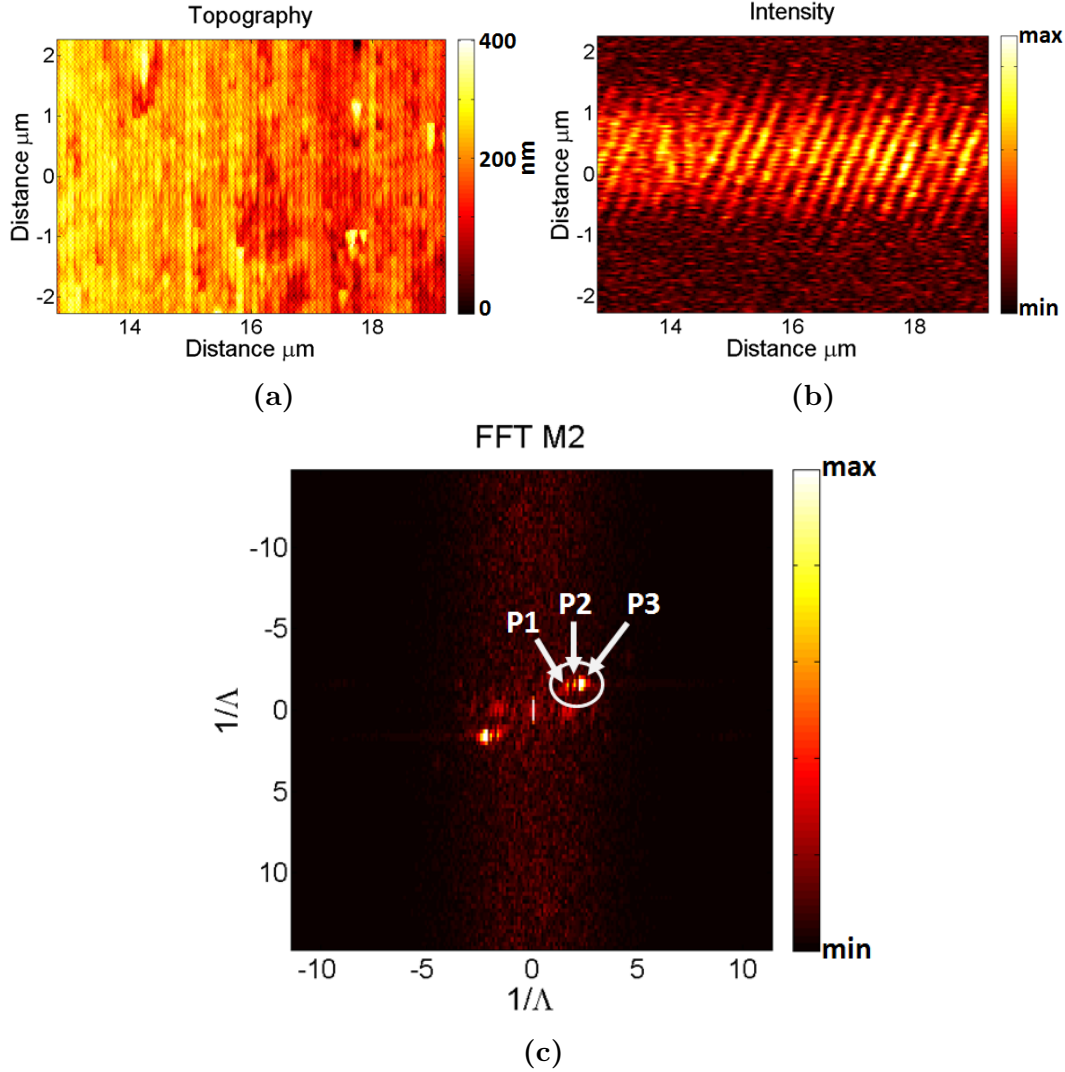


Figure 4.24: (a) Topography and (b) intensity NSOM near-field maps of the $M2$ region. (c) The corresponding FFT of this region reveals the presence of three spatial frequencies marked as $P1$, $P2$ and $P3$. They correspond, respectively, to the light-line of the substrate, a substrate radiated mode and the TM0 mode.

Regarding the FFT map corresponding to the $M2$ region, we can observe two more spatial frequencies near to the one of the TM0 mode. These frequencies are marked as $P1$ and $P2$ in the FFT image of Figure 4.24c. The spatial frequency $P1$ corresponds to a

leaky mode radiating both substrate and superstrate, having an effective index $n_{\text{eff},\text{sup}} = 1.058 \pm 0.073$, near to the light-line of the superstrate. The spatial frequency $P2$ has an effective index $n_{\text{eff},\text{rad}} = 1.35 \pm 0.073$. This value is above the light-line of the substrate, since it has a lower value than the refractive index of the glass ($n_{\text{sub}} = 1.5$). Then, the $P2$ value corresponds to a leaky mode radiating into the substrate.

The $P1$ and $P2$ modes disappear after a few microns inside the grating region. This suggests that they are excited only at the entrance of the grating. In region $M3$, the remaining excited mode is the TM_0 fundamental guided mode. This behavior is expected since all grating diffracted orders are forbidden because of the small period of the grating.

Despite the good extinction of the transmission spectrum (Fig.4.13), no local enhancement of the field is observed in the near-field maps. This is corroborated by the FFT images, where the higher spatial frequency harmonic corresponds to the TM_0 guided mode. This suggest that the MNW are barely excited by the waveguide. The extinction at the waveguide output is thus due to an cumulative effect of the LSP resonances. Then we cannot observe the manifestation of a mode propagating along the chain of MNW, neither a beating pattern nor directional coupling.

A fine analysis of the dispersion curves of Fig.4.3, shows that when the period of the MNW is increased above 120 nm, the dispersion curves converge to an horizontal asymptote line that corresponds to decoupled LSP resonances characterized by a zero group velocity.

To confirm this results, in the following section we perform an spectral analysis of a periodic array of MNW placed on top of a dielectric medium, as a function of their period, considering an illumination by a TM polarized plane wave at a grazing angle.

Interpretation of the experimental results with the FMM

To verify our previous conclusions, we performed a spectral study of the transmission, reflection and absorption of the optical field, as a function of the period of the grating with the FMM, like in the case of the gold nanocones analysis.

To do this parametric study, we considered a structure consisting of a semi-infinite substrate of refractive index $n_{\text{sub}} = 1.52$ (the effective index of the ion exchanged wave-

uide). On top of the substrate, we placed an ITO layer of thickness 10 nm, and then we placed an infinite periodic array of gold nanowires. The width of the MNW was fixed at the value obtained for the fabricated sample and their height to $e = 30$ nm. We varied the period of the grating, Λ , to observe the spectral response of the structure when it was illuminated from the substrate with a TM polarized plane wave forming a grazing angle of 82° relative to the normal at the surface. The superstrate was considered air.

The plots in Figures 4.25, reveal that for periods larger than $\Lambda = 90$ nm, the absorption of the MNW starts to increase, but for periods larger than 120 nm, the wavelength corresponding to the maximum value of the absorption remains almost unchanged.

This suggest that above this period, the absorption is driven by the individual LSP resonances of the MNW, and that the waveguiding properties of the MNW chain are lost. This means that there is no near-field interaction between subsequent nanowires, and then, we cannot expect an efficient coupling with the TM₀ mode of the the ion-exchanged waveguide placed in close vicinity to the grating.

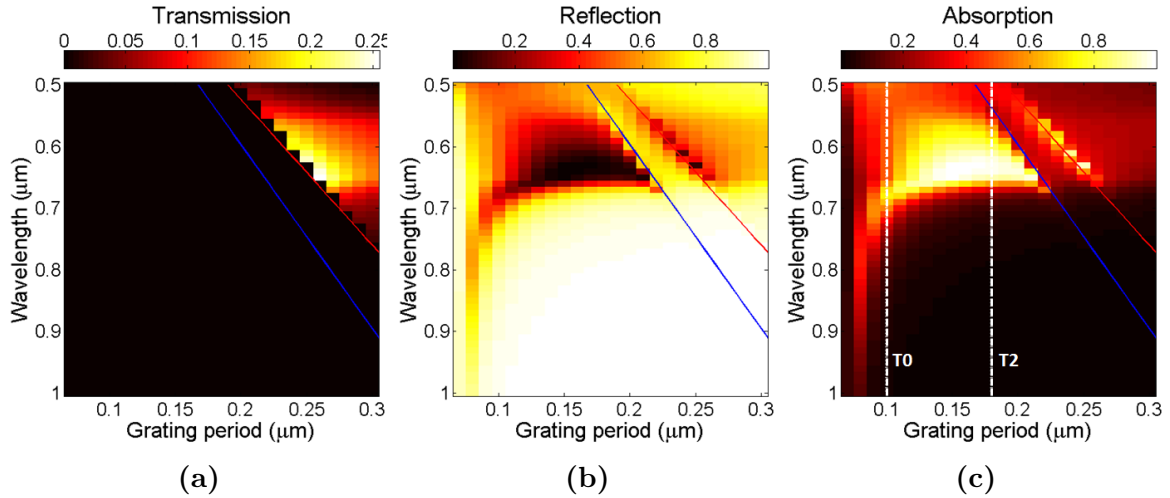


Figure 4.25: (a) Transmission, (b) reflection and (c) absorption spectra for an infinite periodic array as a function of the period when illuminating from the substrate with a TM polarized plane wave at a grazing angle of 82° respect to the normal of the surface. For periods larger than 120 nm, the absorption band remains almost unchanged, meaning that no dipolar coupling between the MNW is expected, only their LSP excitation is achieved. The blue and red lines correspond to the Bragg condition for the substrate and ITO layer, respectively.

Finally, by making use of the aperiodic FMM, we simulated the beam propagation along a finite array of 200 MNW for both periods, excited at a wavelength value of $\lambda = 685$

nm (the wavelength resonance for the efficient excitation of the dipolar longitudinal mode). We observe that for the period of the fabricated sample ($\Lambda = 186$ nm) there is no efficient coupling of the TM₀ mode of the ion-exchanged waveguide with the chain of MNW (Figure 4.26b), while for a period of $\Lambda = 100$ nm, the interaction becomes clear (Figure 4.26a).

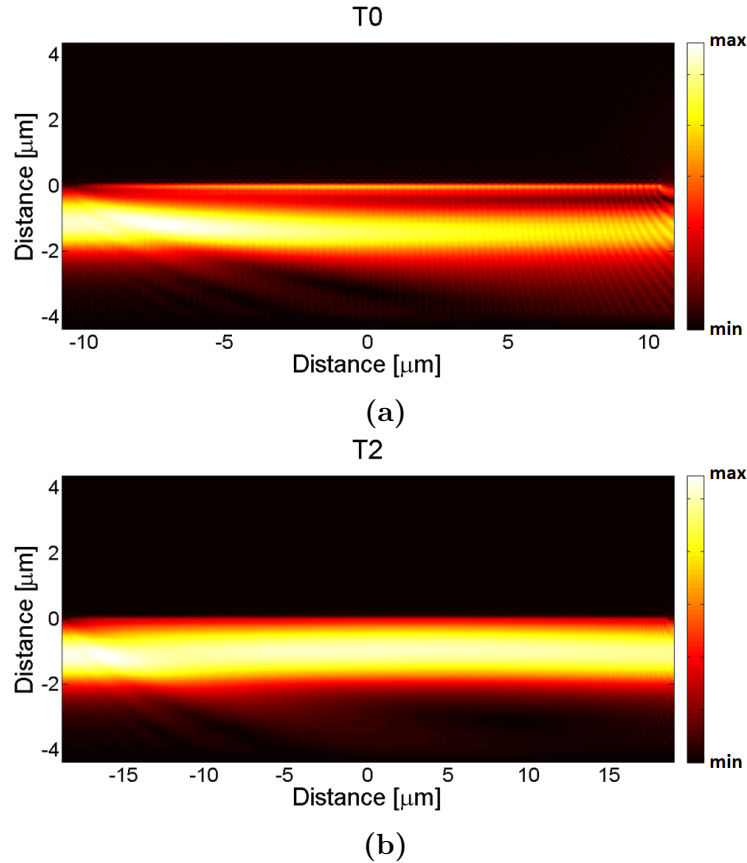


Figure 4.26: Near-field maps of the $|H_y|$ component for a wavelength $\lambda = 685$ nm, computed with the aFMM for a finite chain of 200 gold nanowires with period (a) $\Lambda = 100$ nm (T0), and (b) $\Lambda = 186$ nm (T2). The height of the MNW is $e = 30$ nm. An efficient interaction of the TM₀ mode of the ion exchanged waveguide with the MNW periodic array, is only observable for the shorter period.

The experimental characterization of the obtained samples allowed us to confirm that the FMM is a useful and trustful tool for the modal analysis of integrated structures. However, there are still challenges to meet at fabrication level.

The parameters that we used to fabricate our sample by e-beam lithography, are a good platform for further amelioration of the process. Based on our experience, we can say that in order to reduce the period of the MNW, it is necessary to make a more delicate analysis on the dose factor of the energy of the electron-beam used to pattern the PMMA

resist. Also, recent advances in fabrication of other samples performed by our group work, show that the plasma reactive ion etching process, can significantly help in this size reduction. A balance between these two parameters, can lead us to the fabrication of gratings with periods even shorter.

The sample that we fabricated, allowed us to excite the LSP resonances of a periodic array of metallic nanowires, being observed a weak interaction of these resonances with the TM₀ mode of the ion exchanged waveguide. In order to observe a strong coupling, we must reduce the period of the MNW, and then excite the propagative mode of the chain. This coupling effect can allow us to enhance the field in a small area on the surface of the grating, effect that we can apply, for example, in the detection of biochemical substances.

4.5 Conclusions

With the experimental results presented in this chapter, we demonstrated that the FMM method is a rigorous numerical tool that can be used in the analysis of the modes supported in integrated plasmonic structures. It can give us a full physical interpretation of the behavior of the electromagnetic field interacting in a nano-structured waveguide system.

Concerning to the fabrication process, we observed that the e-beam lithography process requires favorable conditions for the patterning of a short period grating. This is because the glass substrate is a dielectric material that cannot dissipate efficiently the electric charges induced by the electron-beam. By placing an ITO layer, we were able to decrease the charges dissipation at the substrate-resist interface, allowing us to fabricate gratings with sub-wavelength periodicity.

Even if we succeeded in the nanofabrication of the gold nanowires, the periodicity of the performed samples were not shorter than 170 nm, and then no excitation of the longitudinal dipolar mode was expected, neither an energy exchange with the TM₀ mode of the ion exchanged waveguide.

In order to validate the numerical results, we characterized the fabricated samples in far and near-field regimes. In the far-field regime, we observed an optical field enhanced

in the MNW region when they were excited with the TM₀ fundamental mode of the glass waveguide. When we injected the TE₀ mode into the dielectric waveguide, no field enhancement of the gold nanowires was observed. This was an expected result because according to the theory, for a system invariant in the out-of-plane direction, the LSP resonance can be only excited with TM polarized wave.

When we measured the transmission spectra of the samples, we observed that the LSP resonance (minimum in the transmission curves) was red-shifted when the period of the grating was reduced. The three measured spectra agreed with the simulation results, being observed a difference in the LSP resonance wavelengths values due to the bidimensional character of the simulation, to the number of MNW used in the simulations (fewer than the fabricated sample), and also to the values of the dielectric functions used for the materials. However, the transmission profile was also the same.

Concerning to the near-field measurements, by using the H-NSOM technique we determined an effective index of $n_{wg} = 1.52$ for the guided mode propagating through the ion-exchanged waveguide.

In the intensity near-field maps obtained with the apertureless NSOM, we noted an enhancement of the optical field in the MNW grating region. Nevertheless, as predicted by the FMM simulations, this field enhancement was not due to a propagative mode in the gold nanowires, but to a cumulative effect of the LSP excitation of the gold nanowires. Also, with the apertureless NSOM, we were able to determine the effective index of the TM₀ fundamental mode propagating in the structure by performing a Fourier analysis of the obtained images.

Finally, by performing a spectral analysis with the FMM method, we were able to corroborate that the fabricated sample was not adequate to excite the propagation of the dipolar longitudinal mode. However, we could estimate the correct parameters of the integrated plasmonic structure to observe the mode coupling between the MNW and an ion exchanged glass waveguide.

For example, the near-field map of Figure 4.27a and the transmission spectrum of Figure 4.27b, show an efficient coupling between the TM₀ mode of the ion exchanged waveguide and the dipolar longitudinal mode supported by the MNW chain. This struc-

ture corresponds to a periodic array of 200 MNW of height $e = 30$ nm, width $w = 80$ nm and period $\Lambda = 100$ nm, placed on top of an ion exchanged glass waveguide (without the presence of the ITO layer).

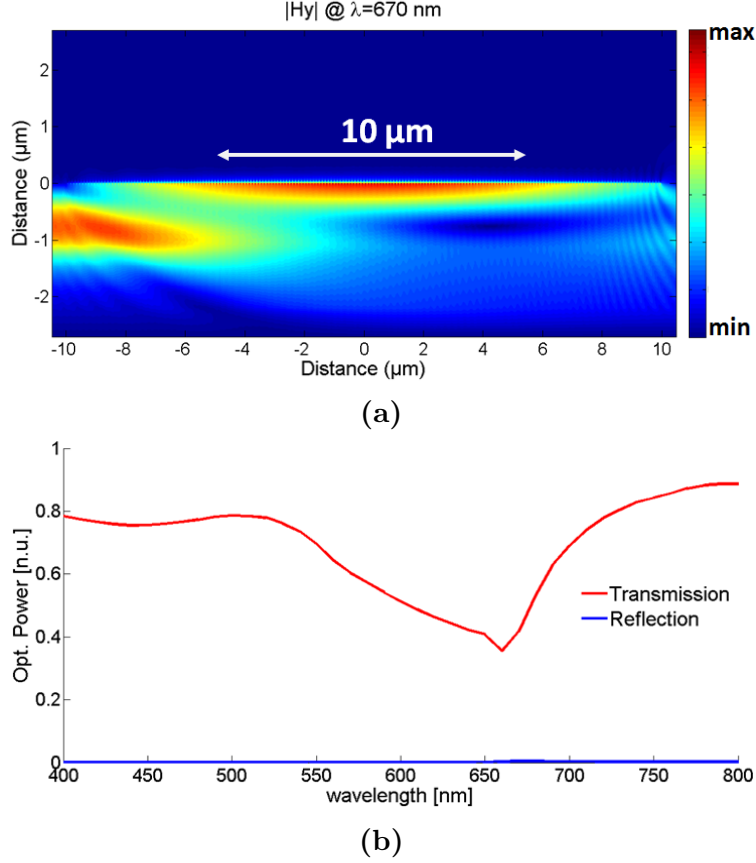


Figure 4.27: (a) Near-field map of the $|H_y|$ component at $\lambda = 670$ nm, and (b) transmission and reflection spectra, of a periodic array of 200 gold nanowires of width $w = 80$ nm, height $e = 30$ nm and period $\Lambda = 100$ nm, placed on top of an ion exchanged glass waveguide with core effective index $n_{wg} = 1.505$. The transmission spectrum exhibits a minimum value at a wavelength $\lambda = 670$ nm, where the near-field map exhibits a strong coupling between the TM_0 mode of the photonic waveguide, and the dipolar longitudinal mode of the plasmonic structure.

Then, to achieve this strong coupling, it is necessary to fabricate a sample with a period around 100 nm, a challenging task that opens new perspectives in the nano-fabrication processes of this kind of integrated structures.

Chapter 5

Summary and Conclusions

In general, we have demonstrated that a chain on metallic nanoparticles behaves as a plasmonic waveguide, supporting propagation modes that can be coupled to the fundamental TM₀ mode of a dielectric waveguide -like an ion exchanged waveguide- forming an optical integrated system that can be potentially used as a nano-sensing device.

We performed the design and analysis of the proposed structures, by making use of the Fourier modal method (FMM), a rigorous numerical method that solves the Maxwell equations in the frequency domain. This method is based on the Fourier series expansions of the periodic structure, the permittivity and the electromagnetic field. This formulation allowed us to find the proper modes of the plasmonic waveguide and its dispersion relations as an eigen-value problem. Also, we were able to simulate the beam propagation along the structure (see Chapter 2).

Even if the FMM present some computational limitations (large computational time, numerical instabilities for large number of nanoparticles, step discretization for non rectangular shapes of nanoparticles), it is a solid tool to analyze in detail the near-field electromagnetic interaction as well as to explain the physical phenomena related to the optical field propagation in optical integrated systems.

Proof of the capabilities of this method was presented in Chapter 3, where we performed some numerical examples to explain two optical integrated systems: a chain of metallic nanowires and a chain of metallic nano-cones interacting with a dielectric waveguide, as we summarize in the following section.

5.1 Numerical results

5.1.1 Metallic nanowires

We observed that a periodic array of gold nanowires immersed in a glass homogeneous dielectric medium supported the propagation of Bloch modes due to a near-field interaction when they were excited at their localized surface plasmon resonance (LSP). Since the LSP resonance depends on the geometry of the metallic nanoparticles, we studied two cases of the height of the nanowires. When the MNW had a short height of 20 nm, it was propagated only one mode through them. This mode was characterized by a dipolar interaction parallel to the propagation direction of the electromagnetic field, and therefore we called it the dipolar longitudinal mode (Fig. 3.4).

When we increased the height of the MNW to 150 nm, two modes were propagated. The first one was due to a quadrupolar interaction, while the second one was due to a dipolar interaction but with the dipoles oriented perpendicularly to the propagation direction of the field (Fig. 3.6). These quadrupolar and dipolar transverse modes are analogous to the anti-symmetric and symmetric modes of the surface plasmon polariton (SPP) observed in a thin metallic layer (Fig. 1.5).

For a periodic chain of MNW placed on top of a dielectric substrate of refractive index $n_{sub} = 2.0$, we observed that the three previous modes were still observable and that they also were confined modes, appearing below the light line of the substrate, as schemed in the dispersion curves of Figures 3.8 and 3.10.

For the MNW of short height we observed that the dipolar longitudinal mode was confined below the light-line of the substrate (Figure 3.9).

For the case of taller height MNW, the quadrupolar and dipolar transverse modes were confined below the substrate light-line, but we also observed a dipolar longitudinal mode that was confined in the substrate-metal interface (Fig. 3.11). This mode was similar to the longitudinal symmetric SPP mode of a metal-dielectric interface. The longitudinal anti-symmetric mode was not observed because the height of the MNW was larger than the skin-depth of the metal.

With these results, we demonstrated that a chain of MNW behaves as a plasmonic waveguide, whose modes could be coupled to the fundamental TM₀ mode of a single-mode dielectric waveguide placed in close proximity to them, giving rise to an energy beating between both waveguides as depicted in Figure 3.18.

For the integrated system with short MNW, we observed an efficient coupling of the dipolar longitudinal mode with the TM₀ fundamental mode of the dielectric waveguide. When we simulated the beam propagation, we observed two minimum values in the transmission spectrum (Fig.3.19). The first one was associated to a Bragg reflection due to the periodicity of the structure, and the second one corresponded to the efficient excitation of the dipolar longitudinal mode. For the later, the near-field maps revealed an energy exchange between the plasmonic and the dielectric waveguides (Fig. 3.22).

For the MNW of taller height, the transmission spectrum of the integrated system also showed the efficient excitation of the quadrupolar and the dipolar transverse mode, as well as their corresponding Bragg reflections and a cavity resonance (Fig. 3.23). The near-field maps also revealed an energy exchange between both waveguides as well as the field enhancement in the MNW chain for the wavelengths values corresponding to the excitation of the quadrupolar and the dipolar transverse modes (Figures 3.24 and 3.25).

Since the proposed integrated system acted as a vertical coupling system, we can use it as a sensing device. Indeed, if we place a substance with a different refractive index above the MNW chain, the LSP resonance of the MNW is affected: if the refractive index is increased the LSP resonance is red-shifted (longer wavelength values), and if the refractive index is reduced a blue-shift (shorter wavelengths) takes place.

5.1.2 Triangular-shaped nanowires

As the LSP resonance is highly dependent on the shape of the nanoparticles, and motivated by their applications in optical integrated systems, we proposed to study a periodic array of triangular-shaped metallic nanowires (metallic nanocones). We chose this particular shape because the metallic nanocones (MNC) enhance the electromagnetic field at their vertexes, representing an advantage in sensing applications.

In first instance, we studied the LSP resonance of a single gold nanocone placed on top of a glass homogeneous dielectric substrate of refractive index $n_{sub} = 1.5$. We studied this resonance as a function of the incidence angle of the TM plane wave impinging from the substrate, as depicted in Figure 3.26. We observed that the nanocone exhibited a LSP resonance that was excited when the light impinged the sample at total internal reflection regime (Fig.3.27), enhancing the optical field at the vertexes of the nanocone (Fig.3.29).

Secondly, we studied a periodic array of MNC on top of the glass substrate (Fig.3.30). We studied the spectral response of the structure as a function of the incidence angle of the light, when its period was fixed to $\Lambda = 200$ nm. The results showed us that two modes were excited. The first one was excited when the incidence angle of the light was around 43° (near to the critical angle), while the second one was only excited at grazing angles (Fig. 3.31).

When we fixed the incidence angle of the TM polarized plane wave to a grazing angle (total internal reflection regime), we observed the same previous propagating modes. These modes were only excited when the period of the chain was short enough to allow the interaction between the MNC (Fig. 3.33). These modes were characterized by multipolar and dipolar transverse resonances. The first enhanced the optical field at the lower vertexes of the MNC (Fig. 3.34), while the second one exhibited a field enhancement at the upper apexes of the MNC (Fig. 3.35).

These results led us to the conclusion that the dipolar transverse mode could be excited by placing a dielectric waveguide in close vicinity to the periodic array of nanocones, generating an integrated system as depicted in Figure 3.37.

The modal analysis of the integrated structure showed us that the dipolar transverse mode supported by the chain of MNC was efficiently excited with the TM₀ fundamental mode of a single-mode dielectric waveguide placed below the MNC (Fig. 3.38). This coupling effect enhanced the optical field at the top apex of the nanocones (Fig. 3.39).

When we performed the beam propagation study, we observed that the transmission spectrum presented two minimum values (Fig. 3.40), the first one corresponded to a Bragg reflection, and the second to the excitation of the dipolar transverse mode. For the later, the near-field maps confirmed the interaction of the dielectric waveguide with the

periodic array of nanocones, as well as the presence of coupled hot-spots at the apex of the MNC (fig. 3.42).

The chain of triangular-shaped nanowires represents an advantage from the rectangular nanowires, since the field could be strongly focused in a smaller area, but it also represents a challenge in fabrication terms. In this work, we were only capable to fabricate a periodic array of MNW. The MNC case is proposed for further work.

5.2 Experimental results

In order to validate experimentally the numerical results provided by the FMM, we fabricated periodic arrays of gold nano-wires by electron-beam lithography, on the surface of a glass substrate containing ion exchanged waveguides.

We fabricated three different structures of nano-wires, with periods $T1 = 173$ nm, $T2 = 186$ nm and $T3 = 198$ nm, and thickness of 30 nm, as shown in Figure 4.6.

We characterized the samples by measuring their transmission spectra at the output of the ion exchanged waveguides using the experimental setup schemed in Figure 4.8. These transmission spectra were normalized to a reference waveguide (Figs. 4.12, 4.13 and 4.14).

With these transmission measurements, we demonstrated that the periodic arrays of MNW were efficiently excited at their LSP wavelength resonance, but we did not observe a coupling effect of the dipolar longitudinal mode. This result was because the periods of the fabricated samples were larger than the optimal period required for an energy exchange between the MNW chain and the ion-exchanged waveguide.

When we compared the transmission spectra to the theoretical curves obtained with the FMM, we observed that the shape of the curve was the same, but the resonances were shifted to longer wavelengths values. These differences arise from imperfections in the fabricated samples and, overall, for the variation of the values of the dielectric function of the gold, as well as the refractive indexes of the dielectric media and the ion exchanged waveguides that we used in the numerical simulations. Nevertheless, the model allowed us to explain the optical field enhancement observed in the fabricated integrated plasmonic

structure.

By making use of the apertureless near-field optical microscopy (aNSOM) we generated amplitude maps of the light propagating along the T_2 -type structure for an excitation near to the wavelength of resonance of the integrated structure.

With the obtained results by the a-NSOM, we confirmed that the LSP resonance of the MNW periodic array was excited with the fundamental TM mode propagating along the ion-exchanged waveguide, but the observed optical field enhancement was due to the excitation of a radiated mode and not to a confined one. This result was also explained by a spectral analysis of the absorption of a periodic array of MNW placed on top of a substrate with similar characteristics of the sample, as a function of the period of the chain.

From this spectral analysis we deduced that when the period of the MNW chain was larger than 120 nm, the LSP resonance remained unchanged, meaning that only the excitation of the LSP resonance could be achieved for these periods, but not near-field interaction between the MNW would be observed (Figure 4.26).

5.3 Integrated plasmonic structures as nanosensing devices

The numerical method used to characterize the designed structures, allowed us to demonstrate that the designed integrated plasmonic structures can be applied as sensing devices for chemical or biological substances.

This conclusion can be verified in the transmission spectra of Figure 5.1, where are presented the transmission and reflection spectra for the case of a MNW chain of height $e = 20$ nm immersed in a glass substrate, excited with the TM_0 mode of the dielectric waveguide of refractive index of the core $n_{wg} = 2.0$ (case studied in section 3.3.1, Fig. 3.19). The blue, red and green continuous curves represent the transmission spectra when the refractive index of the superstrate is $n_{sup} = 1.45, 1.50, 1.55$, respectively. The dashed curves represent their corresponding reflection spectra.

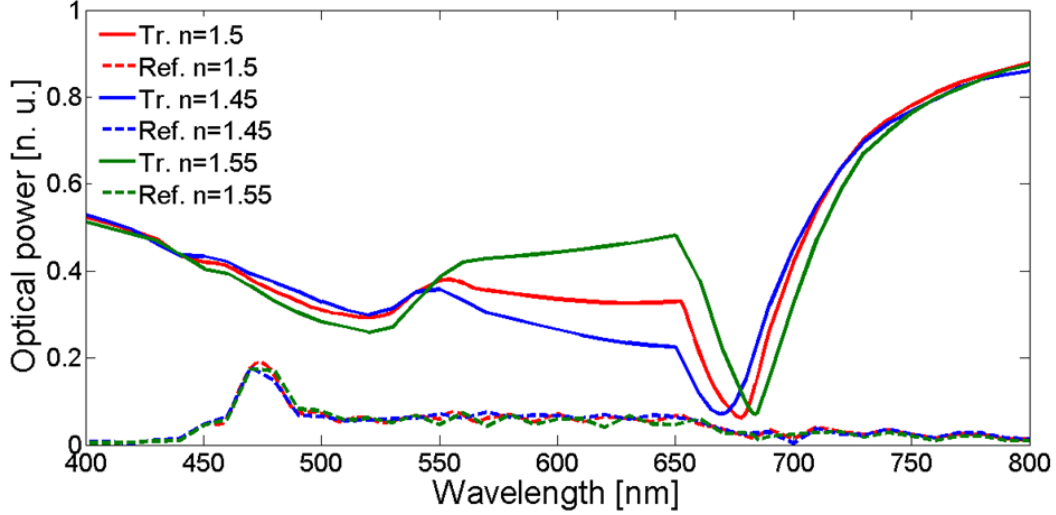


Figure 5.1: Transmission and reflection spectra corresponding to the case of the MNW chain of short height studied in section 3.3.1, when the superstrate refractive index is $n_{sup} = 1.45$ (blue), $n_{sup} = 1.50$ (red), and $n_{sup} = 1.55$ (green). The Bragg reflection remains at the same wavelength, while the longitudinal dipolar resonance is red-shifted when increasing the refractive index.

The transmission spectra reveal that the resonance wavelength of the LSP (dipolar longitudinal mode) is shifted to longer wavelengths (red shift) when the refractive index of the superstrate is increased. Also, we observe that the Bragg reflection is insensitive to refractive index variations. Then, this structure can be used as a real-time sensing device by measuring environmental variations of the refractive index in the superstrate.

Concerning to biological applications, for example, if we attach antibodies to the MNW chain, it is possible to detect the presence of certain antigens (the antibodies are selective to specific antigens) since the LSP resonance of the MNW is modified, being expected a shift in the minimum value of the transmission spectra (Figure 5.2).

The advantage of using periodic arrays of metallic nanoparticles instead of a uniform metallic layer as sensing area, is that the optical field is enhanced in each nanoparticle, providing an array of localized sources that can interact with more efficiency with the measuring probes.

The scope of applications of the integrated plasmonic structures analyzed in the present work, is not only limited to the detection of chemical or biological substances. They can also be implemented for the generation of localized light sources.

For example, since the MNW chains act as an optical cavity in a relative large band-

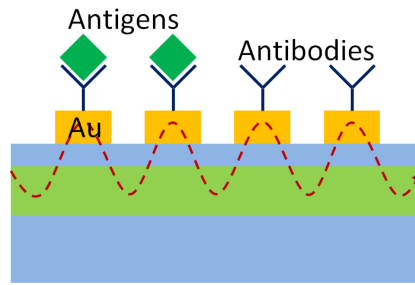


Figure 5.2: *Integrated plasmonic structure for sensing applications in biological sciences. Antibodies are easily attached to the chain of MNW. The presence of an antigen will change the refractive index of the superstrate, leading to a shift in the wavelength resonance of the mode supported by the MNW chain.*

width spectra, it is possible to create stimulated emission light sources, whose emission wavelengths can be tuned by varying the period of the structures or by simply locally changing the refractive index of the superstrate. By placing subsequent arrays of MNW with different periods, several light sources can be also fabricated in a single integrated system.

5.4 Perspective work

The novel research results that we present in this thesis, suggest a further continuation in short and long terms in the development of different scientific research areas. Among the perspective works to be performed, we can list:

1. Nano-fabrication challenges
 - (a) Reduction of the period of the MNW on top of a glass substrate, and increment on the height of the MNW
 - (b) Fabrication of periodic arrays of metallic nanocones on top of an ion-exchanged waveguide
2. Sensing device characterization
 - (a) Study of the interaction of an optical electromagnetic field with chemical or biological analytes
 - (b) Near and far-field characterization of biochemical substances

- (c) Comparison of the sensing efficiency of the proposed integrated structures with other biosensors

3. Extension to other research areas

- (a) Nonlinear effects
- (b) Rainbow trapping and localized field exaltation

The numerical method that we presented in this work can also be applied for the characterization of periodic structures, like photonic crystals, unidimensional structures of graphene, or even meta-materials, areas that currently have attracted the attention of many research groups around the world.

The work performed in this thesis contributes to the development and understanding of the plasmonic interactions in integrated structures, a branch of science currently exploited that promises very varied and interesting applications in different scientific and technological areas.

Appendices

Appendix A

T and S matrix algorithms

A.1 Boundary conditions

The propagation constant $\beta(\alpha_m)$ that satisfies the dispersion relation (2.15) can be determined as an eigenvalue problem. To do so, boundary conditions are needed. The first condition to be satisfied is that the field in each interface between two adjacent layers must be continuous,

$$\psi_m(x, z|\omega)|_{z=d_m} = \psi_{m+1}(x, z|\omega)|_{z=d_m}, \quad (\text{A.1})$$

and the second condition consist on the conservation of the tangential components of the fields when passing through two different media (Jackson, 1998), given as

$$\frac{1}{\nu_m} \frac{\partial \psi_m(x, z|\omega)}{\partial z} \Big|_{z=d_m} = \frac{1}{\nu_{m+1}} \frac{\partial \psi_{m+1}(x, z|\omega)}{\partial z} \Big|_{z=d_m}, \quad (\text{A.2})$$

where

$$\nu_m = \begin{cases} 1, & \text{TE polarization} \\ \varepsilon_m, & \text{TM polarization} \end{cases} \quad (\text{A.3})$$

The values d_m correspond to the coordinate of the m -th interface in the z axis, with $m = 1, \dots, N$. The refractive index can be related to the dielectric function via $n_m = \sqrt{\varepsilon_m \mu_m}$. In the visible spectra, the permeability μ_m is almost equal to 1, so we will avoid this term.

By substituting eq. (2.14) into eqs. (A.1) and (A.2) are obtained, respectively

$$A_m e^{-i\alpha_m d_m} + B_m e^{i\alpha_m d_m} = A_{m+1} e^{-i\alpha_{m+1} d_m} + B_{m+1} e^{i\alpha_{m+1} d_m}, \quad (\text{A.4})$$

$$\frac{\alpha_m \nu_{m+1}}{\nu_m \alpha_{m+1}} \left[-A_m e^{-i\alpha_m d_m} + B_m e^{i\alpha_m d_m} \right] = -A_{m+1} e^{-i\alpha_{m+1} d_m} + B_{m+1} e^{i\alpha_{m+1} d_m}. \quad (\text{A.5})$$

The set of equations (A.4) and (A.5) give us the relationship between the incoming and outgoing fields at the m -th interface of the multilayered system.

A.2 T-matrix method

In order to find the modes that can be supported by the multilayered structure, the equations (A.4) and (A.5) can be expressed in a matrix form in order to have an eigenvalue problem, being the eigenvectors the characteristic modes supported by the structure. This can be written as (Li, 1996)

$$\begin{bmatrix} A_{m+1} \\ B_{m+1} \end{bmatrix} = [W_{m+1}]^{-1} W_m \begin{bmatrix} A_m \\ B_m \end{bmatrix}, \quad (\text{A.6})$$

where

$$W_m = \begin{bmatrix} e^{-ik_m} & e^{ik_m} \\ -\gamma e^{-ik_m} & \gamma e^{ik_m} \end{bmatrix}, \quad (\text{A.7})$$

$$W_{m+1} = \begin{bmatrix} e^{-ik_{m+1}} & e^{ik_{m+1}} \\ -e^{-ik_{m+1}} & e^{ik_{m+1}} \end{bmatrix}, \quad (\text{A.8})$$

with $k_m = \alpha_m d_m$, $k_{m+1} = \alpha_{m+1} d_m$, and $\gamma = (\alpha_m \nu_{m+1}) / (\nu_m \alpha_{m+1})$. By computing the matrix product $[W_{m+1}]^{-1} W_m$, it is obtained

$$\begin{bmatrix} A_{m+1} \\ B_{m+1} \end{bmatrix} = \mathbf{T}_m \begin{bmatrix} A_m \\ B_m \end{bmatrix}, \quad (\text{A.9})$$

with

$$\mathbf{T}_m = \frac{1}{2} \begin{bmatrix} (1 + \gamma) e^{-i(k_m - k_{m+1})} & (1 - \gamma) e^{i(k_m + k_{m+1})} \\ (1 - \gamma) e^{-i(k_m + k_{m+1})} & (1 + \gamma) e^{i(k_m - k_{m+1})} \end{bmatrix}. \quad (\text{A.10})$$

Equation (A.10) represents the so-called \mathbf{T} -matrix, and relates the propagative and counter-propagative modes at the m -th interface of the multilayered media. Since there are $N + 1$ different media, when computing the total \mathbf{T} matrix of the multilayered system only must be taken into account N matrices, with the correction that $d_{N+1} = d_N$. In other words, the complete characteristic matrix of the complete structure is the product of the characteristic sub-matrices in each layer, such that

$$\begin{bmatrix} A_{N+1} \\ B_{N+1} \end{bmatrix} = \prod_{m=1}^N \mathbf{T}_m \begin{bmatrix} A_1 \\ B_1 \end{bmatrix} = \begin{bmatrix} t_{11} & t_{12} \\ t_{21} & t_{22} \end{bmatrix} \begin{bmatrix} A_1 \\ B_1 \end{bmatrix}. \quad (\text{A.11})$$

As depicted in Fig. 2.2, the substrate (ε_1) and the superstrate (ε_{N+1}) are considered as semi-infinite media and no external sources are considered. Then, no reflected waves are expected at the boundaries, and amplitudes A_1 and B_{N+1} vanish at the infinite. With this, the value of the propagation constant for each mode, β , can be determined by equating the t_{22} element of the \mathbf{T} matrix to zero and using the dispersion relation of Eq. (17).

In general, the solution of the relation $t_{22} = 0$ can not be solved analytically, and numerical methods must be implemented.

A.2.1 Example: asymmetric waveguide

Since the \mathbf{T} matrix algorithm can be used for any 2D multilayered system, let us determine the dispersion relation of an asymmetric waveguide as depicted in Fig. A.1.

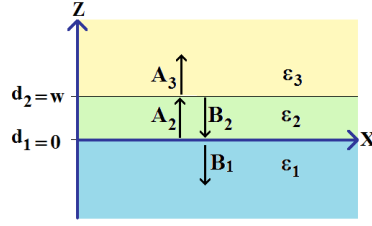


Figure A.1: Scheme of an asymmetric 2D waveguide of width $d_2 = w$ and dielectric function ε_2 . The substrate ε_1 and superstrate ε_3 are semi-infinite in regions $z < 0$ and $z > d_2$, respectively, and the interfaces are localized at $d_1 = 0$ and at $d_2 = w$.

According to eq. (A.11), the \mathbf{T} matrix for TM polarization is

$$\mathbf{T} = \prod_{m=1}^2 \mathbf{T}_m = \begin{pmatrix} \left[1 + \frac{\varepsilon_3 \alpha_2}{\varepsilon_2 \alpha_3}\right] e^{-i(\alpha_2 - \alpha_3)w} & \left[1 - \frac{\varepsilon_3 \alpha_2}{\varepsilon_2 \alpha_3}\right] e^{i(\alpha_2 + \alpha_3)w} \\ \left[1 - \frac{\varepsilon_3 \alpha_2}{\varepsilon_2 \alpha_3}\right] e^{-i(\alpha_2 + \alpha_3)w} & \left[1 + \frac{\varepsilon_3 \alpha_2}{\varepsilon_2 \alpha_3}\right] e^{i(\alpha_2 - \alpha_3)w} \end{pmatrix} \cdot \begin{pmatrix} \left[1 + \frac{\varepsilon_2 \alpha_1}{\varepsilon_1 \alpha_2}\right] & \left[1 - \frac{\varepsilon_2 \alpha_1}{\varepsilon_1 \alpha_2}\right] \\ \left[1 - \frac{\varepsilon_2 \alpha_1}{\varepsilon_1 \alpha_2}\right] & \left[1 + \frac{\varepsilon_2 \alpha_1}{\varepsilon_1 \alpha_2}\right] \end{pmatrix}. \quad (\text{A.12})$$

Equating to zero the $t_{2,2}$ element of the \mathbf{T} matrix is obtained:

$$\left[1 - \frac{\varepsilon_3 \alpha_2}{\varepsilon_2 \alpha_3}\right] e^{-i(\alpha_2 + \alpha_3)w} \left[1 - \frac{\varepsilon_2 \alpha_1}{\varepsilon_1 \alpha_2}\right] + \left[1 + \frac{\varepsilon_3 \alpha_2}{\varepsilon_2 \alpha_3}\right] e^{i(\alpha_2 - \alpha_3)w} \left[1 + \frac{\varepsilon_2 \alpha_1}{\varepsilon_1 \alpha_2}\right] = 0, \quad (\text{A.13})$$

which after some algebra leads to

$$\frac{\left(\frac{\alpha_2}{\varepsilon_2} - \frac{\alpha_3}{\varepsilon_3}\right) \left(\frac{\alpha_2}{\varepsilon_2} - \frac{\alpha_1}{\varepsilon_1}\right)}{\left(\frac{\alpha_2}{\varepsilon_2} + \frac{\alpha_3}{\varepsilon_3}\right) \left(\frac{\alpha_2}{\varepsilon_2} + \frac{\alpha_1}{\varepsilon_1}\right)} = e^{i2\alpha_2 w}, \quad (\text{A.14})$$

with

$$\alpha_i = \pm \sqrt{\left(\frac{\omega}{c}\right)^2 \varepsilon_i - \beta^2}, \quad (\text{A.15})$$

for $i = 1, 2, 3$. This same expression can be found in several textbooks; nevertheless, there is no analytical solution for this transcendental function.

If the substrate and superstrate were equal (symmetric waveguide), $\alpha_1 = \alpha_3$ and $\varepsilon_1 = \varepsilon_3$, equation (A.14) results in

$$\frac{\frac{\alpha_2}{\varepsilon_2} - \frac{\alpha_1}{\varepsilon_1}}{\frac{\alpha_2}{\varepsilon_2} + \frac{\alpha_1}{\varepsilon_1}} = e^{i\alpha_2 w}. \quad (\text{A.16})$$

A.3 S matrix algorithm

At this point, it is simple to solve the multilayered problem by making use of the **T**-matrix algorithm. However, it is well known that this method is numerically unstable when the total layer thickness of the multilayered structure and the matrix dimensions are large (Li, 1996). This numerical instability is attributed to the presence of growing exponential functions in the algorithm: loss of significant digits when are computed small numbers by subtracting two larger numbers by a computer of finite precision. This numerical instability can not be removed by simply reducing the individual layer thickness without lowering the total thickness, because the **T**-matrix algorithm accumulates the magnitudes of the exponential functions as the \mathbf{T}_m layer matrices are multiplied together.

In order to guarantee a numerical stability, it is proposed the **S**-matrix method, which is quite similar to the **T** method, but the equations (A.4) and (A.5) should be arranged in order to link the waves in the m -th layer as

$$\begin{bmatrix} A_{m+1} \\ B_m \end{bmatrix} = [s_{m+1}]^{-1} s_m \begin{bmatrix} A_m \\ B_{m+1} \end{bmatrix}, \quad (\text{A.17})$$

being

$$s_{m+1} = \begin{bmatrix} e^{-ik_{m+1}} & -e^{ik_m} \\ e^{-ik_{m+1}} & \gamma e^{ik_m} \end{bmatrix}, \quad (\text{A.18})$$

$$s_m = \begin{bmatrix} e^{-ik_m} & -e^{ik_{m+1}} \\ \gamma e^{-ik_m} & e^{ik_{m+1}} \end{bmatrix}, \quad (\text{A.19})$$

with $k_i = \alpha_i d_i$ for $i = m, m + 1$, and $\gamma = (\alpha_m \nu_{m+1}) / (\nu_m \alpha_{m+1})$. Computing the matrices product it is obtained

$$\begin{bmatrix} A_{m+1} \\ B_m \end{bmatrix} = \mathbf{S}_m \begin{bmatrix} A_m \\ B_{m+1} \end{bmatrix}, \quad (\text{A.20})$$

with

$$\mathbf{S}_m = \frac{e^{-i(k_m - k_{m+1})}}{1 + \gamma} \begin{bmatrix} 2\gamma & (1 - \gamma) e^{i(k_m + k_{m+1})} \\ -(1 - \gamma) e^{-i(k_m + k_{m+1})} & 2 \end{bmatrix}. \quad (\text{A.21})$$

Once again, by defining $d_{N+1} = d_N$, the characteristic matrix of the complete multi-layered media is obtained by an iterative application of eq. (A.21)

$$\begin{bmatrix} A_{N+1} \\ B_1 \end{bmatrix} = \prod_{m=1}^N \mathbf{S}_m \begin{bmatrix} A_1 \\ B_{N+1} \end{bmatrix} = \begin{bmatrix} s_{11} & s_{12} \\ s_{21} & s_{22} \end{bmatrix} \begin{bmatrix} A_1 \\ B_{N+1} \end{bmatrix}. \quad (\text{A.22})$$

The \mathbf{S} matrix given by the expression (A.22), can be related to the t_{ij} elements of the \mathbf{T} matrix of equation (A.10) according to (Li, 1996)

$$\mathbf{S}_m = \begin{bmatrix} t_{11} - t_{12}t_{22}^{-1}t_{21} & t_{12}t_{22}^{-1} \\ -t_{22}^{-1}t_{21} & t_{22}^{-1} \end{bmatrix}, \quad (\text{A.23})$$

being possible to obtain recursion equations for each one of the total \mathbf{S} matrix as (Arnaud, 2008)

$$S_{11}^N = (t_{22}^N - s_{12}^N t_{12}^N) s_{11}^{N-1}, \quad (\text{A.24})$$

$$S_{12}^N = (t_{21}^N + t_{22}^N s_{12}^{N-1}) Z_{N-1}, \quad (\text{A.25})$$

$$S_{21}^N = s_{21}^{N-1} - s_{22}^N t_{12}^N s_{11}^{N-1}, \quad (\text{A.26})$$

$$S_{22}^N = s_{22}^{N-1} Z_{N-1}, \quad (\text{A.27})$$

where

$$Z_{N-1} = [t_{11}^N + t_{12}^N s_{12}^{N-1}]^{-1}. \quad (\text{A.28})$$

The \mathbf{S} matrix recursion can be initialized by setting

$$S_0 = \begin{bmatrix} 1 & 0 \\ 0 & 1 \end{bmatrix}. \quad (\text{A.29})$$

It must be remarked that if there are no incident waves in the 1st medium ($A_1 = 0$),

then

$$\begin{aligned} A_{N+1} &= s_{12}B_{N+1} \\ B_1 &= s_{22}B_{N+1} \end{aligned} \quad . \quad (\text{A.30})$$

The numerical stability of the **S** matrix algorithm is ensured since the growing exponential function that was originally in the **T** matrix, is now inverted in equation (A.21). Furthermore, the sub-matrices of s appear in the recursion formulas only as additive or multiplicative terms. Thus the stability of the algorithm is ensured.

Appendix B

S matrix of a periodic grating

In a lamellar grating, the propagation constant of the modes is given by a simple dispersion equation resulting from periodic boundary conditions at the groove interfaces.

According to the Sturm-Liouville theorem, the modal solutions of equation (2.30) give an orthogonal and complete functional basis $\psi_q(x)$, for $q = 0, 1, \dots, \infty$, where the orthogonality condition is given by

$$\frac{1}{\Lambda} \int_0^\Lambda \bar{\psi}_q^*(x) \psi_r(x) dx = \delta_{qr}, \quad (\text{B.1})$$

for TE polarization, and

$$\frac{1}{\Lambda} \int_0^\Lambda \bar{\psi}_q^*(x) \frac{\psi_r(x)}{\varepsilon(x)} dx = \delta_{qr}, \quad (\text{B.2})$$

for TM polarization, being δ_{qr} the Kronecker delta.

When the grating is of finite height t , the grating field must be matched to the diffraction field in the adjacent media. Like in the grating region, the electromagnetic field under and above the grating layer can be represented by their diffraction modes with a Rayleigh-Fourier expansion given by

$$\psi_y^{(l)}(x, z) = \sum_{m=-\infty}^{\infty} e^{i\alpha_m x} \left[A_m^{(l)} e^{-i\beta_m^{(l)}(z-z_0)} + B_m^{(l)} e^{i\beta_m^{(l)}(z-z_0)} \right], \quad (\text{B.3})$$

with $z_0 = t/2$ for the region $l = 1$, and $z_0 = -t/2$ for $l = 2$. To find the unknown amplitudes A and B in each layer, the S matrix algorithm can be implemented (Appendix

A). So, the S matrix for the grating layer can be found by applying boundary conditions (continuity of the field and its tangential components) to equations (2.23) and (B.3) at the interfaces $z_0 = \pm t/2$:

$$\psi_y^{(1)}(x, z) \Big|_{z=t/2} = \psi_y^{(g)}(x, z) \Big|_{z=t/2}, \quad (\text{B.4})$$

$$\left(\frac{1}{\varepsilon(1)} \right)^p \frac{\partial \psi_y^{(1)}(x, z)}{\partial z} \Big|_{z=t/2} = \left(\frac{1}{\varepsilon(x)} \right)^p \frac{\partial \psi_y^{(g)}(x, z)}{\partial z} \Big|_{z=t/2}, \quad (\text{B.5})$$

$$\psi_y^{(2)}(x, z) \Big|_{z=-t/2} = \psi_y^{(g)}(x, z) \Big|_{z=-t/2}, \quad (\text{B.6})$$

$$\left(\frac{1}{\varepsilon(2)} \right)^p \frac{\partial \psi_y^{(2)}(x, z)}{\partial z} \Big|_{z=-t/2} = \left(\frac{1}{\varepsilon(x)} \right)^p \frac{\partial \psi_y^{(g)}(x, z)}{\partial z} \Big|_{z=-t/2}, \quad (\text{B.7})$$

whit $p = 0$ for TE polarization, and $p = 1$ for TM polarization. The orthogonality of the Rayleigh-Fourier harmonics is applied by multiplying the obtained equations by $e^{-i\alpha_n x}$, and integrating over one period for every fixed integer n . The resulting infinite set of equations relates the incident and reflected grating modes amplitudes, which can be represented as (Tishchenko, 2005)

$$\begin{bmatrix} A_n^2 \\ B_n^1 \end{bmatrix} = \sum_{q=0}^{\infty} \begin{bmatrix} \frac{\beta_n^2 F_q^n + \varepsilon_2 \beta_q G_q^n}{2\beta_n^2} & \frac{\beta_n^2 F_q^n - \varepsilon_2 \beta_q G_q^n}{2\beta_n^2} e^{i\beta_q t} \\ \frac{\beta_n^1 F_q^n - \varepsilon_1 \beta_q G_q^n}{2\beta_n^1} e^{i\beta_q t} & \frac{\beta_n^1 F_q^n + \varepsilon_1 \beta_q G_q^n}{2\beta_n^1} \end{bmatrix} \begin{bmatrix} A_q e^{-i\beta_q \frac{t}{2}} \\ B_q e^{-i\beta_q \frac{t}{2}} \end{bmatrix} = \sum_{q=0}^{\infty} Q_{nq} A_q, \quad (\text{B.8})$$

$$\begin{bmatrix} B_n^2 \\ A_n^1 \end{bmatrix} = \sum_{q=0}^{\infty} \begin{bmatrix} \frac{\beta_n^2 F_q^n - \varepsilon_2 \beta_q G_q^n}{2\beta_n^2} & \frac{\beta_n^2 F_q^n + \varepsilon_2 \beta_q G_q^n}{2\beta_n^2} e^{i\beta_q t} \\ \frac{\beta_n^1 F_q^n + \varepsilon_1 \beta_q G_q^n}{2\beta_n^1} e^{i\beta_q t} & \frac{\beta_n^1 F_q^n - \varepsilon_1 \beta_q G_q^n}{2\beta_n^1} \end{bmatrix} \begin{bmatrix} A_q e^{-i\beta_q \frac{t}{2}} \\ B_q e^{-i\beta_q \frac{t}{2}} \end{bmatrix} = \sum_{q=0}^{\infty} R_{nq} A_q, \quad (\text{B.9})$$

where

$$F_q^n = \frac{1}{\Lambda} \int_0^{\Lambda} \psi_q(x) e^{-i\alpha_n x} dx, \quad (\text{B.10})$$

$$G_q^n = \frac{1}{\Lambda} \int_0^{\Lambda} \left(\frac{1}{\varepsilon(x)} \right)^p \psi_q(x) e^{-i\alpha_n x} dx. \quad (\text{B.11})$$

The resulting S matrix of the grating

$$\begin{bmatrix} B_m^2 \\ A_m^1 \end{bmatrix} = \sum_{n=-\infty}^{\infty} S_{mn} \begin{bmatrix} A_n^2 \\ B_n^1 \end{bmatrix}, \quad (\text{B.12})$$

is found by matrix inversion $S = RQ^{-1}$.

Appendix C

Perfectly matched layers

A perfectly matched layer (PML) can be defined as an homogeneous medium that absorbs the electromagnetic waves scattered from a dielectric adjacent medium, and where the reflection factor of a plane wave striking the dielectric-layer interface is null at any frequency and at any incidence angle. To achieve this condition, it must be supposed that the layer have an electric and magnetic conductivity, such that its impedance equals that of the dielectric medium (Berenger, 1994).

With this technique, the layer surrounding the computational domain can theoretically absorb without reflection any kind of wave traveling towards the boundaries.

The PML formalism actually introduces anisotropy into the permittivity and permeability. This anisotropy is only a mathematical construct that is active within the PML absorbing layer region (Elson, 2001).

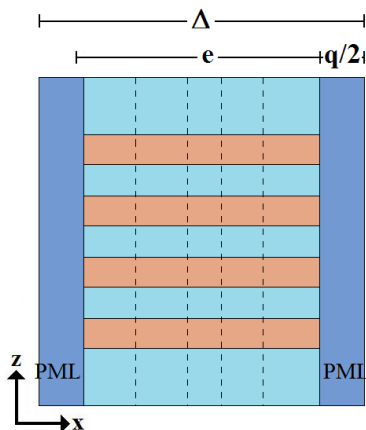


Figure C.1: Scheme of the computational window of size e , between two PML layers of width $q/2$. The total length of the unitary cell is Δ .

Since the case for TE or TM polarization are mathematically equivalent, here will be explained only the case for TM polarization as described in reference (Hugonin and Lalanne, 2005).

The first step is to assume that the materials are magnetic with relative permeability $\mu(x, z)$ and anisotropic with a relative tensor of permittivity defined by

$$\varepsilon = \begin{bmatrix} \varepsilon_{xx} & 0 & 0 \\ 0 & \varepsilon_{yy} & 0 \\ 0 & 0 & \varepsilon_{zz} \end{bmatrix}. \quad (\text{C.1})$$

Then, using the Maxwell equations the resulting Helmholtz equation for TM polarization is

$$\frac{\partial}{\partial z} \left(\frac{1}{\varepsilon_{xx}} \frac{\partial H_y}{\partial z} \right) + \frac{\partial}{\partial x} \left(\frac{1}{\varepsilon_{zz}} \frac{\partial H_y}{\partial x} \right) + k_0^2 \mu H_y = 0. \quad (\text{C.2})$$

In the region of the PML, the magnetic field $H_y = H_y^{in} + H_y^{out}$ can be expanded in a modal basis of the form

$$H_y^{out} = \sum_p a_p h_p(z) e^{ik_p x}, \quad (\text{C.3})$$

$$H_y^{in} = \sum_p b_p h_p(z) e^{-ik_p x}, \quad (\text{C.4})$$

with $\text{Re}[k_p] > 0$, $\text{Im}[k_p] \geq 0$. H_y^{out} admits an analytic continuation $H_y^{out}(X_I, z)$ in the complex domain defined by $\text{Re}[X_I] \geq e/2$ and $\text{Im}[X_I] \geq 0$, with $H_y^{out} \rightarrow 0$ as $X_I \rightarrow \infty + i\infty$, being e the region of the computational window (Fig. C.1). This does not hold for H_y^{in} , since all propagative or evanescent modes exponentially diverge as $e^{-ik_p X_I}$ for $X_I \rightarrow \infty + i\infty$.

Thus, equation (C.2) remains valid in a complex space formed by the semi-infinite domain X_I , and by a real segment $X_{III} = x$ for $|x'| \leq e/2$. So, instead of solving this equation in the open domain $x \in (-\infty, \infty)$, we solve it rather in the complex domain X , through a continuous complex coordinate transform $X = F(x')$ that must satisfy

- $F(x')$ is real for $|x'| < e/2$,
- $F(x') \rightarrow \infty + i\infty$ for $x' \rightarrow d/2$, and

- $F(x') \rightarrow -\infty - i\infty$ for $x' \rightarrow -d/2$.

Defining $F(x') = x$, the Helmholtz equation remains without change in the region $|x'| < e/2$. For expressing the equation (C.2) in the new coordinate space, we only need to specify the derivative $dx'/dX = (dF/dx')^{-1}$. It is convenient to express this function in the form of the product of a continuous complex function $f(x')$ by a constant complex function $f_{PML}(x')$:

$$\frac{dx'}{dX} = f(x') f_{PML}(x'), \quad (\text{C.5})$$

obtaining

$$\frac{\partial}{\partial z} \left(\frac{1}{f_{PML} \varepsilon_{xx}} \frac{\partial H_y}{\partial z} \right) + f \frac{\partial}{\partial x'} \left(\frac{f_{PML}}{\varepsilon_{zz}} f \frac{\partial H_y}{\partial x'} \right) + k_0^2 \frac{\mu}{f_{PML}} H_y = 0. \quad (\text{C.6})$$

The net effect of the constant function f_{PML} is a renormalization of the permittivity and permeability coefficients.

As long as the basis is regular, incoming waves are prohibited and the outgoing wave condition is perfectly satisfied.

Bibliography

- M. Abashin, P. Tortora, I. Marki, U. Levy, W. Nakagawa, L. Vaccaro, H. P. Herzig, and Y. Fainman. Near-field characterization of propagating optical modes in photonic crystal waveguides. *Optics Express*, 14(4):1643–1657, 2006.
- A. Apuzzo, M. Fevrier, R. Salas-Montiel, A. Bruyant, A. Chelnokov, G. Lerondel, B. Dagens, and S. Blaize. Observation of near-field dipolar interactions involved in a metal nanoparticle chain waveguide. *Nano letters*, 13(3):1000–1006, 2013.
- F. B. Arango, A. Kwadrin, and A. F. Koenderink. Plasmonic antennas hybridized with dielectric waveguides. *ACS Nano*, 6(11):10156–10167, 2012.
- L. Arnaud. *Diffraction et diffusion de la lumière: modélisation tridimensionnelle et application à la métrologie de la microélectronique et aux techniques d’imagerie sélective en milieu diffusant*. PhD thesis, Université Paul Cézanne, Marseille, France, 2008.
- R. M. A. Azzam. Circular and near-circular polarization states of evanescent monochromatic light fields in total internal reflection. *Applied Optics*, 50(33):6272 – 6276, 2011.
- M. L. M. Balistreri, J. P. Korterik, L. Kuipers, and N. F. van Hulst. Local observations of phase singularities in optical fields in waveguide structures. *Physical Review Letters*, 85(2):294–297, 2000.
- J. P. Berenger. A perfectly matched layer for the absorption of electromagnetic waves. *Journal of Computational Physics*, 114:185–200, 1994.
- S. Blaize, S. Aubert, A. Bruyant, R. Bachelot, G. Lerondel, P. Royer, J. E. Broquin, and

- V. Minier. Apertureless scanning near-field optical microscopy for ion exchange channel waveguide characterization. *Journal of Microscopy*, 209:155–161, 2002.
- C. F. Bohren and D. R. Huffman. *Absorption and scattering of light by small particles*. Wiley, 1998.
- L. C. Botten, M. S. Craig, R. C. McPhedran, J. L. Adams, and J. R. Andrewartha. The dielectric lamellar diffraction grating. *Optica Acta*, 28(3):413 – 428, 1981a.
- L. C. Botten, M. S. Craig, R. C. McPhedran, J. L. Adams, and J. R. Andrewartha. The finitely conducting lamellar diffraction grating. *Optica Acta*, 28(8):1087 – 1102, 1981b.
- C. B. Burckhardt. Diffraction of plane wave at a sinusoidally stratified dielectric grating. *Journal of Optical Society of America A*, 56(11):1502–1509, 1966.
- Q. Cao, P. Lalanne, and J. P. Hugonin. Stable and efficient bloch-mode computational method for one-dimensional grating waveguides. *Journal of Optical Society of America A*, 19(2):335–338, 2002.
- K. R. Catchpole. Nanostructures in photovoltaics. *Phil. Trans. Royal Society A*, 364: 3493–3503, 2006.
- N. Chateau and J. P. Hugonin. Algorithm for the rigorous coupled-wave analysis of grating diffraction. *Journal of Optical Society of America A*, 11(4):1321–1331, 1994.
- N. Chateau and J. P. Hugonin. Note on the s-matrix propagation algorithm. *Journal of Optical Society of America A*, 29(4):655–660, 2003.
- A. Christ, S. G. Tikhodeev, N. A. Gippius, J. Kuhl, and H. Giessen. Waveguide-plasmon polaritons: Strong coupling of photonic and electronic resonances in a metallic photonic crystal slab. *Physical Review Letters*, 91(18):183901, 2003.
- R. M. Cordova-Castro. Efectos de forma en las resonancias plasmónicas de nanopartículas. Master’s thesis, Universidad Nacional Autónoma de México, Ensenada, Baja California, Mexico, 2014.

- K. B. Crozier, E. Togan, E. Simsek, and T. Yang. Experimental measurement of the dispersion relations of the surface plasmon modes of metal nanoparticles chains. *Optics Express*, 15(26):17482–17493, 2007.
- S. D’Agostino, F. D. Sala, and L. C. Andreani. Dipole-excited surface plasmons in metallic nanoparticles: Engineering decay dynamics within the discrete-dipole approximation. *Physical Review B*, 87(20):205413, 2013.
- J. A. Dionne, L. A. Sweatlock, and H. A. Atwater. Plasmon slot waveguides: Towards chip-scale propagation with subwavelength-scale localization. *PHYSICAL REVIEW B*, 73(3):035407, 2006.
- J. M. Elson. Propagation in planar waveguides and the effects of wall roughness. *Optics Express*, 9(9):461–475, 2001.
- M. Fevrier, P. Gogol, A. Aassime, R. Meegy, C. Delacour, A. Chelnokov, A. Apuzzo, S. Blaize, J. M. Lourtioz, and B. Dagens. Giant coupling effect between metal nanoparticle chain and optical waveguide. *Nano Letters*, 12(2):1032–1037, 2012a.
- M. Fevrier, P. Gogol, A. Aassime, R. Megy, D. Bouville, J. M. Lourtioz, and B. Dagens. Localized surface plasmon bragg grating on soi waveguide at telecom wavelengths. *Applied Physics A*, 109(4):935–942, 2012b.
- M. Foresti, L. Menez, and A. V. Tishchenko. Modal method in deep metal-dielectric gratings: the decisive role of hidden modes. *Journal of Optical Society of America A*, 23(10):2501–2509, 2006.
- C. Gell, M. Berndt, J. Enderlein, and S. Diez. TIRF microscopy evanescent field calibration using tilted fluorescent microtubules. *Journal of Microscopy*, 234(1):38 – 46, 2009.
- M. T. Hill, Y.-S. Oei, B. Smalbrugge, Y. Zhu, T. de Vries, P. J. van Veldhoven, F. W. M. van Otten, T. J. Eijkemans, J. P. Turkiewicz, H. de Waardt, E. J. Geluk, S.-H. Kwon, Y.-H. Lee, R. Nötzel, and M. K. Smit. Lasing in metallic-coated nanocavities. *Nature photonics*, 1(10):589 – 594, 2007.

- A. Hochman and Y. Leviatan. Rigorous modal analysis of metallic nanowire chains. *Optics Express*, 17(16):13561–13575, 2009.
- Y. Hu, X. Diao, C. Wang, W. Hao, and T. Wang. Effects of heat treatment on properties of its films prepared by rf magnetron sputtering. *Vacuum*, 75(2):183–188, 2004.
- J. P. Hugonin and P. Lalanne. Perfectly matched layers as nonlinear coordinate transforms: a generalized formalization. *Journal of Optical Society of America A*, 22(9):1844–1849, 2005.
- E. Hutter and J. Fendler. Exploitation of localized surface plasmon resonance. *Advanced Materials*, 16(19):1685–1706, 2004.
- T. Ishi, J. Fujikata, K. Makita, T. Baba, and K. Ohashi. Si nano-photodiode with a surface plasmon antenna. *Japanese Journal of Applied Physics*, 44(12):L364–L366, 2005.
- J. D. Jackson. *Classical electrodynamics*. John Wiley and Sons, 3rd edition, 1998.
- K. L. Kelly, E. Coronado, L. L. Zhao, and G. C. Schatz. The optical properties of metal nanoparticles: the influence of size, shape, and dielectric environment. *Journal of Physical Chemistry B*, 107(3):668–677, 2003.
- K. Y. Kim, H. T. M. C. M. Baltar, K. Drozdowicz-Tomsia, and E. M. Goldys. *Plasmonics - Principles and Applications*. Intech, 2012.
- C. Kittel. *Introduction to solid state physics*. John Wiley and Sons, 8th edition, 2004.
- A. F. Koenderink and A. Polman. Complex response and polariton-like dispersion splitting in periodic metal nanoparticle chains. *Physical Review B*, 74(3):033402, 2006.
- A. F. Koenderink, R. de Waele, J. C. Prangma, and A. Polman. Experimental evidence for large dynamic effects on the plasmon dispersion of subwavelength metal nanoparticle waveguides. *Physical Review B*, 76(20):201403, 2007.
- J. M. Kontio, H. Husu, J. Simonen, M. J. Huttunen, J. Tommila, M. Pessa, and M. Kauhanen. Nanoimprint fabrication of gold nanocones with 10 nm tips for enhanced optical interactions. *Optics Express*, 34(13):1979–1981, 2009.

- N. N. Lal, B. F. Soares, J. K. Sinha, F. Huang, S. Mahajan, P. N. Bartlett, N. C. Greenham, and J. J. Baumberg. Enhancing solar cells with localized plasmons in nanovoids. *Optics Express*, 19(12):11256–11263, 2011.
- P. Lalanne and M. P. Jurek. Computation of the near-field pattern with the coupled-wave method for transverse magnetic polarization. *Journal of Modern Optics*, 45(7):1357–1374, 1998.
- P. Lalanne and E. Silberstein. Fourier-modal methods applied to waveguide computational problems. *Optics Letters*, 25(15):1092–1094, 2000.
- G. Leblond. *Etude et developpement d' un micro-spectromètre à ondes guidées contra-propagatives*. PhD thesis, Université de Technologie de Troyes, Troyes, France, 2009.
- L. Li. Formulation and comparison of two recursive matrix algorithms for modeling layered diffraction gratings. *Journal of Optical Society of America A*, 13(5):1024–1035, 1996.
- L. Li and C. W. Haggans. Convergence of the coupled-wave method for metallic lamellar diffraction gratings. *Journal of Optical Society of America A*, 10(6):1184–1189, 1993.
- M. J. Linman and Q. J. Cheng. *Optical guided-wave chemical and biosensors*. Springer, 2010.
- A. Lobnik, M. Turel, and S. K. Urek. *Advances in chemical sensors. Optical chemical sensors: design and applications*. Intech, 2012.
- S. A. Maier. *Plasmonics: fundamentals and applications*. Springer, 2007.
- D. Marcuse. *Principles of optical fiber measurements*. Academic Press Inc., 1981.
- M. G. Moharam and T. K. Gaylord. Rigorous coupled-wave analysis of planar-grating diffraction. *Journal of Optical Society of America A*, 71(7):811–818, 1981.
- M. G. Moharam, E. B. Grann, D. A. Pommet, and T. K. Gaylord. Formulation for stable and efficient implementation of the rigorous coupled-wave analysis of binary gratings. *Journal of Optical Society of America A*, 12(5):1068–1076, 1995.

- T. Nikolajsen, K. Leosson, and S. I. Bozhevolnyi. Surface plasmon polariton based modulators and switches operating at telecom wavelengths. *Applied Physics Letters*, 85(24):5833–5835, 2007.
- C. Noguez. Surface plasmons on metal nanoparticles: the influence of shape and physical environment. *Journal of Physical Chemistry C*, 111(10):3806–3819, 2007.
- L. Novotny and B. Hecht. *Principles of nano-optics*. Cambridge University Press, 2006.
- E. D. Palik. *Handbook of optical constants of solids*. Academic Press, 4th edition, 1985.
- V. M. N. Passaro, F. Dell’Olio, B. Casamassima, and F. D. Leonardis. Guided-wave optical biosensors. *Sensors*, 7(4):508–536, 2007.
- J. B. Pendry. Negative refraction makes a perfect lens. *Physical Review Letters*, 85(18):3966–3969, 2000.
- E. Popov and M. Neviere. Maxwell equations in fourier space: fast-converging formulation for diffraction by arbitrary shaped, periodic, anisotropic media. *Journal of Optical Society of America A*, 18(11):2886–2894, 2001.
- E. Popov, M. Neviere, B. Gralak, and G. Tayeb. Staircase approximation validity for arbitrary-shaped gratings. *Journal of Optical Society of America A*, 19(1):33–42, 2002.
- E. K. Popov, N. Bonod, and S. Enoch. Comparison of plasmon surface waves on shallow and deep metallic 1d and 2d gratings. *Optics Express*, 15(7):4224–4237, 2007.
- R. Quidant, C. Girard, J. C. Weber, and A. Dereux. Tailoring the transmittance of integrated optical waveguides with short metallic nanoparticle chains. *Physical Review B*, 69(8):085407, 2004.
- C. Schafer, D. A. Gollmer, A. Horrer, J. Fulmes, A. Weber-Bargioni, S. Cabrini, P. J. Schuck, D. P. Kern, and M. Fleischer. A single particle plasmon resonance study of 3d conical nanoantennas. *Nanoscale*, 5(17):7861–7866, 2013.

- P. Sheng, R. S. Stepleman, and P. N. Sanda. Exact eigenfunctions for square-wave gratings: Application to diffraction and surface-plasmon calculations. *Physical Review B*, 26(6):2907–2917, 1982.
- E. Silberstein. *Généralization de la méthode modale de Fourier aux problèmes de diffraction en optique intégrée. Application aux convertisseurs modaux par ingénierie des modes de Bloch*. PhD thesis, Université Paris 6, Paris, France, 2002.
- E. Simsek. Full analytical model for obtaining surface plasmon resonance modes of metal nanoparticle structures embedded in layered media. *Optics Express*, 18(2):1722–1733, 2010.
- C. Tan, J. Simonen, and T. Niemi. Hybrid waveguide-surface plasmon polariton modes in a guided-mode resonance grating. *Optics Communications*, 285(21-22):4381 – 4386, 2012.
- R. Tellez-Limon. Lentes de nano-rendijas. Master’s thesis, Centro de Investigación Científica y de Educación Superior de Ensenada, Ensenada, Baja California, Mexico, 2011.
- R. Tellez-Limon, M. Fevrier, A. Apuzzo, R. Salas-Montiel, and S. Blaize. Modal analysis of lsp propagation in an integrated chain of gold nanowires. In S. Cabrini, G. Lerondel, A. M. Schwartzberg, and T. Mokari, editors, *Proc. of SPIE*, volume 8807, page 88070J. SPIE, 2013.
- R. Tellez-Limon, M. Fevrier, A. Apuzzo, R. Salas-Montiel, and S. Blaize. Theoretical analysis of bloch modes propagation on an integrated chain of gold nanowires. *Photonics Research*, 2(1):24–30, 2014.
- A. Tervonen and B. R. W. ans S. Honkanen. Ion-exchanged glass waveguide technology: a review. *Optical engineering*, 50(7):071107, 2013.
- A. V. Tishchenko. Phenomenological representation of deep and high contrast lamellar gratings by means of the modal method. *Optical and Quantum Electronics*, 37:309–330, 2005.

- C. I. Valencia, E. R. Méndez, and B. S. Mendoza. Second-harmonic generation in the scattering of light by two-dimensional particles. *Journal of Optical Society of America B*, 20(10):2150–2161, 2003.
- W. Wang, T.-M. Hwang, W.-W. Lin, and J.-L. Liu. Numerical methods for semiconductor heterostructures with band nonparabolicity. *Journal of Computational Physics*, 190(1): 141 – 158, 2003.
- W. H. Weber and G. W. Ford. Propagation of optical excitations by dipolar interactions in metal nanoparticle chains. *Physical Review B*, 70(12):125429, 2004.
- H. Wei, A. Reyes-Coronado, P. Nordlander, J. Aizpurua, and H. Xu. Multipolar plasmon resonances in individual ag nanorice. *ACS Nano*, 4(5):2649–2654, 2010.
- T. Yang and K. B. Crozier. Surface plasmon coupling in periodic metallic nanoparticle structures: a semi-analytical model. *Optics Express*, 16(17):13070–13079, 2008.
- A. Yariv and P. Yeh. *Optical waves in crystals. Propagation and control of laser radiation*. John Wiley and Sons, 2003.

Chapter 6

Résumé de la thèse

6.1 Présentation

Depuis l'invention du microscope, l'optique a été étroitement liée au développement de systèmes de détection et d'analyse de substances chimiques et biologiques. Ces dispositifs de détection jouent un rôle essentiel dans différents domaines du développement humain, comme la conservation et la surveillance de l'environnement, la prévention des catastrophes et des maladies, l'analyse industrielle et les sciences médicales.

Les systèmes optiques intégrés ont été largement utilisés dans la détection et la caractérisation des substances biochimiques. En plus, le développement de nouvelles technologies nous permettent la fabrication des structures intégrées à l'échelle nanométrique. Cette caractéristique ouvre une nouvelle fenêtre pour le développement d'une nouvelle génération de capteurs biochimiques.

Au cours des dernières années, des différentes configurations de systèmes optiques intégrés basés sur les plasmons de surface localisés, ont été proposés. Ceux-ci permettent une l'exaltation locale du champ électromagnétique qui favorise l'interaction de celui-ci avec des substances biochimiques.

Parmi ces systèmes optiques intégrés, on trouve des systèmes du couplage entre un guide d'onde diélectrique et un guide d'onde plasmonique formé par un réseau périodique des nanoparticules métalliques. Cependant, l'absence d'une interprétation généralisée sur le mécanisme de couplage des modes entre les deux guides d'ondes, limite leur étude à

l'interaction dipolaire entre les nanoparticules.

Pour cette raison, dans ce travail de thèse nous avons réalisé une analyse exhaustive des modes guidés dans un réseau périodique de nanofils métalliques intégrés sur une guide d'onde diélectrique.

Cette analyse est basée sur la méthode modale de Fourier (FMM par ces sigles en anglais). La mise en œuvre de couches parfaitement absorbantes, permet d'adapter cette méthode pour simuler la propagation du faisceau le long de la structure intégrée et, par conséquent, de caractériser les propriétés optiques de cette structure.

Deux géométries de chaînes de nanofils métalliques ont été étudiées: nanofils avec section transversale rectangulaire et section transversale triangulaire. On montre que pour le dernier cas a lieu un meilleur renforcement du champ optique lorsqu'ils sont excités à leur résonance plasmonique avec une guide d'ondes diélectrique placée à proximité d'eux.

Afin de valider les résultats numériques fournis par la méthode proposée, nous avons fabriqué et caractérisé expérimentalement un dispositif intégré constitué par un réseau périodique de nanofils d'or placés au-dessus d'un substrat de verre contenant une guide d'onde à échange d'ions. La caractérisation des échantillons a été réalisée en champ lointain par la mesure des spectres de transmission à la sortie du guide d'onde sur verre, et en champ proche en utilisant la microscopie optique en champ proche (NSOM).

Les résultats numériques et expérimentaux obtenus suggèrent que le dispositif plasmonique intégrée proposée peut être appliqué à la détection de substances chimiques ou biologiques.

6.2 Concepts préliminaires

L'interaction des champs électromagnétiques avec des métaux nanostructurés présente des propriétés optiques très complexes et intéressantes. Ce sujet a été largement étudié depuis le début du 20^{ème} siècle. Cependant, les progrès récents concernant la structuration, la manipulation et l'observation à l'échelle nanométrique, ont attiré l'attention de la communauté scientifique, donnant naissance à un nouveau domaine de recherche: la plasmonique, la science de plasmons.

Les plasmons sont essentiellement la quantification de l'oscillation d'un gaz d'électrons libres qui se déplace dans un fond d'ions positifs en raison de la présence d'un champ électromagnétique. Il existe deux types de plasmons: les plasmons de volume et les plasmons polaritons de surface. Les premiers ne sont excités que par la collision d'une particule avec le gaz, tandis que les seconds peuvent être excités par l'interaction des photons avec le plasma.

6.2.1 Plasmons polaritons de surface

Les plasmons polaritons de surface (SPP) sont des excitations électromagnétiques évanescentes qui se propagent à l'interface entre un diélectrique et un matériau conducteur. À l'interface diélectrique-métal, les électrons de conduction du métal peuvent être traités comme un gaz d'électrons libres se déplaçant vers un fond de cœurs positifs. Comme les électrons oscillent en réponse à un champ électromagnétique appliqué, des ondes électromagnétiques se produisent via le couplage du champ électromagnétique avec les oscillations du plasma d'électrons du matériau conducteur (Kim et al., 2012).

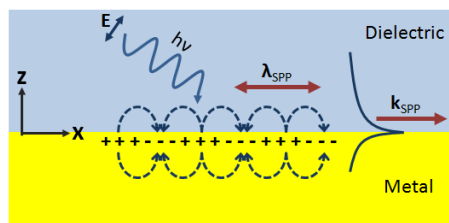


Figure 6.1: Plasmon polariton de surface : l'incidence d'une onde électromagnétique avec polarisation TM donne lieu à une onde évanescente qui se propage parallèlement à la surface d'interface.

Une des caractéristiques les plus importantes des plasmons de surface est que la fréquence de résonance du plasmon dépend des propriétés optiques du métal et du matériau diélectrique. Cette importante propriété a été largement étudiée pour l'application potentielle des SPP pour la détection des substances biochimiques.

Les plasmons de surface ne peuvent pas être directement excités par des faisceaux lumineux parce que le moment angulaire du vecteur d'onde du plasmon est toujours plus grand que le moment angulaire de la lumière se propageant dans le matériau diélectrique. Donc, pour les exciter, il faut utiliser des techniques spéciales, comme le couplage pour

prismes en configuration de Kretschmann ou d'Otto, et le couplage en utilisant réseaux de Bragg (Maier, 2007).

6.2.2 Plasmons localisés de surface

Les plasmons localisés de surface (LSP) sont un autre type d'excitation des plasmons. Ce sont des modes de surface électromagnétiques associées aux oscillations collectives des électrons de conduction dans les limites de nanoparticules métalliques (MNP) (Bohren and Huffman, 1998). Ces modes créent un renforcement du champ optique à l'intérieur de la nanoparticule, ainsi que dans la zone de champ proche autour d'elle. La longueur d'onde de résonance des LSP dépend fortement de l'indice de réfraction du milieu environnant, de même que la géométrie de la nanoparticule.

Au cours des dernières années, il a été démontré que la lumière peut se propager à travers des réseaux périodiques de MNP (Weber and Ford, 2004; Koenderink and Polman, 2006; Simsek, 2010). Ce mécanisme de propagation s'explique par le couplage en champ proche entre les particules consécutives excitées à leurs résonances plasmoniques. En raison de cet effet de couplage, les chaînes de MNP peuvent se comporter comme des guides d'ondes plasmoniques.

6.2.3 Biocapteurs plasmoniques intégrés

Comme a été mentionné précédemment, l'excitation de plasmons peut renforcer le champ optique dans une zone proche autour de la région métallique excitée. En outre, leur longueur d'onde de résonance dépend fortement des propriétés des matériaux, pas seulement du métal, mais aussi du milieu diélectrique environnant. Pour le cas particulier des plasmons de surface localisés, ils sont aussi très dépendants de la forme de la nanoparticule métallique.

Pour cette raison, les plasmons peuvent être appliqués dans différents domaines de recherche, tels que les télécommunications, l'information quantique, la biologie, la chimie, l'électronique, et la médecine, parmi beaucoup d'autres. D'un intérêt particulier dans le cadre de la présente thèse, est l'utilisation de structures optiques intégrées pour des appli-

cations de capteur des substances chimiques ou biologiques. Ces systèmes sont nommés biocapteurs.

Le principe général d'un biocapteur est assez simple: un analyte (substance à détecter) est piégé par un bio-récepteur. Ensuite, un transducteur est utilisé pour transformer le mesurande (l'objet de la mesure) en un signal utile.

Entre les mécanismes de transduction utilisés dans des biocapteurs optiques on trouve la fluorescence, la diffusion Raman, la spectroscopie de migration de photons et, bien sûr, les résonances plasmoniques de surface.

Les capteurs optiques intégrés sont les structures les plus couramment exploitées pour des applications de détection biochimiques. Ces structures adoptent une guide d'onde pour confiner la puissance optique, et sont basés sur la détection du champ évanescent. Ils présentent des avantages intéressants tels que la compacité, la très grande sensibilité et la possibilité de leur production en masse.

6.2.4 Objectif de la thèse

Bien que des réseaux plasmoniques intégrés sur une guide d'onde ont été proposées, il est nécessaire de développer une interprétation générale du mécanisme de couplage de modes dans des réseaux périodiques de MNP. Cette situation suggère la mise en œuvre d'une méthode numérique capable d'expliquer les phénomènes physiques impliqués dans la conception et la caractérisation des structures intégrées.

L'objectif principal de cette thèse est donc d'effectuer une analyse modale du mécanisme de couplage en champ proche d'une structure plasmonique intégrée formée par une structure périodique de nanofils métalliques placées sur la surface d'une guide d'onde diélectrique, une structure qui peut être appliquée pour la détection des substances chimiques ou biologiques.

Cette analyse modale est effectuée en utilisant la méthode modale de Fourier (FMM), un outil numérique rigoureux qui peut être adapté à l'analyse des courbes de dispersion des modes supportés par la structure intégrée, et de simuler la propagation d'un faisceau de lumière le long de la structure.

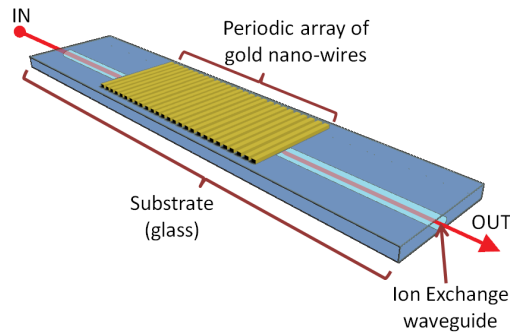


Figure 6.2: Schéma d'une structure plasmonique intégrée pour des applications de capteur.

Deux types de structures intégrées sont analysées, la première correspondant à un réseau périodique de nanofils métalliques rectangulaires (MNW), et la seconde à un réseau périodique de nanofils métalliques triangulaires (nanocônes).

Pour fournir la preuve expérimentale des résultats numériques obtenus avec la méthode proposée, nous avons fabriqué et caractérisé (en champ lointain et en champ proche) un dispositif plasmonique intégré composé d'un réseau périodique de nanofils d'or placés sur la surface d'un substrat de verre contenant un guide d'onde de verre à échange d'ions (Fig. 6.2).

6.3 La méthode numérique

L'étude analytique des modes de propagation dans un réseau métallique périodique dans la direction de propagation du champ électromagnétique, entre deux milieux semi-infinis homogènes, peut être effectuée en utilisant la méthode modale (Tishchenko, 2005).

L'idée de la méthode modale est d'abord de présenter le champ à l'intérieur du réseau sous forme de modes d'une structure périodique infinie, puis, de faire correspondre les modes du réseau aux interfaces avec le substrat et le superstrat avec les ordres de diffraction sous et au-dessus du réseau.

En utilisant l'équation de Helmholtz, les conditions aux limites entre deux milieux (la conservation des composantes tangentes), et conditions de périodicité (le théorème de Bloch), on trouve que la constante de propagation $\beta_q = k_0 n_{\text{eff},q}$ pour le mode de propagation q , doit vérifier la relation de dispersion

$$\cos(\alpha_I g) \cos(\alpha_{II} w) - \frac{1}{2} \left[\frac{\alpha_I \nu_{II}}{\nu_I \alpha_{II}} + \frac{\alpha_{II} \nu_I}{\nu_{II} \alpha_I} \right] \sin(\alpha_I g) \sin(\alpha_{II} w) = \cos(k_x \Lambda), \quad (6.1)$$

où

$$\alpha_{I,II} = k_0 \sqrt{n_{I,II}^2 - n_{\text{eff},q}^2}, \quad (6.2)$$

$k_0 = 2\pi/\lambda$ est le vecteur d'onde dans l'espace libre, n_I et n_{II} sont les indices de réfraction dans le métal de largeur w et le diélectrique de largeur g , respectivement, et $\nu_I = \nu_{II} = 1$ si le champ électromagnétique incident a une polarisation TE, et $\nu_{I,II} = n_{I,II}^2$ pour une polarisation TM.

Cette relation de dispersion est une fonction transcendante sans solution analytique, et des outils numériques doivent être utilisés.

Une autre façon possible et efficace de trouver les modes électromagnétiques d'un réseau périodique est l'expansion des paramètres du milieu et du champ électromagnétique en séries de Fourier. Cette méthode de résolution est la méthode modale de Fourier (FMM).

La FMM est une méthode numérique qui résout les équations de Maxwell dans le domaine des fréquences. Il s'agit d'une méthode modale qui est basée sur l'expansion en série de Fourier de toutes les quantités électromagnétiques impliquées dans les équations de Maxwell (Moharam and Gaylord, 1981; Chateau and Hugonin, 1994; Hugonin and Lalanne, 2005).

La solution générale de la FMM consiste en deux étapes principales:

- i) Le calcul des valeurs propres et des vecteurs propres d'une matrice d'éléments constants qui caractérise la propagation et couplage de l'onde diffractée dans un profil de l'axe de propagation, ainsi que les indices effectifs correspondant à ces modes, et
- ii) La reconstruction du champ électromagnétique totale en résolvant un système linéaire conditionné par les conditions aux limites (conservation des composants tangentiels des champs électrique et magnétique), en tenant compte du fait que pour chaque mode existe un composant propagé et un autre composant contra-propagé.

L'avantage de cette méthode est qu'elle permet non seulement l'étude des modes propagés dans systèmes périodiques infinies de nanoparticules intégrées sur une guide d'onde diélectrique, mais aussi l'étude de la propagation des modes dans une structure périodique finie, c'est-à-dire, de caractériser une structure plasmonique intégrée réelle (Tellez-Limon et al., 2014).

La description détaillée de la méthode et leur implémentation numérique est décrite dans le chapitre 2 de la thèse.

6.4 Analyse numérique des structures plasmoniques intégrées

Comme nous avons dit précédemment, un réseau périodique de nanoparticules métalliques (MNP) peut se comporter comme une guide d'onde plasmonique permettant ainsi la propagation des modes guidés. Cet effet de guidage est dû au couplage en champ proche entre particules consécutives lorsqu'elles sont excitées à leur résonance plasmonique.

Néanmoins, la grande majorité des travaux consacrés à ce sujet, a été effectuée au-dessus de la ligne de lumière dans les relations de dispersion, où les modes sont rayonnés soit vers le substrat, soit vers le superstrat.

Afin d'étudier la propagation des modes confinés le long de la chaîne des MNP en dessous de la limite de la ligne de lumière, nous étudions des chaînes périodiques de nanoparticules métalliques intégrées sur la surface d'une guide d'onde diélectrique.

En utilisant la méthode modale de Fourier, deux géométries des nanoparticules sont présentées. Premièrement, un réseau périodique de nanofils métalliques rectangulaires (MNW), et ensuite, un réseau périodique de nanofils métalliques triangulaires (nanocônes). Pour les deux cas sont présentés les courbes de dispersion, ainsi que les spectres de transmission, réflexion et absorption pour le système fini intégré.

6.4.1 Modes de propagation dans un réseau périodique de nanofils métalliques

La Figure 6.2 montre la structure plasmonique intégrée à analyser. Cette structure est composée de un réseau périodique de nanofils d'or de largeur $w = 80$ nm, période $\Lambda = 130$ nm, et hauteur e , immergé dans un milieu diélectrique homogène avec un indice de réfraction $n_d = 1.5$ (du verre). A une distance $h_2 = 30$ nm est placée une guide d'onde diélectrique d'indice de réfraction $n_w = 2.0$ et épaisseur $h_1 = 200$ nm. Afin d'observer l'effet du rapport d'aspect des nanofils, deux cas ont été analysés, $e = 20$ nm et $e = 150$ nm.

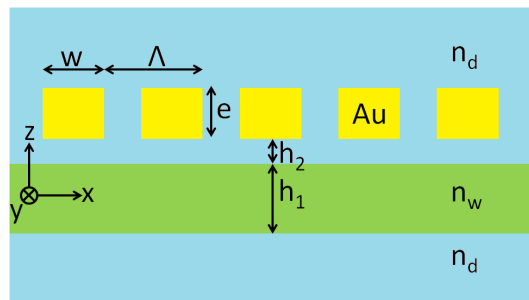


Figure 6.3: Chaîne périodique de nanofils d'or intégrée sur une guide d'onde diélectrique.

Nanofils métalliques de faible hauteur

La Figure 6.4 montre les courbes de dispersion pour le système intégré lorsque la hauteur des nanofils est fixée à 20 nm. Les courbes en noir, vert et rose représentent respectivement la condition de Bragg (limite de la première zone de Brillouin), et les lignes de lumière du verre et du guide d'onde. La courbe des triangles en bleu représente le mode fondamental TM₀ supporté par la guide d'onde diélectrique, et les astérisques en vert correspondent au mode supporté par les nanofils. Pour déduire la nature de ce mode, nous avons calculé leur densité d'énergie en champ proche à la condition de Bragg à une longueur d'onde $\lambda = 645$ nm (Fig. 6.5). Dans cette cartographie on observe que les nanofils se comportent comme des dipôles électriques orientés parallèlement à la direction de propagation du champ électromagnétique. C'est-à-dire, il s'agit d'un mode dipolaire longitudinal.

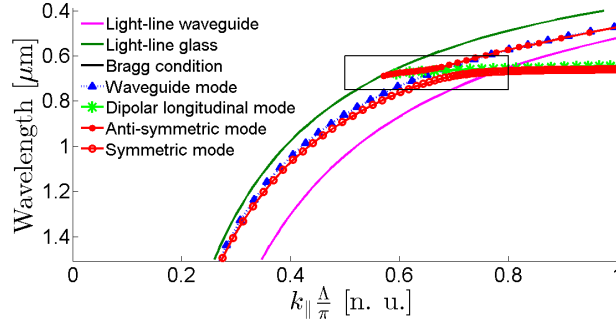


Figure 6.4: Courbes de dispersion pour une structure périodique de nanofils d'or de $e = 20$ nm d'hauteur intégrée sur une guide d'onde diélectrique. Le mode dipolaire longitudinal est couplé avec le mode fondamentale TM0 du guide d'onde diélectrique à une longueur d'onde $\lambda = 664$ nm.

Dans les courbes de dispersion on observe un point de croisement entre le mode dipolaire longitudinal et le mode fondamental TM0 du guide d'onde à une longueur d'onde de $\lambda = 664$ nm, c'est-à-dire, que le mode dipolaire est couplé avec le mode TM du guide d'onde. Ce couplage génère l'apparition de deux branches, à savoir, le mode symétrique et le mode antisymétrique (représentés par les cercles et points rouges dans les courbes de dispersion, respectivement). Ce phénomène est le comportement typique d'un système de deux guides d'onde couplés.

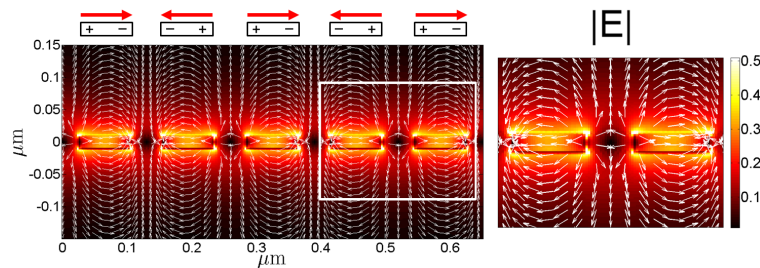


Figure 6.5: Densité d'énergie et distribution des lignes de champ électrique pour le mode dipolaire longitudinal à la condition de Bragg à une longueur d'onde $\lambda = 645$ nm.

Lorsque nous avons effectué la simulation de la propagation des modes le long du système intégré constitué par une chaîne finie de 27 nanofils, nous avons observé deux valeurs minimales dans le spectre de transmission (Fig. 6.6a). Le premier, à une longueur d'onde $\lambda = 520$ nm, est dû à une réflexion de Bragg (également observable dans le spectre de réflexion à $\lambda = 474$ nm), tandis que le second minimum, à une longueur d'onde $\lambda = 678$ nm, est dû à l'excitation efficace du mode longitudinal dipolaire, ce qui donne lieu à un échange d'énergie entre la guide d'onde diélectrique et les nanofils métalliques, comme on

peut observer dans les cartographies de champ proche sur la Fig. 6.6b.

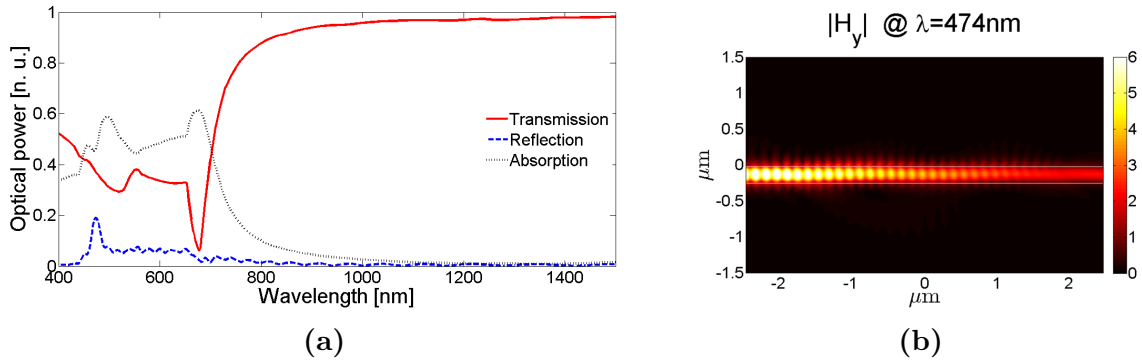


Figure 6.6: (a) Spectres de transmission, réflexion et absorption pour une chaîne de 27 nanofils d'or d'hauteur 20 nm, intégrée sur une guide d'onde diélectrique. La première valeur minimale dans la courbe de transmission ($\lambda = 520 \text{ nm}$) est due à une réflexion de Bragg, et la deuxième ($\lambda = 678 \text{ nm}$) à l'excitation du mode dipolaire longitudinal. (b) Quand le mode dipolaire longitudinal est excité, il y a un échange d'énergie entre les nanofils d'or et le guide d'onde.

Nanofils métalliques de grande hauteur

Les courbes de dispersion pour le cas des nanofils d'hauteur 150 nm sont montrées dans la Figure 6.7. Là encore, les lignes en noir, vert et rose représentent, respectivement, la condition de Bragg, et les lignes de lumière du verre et du guide d'onde. Le mode fondamentale TM_0 du guide d'onde est représenté par la ligne des triangles bleus.

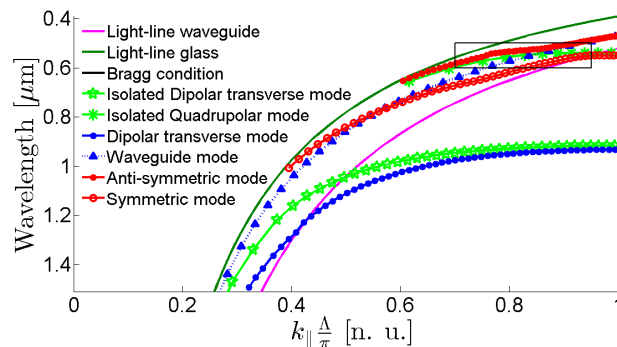


Figure 6.7: Courbes de dispersion pour une structure périodique de nanofils d'or d'hauteur $e = 150 \text{ nm}$ intégrée sur une guide d'onde diélectrique. Le mode quadripolaire est couplé avec le mode fondamental TM_0 du guide d'onde diélectrique à une longueur d'onde $\lambda = 546 \text{ nm}$.

Pour ce cas, il existe deux modes supportés par la chaîne des nanofils d'or. Le premier (étoiles vertes) est un mode quadripolaire, et le second (astérisques verts) est un

mode dipolaire transversal. Ces modes sont identifiés dans les cartographies de densité d'énergie calculées à la condition de Bragg, aux longueurs d'onde $\lambda = 540$ nm pour le mode quadripolaire (Fig. 6.8a 8a), et à $\lambda = 916$ nm pour le mode dipolaire transversal (Fig. 6.8b).

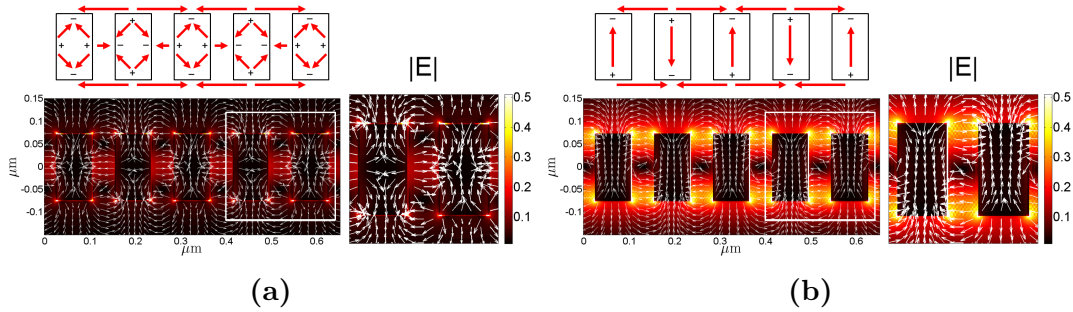


Figure 6.8: Densité d'énergie et distribution des lignes du champ électrique des nanofils d'or avec une hauteur de 150 nm, calculés à la condition de Bragg pour (a) le mode quadripolaire ($\lambda = 540$ nm) et (b) le mode dipolaire transversal ($\lambda = 916$ nm).

Dans les courbes de dispersion nous observons un point d'anti-croisement entre le mode quadripolaire et le mode fondamentale TM₀ du guide d'onde diélectrique à une longueur d'onde de $\lambda = 546$ nm, issu de la création de modes hybrides symétrique et anti-symétrique (représentés par les cercles et points rouges, respectivement). Comme dans le cas des nanofils de 20 nm d'hauteur, cela signifie qu'il y a un couplage entre le mode quadripolaire propagé le long du réseau de nanofils et la mode fondamentale TM du guide d'onde diélectrique. Cependant, pour le cas du mode dipolaire transversal il n'y a pas un croisement avec le mode TM₀, donc il n'est pas envisagé un couplage efficace entre ces modes.

Pour observer l'interaction entre le mode TM₀ du guide d'onde et les modes quadripolaire et dipolaire transversal supportés par la chaîne des nanofils d'or, nous avons réalisé des simulations de la propagation des modes le long du système intégré, avec une chaîne finie de 27 nanofils d'or. Le spectre de transmission (Fig. 6.9) montre plusieurs valeurs minimales. Les deux premières localisées aux longueurs d'onde $\lambda = 534$ nm et $\lambda = 559$ nm, correspondent à la réflexion de Bragg et à l'excitation du mode quadripolaire, respectivement. La cartographie du champ proche illustré dans la Figure 10a, montre le couplage entre le mode fondamental TM₀ du guide d'onde et le mode quadripolaire.

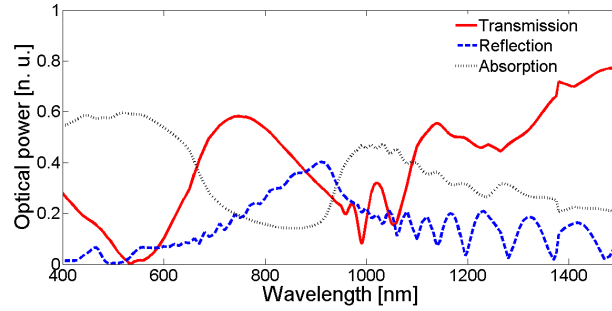


Figure 6.9: Spectres de transmission, réflexion et absorption pour la structure plasmonique intégrée de nanofils d'or avec une hauteur de 150 nm. L'excitation des modes quadripolaire et dipolaire transversal sont trouvés aux longueurs d'onde $\lambda = 559$ nm et $\lambda = 990$ nm, respectivement.

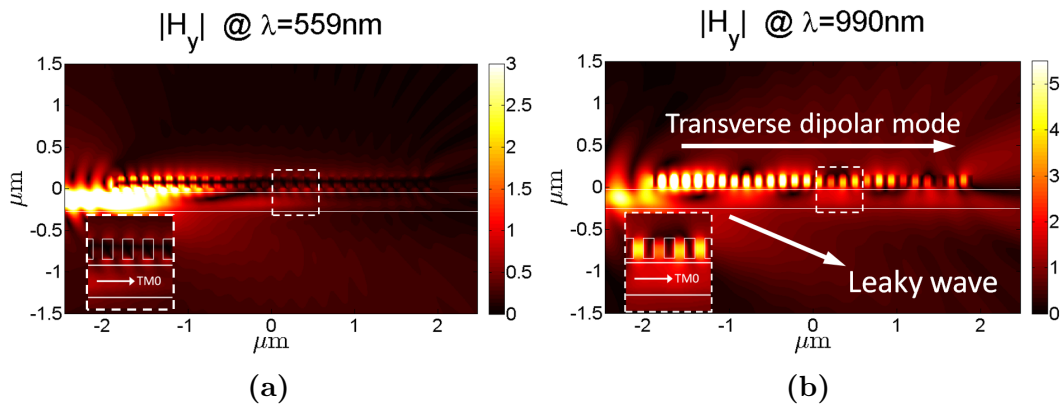


Figure 6.10: Cartes de champ proche (a) du mode quadripolaire et (b) du mode dipolaire transversal. Dans les deux cas est observé un échange d'énergie entre la guide d'onde diélectrique et le réseau de nanofils d'or.

D'autre part, les valeurs minimales observées dans le spectre de transmission aux longueurs d'onde $\lambda = 960$ nm, $\lambda = 990$ nm et $\lambda = 1055$ nm, correspondent, respectivement, à la réflexion de Bragg et l'excitation du mode dipolaire transversal, et un mode de cavité ce qui est dû à la dimension finie du réseau des nanofils. Bien que nous n'avons pas attendu une excitation efficace du mode dipolaire transversal, la cartographie de champ proche (Fig. 6.10b) montre tout le contraire : il y a un échange d'énergie entre la chaîne de nanofils et la guide d'onde diélectrique. Ce fait est dû à une interférence entre le mode guidé et un mode à fuite (Tellez-Limon et al., 2014).

Les résultats obtenus démontrent que le réseau périodique de nanofils métalliques intégré sur une guide d'onde diélectrique se comporte comme un système de deux guides d'ondes couplés. Ceci suggère que la structure plasmonique intégrée peut être utilisée comme un biocapteur.

6.4.2 Modes de propagation dans un réseau périodique de nanocônes métalliques

Il est bien connu que les résonances des plasmons localisés dépendent fortement de la géométrie des nanoparticules métalliques (Noguez, 2007). Une des formes les plus intéressantes et peu exploitées dans les systèmes intégrés, sont les particules en forme de nanocône. En effet les nanocônes présentent un renforcement du champ optique (points chauds) au sommet (D'Agostino et al., 2013), propriété qui peut être appliquée, par exemple, dans la détection de molécules individuelles.

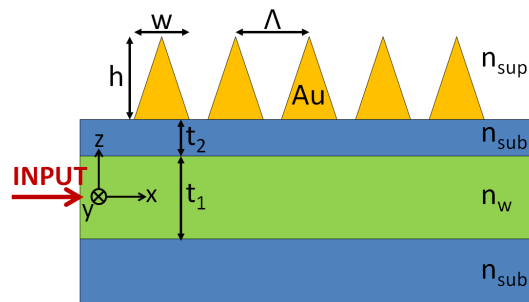


Figure 6.11: Structure plasmonique intégrée conformée par un réseau périodique de 5 nanocônes d' hauteur $h = 144$ nm, largeur $w = 72$ nm et périodicité $\Lambda = 200$ nm, placée sur la surface d'un substrat du verre ($n_{sub} = 1.5$) contenant un guide d'onde diélectrique d'indice de réfraction $n_w = 2.0$, d'épaisseur $t_1 = 200$ nm, enterré à une profondeur $t_2 = 30$ nm. Le superstrat est de l'air ($n_{sup} = 1.0$).

Sur la base de la méthode modale de Fourier, nous avons réalisé une étude paramétrique des résonances des plasmons localisés d'une chaîne de nanocônes d'or, placés sur la surface d'un substrat du verre, en fonction de l'angle d'incidence de la lumière incidente et de leur périodicité. Une fois déterminés les conditions optimales de la structure périodique pour avoir une bonne excitation des résonances plasmoniques, est simulée la propagation du champ électromagnétique le long de la structure plasmonique intégrée (Fig. 6.11).

Réseau périodique de nanocones métalliques sur un substrat diélectrique

Dans les tracés de la Figure 6.12 sont présentés les spectres de transmission, de réflexion et d'absorption du champ électromagnétique en fonction de l'angle d'incidence de l'onde plane avec polarisation TM, en fixant la période de la structure à $\Lambda = 200$ nm. Dans la

carte d'absorption, on peut regarder deux branches de résonances. La première est excitée proche à l'angle critique ($\theta_{inc} = 43^\circ$) et une longueur d'onde $\lambda = 530$ nm. La deuxième résonance est excitée à un angle rasant $\theta_{inc} = 88^\circ$ et une longueur d'onde $\lambda = 800$ nm. Cette deuxième résonance n'a pas été observée pour le cas d'un nanocône isolé (voir section 3.4.1), donc, on assume qu'il s'agit d'un mode de chaîne dû à l'interaction en champ proche entre les nanocônes.

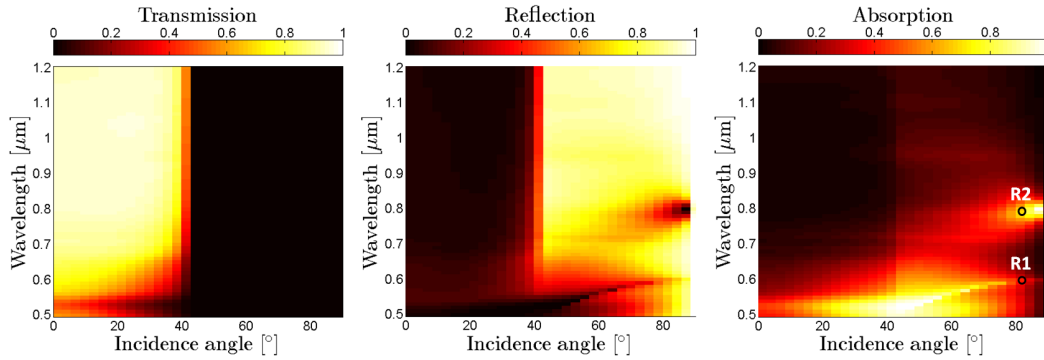


Figure 6.12: Spectres de transmission, de réflexion et d'absorption d'une chaîne de nanocônes d'or en fonction de l'angle d'incidence d'une onde plane avec polarisation *TM*. La période de la structure est fixée à 200 nm. Le mode dipolaire transversal *R2* est excité seulement aux angles rasants.

Pour vérifier si la deuxième résonance est due à une mode de la chaîne de nanocônes, nous avons calculé les spectres de transmission, de réflexion et d'absorption, en fonction de la période de la chaîne des nanocônes (Fig. 6.13). La chaîne est illuminée dès le substrat avec une onde plane en polarisation *TM* à un angle d'incidence de 82° par rapport à la normale de la surface. Les lignes bleues et rouges représentent des zones de Brillouin du substrat de verre et de la couche supérieure d'air, respectivement (des ordres consécutifs de diffraction).

Dans les spectres de réflexion et d'absorption peuvent être observées deux branches au-dessus de la ligne du substrat dans la première zone de Brillouin (minimal dans la réflexion et maximal dans l'absorption). Ces résonances correspondent aux modes de propagation. A la condition de Bragg de la première zone de Brillouin, la première branche (longueurs d'onde plus courtes) présente une valeur maximale à une longueur d'onde $\lambda = 560$ nm et une période $\Lambda = 187$ nm, tandis que la seconde branche (longues longueurs d'onde) présente une valeur maximale à la condition de Bragg à $\lambda = 830$ nm et $\Lambda = 277$ nm. Dans

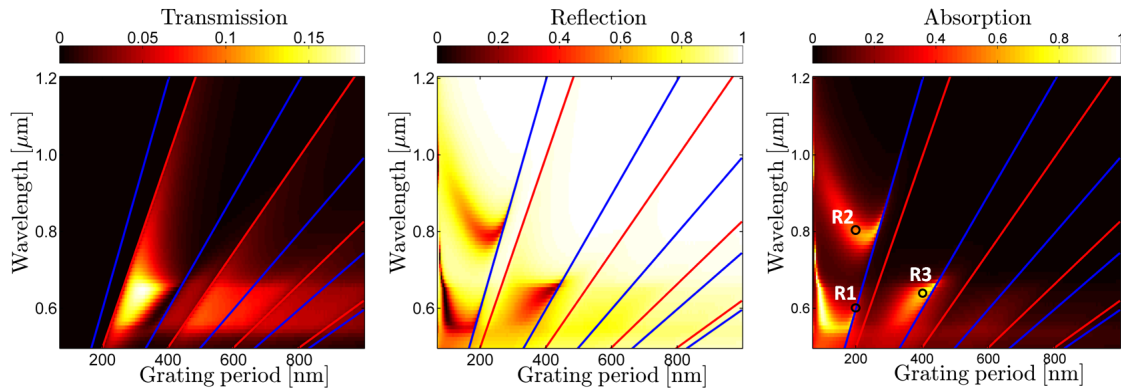


Figure 6.13: Spectres de transmission, réflexion et absorption d'une chaîne de nanocônes d'or en fonction de leur périodicité. Des valeurs maximales d'absorption sont localisées aux longueurs d'onde $\lambda = 560$ nm (proche du point R1), $\lambda = 830$ nm (proche du point R2), et $\lambda = 660$ nm (proche du point R3).

la seconde zone de Brillouin, on peut également observer une troisième branche avec une valeur maximale dans le second ordre de la condition de Bragg à $\lambda = 660$ nm et une période $\Lambda = 442$ nm.

Afin de déterminer la nature de chacune de ces branches, des cartographies de densité d'énergie sont tracées en régime du champ proche pour trois valeurs différentes, marquées par les points R1, R2 et R3 sur les cartographies du Fig. 6.14.

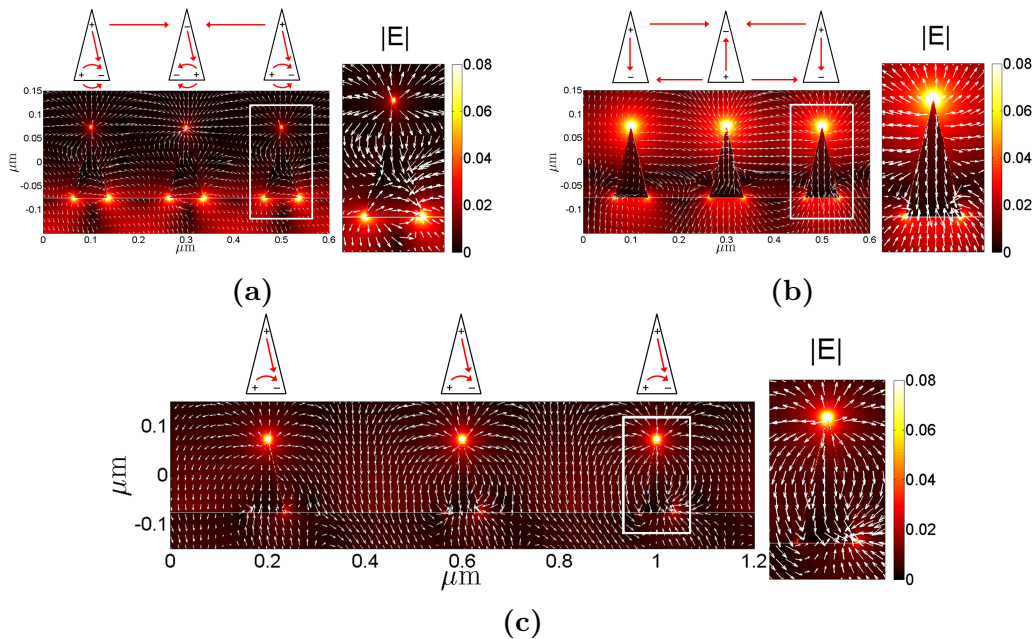


Figure 6.14: Distribution de la densité d'énergie (normalisées aux valeurs maximales) et lignes du champ électrique pour les résonances (a) R1 ($\lambda = 600$ nm, $\Lambda = 200$ nm), (b) R2 ($\lambda = 800$ nm, $\Lambda = 200$ nm), et (c) R3 ($\lambda = 660$ nm, $\Lambda = 400$ nm).

A la résonance R1 est observé un comportement multipolaire des nanocônes (une sorte de mélange entre un mode dipolaire longitudinal et un mode dipolaire transversal). Dans la résonance R2 est clairement identifié un comportement dipolaire transversal qui, en plus de favoriser le couplage entre les nanocônes, montre un renforcement du champ optique au sommet des nanocônes. La résonance R3 montre le même comportement que la résonance R2, parce qu'elle est la projection de R2 sur la deuxième zone de Brillouin.

Ces nouveaux résultats montrent que le mode dipolaire transversal ne peut être excité qu'avec une onde incidente à un angle rasant et si la période du réseau des nanocônes est plus courte que la longueur d'onde de la lumière incidente. Cela signifie qu'on pourrait exciter le mode dipolaire transversal avec le mode fondamental TM0 d'un guide d'onde diélectrique placé au-dessous de la chaîne.

Réseau périodique des nanocônes métalliques dans un système intégré

A l'aide de la FMM, nous avons calculé les spectres de transmission et de réflexion pour une chaîne de 5 nanocônes intégrées sur la surface d'un substrat de verre qui contient une guide d'onde diélectrique (Fig.6.11). Les courbes de dispersion, ainsi que les spectres de transmission et réflexion sont tracés dans la Figure 6.15.

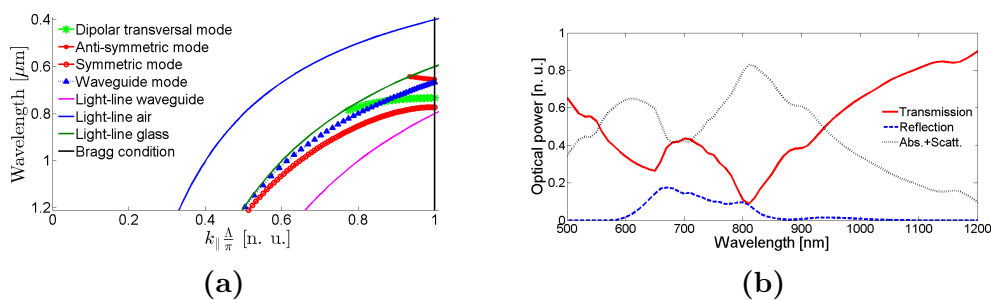


Figure 6.15: (a) Courbes de dispersion du réseau périodique de nanocônes d'or intégré avec une guide d'onde, et (b) spectres de transmission, de réflexion et d'absorption pour une chaîne de 5 nanocônes.

Les courbes de dispersion montrent que le mode dipolaire transversal de la chaîne infinie de nanocônes d'or, est couplé avec le mode fondamental TM0 du guide d'onde diélectrique à une longueur d'onde $\lambda = 747$ nm. Puis, en mesurant le spectre de transmission pour une chaîne fini de 5 nanocônes intégrés avec une guide d'onde, on observe deux valeurs minimales de transmission, correspondant à la réflexion de Bragg ($\lambda = 650$

nm) et l'excitation du mode dipolaire transversal ($\lambda = 810$ nm). La distribution du champ électrique correspondant à l'excitation du mode dipolaire transversal est tracée dans la Figure 6.16. Lorsque l'on regarde cette cartographie, il est clair que le champ électrique est fortement exalté au sommet des nanocônes. Cette exaltation du champ optique représente un avantage pour des systèmes de détection.

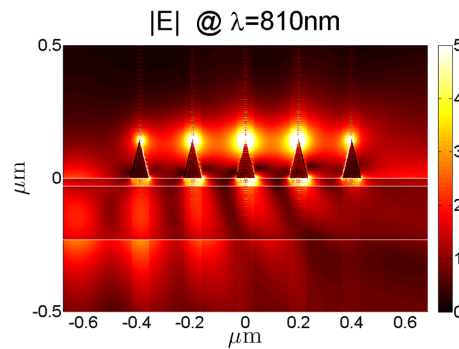


Figure 6.16: Distribution de champ électrique à une longueur d'onde $\lambda = 810$ nm. Le mode dipolaire transversal est efficacement excité avec le mode fondamental TM_0 du guide d'onde, on obtient en conséquence une forte exaltation du champ optique au sommet des nanocônes.

6.5 Résultats expérimentaux

Comme a été déjà montré par des calculs numériques, un réseau périodique de nanofils d'or de faible hauteur support la propagation d'un mode dipolaire longitudinal. Ce mode peut être excité avec le mode fondamental TM_0 d'une guide d'onde diélectrique placée à proximité du réseau.

Nous avons étudié expérimentalement une telle structure de nanofils d'or, intégrée sur un guide optique obtenu par échange d'ions dans un substrat de verre. Ce type de guides est largement utilisé dans des systèmes intégrés parce qu'elles ne sont pas très coûteux, elles sont compatibles avec des fibres optiques, et sont optiquement stables.

Donc, en utilisant la méthode modale de Fourier, nous avons calculé des courbes de dispersion pour différents périodes de la chaîne des nanofils d'or afin de déterminer les conditions optimales pour exciter et propager le mode dipolaire longitudinal.

D'après les résultats obtenus avec la FMM, quand on utilise une guide d'onde à échange d'ions enterré dans un substrat de verre, on peut exciter de façon efficace la propagation

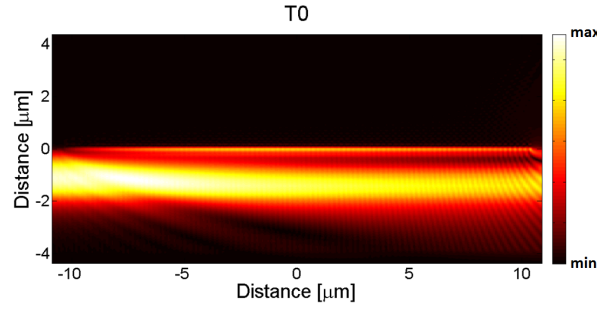


Figure 6.17: Cartographie du champ proche du composant $|H_y|$ pour une chaîne de 200 nanofils d'or de hauteur 30 nm et période $\Lambda = 100$ nm, intégrée sur la surface d'une guide à échange d'ions. Quand la longueur d'onde du mode fondamental TM_0 est $\lambda = 685$ nm, le mode dipolaire longitudinal est excité.

du mode dipolaire longitudinale quand la hauteur des nanofils est de 30 nm, et une période $\Lambda = 100$ nm. Dans la Figure 6.17 est montrée la cartographie du composant $|H_y|$ du champ électromagnétique qui se propage le long de la structure intégrée. Dans cette figure on observe clairement que le mode dipolaire transversal est couplé avec le mode fondamental TM_0 du guide d'onde à échange d'ions.

Pour valider ces résultats, nous avons fabriqué sur la surface d'une guide d'onde à échange d'ions, un réseau périodique de nanofils d'or, comme le système illustré dans la Figure 6.2. La fabrication des nanofils a été réalisée en utilisant la lithographie électronique. Tous les paramètres du processus de fabrication sont détaillés dans le chapitre 4 de la thèse.

Structure	Largueur	Période
T1	79 nm	173 nm
T2	74 nm	186 nm
T3	67 nm	198 nm

Table 6.1: Longueur totale et période des réseaux de nanofils fabriqués par lithographie électronique dans la surface d'un substrat du verre.

Trois réseaux de nanofils avec différents périodes ont été fabriqués. Leur largeur totale et leur période sont donnés dans la Table 6.1. Dans la Figure 6.18 sont montrées les images obtenues par microscopie électronique pour chacune des différentes structures, identifiées comme T1, T2 et T3.

Les réseaux fabriqués ont une période plus courte que la longueur d'onde de la lumière

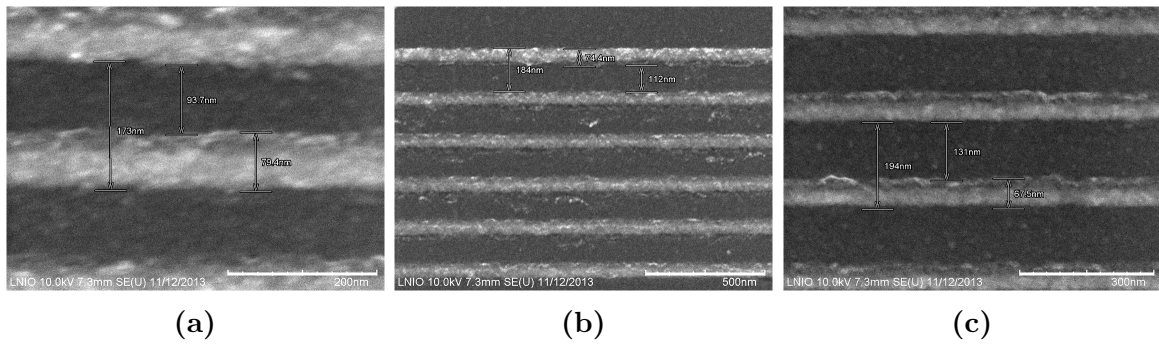


Figure 6.18: Images par microscopie électronique des réseaux type (a) T1, (b) T2 et (c) T3, fabriqués sur un substrat de verre.

dans le spectre visible. Mais malgré cela, les simulation FMM montrent que cette période n'est pas assez courte pour obtenir un couplage efficace entre le mode TM₀ du guide d'onde à échange d'ions et le mode dipolaire longitudinal excité dans la chaîne.

Pour vérifier ces prédictions, nous avons caractérisé les échantillons fabriqués dans le champ-lointain, en mesurant leurs spectres de transmission à la sortie du guide d'onde à échange d'ions. De la même façon, en utilisant la technique microscopie optique de balayage en champ-proche (NSOM), nous avons mesurée l'amplitude du champ électromagnétique dans le réseau de nanofils.

6.5.1 Caractérisation de l'échantillon dans le champ lointain

Des spectres de transmission sont obtenus en utilisant une source blanche à super-continuum. Le système expérimental contient également un contrôleur de polarisation à l'entrée permettant de sélectionner les modes fondamentaux TE ou TM du guide d'onde à échange d'ions. Comme nous pouvons observer dans les images de la Figure 6.19, quand est sélectionné le mode de polarisation TM, il y a une exaltation du champ optique diffusé dans la zone correspondant aux nanofils d'or. Par contre, quand le mode de polarisation TE a été sélectionné, nous n'avons pas observé cette exaltation du champ optique diffusé. Ce résultat est cohérent avec ce qui a été étudié dans la théorie et confirme que nous avons bien choisi le mode de propagation TM₀ dans les simulations réalisées.

Les spectres de transmission mesurés expérimentalement pour chacune des types de structures fabriquées (T1, T2 et T3), sont illustrés dans la colonne à gauche de la Figure 6.20. Pour chacun de ces spectres, sont montrés leurs spectres de transmission respectifs,

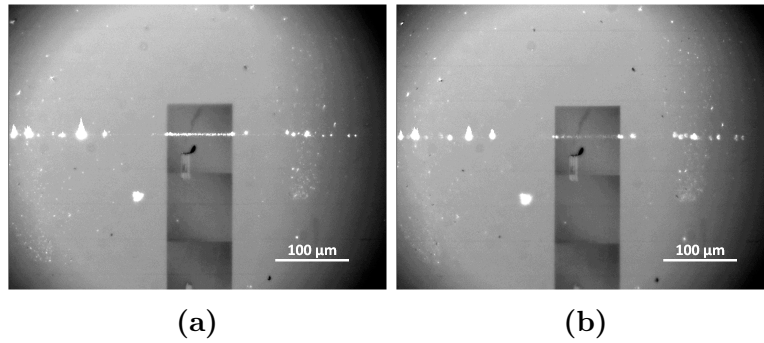


Figure 6.19: Images en champ-lointain de la diffusion des nanofils d'or quand ils sont excités avec le mode (a) TM_0 et (b) TE_0 du guide d'onde à échange d'ions. Sous polarisation TM , la résonance du plasmon localisé est bien excitée le long la chaîne de nanofils, tandis que pour le mode TE il y a une faible interaction.

obtenus avec la FMM.

Dans chaque spectre mesuré, nous avons observé une valeur minimale de transmission à une longueur d'onde constante de $\lambda = 785$ nm, qui correspond à la faible interaction du mode TE_0 avec les nanofils. Cependant comme le mode TE n'excite pas la résonance du plasmon localisé cette valeur est plutôt associée à la diffusion de la lumière vers le substrat.

Par contre, l'excitation de la résonance plasmonique est obtenue avec le mode TM . Cette excitation est identifiée comme une valeur minimum dans les spectres de transmission. Comment on le peut constater, la longueur d'onde de résonance est modifiée en fonction de la période des nanofils.

Dans les spectres expérimentaux, il est observé que pour la chaîne type T1 la résonance du plasmon localisé est excitée à une longueur d'onde $\lambda = 702$ nm (Fig. 6.20a), pour la structure type T2 à $\lambda = 675$ nm (Fig. 6.20c), et pour T3 à $\lambda = 668$ nm (Fig. 6.20e). Cela signifie que quand la période des nanoparticules est réduite, la longueur d'onde de la résonance du plasmon localisé est incrémentée.

Lorsque l'on compare les spectres de transmission mesurés expérimentalement avec les spectres théoriques obtenus avec la FMM, on peut observer la même dépendance de la longueur d'onde de résonance en fonction de la période du réseau des nanofils d'or. Cependant, il y a des différences entre les valeurs minimales des courbes de transmission expérimentales et théoriques. Les spectres obtenus avec la FMM montrent que pour la

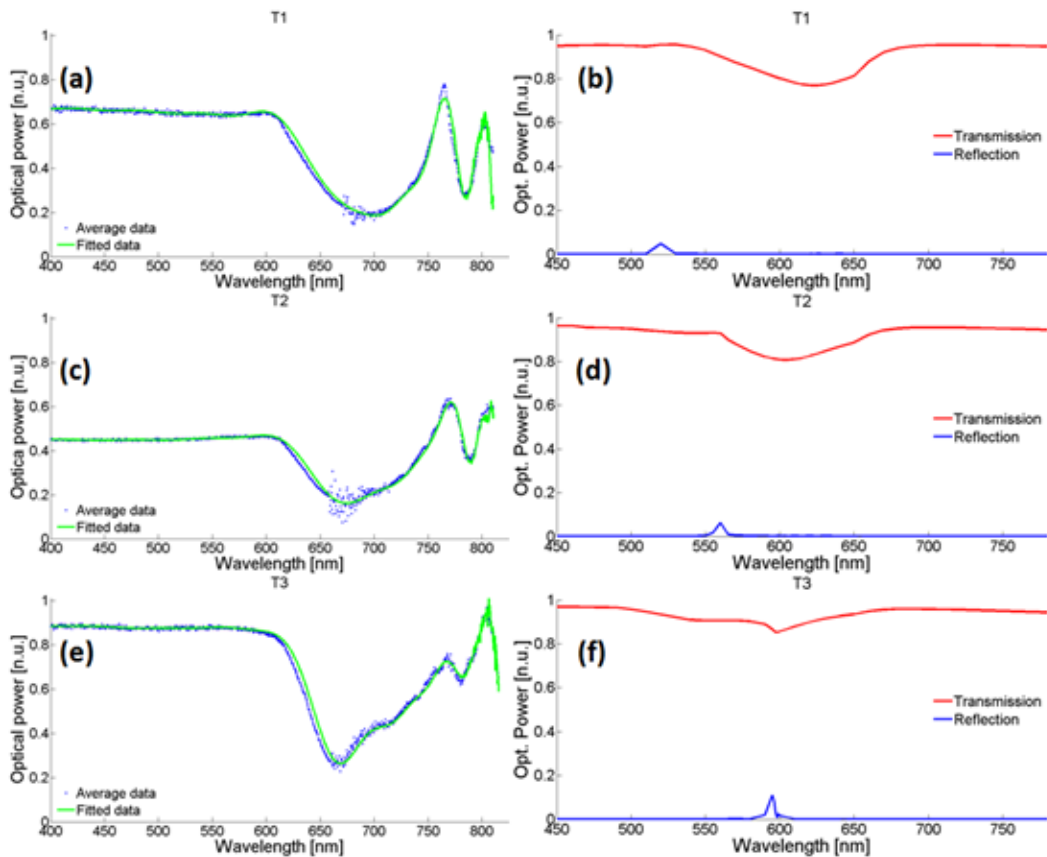


Figure 6.20: Spectres de transmission expérimentaux (à gauche) et théoriques (à droite) pour chacune des structures: (a) et (b) pour la structure T1; (c) et (d) pour la structure T2; (e) et (f) pour la structure T3.

structure type T1, l'excitation du plasmon localisé correspond à une longueur d'onde $\lambda = 625$ nm (Fig. 6.20b), pour la structure T2 à $\lambda = 605$ nm (Fig. 6.20d), et pour la structure T3 à $\lambda = 598$ nm (Fig. 6.20f).

Différents facteurs contribuent à ces décalages dans la longueur d'onde. Tout d'abord, le modèle numérique a été développé pour des structures bidimensionnelles alors que les structures réelles sont tridimensionnelles. Aussi, pour les calculs numériques nous avons utilisé un nombre de 200 nanofils d'or, tandis que le réseau fabriqué a 500 nanofils d'or. En plus, les échantillons fabriqués ne sont pas sans défauts, les nanofils présentent des rugosités et leur période peut changer un peu. Mais le facteur le plus important est la différence entre les valeurs théoriques et réelles de la fonction diélectrique de l'or et de la couche d'ITO. Malgré ces différences dans les valeurs des résonances d'excitation, la forme des courbes spectrales sont vraiment pareilles entre eux. Donc, la FMM est un outil numérique qui nous a permis caractériser le comportement des spectres de transmission

pour une structure plasmonique intégrée.

6.5.2 Observations en champ proche

L'une des plus efficaces techniques de caractérisation des structures plasmoniques intégrées en champ proche est la microscopie optique du balayage (NSOM pour leur acronyme en anglais), une technique qui a été maîtrisée au long des dernières années au sein du LNIO à l'UTT.

Deux configurations du NSOM ont été utilisées pour la caractérisation des échantillons fabriqués : le NSOM-hétérodyne (H-NSOM) et le NSOM sans ouverture (A-NSOM). La première a été utilisée pour caractériser une guide d'onde à échange d'ions, et la deuxième pour la caractérisation de la structure plasmonique intégrée type T2. Une description plus détaillée de ces techniques est donnée dans le chapitre 4 de la thèse.

Dans la Figure 6.21 sont montrés les cartes de l'intensité et de la phase du champ électromagnétique propagé le long du guide d'onde à échange d'ions. En effectuant la transformée de Fourier dans un profil le long de la carte de phase, on a déterminé que l'indice effective du mode qui se propage dans la guide d'onde à une longueur d'onde $\lambda = 632.8$ nm, a une valeur $n_{eff} = 1.52 \pm 0.17$.

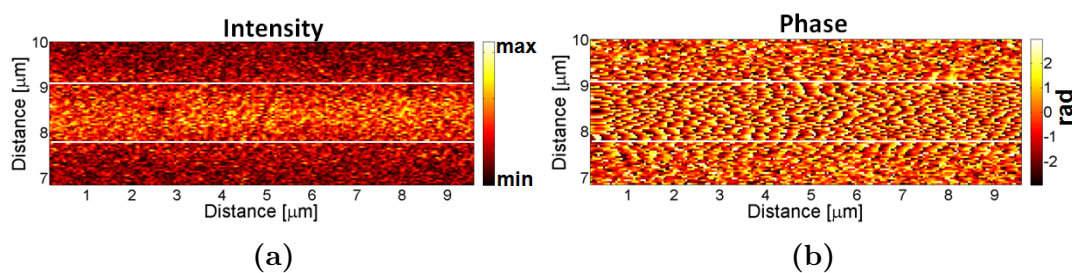


Figure 6.21: Cartes de l'intensité (a) et de la phase (b) du champ électromagnétique du mode propagé à une longueur d'onde $\lambda = 632.8$ nm, mesurées avec l'H-NSOM. En utilisant la transformée de Fourier, on a trouvé que l'indice effective du mode propagé à une valeur $n_{eff} = 1.52 \pm 0.17$.

Concernant à la structure plasmonique intégrée, seulement a été mesuré la topographie sur la surface de la structure, et l'amplitude du champ électromagnétique. La phase ne peut pas être mesurée avec l'A-NSOM. Ces résultats sont montrés dans la Figure 6.22.

Dans la carte d'intensité, on peut regarder que le champ optique est exalté dans la

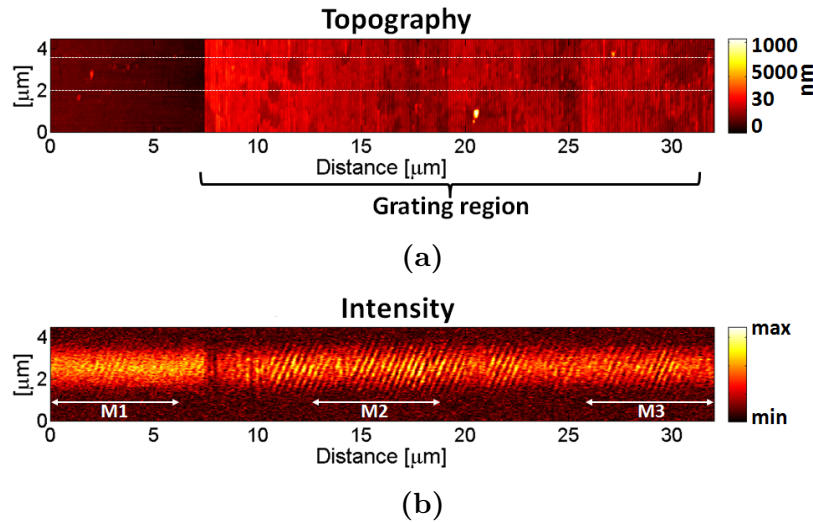


Figure 6.22: Cartes de (a) la topographie et (b) l'amplitude de la structure intégrée. L'exaltation du champ optique n'est pas dû à un mode propagatif, mais à l'exaltation collective des plasmons localisés.

guide d'onde, ainsi que dans le réseau des nanofils, mais avec un faible contraste entre eux. Après avoir traité les images obtenues dans l'espace de fréquences spatiales, on a trouvé que l'indice effectif du mode TM_0 propagé le long la structure plasmonique intégrée à une longueur d'onde $\lambda = 660$ nm, a une valeur $n_{eff} = 1.496 \pm 0.073$, proche de la valeur que nous avons obtenu avec le H-NSOM. Avec une analyse plus fine, nous avons observé à l'entrée du réseau de nanofils d'autres modes rayonnés vers l'extérieur, avec un indice effectif de $n_{eff,sup} = 1.058 \pm 0.073$ et $n_{eff,rad} = 1.35 \pm 0.073$. Cela signifie que l'exaltation du champ optique observé est dû seulement à l'excitation de la résonance du plasmon localisé, mais cette exaltation ne constitue pas un mode de propagation le long du réseau des nanofils.

Pour avoir un couplage efficace entre le mode dipolaire longitudinal et le mode fondamental TM_0 du guide d'onde à échange d'ions, il faut que la période du réseau des nanofils soit inférieure à 140 nm, et les périodes des structures fabriqués ont été supérieures à 170 nm. Avec une telle période on n'arrive qu'à exciter les plasmons localisés, mais pas de mode propagatif dans la chaîne. Une analyse plus détaillée est décrit dans le chapitre 4 de la thèse.

6.6 Résumé et conclusions

Nous avons montré qu'une chaîne de nanoparticules métalliques se comporte comme une guide d'onde plasmonique, supportant des modes de propagation qui peuvent être couplés à une guide d'ondes diélectrique formant un système optique intégré qui peut être potentiellement utilisé comme un nanocapteur.

La conception et l'analyse des structures proposées, ont été réalisées en utilisant la méthode modale de Fourier (FMM), une méthode numérique rigoureuse qui résout les équations de Maxwell dans le domaine fréquentiel. Cette méthode est basée sur l'expansion en séries de Fourier de la structure périodique, la permittivité et le champ électromagnétique. Cette formulation nous a permis de trouver les modes propres du guide d'onde plasmonique et ses relations de dispersion comme un problème valeurs propres. En plus, il a été possible de simuler la propagation du faisceau le long de la structure plasmonique intégrée.

Concernant au réseau périodique des nanofils métalliques, nous avons montré que quand les nanofils ont une hauteur courte (20 nm), le couplage entre les nanofils est dû à l'excitation d'une mode dipolaire longitudinal. Quand la hauteur des nanofils était plus grande (150 nm), deux modes ont été observés, un mode quadripolaire et un mode dipolaire transversal. En utilisant la FMM, a été montré que ces trois modes peuvent être couplés avec le mode fondamental TM₀ d'une guide d'onde diélectrique placé en proximité au réseau des nanofils.

Quand la géométrie des nanofils a été modifiée pour une forme triangulaire (nanocônes), nous avons observé la propagation d'un mode dipolaire transversal le long du réseau des nanocônes. En plus, ce mode peut être exalté seulement s'il est excité à des angles rasants ou bien, avec une guide d'onde diélectrique placé en proximité. Quand ce mode est couplé avec le mode fondamental TM₀ du guide d'onde diélectrique, a été observé que le champ optique est fortement exalté au sommet des nanocônes, ce qui représente un avantage par rapport aux nanofils, puisque le champ est fortement localisé.

Pour valider les résultats numériques donnés par la FMM, on a fabriqué des réseaux de

nanofils d'or dans la surface d'une guide d'onde à échange d'ions. Après avoir caractérisé les échantillons fabriqués en champ lointain (spectres de transmission) et en champ proche (avec le NSOM), nous avons constaté que les résultats obtenus par la FMM sont valables, c'est-à-dire, la méthode modale de Fourier est un outil appropriée pour la conception et analyse des structures plasmoniques intégrées.

6.6.1 Perspectives de travail

La série des résultats que nous avons montrés dans cette thèse suggèrent la continuation du travail de recherche, notamment dans trois axes principaux :

1. Nanofabrication :
 - (a) Réduction de la période des nanofils d'or et l'incrémentation de leur hauteur
 - (b) Fabrication des réseaux de nanocônes
2. Caractérisation du biocapteur
3. Application des systèmes plasmoniques intégrées dans d'autres domaines de recherche.

Le travail effectué dans cette thèse a contribué au développement et à la compréhension des interactions plasmoniques dans des structures optiques intégrées, une branche de la science qui est actuellement exploitée et qui promet des applications très variées et intéressantes dans différents domaines scientifiques et technologiques.

Ricardo TELLEZ LIMON

Doctorat : Optique et Nanotechnologies

Année 2014

Propagation de la lumière dans des chaînes de nanofils métalliques intégrées : vers un nano-capteur

Les plasmons de surface localisés (LSP) sont utilisés pour contrôler et concentrer le champ électromagnétique dans des petits volumes de matière. Cette propriété est très intéressante dans le contexte de la biophotonique. En effet elle permet un renforcement de l'interaction lumière-matière à l'échelle de la cellule, voire de la molécule unique. L'enjeu technologique est de proposer des composants optiques permettant de coupler efficacement la lumière dans des modes plasmoniques localisés et d'améliorer la détection des signaux issus de l'interaction entre la lumière confinée et l'analyte à détecter.

Dans ce travail de thèse, nous étudions théoriquement et expérimentalement les propriétés de guidage et de confinement de la lumière dans des arrangements périodiques de nanofils métalliques de section rectangulaire ou triangulaire (nanocônes) supportant des plasmons localisés. Ces nanofils sont intégrés dans un circuit photonique qui permet un couplage efficace de la lumière. Les spectres d'extinction des résonances plasmoniques sont obtenus directement en analysant la lumière transmise dans les composants. Grâce à la méthode modale de Fourier, nous réalisons une étude théorique exhaustive des modes de Bloch plasmoniques qui se propagent grâce au couplage en champ proche des résonances de plasmons localisés. Il est démontré que pour les nanocônes métalliques le champ optique peut être fortement exalté par un effet de pointe contrôlable et remarquablement intense.

Mots clés : optique intégrée - nanophotonique - plasmons - résonance plasmonique de surface - capteurs optiques.

Light Propagation in Integrated Chains of Metallic Nanowires: Towards a Nano-sensing Device

Localized surface plasmons (LSP) are used to control and concentrate the electromagnetic field in small volumes of matter. This is a very interesting property in the context of biophotonics. Indeed, it allows an enhancement of the light-matter interaction at the cell scale, or even at a single molecule scale. The technological challenge is to propose optical devices able to efficiently couple light into localized plasmonic modes and to improve the detection of signals resulting from the interaction between the confined light and the analyte under detection.

In this thesis work, we theoretically and experimentally study the guiding and confinement properties of light in periodic arrays of metallic nanowires of rectangular and triangular (nanocones) cross section that support localized plasmons. These nanowires are integrated in a photonic circuit that enables an efficient light coupling. The extinction spectra of the plasmonic resonances are directly obtained by analyzing the transmitted light in the device. By making use of the Fourier modal method, we perform an exhaustive theoretical study of the plasmonic Bloch modes that propagate due to the near-field coupling of the localized plasmons resonances. It is demonstrated that for the metallic nanocones, the optical field can be strongly enhanced by a controllable tip effect and remarkably intense.

Keywords: integrated optics - nanophotonics - plasmons (physics) - surface plasmon resonance - optical detectors.

Thèse réalisée en partenariat entre :

